
SEARCH FOR TOP SQUARKS VIA ALL-HADRONIC DECAY CHANNELS WITH HEAVY OBJECT TAGGING



Thesis: Doctor of Philosophy
Physics and Astronomy
Rice University, Houston, Texas (December 2019)

RICE UNIVERSITY

**Search for Top Squarks via All-Hadronic Decay
Channels with Heavy Object Tagging**

by

Matthew Cavenaugh Kilpatrick

A THESIS SUBMITTED
IN PARTIAL FULFILLMENT OF THE
REQUIREMENTS FOR THE DEGREE

Doctor of Philosophy

APPROVED, THESIS COMMITTEE:

Karl Ecklund, Chair
Professor of Physics and Astronomy

Paul Padley
Professor of Physics and Astronomy

David Scott
Noah Harding Professor

Houston, Texas

December, 2019

ABSTRACT

Search for Top Squarks via All-Hadronic Decay Channels with Heavy Object
Tagging

by

Matthew Cavenaugh Kilpatrick

A search for the top squark from direct production via the all-hadronic decay channel is performed on 136.7 fb^{-1} at a center-of-mass energy of 13 TeV from Run 2 of the LHC. Events are categorized into exclusive regions designed to optimize the different search topologies of the analysis. The analysis concentrates on identifying heavy objects such as top quarks and W boson, from their decays using a custom tagger for resolved tops and multivariate methods for others. A low Δm spectra is enhanced using the soft b quark jet transverse momentum which is typical of signal in a boosted regime with initial-state radiation. We then provide exclusion limits for each signal in the simplified models with multiple decay products.

Chapter 1

Acknowledgements

I would like to thank my parents, John and Laura Kilpatrick, for all of their support. My dog Kal-El for distracting me when I was working for too long. The Rice Bonner lab for providing the guidance and materials to complete this analysis.

Contents

Abstract	ii
1 Acknowledgements	iii
List of Figures	viii
List of Tables	xi
2 Introduction	1
2.1 Motivation	1
2.2 Search	2
3 Supersymmetry and the Standard Model	4
3.1 The Standard Model	4
3.1.1 The Fundamental Particles	4
3.1.2 Quantum Field Theory	5
3.1.3 Noether's Theorem	5
3.1.4 Quantum Electrodynamics (QED)	7
3.1.5 Quantum Chromodynamics	10
3.1.6 Weak Force	12
3.1.7 The Electroweak Lagrangian	14
3.1.8 The Higgs Mechanism	16
3.1.9 Electroweak	17
3.1.10 The Standard Model Lagrangian	19
3.2 Fundamental Problems in the Standard Model	20
3.2.1 Dark Matter	21
3.2.2 Hierarchy Problem	22

3.2.3	Grand Unified Theory	23
3.3	Supersymmetry	24
3.3.1	Supermultiplets and Chirality	26
3.3.2	Minimal Supersymmetric Standard Model	26
3.3.3	R Parity	28
3.3.4	Mass Spectra	29
3.3.5	SUSY Searches	30
3.4	Current SUSY Results	31
3.5	What are we looking for? And why?	36
4	Compact Muon Solenoid	37
4.1	The Detector	37
4.1.1	Tracker	39
4.1.2	Electromagnetic Calorimeter	43
4.1.3	Hadronic Calorimeter	45
4.1.4	Superconducting solenoid	45
4.1.5	Muon Chambers	46
4.2	Detector Methods	47
5	Search Strategy	48
5.1	Physics Objects	48
5.1.1	Jets	48
5.1.2	Heavy Object Tagging	50
5.1.3	Missing Transverse Momentum	53
5.1.4	H_T	54
5.1.5	Soft b -Tagging	54
5.1.6	Initial-state Radiation	56
5.1.7	Electron and Muon Identification	56
5.1.8	Tau Identification	58
5.1.9	Transverse Energy between b quarks and p_T^{miss}	59
5.2	Samples and Filters	60

5.3	Baseline Selection	60
5.3.1	Search Regions	62
6	Top Squark Production and Backgrounds	67
6.1	Production and Decay Modes	67
6.2	Standard Model Background	69
6.3	Lost Lepton	70
6.3.1	Combining All Run 2 Eras	71
6.3.2	Transfer Factors	71
6.4	Z Boson Decay to Neutrinos	88
6.4.1	Prediction Method	88
6.4.2	Combination of Eras and Prediction	89
6.5	Quantum Chromodynamic Events	103
6.5.1	QCD Local Smearing	105
6.5.2	QCD Corrections	106
6.5.3	QCD Prediction	106
6.6	Rare Interactions	122
7	Uncertainties and Estimation	124
7.1	Systematic Uncertainties	124
7.2	Validation	127
7.3	Statistics	132
7.3.1	Profile Likelihood Asymptotic Approximation	132
7.4	Higgs Combined Tool	133
7.4.1	Observed Limits	134
7.4.2	Expected Limits	135
7.5	Combination of Search region	135
7.6	Results	141
8	Conclusions	142
8.1	Interpreting Results	142

8.2 Outlook	142
A Tau Multivariate Analysis	144
Appendix A	144
B Samples	149
B.0.1 Filters	150
C List of Acronyms and Initialisms	153
Bibliography	155

Figures

3.1	Standard Model particles	6
3.2	QED Feynman Diagrams	9
3.3	QCD Feynman Diagrams	12
3.4	Weak Feynman Diagrams	14
3.5	Hierarchy Problem Loop Correction	22
3.6	GUT Force Energy Dependence	24
3.7	Supersymmetry and Standard Model Particles	25
3.8	Top squark mass hierarchy	29
3.9	T2tt Limits	32
3.10	T2bW Limits	33
3.11	T2tb Limits	33
3.12	T2fb _d Limits	34
3.13	T2bWC Limits	34
3.14	T2bWC Limits	35
3.15	T2tt Limits for all decay modes	35
4.1	CMS Cross Section	38
4.2	CMS Tracker Geometry	39
4.3	Pixel Modules	41
4.4	FED Throughput	42
4.5	Strip Tracker Module	44
4.6	Muon Chambers	47
5.1	Jet Hadronization	50

5.2	Anti- k_T Jet Reconstruction	51
5.3	Top Decays	52
5.4	Secondary Vertex Diagram	55
5.5	Top Squark Decay Modes	64
6.1	Direct stop production	68
6.2	Gluino mediated stop production	69
6.3	$t\bar{t}$ Production	70
6.4	Lost Lepton LM Eras	72
6.5	Lost Lepton HM Eras	73
6.6	Transfer Factor Comparison	75
6.7	Separated Transfer Factor Comparison	76
6.8	Lost Lepton LM Control Region $N_b = 0$	77
6.9	Lost Lepton LM Control Region $N_b = 1$	82
6.10	Lost Lepton HM Control Region	83
6.11	Lost Lepton HM Control Region $N_b = 1$	84
6.12	Lost Lepton HM Control Region $N_b = 2$ with 1 heavy object	85
6.13	Lost Lepton HM Control Region $N_b = 2$ with 2 heavy objects	86
6.14	Lost Lepton HM Control Region $N_b \geq 3$ with 1 heavy object	87
6.15	$Z \rightarrow \nu\nu$ Normalization in low Δm for muons	91
6.16	$Z \rightarrow \nu\nu$ Normalization in high Δm for muons	92
6.17	$Z \rightarrow \nu\nu$ Normalization in low Δm for electronss	93
6.18	$Z \rightarrow \nu\nu$ Normalization in high Δm for electrons	94
6.19	$Z \rightarrow \nu\nu$ Shape by Era	95
6.20	$Z \rightarrow \nu\nu$ Shape by Era	96
6.21	$Z \rightarrow \nu\nu$ Normalization Low Δm Comparisons	97
6.22	$Z \rightarrow \nu\nu$ Normalization High Δm Comparisons	98
6.23	Light Jet Response	107
6.24	B Jet Response	108
6.25	QCD Jet Response Scale Factor	109
6.26	QCD Jet Response Correction	110

6.27	QCD Multijet LM Control Region $N_b = 0$	111
6.28	QCD Multijet LM Control Region $N_b = 1$	112
6.29	QCD Multijet HM Control Region	113
6.30	QCD Multijet HM Control Region $N_b = 1$	114
6.31	QCD Multijet HM Control Region $N_b = 2$ with 1 heavy object	115
6.32	QCD Multijet HM Control Region $N_b = 2$ with 2 heavy objects	116
6.33	QCD Multijet HM Control Region $N_b \geq 3$ with 1 heavy object	117
6.34	Diboson and $t\bar{t}Z$ Feynman Diagrams	122
6.35	$t\bar{t}Z$ Normalization Comparisons	123
7.1	LM Validation Region	130
7.2	Lost Lepton HM Control Region	131
7.3	Example Datacard of T2tt(175,1)	136
7.4	Example Datacard of LL CR	137
7.5	Example Datacard of $Z \rightarrow \nu\nu$ CR	137
7.6	Example Datacard of QCD CR	137
7.7	Run 2: T2tt Limits	139
7.8	Run 2: T2tt Limits	140
A.1	Tau MVA ROC Curve	145
A.2	Tau MVA Discriminator	146

Tables

3.1	Fermion Currents	8
3.2	Chiral supermultiplets for fermions and bosons	27
3.3	Chiral supermultiplets for gauge bosons	27
5.1	High Δm Search Regions	65
5.2	Low Δm Search Regions	66
6.1	LL LM CR bins 0-52	78
6.2	LL HM CR bins 53-93	79
6.3	LL HM CR bins 94-134	80
6.4	LL HM CR bins 135-182	81
6.5	$Z \rightarrow \nu\nu$ LM CR bins 0-52	99
6.6	$Z \rightarrow \nu\nu$ HM CR bins 53-93	100
6.7	$Z \rightarrow \nu\nu$ HM CR bins 94-134	101
6.8	$Z \rightarrow \nu\nu$ HM CR bins 135-182	102
6.9	QCD LM CR bins 0-52	118
6.10	QCD HM CR bins 53-93	119
6.11	QCD HM CR bins 94-134	120
6.12	QCD HM CR bins 135-182	121
7.1	Low Δm Search Regions	127
7.2	High Δm Search Regions	128
A.1	TauMVA Background Optimization	147

A.2	TauMVA Signal Optimization	147
A.3	Tau Identification Comparisons	147
B.1	Data Samples	150
B.2	Standard Model Samples	151
B.3	Signal Samples	152

Chapter 2

Introduction

The Standard Model (SM) [1] is a robust framework that allows for accurate predictions of processes involving the interactions of elementary particles. It has been developed over the course of many decades, which involved many additions such as three generations of quarks and leptons and the combination of Electromagnetism and the Weak force into a single theory. Unfortunately, we have evidence for phenomena that is not explained by the SM and eludes physicists for intend to do a search for a potential particle, that new models have, beyond the curr

2.1 Motivation

Through various methods of experiment, we have seen that the elementary particles in the SM do not explain all of the known matter in the universe. From galactic velocity rotational curves we can deduce that the mass of galaxies must be much more than the visible matter that can be measuredmust act quite weakly with the three forces of the SM, but can still be quite important for gravitational effects. There are many theories beyond the SM that can explain these effects, but we will concentrate on Supersymmetry (SUSY) [2–10] because of the potential for a dark matter candidate [11,12], a solution to the hierarchy problem, and a potential Grand Unified Theory (GUT) [13–15].

SUSY allows for every fermion to have a bosonic partner, and vice-versa, which

has all of the same quantum numbers except for a difference of $\frac{1}{2}$ -integer spin. We know that since it has not yet been found that the theory must be a broken symmetry, such that the masses of the SUSY partners must have a higher mass than the SM particle. One of the main aspects of simplified SUSY, is the conservation of R -parity, which implies the existence of a Lightest Supersymmetric Particle (LSP). There are other models with R -parity violating decays [16, 17], but we are not considering them. This LSP could be a potential dark matter candidate since it is stable and weakly interacting.

The hierarchy problem is due to the loop interactions of massive quarks with the Higgs boson. This coupling causes a quadratic divergence of the Higgs mass, m_H , and can only be renormalized by fine tuning the coupling parameters. A potential solution is the coupling of an additional bosonic particle to the quarks. This additional coupling allows for a cancellation of quadratic divergence into a logarithmic divergence, which is then renormalizable by the normal methods. This can renormalize the mass of the Higgs boson to the measured value of $m_H = 125.18$ GeV [18–21] that was discovered in 2012. Finally, SUSY also allows for a mechanism for a potential GUT. The additional superpartners allow for the three forces of the SM to converge at a large energy scale of the order 10^{16} GeV. We now need to develop a search strategy to try and detect these potential SUSY particles.

2.2 Search

There are many possible searches for SUSY particles. In the Minimal Supersymmetric Standard Model (MSSM) [22], it can be determined that the lightest squark that can be produced at the Large Hadron Collider (LHC) is the top quark, \tilde{t}_1 , which will then decay into SM particles and the LSP. We are developing an all-hadronic

search to find the \tilde{t}_1 which will be as inclusive as possible, so we will include all possible decay modes to get additional limits or possible detection.

Due to the all hadronic aspect of the decay, the main backgrounds are caused by, a lost lepton due to a lepton being missed for various reasons, $Z \rightarrow \nu\nu$ background where the missing energy is caused by the neutrinos escaping the detector, Quantum Chromodynamics (QCD) background which can be caused by the mis-measurement of jets in the event, and a rare background caused by many different types of processes which are estimated by a three lepton method of identification. We have developed 183 search regions to look for the top squark, \tilde{t}_1 . This is then used to get a statistical estimation of the limits on the cross section for each of the processes that we are interested in searching. In the following chapters, we will: look into the derivation of the SM and motivations for SUSY; provide a description of the Compact Muon Solenoid (CMS) detector and the various subdetectors; next the description of the object selection and search strategy for the analysis; the methods of each individual background are described; and the description and analysis of the results and limits.

Chapter 3

Supersymmetry and the Standard Model

The fundamental theory of particle physics, known as the SM, can predict interactions between the fundamental particles in our universe. With these predictions we can look for and confirm these processes, but there are some aspects of the universe that have not yet been explained. In this Chapter, we will analyze the SM, look at some specific shortcomings, and introduce supersymmetry as a possible solution.

3.1 The Standard Model

After decades of theoretical and experimental research the SM has been developed into a theory that explains the Electromagnetic (EM), Strong, and Weak forces. The SM has not yet been able to include Gravity within the theory. With the robust theoretical and experimental methods used in the SM, we have discovered new elementary particles and predicted others.

3.1.1 The Fundamental Particles

All matter can be explained by three kinds of elementary particles: leptons, quarks, and gauge bosons. Each of these can be distinguished by various quantum properties. The leptons and quarks are fermions, which are particles that have half-integer spin. Leptons are particles that only interact with the EM and Weak force, while quarks interact with all three forces of the SM. The gauge bosons are the force

carriers for each respective force and have integer spin.

There are three generations of leptons and quarks which are differentiated by a charge $\pm e$, the charge of an electron, and the mass of the respective lepton. Leptons have three different charged particles: electron (e), muon (μ), and tau (τ), with each charged particle having a corresponding neutrino (ν) of the same flavor, see Fig. 3.1 [23]. Quarks are also separated into three generations of doublets, the down-type ($-\frac{1}{3}e$): down (d), strange (s), and bottom (b) and up-type ($\frac{2}{3}e$): up (u), charm (c), and top (t), see fig 3.1. Each of the quarks has a color associated with it which is analogous to an electric charge, except there are three color charges: red, blue, and green [23].

3.1.2 Quantum Field Theory

The interactions of all these particle fields are described by quantized fields whose operators describe the creation and annihilation of particles. Each of the forces of the SM have a corresponding gauge boson which is described by a quantized gauge field, see Fig. 3.1. The most well-known particle field is the EM field and its interactions. In order to write a concise theory of the particles in the SM, the symmetry and conservation laws of the SM can be derived by starting with Noether's Theorem.

3.1.3 Noether's Theorem

Noether's theorem states, "to each symmetry of a local Lagrangian, there corresponds a conserved current" [25]. This can be done by allowing for an infinitesimal symmetry variation. Requiring the Lagrangian to be invariant under $\phi(x) \rightarrow \phi'(x) = \phi(x) + \alpha\Delta\phi(x)$, where α is infinitesimal real parameter and $\Delta\phi$ is a deformation to

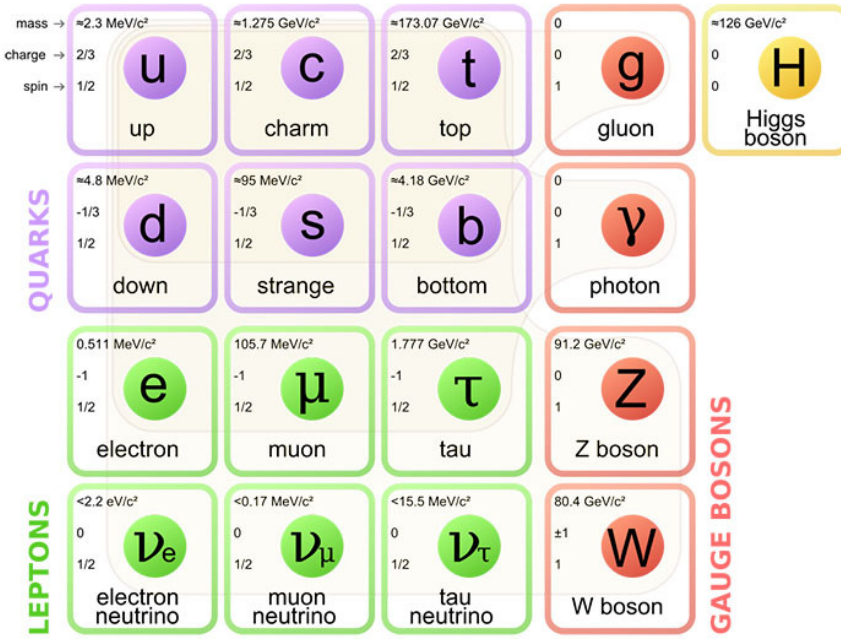


Figure 3.1 : The fundamental particles of the Standard Model. There are three generations of quarks and leptons. Along with the five bosons, where four of them relate to the interactions of the three forces included in the SM: Electromagnetism, the Weak force, and the Strong force and the final being the Higgs boson [24].

the field, up to a 4-divergence, the Lagrangian transforms as,

$$\mathcal{L}(x) \rightarrow \mathcal{L}(x) + \alpha \partial_\mu \mathcal{J}^\mu(x), \quad (3.1)$$

where \mathcal{J}^μ is a current. If we apply the Euler-Lagrange equation,

$$\partial_\mu \left(\frac{\partial \mathcal{L}}{\partial (\partial_\mu \phi)} \right) - \frac{\partial \mathcal{L}}{\partial \phi} = 0, \quad (3.2)$$

to Eqn. 3.1 with the addition of the fluctuation of the particle field. After some simplification we get a conserved current [25, 26],

$$\begin{aligned} \partial_\mu j^\mu(x) &= 0, \text{ where} \\ j^\mu(x) &= \frac{\partial \mathcal{L}}{\partial (\partial_\mu \phi)} \Delta \phi - \mathcal{J}^\mu. \end{aligned} \quad (3.3)$$

We see from the above equation that the current $j^\mu(x)$ of the Lagrangian is conserved. Now let's apply this to the particle fields of the SM [25, 26].

3.1.4 Quantum Electrodynamics (QED)

First, we start with the assumption that the wave function $\psi(x)$ should transform as,

$$\psi(x) \rightarrow e^{i\alpha(x)} \psi(x), \quad (3.4)$$

where $\alpha(x)$ has an arbitrary dependence on space and time because we want the theory to be invariant in space and time. If one were to include this into the Lagrangian for a spin-1/2 particle in a vacuum,

$$\mathcal{L}_{QED}^{vac} = i\bar{\psi} \gamma^\mu \partial_\mu \psi - m\bar{\psi} \psi \quad (3.5)$$

Type	Form	Components	Space Inversion
Scalar	$\bar{\psi}\psi$	1	+ under P
Vector	$\bar{\psi}\gamma^\mu\psi$	4	Space comps.: - under P
Tensor	$\bar{\psi}\sigma^{\mu\nu}\psi$	6	
Axial Vector	$\bar{\psi}\gamma^5\gamma^\mu\psi$	4	Space comps.: + under P
Pseudoscalar	$\bar{\psi}\gamma^5\psi$	1	- under P

Table 3.1 : A table showing all forms of the fermion currents. These can be symmetric under parity transformation in all or some components [26].

where the γ^μ are the Dirac matrices, ∂_μ is the partial derivative, $\bar{\psi}$ is the hermitian conjugate of the wave function ψ , and m is the mass of the particle [25, 26]. As a small aside, the bilinear quantities $\bar{\psi}(4 \times 4)\psi$ have certain properties under Lorentz transformations when the 4×4 matrix is a γ -matrices. These are of the form,

$$\gamma^0 = \begin{bmatrix} \mathbf{I} & 0 \\ 0 & -\mathbf{I} \end{bmatrix}, \boldsymbol{\gamma} = \begin{bmatrix} 0 & \boldsymbol{\sigma} \\ -\boldsymbol{\sigma} & 0 \end{bmatrix}, \gamma^5 = \begin{bmatrix} 0 & \mathbf{I} \\ \mathbf{I} & 0 \end{bmatrix}, \quad (3.6)$$

where the \mathbf{I} is the identity matrix and $\boldsymbol{\sigma}$ are the Dirac matrices [25, 26]. We can combine the first two parts of Eqn. 3.6 and write it compactly as γ^μ where $\mu = 0, 1, 2$, and 3 . The possible interesting quantities of the above transformations are shown in Table 3.1.

To allow for the field to be invariant, we must include a derivative, D_μ , that is covariant under phase transformations,

$$D_\mu \equiv \partial_\mu - ieA_\mu. \quad (3.7)$$

The covariant derivative includes the vector field A_μ which must also transform

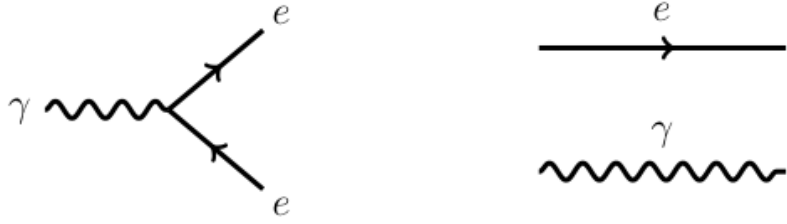


Figure 3.2 : The possible Feynman diagrams in QED. The e can be replaced with any spin-1/2 charged particle. We see that the electron and photon can propagate freely in space or a vertex with one photon and a particle-antiparticle pair is allowed [27].

as [25, 26],

$$A_\mu \rightarrow A_\mu + \frac{1}{e} \partial_\mu \alpha. \quad (3.8)$$

So after requiring that there be a local gauge transformation, we were forced to introduce a vector field A_μ , called the gauge field, which couples to Dirac particles in the same way as the photon field. We will think of this new field as the real photon field, which means we need to add a kinematic energy portion to the Lagrangian. This kinematic term will be invariant under Eqn. 3.8, which leads us to the final representation of the QED Lagrangian which can be written down concisely as,

$$\mathcal{L}_{QED} = \bar{\psi}(i\gamma^\mu \partial_\mu - m)\psi + e\bar{\psi}\gamma^\mu A_\mu \psi - \frac{1}{4}F^{\mu\nu}F_{\mu\nu}, \quad (3.9)$$

where A_μ is the EM field operator and $F^{\mu\nu}$ is the EM field tensor. This Lagrangian describes the interactions between spin-1/2 charged particles and the $U(1)$ EM force. Each of the parts of this equation is Lorentz invariant which allows this to be true in all reference frames. We also find that the conserved current of QED is the electric charge, $Q = \int d^3x j^0$ [25, 26].

From the QED Lagrangian Eqn. 3.9, we see that particles that interact elec-

tromagnetically can interact with the photon. This can be shown as a Feynman diagram, see Fig. 3.2, which has a vertex interaction with a photon and a particle-antiparticle pair. These, and the inclusion of freely moving particles, are the basic types of Feynman diagrams for QED.

3.1.5 Quantum Chromodynamics

Let's now transition from the description of the $U(1)$ EM field to the $SU(3)$ Quantum Chromodynamic (QCD) field and the transformation of quark fields. A quark in a vacuum is described by,

$$\mathcal{L}_{QCD}^{vac} = \bar{q}_j(i\gamma^\mu \partial^\mu - m)q_j, \quad (3.10)$$

where q_1, q_2 , and q_3 are quark fields with three possible color charges [25, 26]. From this we want to require that the field is again invariant under another local phase transformation such as,

$$q(x) \rightarrow Uq(x) \equiv e^{i\alpha_a(x)T_a}q(x), \quad (3.11)$$

where U is a 3×3 unitary matrix, T_a with $a = 1, \dots, 8$ are a set of linearly independent traceless 3×3 matrices, and α_a are the group parameters. Since the generators T_a do not necessarily commute with each other, we can see that it is a non-Abelian transformation and the commutator can be represented as,

$$[T_a, T_b] = if_{abc}T_c, \quad (3.12)$$

where f_{abc} are constants [25, 26].

We need to impose $SU(3)$ local gauge invariance on Eqn. 3.10, to allow for the following phase transformations,

$$\begin{aligned} q(x) &\rightarrow (1 + i\alpha_a(x)T_a)q(x), \\ \partial_\mu q &\rightarrow (1 + i\alpha_a T_a)\partial_\mu q + iT_a q \partial_\mu \alpha_a. \end{aligned} \quad (3.13)$$

From this it seems straight forward that we can proceed in exactly the same manner as QED, which is to add a transformation to the derivative,

$$D_\mu = \partial_\mu + ig_Q T_a G_\mu^a, \quad (3.14)$$

where the field G_μ^a , which are the gluons, transforms as,

$$G_\mu^a \rightarrow G_\mu^a - \frac{1}{g_Q} \partial_\mu \alpha_a, \quad (3.15)$$

where g_Q is the coupling strength of QCD interactions. This will give us a similar Lagrangian to the QED one described above, but this is not sufficient for a non-Abelian gauge transformation and it does not produce a gauge-invariant Lagrangian. One final transformation is required for the G_μ^a fields [25],

$$G_\mu^a \rightarrow G_\mu^a - \frac{1}{g_Q} \partial_\mu \alpha_a - f_{abc} \alpha_b G_\mu^c. \quad (3.16)$$

This finally gives us a gauge invariant kinetic energy term for all the G_μ^a fields and thus we can write the QCD interactions as,

$$\mathcal{L}_{QCD} = \bar{q}(i\gamma^\mu \partial_\mu - m)q - g_Q(\bar{q}\gamma^\mu T_a q)G_\mu^a - \frac{1}{4}G_{\mu\nu}^a G_a^{\mu\nu}. \quad (3.17)$$

From the QCD Lagrangian Eqn. 3.17, we can see that it includes all of the same

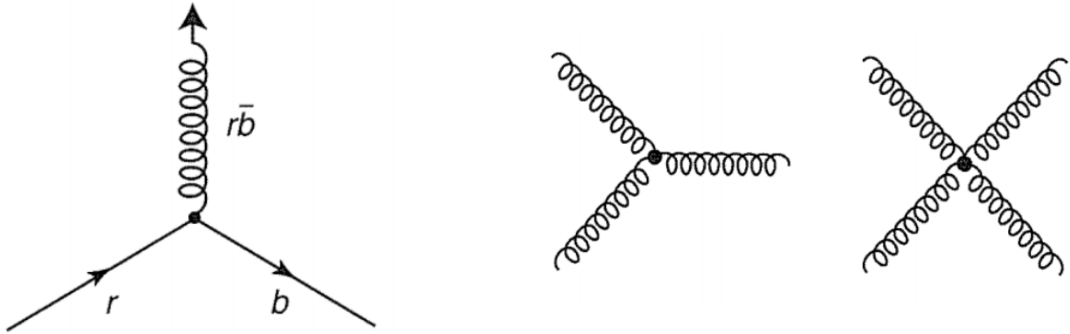


Figure 3.3 : The possible Feynman diagrams in QCD where each vertex needs to conserve color charge. Here is just an example of a red-blue vertex and QCD also includes a 3- and 4-vertex with gluons [23].

interactions we showed for QED, but also includes a $SU(3)$ interaction due to the quark-gluon interactions with a certain color charge, see Fig. 3.3. However, QCD also included a 3- and 4-vertex interaction between the gluons, which arises due to the non-Abelian nature of the force [25, 26]. From this, it is easy to tell that QCD is a much more complicated theory. We seem to be missing a vital part of the SM, specifically a theory for the Weakly interacting processes which is mediated by the massive bosons, W and Z from Fig. 3.1.

3.1.6 Weak Force

The Weak force is responsible for nuclear decay. The Weak force has an interaction of the type $\frac{1}{2}\gamma^\mu(1 - \gamma^5)$, so it is a $V - A$ interaction with $SU(2)$ symmetry. From this, we can conclude that it violates Parity (P). Parity is a transformation from $(x, y, z) \rightarrow (-x, -y, -z)$ or space inversion. Since it violates Parity, the next step is to consider a conservation of CP , where C is charge conjugation (particle-to-antiparticle).

Now the Weak force is mediated by two vector bosons, W and Z , see Fig. 3.1. These are unlike the other forces because these vector bosons have a large mass of $m_W = 80.379 \pm 0.012$ GeV and $m_Z = 91.1876 \pm 0.0021$ GeV [28]. The W boson is a charged particle and interacts with many nuclear decays.

The W boson interacts very interestingly for quarks in the SM. There is a mixing of flavors of quarks for particles. They will mix partners between up-type and down-type particles [29]. The interactions for the generalized three generations of quarks is known as the Cabibbo-Kobayashi-Maskawa (CKM) matrix [23, 26],

$$\begin{bmatrix} d' \\ s' \\ b' \end{bmatrix} = \begin{bmatrix} V_{ud} & V_{us} & V_{ub} \\ V_{cd} & V_{cs} & V_{cb} \\ V_{td} & V_{ts} & V_{tb} \end{bmatrix} \begin{bmatrix} d \\ s \\ b \end{bmatrix}, \quad (3.18)$$

where for example, V_{ud} is the coupling of u to d which is exactly ($d \rightarrow u + W^-$). This matrix can be reduced to a form which has three generalized Cabibbo angles ($\theta_{12}, \theta_{23}, \theta_{13}$) and a phase factor (δ). The coupling between the third generation does not mix with the other two generations. For the moment, we can only determine these values from experimentation.

The Z boson is known as the neutral current. This boson mediates forces between particles and their respective antiparticles, see Fig. 3.4. This interaction for the neutral weak force is $\gamma^\mu (c_V^f - c_A^f \gamma^5)$ which is quite similar to the charged weak interaction, but differs by the constants c_V^f and c_A^f . The Weak interactions are shown in Fig. 3.4. We see the charged W boson interacts with the charged leptons and their respective neutrinos or allows for flavor changing interactions with quarks. Even though the neutral Z boson interacts with a $V - A$ interaction we can still replace the γ in any QED Feynman diagram with a Z [23, 26].

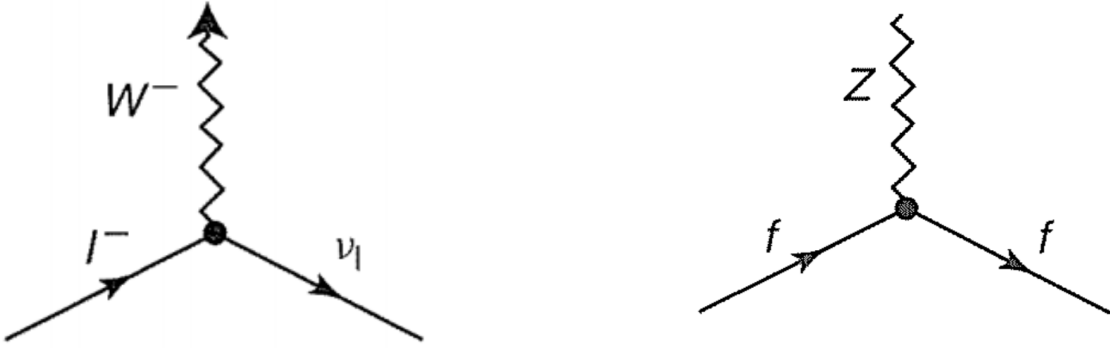


Figure 3.4 : Feynman diagram for Neutral Weak interaction and the charged Weak current [23].

3.1.7 The Electroweak Lagrangian

The simplest group for the Electroweak interaction is $SU(2)_L \times U(1)_Y$, which will give the left-handed interactions in doublets with the addition of massive gauge bosons W and Z with a massless photon. We first consider the free Lagrangian,

$$\mathcal{L} = \bar{\psi}_j \gamma^\mu \psi_j, \quad (3.19)$$

where j is the fermion wave function [23, 26]. We are not including the mass parameter because it would cause the left and right-handed parts to mix. This is assumed to transform under the global invariant,

$$\begin{aligned} \chi_L &\rightarrow \chi'_L = e^{i\frac{\tau_a}{2}\alpha^a(x) + i\beta(x)Y} \chi_L, \\ \psi_R &\rightarrow \psi'_R = e^{i\beta(x)Y} \psi_R \end{aligned} \quad (3.20)$$

where the transformation $e^{i\frac{\tau_a}{2}\alpha^a(x)}$ with $a = 1, 2, 3$ is the $SU(2)_L$ transformation and only acts on the left-handed doublet. The next step is to require that the

Lagrangian is invariant under local $SU(2)_L \times U(1)_Y$. We allow for the following covariant derivatives [26],

$$\begin{aligned} D_\mu \psi_1 &= [\partial_\mu - ig_W \frac{\tau_a}{2} W_\mu^a - ig'_W y_1 B_\mu] \psi_1 \\ D_\mu \psi_2 &= [\partial_\mu - ig'_W y_2 B_\mu] \psi_2 \\ D_\mu \psi_3 &= [\partial_\mu - ig'_W y_3 B_\mu] \psi_3 \end{aligned} \quad , \quad (3.21)$$

where g_W and g'_W are the Weak force coupling constants while W_μ^a and B_μ are four gauge bosons and can be the possible candidates for W^\pm , Z and γ [23, 26].

Just like the above descriptions, the fields need to transform along with the wave functions and derivatives. These transformations are,

$$\begin{aligned} B_\mu \rightarrow B'_\mu &= B_\mu + \frac{1}{g'_W} \partial_\mu \beta(x) \\ W_\mu \rightarrow W'_\mu &= U_L W_\mu U_L^\dagger - \frac{1}{g_W} \partial_\mu U_L U_L^\dagger \end{aligned} \quad , \quad (3.22)$$

where $U_L = e^{i \frac{\tau_a}{2} \alpha^a(x)}$ [23, 26]. These transformations are similar to the QED and QCD transformation. If we include all of these invariant transformations in the free Weak Lagrangian Eqn. 3.19, we get a free invariant Lagrangian, but this does not allow us to include a mass term for the fermions. Therefore, it is not a viable procedure to include the Electroweak interactions into the model. In order to do this we must include the Higgs Mechanism.

3.1.8 The Higgs Mechanism

We are interested in the spontaneous symmetry breaking of a local $SU(2)$ group. Specifically, the following Lagrangian,

$$\mathcal{L} = (\partial_\mu \phi)^\dagger (\partial^\mu \phi) - \mu^2 \phi^\dagger \phi - \lambda (\phi^\dagger \phi)^2, \quad (3.23)$$

with ϕ being a $SU(2)$ doublet of complex scalar fields,

$$\phi = \frac{1}{2} \begin{bmatrix} \phi_1 + i\phi_2 \\ \phi_3 + i\phi_4 \end{bmatrix}, \quad (3.24)$$

and is invariant under global $SU(2)$ phase transformations $\phi \rightarrow e^{i\alpha_a \tau_a/2} \phi$ [26]. To allow for local invariance, we first allow for a covariant derivative,

$$D_\mu = \partial_\mu + ig_W \frac{\tau_a}{2} W_\mu^a, \quad (3.25)$$

where we now have three gauge fields, W_μ^a . If we assume an infinitesimal gauge transformation for the $SU(2)$ doublet $\phi(x) \rightarrow \phi'(x) = (1 + i\frac{\tau_a}{2} \alpha^a(x))\phi(x)$, then the gauge fields will transform as,

$$W_\mu^a \rightarrow W_\mu^a - \frac{1}{g_W} \partial_\mu \alpha_a - f_{abc} \alpha_b W_\mu^c. \quad (3.26)$$

You can see that Eqn. 3.26 is similar to Eqn. 3.16 where we have replaced the QCD gauge field with the three gauge fields W_μ^a [23, 26]. If we include these locally

invariant transformations into the above $SU(2)$ Lagrangian we get,

$$\mathcal{L} = (\partial_\mu \phi + ig_W \frac{1}{2} \tau_a W_\mu^a \phi)^\dagger (\partial^\mu \phi + ig_W \frac{1}{2} \tau_a W^{a\mu} \phi) - \mu^2 \phi^\dagger \phi + \lambda (\phi^\dagger \phi)^2 - \frac{1}{4} W_{\mu\nu}^a W^{a\mu\nu}, \quad (3.27)$$

where the gauge field kinetic term has been included at the end [23, 26]. The most interesting regions of this Lagrangian is when $\mu^2 < 0$ and $\lambda > 0$, and the potential has a minimum at $\phi^\dagger \phi = -\frac{\mu^2}{2\lambda}$. With this, we will expand the potential around the minimum and require that,

$$\phi_1 = \phi_2 = \phi_4 = 0, \phi_3^2 = -\frac{\mu^2}{2\lambda} \equiv v^2. \quad (3.28)$$

This is the spontaneous symmetry breaking of the $SU(2)$ symmetry, because of this we are able to substitute an expansion for the field,

$$\phi = \sqrt{\frac{1}{2}} \begin{bmatrix} 0 \\ v + h(x) \end{bmatrix}, \quad (3.29)$$

with this specific transformation of the $SU(2)$ doublet and the simplification of Eqn. 3.27, the only remaining field is $h(x)$ which is referred to as the Higgs field. This is what is known as the Higgs Mechanism for a $SU(2)$ symmetry.

3.1.9 Electroweak

We want to include the Higgs Mechanism into the weak isospin and weak hypercharge, $SU(2)_L \times U(1)_Y$, transformations of electroweak interactions [23, 26]. Weak isospin and hypercharge is defined as $I_3 = \frac{1}{2}(n_u - n_d)$ and $Y \equiv B + S$, respectfully, where n_u, n_d is the number of up or down quarks, B is the baryon number, and S is the strangeness. The weak isospin triplet for weak currents can be written down

using Eqn. 3.27,

$$J_\mu^i(x) = \bar{\chi}_L \gamma_\mu \frac{1}{2} \tau_i \chi_L, \text{ with } i = 1, 2, 3. \quad (3.30)$$

Since this is a current we can calculate the charge by integrating all of space, $T^i = \int J_0^i(x) d^3x$, which will give us the generators of the $SU(2)_L$ symmetry $[T^i, T^j] = i\epsilon_{ijk}T^k$ [23, 26]. Weak hypercharge, Y , is then defined by $Q = T^3 + \frac{Y}{2}$ where Q is the charge and T^3 is the third component of the weak isospin. The weak hypercharge is the conserved quantity of the $U(1)_Y$ symmetry.

First, we need to include the coupling of the Weak current J_μ^a and the gauge field $W^{a\mu}$ such that,

$$-ig_W J_\mu^a W^{a\mu} = -ig_W \bar{\chi}_L \gamma_\mu T^a W^{a\mu} \chi_L, \quad (3.31)$$

which is the basic interaction for the $SU(2)_L$ symmetry [23, 26]. In this basic interaction, we can see that the electric charge that we know from EM is a combination of the Weak isospin and hypercharge and the gauge bosons mix to produce the massless photon that couples to the electric charge. There are three additional massive bosons, one neutral and two charged, that couple to the other combinations of Weak isospin and hypercharge [23, 26]. Then, we also need to include the weak hypercharge current with the fourth vector boson B^μ ,

$$-i\frac{g'_W}{2} j_\mu^Y B^\mu = -ig'_W \bar{\psi} \gamma_\mu \frac{Y}{2} \psi B^\mu, \quad (3.32)$$

where the operators T^a and Y are generators for the $SU(2)_L$ and $U(1)_Y$ gauge transformations, respectively. Now we combine the two symmetries with the transformations of the left and right hand components of ψ and from this we can write down the contributions of the two gauge fields W_μ^3 and B_μ and the missing angle θ_W to

find the interactions of the two neutral currents [23, 26]. The physical fields are thus,

$$-ig_W J_\mu^3 W^{3\mu} - i \frac{g'_W}{2} j_\mu^Y B^\mu = -ie j_\mu^{em} A^\mu - \frac{ie}{\sin\theta_W \cos\theta_W} [J_\mu^3 - \sin^2\theta_W j_\mu^{em}] Z^\mu. \quad (3.33)$$

From this we can write down the Electroweak Lagrangian, for any fermion that interacts with the field. Moreover, we can formulate the Higgs mechanism, such that we can calculate the theoretical masses of the gauge bosons and fermions as,

$$\begin{aligned} M_W &= \frac{1}{2} v g_W \\ M_Z &= \frac{1}{2} v \sqrt{g_W^2 + g'_W^2}. \end{aligned} \quad (3.34)$$

However, these masses cannot be predicted since they depend on the values from the chosen Higgs field.

3.1.10 The Standard Model Lagrangian

Noether's theorem has been used to confirm that QED, QCD, and the Weak force are invariant under local and global gauge transformations. This also allowed us to find that the conserved current of QED is the electric charge, QCD is the color charge, and for the Weak force it's the Weak isospin and hypercharge.

With the inclusion of the Higgs mechanism and the formulation of a local gauge invariant Lagrangian for the Electroweak and QCD fields, we have the complete SM

Lagrangian as,

$$\begin{aligned}
\mathcal{L} = & -\frac{1}{4}W_{\mu\nu}^a W^{a\mu\nu} - \frac{1}{4}B_{\mu\nu} B^{\mu\nu} - \frac{1}{4}G_{\mu\nu}^a G_a^{\mu\nu} \\
& + \bar{L}\gamma^\mu(i\partial_\mu - g_W \frac{1}{2}\tau^a W_\mu^a - g'_W \frac{Y}{2}B_\mu - g_Q T_b G_\mu^b)L \\
& + \bar{R}\gamma^\mu(i\partial_\mu - g'_W \frac{Y}{2}B_\mu - g_Q T_b G_\mu^b)R \\
& + |(i\partial_\mu - g_W \frac{1}{2}\tau^a W_\mu^a - g'_W \frac{Y}{2}B_\mu)\phi|^2 - V(\phi) \\
& - (G_1 \bar{L}\phi R + G_2 \bar{L}\phi_c R + \text{hermitian conjugate}),
\end{aligned} \tag{3.35}$$

where the first terms are the kinetic energies and self-interactions of the W^\pm, Z, g , and γ bosons [1,23,26]. The second and third terms are the kinetic energies and interactions of the leptons and quarks with the W^\pm, Z, g , and γ bosons where L is a left-handed fermion doublet and R is a right-handed fermion singlet. The fourth term is the W^\pm, Z, γ and Higgs masses and couplings. The final term is the lepton and quark masses and couplings to the Higgs field.

3.2 Fundamental Problems in the Standard Model

The SM is able to accurately and precisely describe many facets of the universe, whether it comes to predicting the existence of a sixth quark or the confirmation of the anomalous magnetic moment for the muon to 9 orders of magnitude. Unfortunately, there are some evidence of matter or interactions that cannot be described, such as dark matter, the Hierarchy problem, and a possible GUT. Let's look into each of these further.

3.2.1 Dark Matter

The main motivation for Dark Matter is the difference between the visible matter and the measurable matter in the universe. This has most notably been seen in the radial velocities of stars in galaxies. In a galaxy which is solely made up of visible matter, or matter that interacts with light, the radial velocity of stars should decrease as $1/\sqrt{r}$ the further away it is from the galactic nuclei, although measurements show the velocity becoming constant as a function of radius.

A study of this was on the galaxy NGC 1560, where the measured galactic velocity curve provided a result that was 400 times large than the visible matter in the cluster [30]. To reproduce these features in models, the mass of the galaxy must be significantly more than what is seen. This implies some unseen dark matter [11, 30], that still interacts with the gravitational field, but not with the EM field. The neutrino could be a potential dark matter candidate due to the fact that it interacts weakly with matter and is abundant in the universe. However, the mass, which is nonzero, can only explain a small fraction of the dark matter in the universe where we have limits derived by high-redshift galaxies [12].

We have also measured an effect called gravitational lensing, which is caused by a large amount of mass bending spacetime and the resulting light passing through it. The galaxy cluster Abell 2218 has been viewed to have a gravitational lensing of the galaxy behind it [31]. Using an equivalent of the lens equation in general relativity we can calculate the mass distribution required to cause the lensing. Then with measurement of the visible light in the galaxy we can determine that there is another kind of matter, "dark matter", that is causing the extra mass but interacts weakly with light.

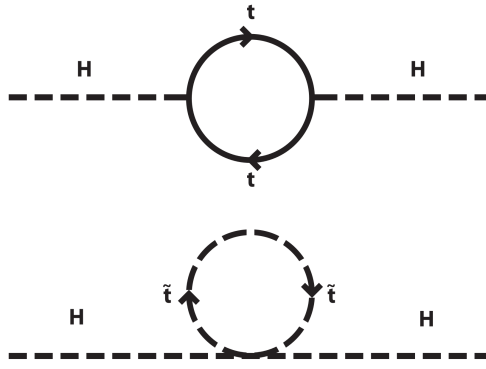


Figure 3.5 : The loop corrections to the Higgs boson interacting with a top quark and its superpartner, the top squark. This is a next-to-leading order (NLO) correction to the Higgs boson mass [22].

3.2.2 Hierarchy Problem

The Higgs boson is a beautiful solution to electroweak symmetry breaking, gives a method for particles to acquire mass, see Sec. 3.1.8, and was discovered to have a measured mass of $m_H = 125.18 \pm 0.16$ GeV [18–21]. This value, however, is not predictable with the SM, but can be constrained and leads to some inconsistencies when you include loop corrections. Since the Higgs boson is strongly coupled to particles with large masses, the dominant loop correction is due to interactions with the t quark. These higher order loop corrections to the Higgs mass, m_H^2 , caused by the fermionic t loop, see Fig 3.5, are,

$$\Delta m_H^2 = -\frac{|\lambda_t|^2}{8\pi^2} \Lambda_{UV}^2 + \dots, \quad (3.36)$$

where λ_f is the vertex factor for the respective fermion and Λ_{UV} is the ultraviolet momentum cutoff. The Higgs boson loop corrections are highly dependent on all

virtual and real particles that couple to the Higgs field. We can see the corrections from Eqn. 3.36 from the t quark will cause a large divergence.

The quadratic divergence of the Higgs mass then requires a fine tuning of the parameters λ_f to solve the divergence. This means the only way for the SM to reconcile this unfortunate fact is to have a relatively lucky cancellation of very large numbers of order m_P^2 , where m_P is the Planck mass, with equally small numbers. Fortunately, if we add the contribution of a bosonic partner of the fermion the Higgs loop corrections reduce to [22],

$$\Delta m_H^2 = \frac{\lambda_S}{16\pi^2} [\Lambda_{UV}^2 - 2m_S^2 \ln(\Lambda_{UV}/m_S) + \dots]. \quad (3.37)$$

With the introduction of a scalar partner to the t , there is a logarithmic divergence to the Higgs boson mass and it can be renormalized through the normal methods.

3.2.3 Grand Unified Theory

The SM is able to accurately describe three of the fundamental forces at typical energy scales, 1 to 10^4 GeV, but ideally the forces would be able to merge into a single force at higher energies. This has not been directly observed, but many theories, such as SUSY, can give a GUT [13–15] that can allow for a common gauge coupling and a simpler theory overall [22].

At standard energies for particle physics experiments the difference in the strength of each force is quite noticeable. But it has been shown that in the SM the strengths of each force are dependent on the energy scale. SUSY could also explain the running coupling constant for QCD interaction. It would be ideal if they converge to a single force at large energies, such as 10^{16} GeV. In Fig. 3.6, we see the extrapolated energy scales of the forces in the SM shown as the dotted line. These unfortunately, do not

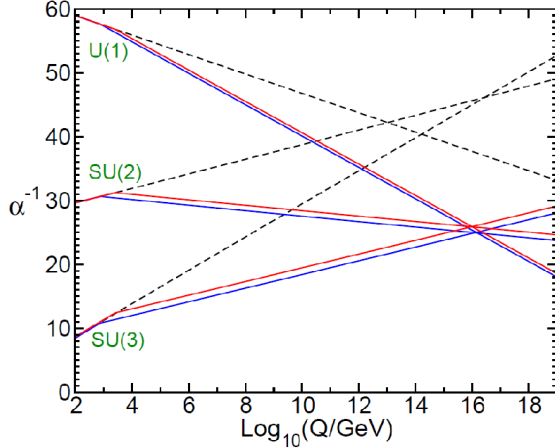


Figure 3.6 : The energy dependence of the inverse gauge coupling of each force in the SM (dashed line) and the MSSM (solid lines). The MSSM gives two thresholds for the sparticle mass 750 GeV and 2.5 TeV [22].

meet at a single point to become one force, but if we include SUSY into the model we get a nice convergence between the forces [22].

3.3 Supersymmetry

We have seen from the above three problems that there is still more to learn about the universe, such as dark matter and the hierarchy problem. SUSY [2–10] also has the ability to be a potential GUT. We saw from the Hierarchy problem that the addition of a bosonic partner to a fermion will allow for the loop corrections to be renormalizable without fine tuning. Fortunately, some theories have allowed for such a problem to be solved. Namely, the theory of SUSY, which essentially states that each particle in the SM has a superpartner that has only the spin changed, that every fermion has a bosonic partner that has all the same quantum numbers except the spins differ by 1/2, and vice-versa.

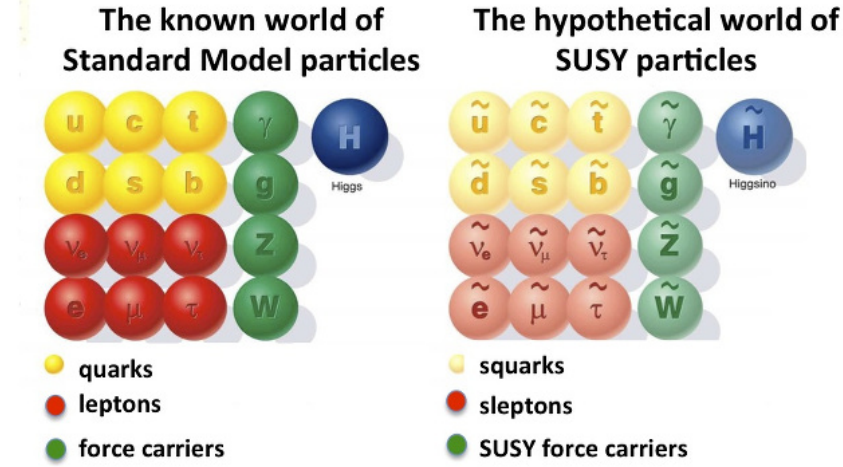


Figure 3.7 : The corresponding SUSY particles which are partners to the SM particles [32].

The partners to the fermions are denoted with a ‘s’ in front of the name to notify that it is the scalar form of the particle and the partners to the bosons have an ‘ino’ attached at the end, such as photino, gluino, wino, and Higgsino. So, for the partners to the fermionic particles in the standard model we have: sup (\tilde{u}), sdown (\tilde{d}), scharm (\tilde{c}), sstrange (\tilde{s}), stop (\tilde{t}_1), and sbottom (\tilde{b}) for the squarks and selectron (\tilde{e}), smuon ($\tilde{\mu}$), and stau ($\tilde{\tau}$) for the charged sleptons. The partners to the neutrinos, which are always left-handed if you neglect the minimal masses, are sneutrinos ($\tilde{\nu}_e$, $\tilde{\nu}_\mu$, $\tilde{\nu}_\tau$), where we have one for each flavor of lepton, see Fig. 3.7.

If the SUSY was unbroken, the superpartners would have exactly the same properties as the SM pairs except their spin. This would cause a massless photino or a $m_{\tilde{e}} = 0.511$ keV selectron. These particles would certainly have been detected at this point, which leads us to think that SUSY is a broken symmetry where all the superpartners have a mass that is significantly higher than their SM partners.

3.3.1 Supermultiplets and Chirality

A supermultiplet is any symmetry where the number of bosonic degrees of freedom and fermionic degrees of freedom are equal, $n_B = n_F$. The simplest way to achieve this is to have a combination of a single Weyl fermion, which is a chiral representation of the fermion, $n_F = 2$, and two real scalars with each having $n_B = 1$. It becomes convenient for the mathematics to combine the two real scalars into one complex scalar field. Now the combination of a complex scalar field and a Weyl fermion is known as a chiral supermultiplet.

3.3.2 Minimal Supersymmetric Standard Model

We have discussed how the fermions transform under the rules of SUSY, but how do the scalar field mediators translate into this new framework. First, we look at the Higgs boson. We know that there is not only one chiral supermultiplet. If there was only one in the electroweak gauge symmetry, with a Higgsino of spin-1/2, we would not have the anomaly cancellation of the traces, $\text{Tr}[T_3^2 Y] \neq 0$ and $\text{Tr}[Y^3] \neq 0$, where T_3 is the third component of weak isospin and Y is the weak hypercharge. In the SM, the traces of these for the fermions are already satisfied. So we must include two chiral supermultiplets of the Higgsino, with $Y = \pm \frac{1}{2}$, see Table 3.2.

It turns out that this is also necessary for the Higgsino field to give mass to different particles in the SM. A Higgs boson with $Y = 1/2$ has the Yukawa couplings that allow it to interact with the up-type quarks (u, c, t). Only a Higgs boson with $Y = -1/2$ has the correct Yukawa couplings to interact with the down-type quarks (d, s, b) and the charged leptons (e, μ, τ).

The SM vector boson will also have a corresponding chiral supermultiplet. They have fermionic superpartners that are referred to as gauginos. The $SU(3)_C$ color

Names		spin 0	spin 1/2	$SU(3)_C, SU(2)_L, U(1)_Y$
squarks, quarks ($\times 3$ families)	Q	$(\tilde{u}_L \ \tilde{d}_L)$	$(u_L \ d_L)$	$(\mathbf{3}, \mathbf{2}, \frac{1}{6})$
	\bar{u}	\tilde{u}_R^*	u_R^\dagger	$(\overline{\mathbf{3}}, \mathbf{1}, -\frac{2}{3})$
	\bar{d}	\tilde{d}_R^*	d_R^\dagger	$(\overline{\mathbf{3}}, \mathbf{1}, \frac{1}{3})$
sleptons, leptons ($\times 3$ families)	L	$(\tilde{\nu} \ \tilde{e}_L)$	$(\nu \ e_L)$	$(\mathbf{1}, \mathbf{2}, -\frac{1}{2})$
	\bar{e}	\tilde{e}_R^*	e_R^\dagger	$(\mathbf{1}, \mathbf{1}, 1)$
Higgs, higgsinos	H_u	$(H_u^+ \ H_u^0)$	$(\tilde{H}_u^+ \ \tilde{H}_u^0)$	$(\mathbf{1}, \mathbf{2}, +\frac{1}{2})$
	H_d	$(H_d^0 \ H_d^-)$	$(\tilde{H}_d^0 \ \tilde{H}_d^-)$	$(\mathbf{1}, \mathbf{2}, -\frac{1}{2})$

Table 3.2 : The chiral supermultiplets of the MSSM. Spin-0 fields are complex scalars and spin-1/2 fields are left-handed two component Weyl fermions [22].

Names	spin 1/2	spin 1	$SU(3)_C, SU(2)_L, U(1)_Y$
gluino, gluon	\tilde{g}	g	$(\mathbf{8}, \mathbf{1}, 0)$
winos, W bosons	$\widetilde{W}^\pm \ \widetilde{W}^0$	$W^\pm \ W^0$	$(\mathbf{1}, \mathbf{3}, 0)$
bino, B boson	\widetilde{B}^0	B^0	$(\mathbf{1}, \mathbf{1}, 0)$

Table 3.3 : The chiral supermultiplets of the MSSM [22].

gauge interactions of QCD, which are a spin-1/2 color-octet, has a partner called a gluino (\tilde{g}). The electroweak gauge theory $SU(2)_L \times U(1)_Y$ has the superpartners \widetilde{W}^+ , \widetilde{W}^0 , \widetilde{W}^- , and \widetilde{B}^0 each with spin-1/2, called winos and bino, see Table 3.3. The gaugino mixtures of \widetilde{W}^0 and \widetilde{B}^0 give the corresponding zino (\widetilde{Z}^0) and photino ($\widetilde{\gamma}$). The chiral supermultiplets shown in Table 3.2 and 3.3 give the particles of the MSSM. These are part of a simplified model for SUSY [33–37].

The five higgsinos and electroweak gauginos mix with each other because of electroweak symmetry breaking [22]. The neutral higgsinos (\widetilde{H}_u^0 and \widetilde{H}_d^0) and neutral gauginos (\widetilde{B} and \widetilde{W}^0) mix into four mass eigenstates, which are called neutralinos, $\widetilde{\chi}_1^0$, $\widetilde{\chi}_2^0$, $\widetilde{\chi}_3^0$, and $\widetilde{\chi}_4^0$. The charged higgsinos (\widetilde{H}_u^+ and \widetilde{H}_d^-) and charged gauginos (\widetilde{W}^+ and \widetilde{W}^-) can mix into two mass eigenstates with charge ± 1 called charginos, $\widetilde{\chi}_1^\pm$ and $\widetilde{\chi}_2^\pm$.

3.3.3 R Parity

R -parity or matter parity is the multiplicatively conserved quantum number [4,38] defined as,

$$P_R = (-1)^{3(B-L)+2s}, \quad (3.38)$$

where B is the baryon number, L is the lepton number, and s is the spin of the particle. From this we can find the R -parity of all the particles in the SM and MSSM. The definition of R -parity is quite useful because all the particles of the SM have an R -parity of $P_R = +1$, while all of the squarks, sleptons, gauginos, and higgsinos have $P_R = -1$.

R -parity is thought to be exactly conserved in SUSY, where there is no mixing between particles ($P_R = +1$) and sparticles ($P_R = -1$). This leads to three important consequences:

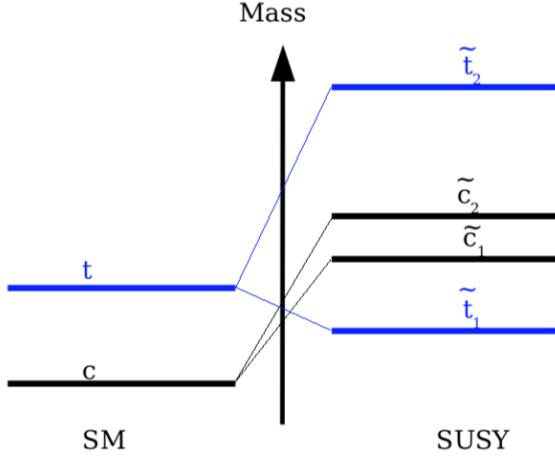


Figure 3.8 : On the right we have the arbitrary masses of the top and charm quarks. The left and right handed states mix into two mass eigenstates. It is possible that the top squark will have the smallest mass of the squarks [22].

- The lightest sparticle that has $P_R = -1$ is called the "lightest supersymmetric particle" or LSP, which must be absolutely stable. It is a possible non-baryonic dark matter candidate.
- Every sparticle, other than the LSP, must eventually decay into an odd number of LSPs.
- For collider experiments, sparticles will only be produced in even numbers.

We are going to be investigating a MSSM that conserves R -parity. This is quite well motivated by the possibility of a dark matter candidate [11].

3.3.4 Mass Spectra

The third family of squarks and sleptons should have quite different masses compared to their first- and second-family counterparts, which is caused by the large

Yukawa (y_t, y_b, y_τ) and soft (a_t, a_b, a_τ) couplings, which are holomorphic parameters proportional to the Yukawa couplings. This causes significant mixing between the chiral superpartners $(\tilde{t}_L, \tilde{t}_R), (\tilde{b}_L, \tilde{b}_R)$, and $(\tilde{\tau}_L, \tilde{\tau}_R)$. We will concentrate on how the mass of the top squark, \tilde{t}_1 evolves in the MSSM, given many contributions to the top squark mass such as, squared-mass terms, 4-vertex interactions terms with the up-type Higgs, the 3-vertex interactions with the down-type Higgs, and scalar potential couplings. We have a square-mass matrix for the top squarks,

$$\mathcal{L}_{\text{stop masses}} = - \begin{bmatrix} \tilde{t}_{1L}^* & \tilde{t}_{1R}^* \end{bmatrix} \mathbf{m}_{\tilde{t}_1}^2 \begin{bmatrix} \tilde{t}_{1L} \\ \tilde{t}_{1R} \end{bmatrix}, \quad (3.39)$$

where,

$$\mathbf{m}_{\tilde{t}_1}^2 = \begin{bmatrix} m_{Q_3}^2 + m_t^2 + (\frac{1}{2} - \frac{2}{3}\sin^2\theta_W)\cos(2\beta)m_Z^2 & v(a_t^*\sin\beta - \mu y_t\cos\beta) \\ v(a_t\sin\beta - \mu^* y_t\cos\beta) & m_{u_3}^2 + m_t^2 + (\frac{2}{3}\sin^2\theta_W)\cos(2\beta)m_Z^2 \end{bmatrix}. \quad (3.40)$$

This is a hermitian matrix and can be diagonalized to give eigenstates \tilde{t}_1 and \tilde{t}_2 which are linear combinations of the left and right-handed \tilde{t}_1 , see Fig. 3.8. Now we get the eigenvalues for the mass states as $m_{\tilde{t}_1}^2 < m_{\tilde{t}_2}^2$. From this, models predict that the \tilde{t}_1 is the lightest squark [22].

3.3.5 SUSY Searches

The SM of particle physics has been a powerful model for predicting interactions between quarks, leptons, and force carriers, with an accurate prediction for precision measurements, but has some faults such as, the Hierarchy problem, dark matter, and a Grand Unified Theory. We have seen that including SUSY can allow for possible solutions, such as; a dark matter candidate as the LSP, bosonic-fermionic

loop corrections for the Higgs boson mass, and a unification of the fundamental forces at large energies. Then once investigating the theory of SUSY, we were able to determine that the top squark could be the lightest squark, which allows us to develop multiple searches for this proposed theory.

3.4 Current SUSY Results

Here we see the most current results from searches for the top squark from CMS. These have been completed with data from 2016 with 35.9 fb^{-1} . This analysis was completed with the most up-to-date identification methods for particles in the SM. From this Analysis [39], all 104 search region bins, as well as the corresponding single-lepton control region bins, the $\gamma+\text{jets}$ control region bins and the QCD control regions, are fit simultaneously in order to evaluate the cross section excluded at 95% confidence level for each signal benchmark point. There are similar searches using data from 2016 in Ref. [40–44]

The easiest way to think about the plots shown in Figs. 3.9, 3.10, 3.11, 3.12, 3.13, 3.14 [11, 33, 34], is that there is a calculated limit for each mass point. The x -axis is the possible mass range for the \tilde{t}_1 , $m_{\tilde{t}_1}$ and the y -axis is the possible range for the $\tilde{\chi}_1^0$, $m_{\tilde{\chi}_1^0}$. Each point in this 2D space has a color representation for the value of the upper limit on the cross section at a confidence level of 95%.

With the comprehensive analysis that was performed in 2016, we have various limits on the multiple decay modes of the \tilde{t}_1 which will be covered completely in Section 6. The comprehensive limits on the \tilde{t}_1 mass range from values of 550 to 1.1 TeV for all of the all-hadronic decay modes. The CMS Collaboration has also combined the limits from the separate analyses which concentrate on the 1-lep, 2-lep, MT2, and HT missing analyses. The combination of these has shown that we can

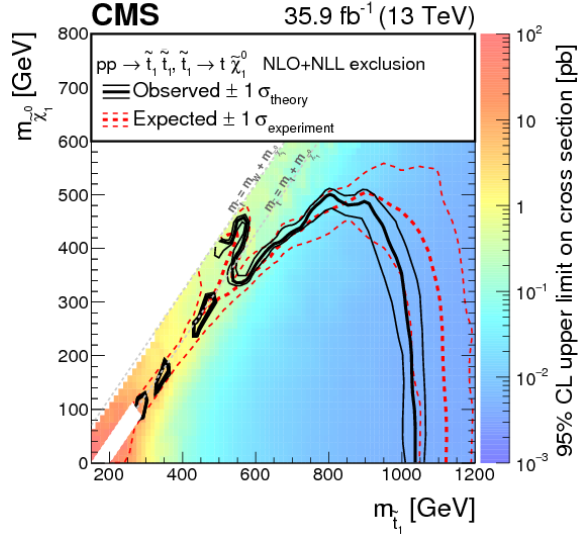


Figure 3.9 : Limits for the mass parameter space for $\tilde{t}_1 \rightarrow t \tilde{\chi}_1^0$ (T2tt) decays. With a current limit of 1.05 TeV for a minimal neutralino mass [43].

set limits on the \tilde{t}_1 mass range for masses of 800 to 1100 GeV.

From the Fig. 3.9, 3.10, 3.11, 3.12, 3.13, and 3.15 [43,46], we know that we are able to exclude a large mass range for the \tilde{t}_1 and $\tilde{\chi}_1^0$. Since this is for a luminosity of 36.8 fb^{-1} , we can expect improved limits with all of the data from Run 2, which is 136.7 fb^{-1} . The new version of the analysis also has a redesigned search region to allow for more sensitive results, while also improving various object definitions.

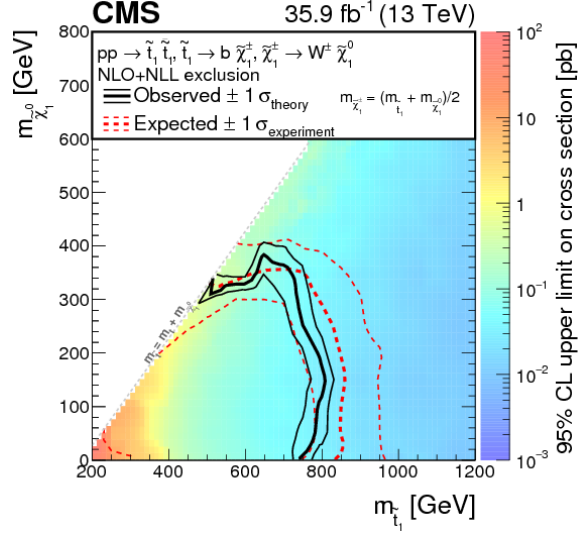


Figure 3.10 : Limits for the mass parameter space for $\tilde{t}_1 \rightarrow b\tilde{\chi}_1^\pm$ (T2bW) decays. With a current limit of 750 GeV for a minimal neutralino mass [43].

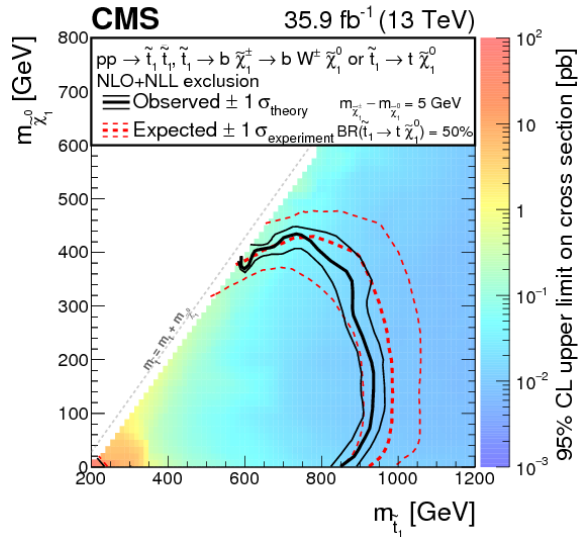


Figure 3.11 : Limits for the mass parameter space for $\tilde{t}_1 \rightarrow b\tilde{\chi}_1^\pm \rightarrow bW^\pm\tilde{\chi}_1^0$ or $\tilde{t}_1 \rightarrow t\tilde{\chi}_1^0$ (T2tb) decays. With a current limit of 850 GeV for a minimal neutralino mass [43].

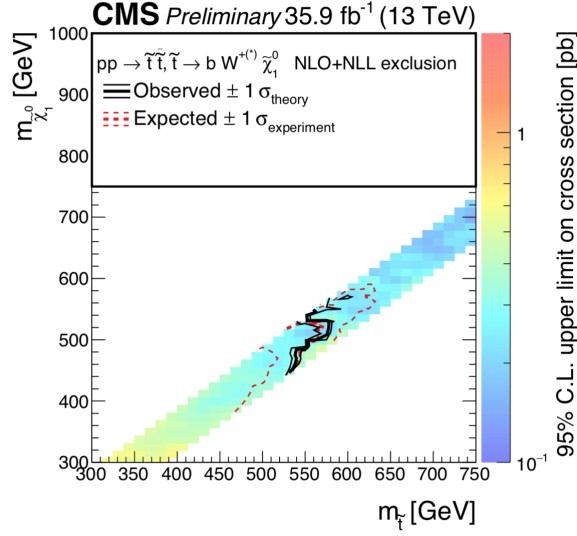


Figure 3.12 : Limits for the mass parameter space for $\tilde{t}_1 \rightarrow b W^+ \tilde{\chi}_1^0$ (T2fbd) decays. Which has a range of 550 GeV for a $\tilde{\chi}_1^0$ mass of approx. 500 GeV [43].

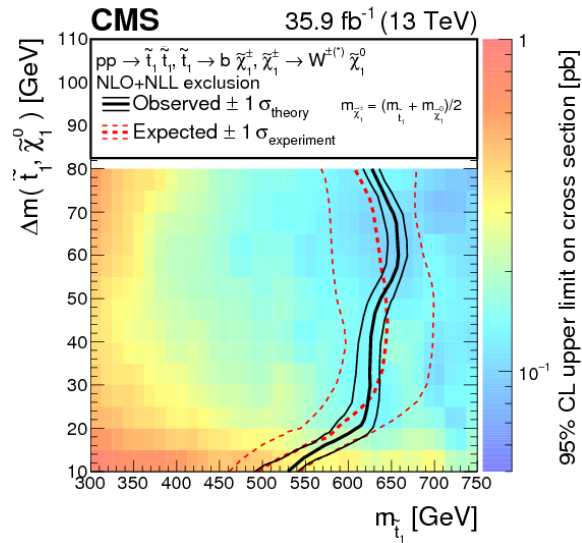


Figure 3.13 : Limits for the mass parameter space for $\tilde{t}_1 \rightarrow b\tilde{\chi}_1^\pm, \tilde{\chi}_1^\pm \rightarrow W^\pm \tilde{\chi}_1^0$ (T2bWC) decays. Which has a range of 550 to 675 GeV for a $\tilde{\chi}_1^0$ mass of 600 GeV [43].

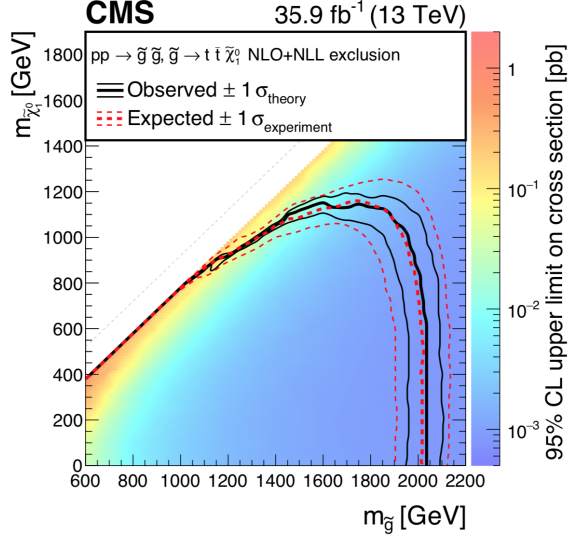


Figure 3.14 : Limits for the mass parameter space for $\tilde{g} \rightarrow t\bar{t}\tilde{\chi}_1^0$ (T1tttt) decays. Which has a limit of 2050 GeV for a minimal neutralino mass [45].

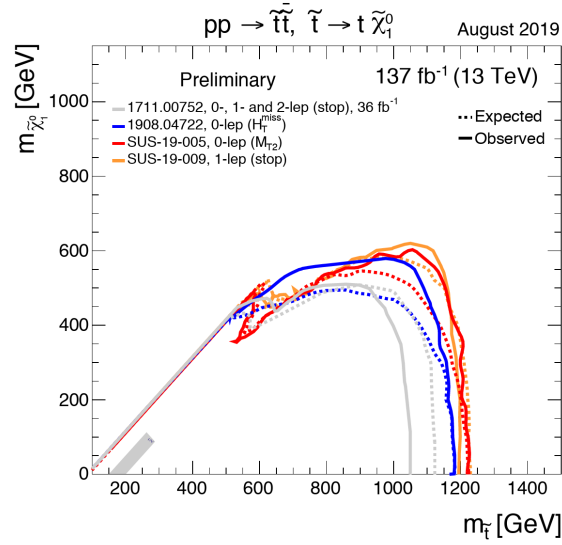


Figure 3.15 : Limits for the mass parameter space for T2tt decays using results from all the analysis in CMS. With a current limit of 1.05 TeV to 1.2 TeV for a minimal neutralino mass [46].

3.5 What are we looking for? And why?

As discussed in Sec. 3.1, the SM is a robust theory that is useful for describing the iterations of visable matter in the universe. It has been through many robust tests, while also able to make many predictions. Unfortunately, we have seen that a few unknowns, such as: dark matter, the hierarchy problem, and a possible GUT, are currently unexplained. We then showed that a possible solution to these is SUSY, Sec. 3.3, which provides a good dark matter candidate, LSP, which allows for the convergence of the EM, Weak, and Strong force at large energy scales, and allows the Higgs mass to be renormalizable without fine tuning.

From this, we have determined that the top squark is most likely to have the smallest squark mass in the MSSM. There have been many searches for the top squark decaying to many modes, which are summarized in Fig. 3.15. As of right now, we have set a limit on the \tilde{t}_1 mass, $m_{\tilde{t}_1} > 800$ GeV or $m_{\tilde{t}_1} > 1100$ GeV, depending on the analysis. Now we plan on using all of the data from Run2, 137 fb^{-1} , along with an improved search design to probe further into the mass parameter space of the \tilde{t}_1 and $\tilde{\chi}_1^0$.

Chapter 4

Compact Muon Solenoid

The Compact Muon Solenoid (CMS) [47] is a particle detector as part of the Large Hadron Collider (LHC) [48] which is located near Geneva, Switzerland as part of the CERN collaboration. The CMS detector is 21.6 m long, 15 m diameter, and 14,000 tons and is used to detect many different species of particles. It is separated into layers that, from the interaction vertex outward are, the silicon tracker, Electromagnetic Calorimeter (ECAL), Hadronic Calorimeter (HCAL), superconducting solenoid, and the muon chambers, see Fig. 4.1.

4.1 The Detector

The CMS detector is designed to detect the decay products of most of the particles of the SM, except for neutrinos since they are weakly interacting and will almost certainly pass through the entire earth without an interaction. A defining feature of CMS is the 12.6-m long, 5.9 m inner diameter, 3.8 T superconducting solenoid. This is used to bend the trajectory of charged particles throughout the detector, such that we can reconstruct the momentum and charge of the particles. The LHC provides a 13 TeV proton-proton beam (4.5 TeV heavy ion) with a bunch crossing every 25 ns (50 ns) to produce interaction at luminosities up to $2.5 \times 10^{34} \text{ cm}^{-2} \text{ s}^{-1}$. Events are selected with a two-level trigger system [49]. An initial hardware trigger using information from the calorimeters and muon chambers and triggers at about

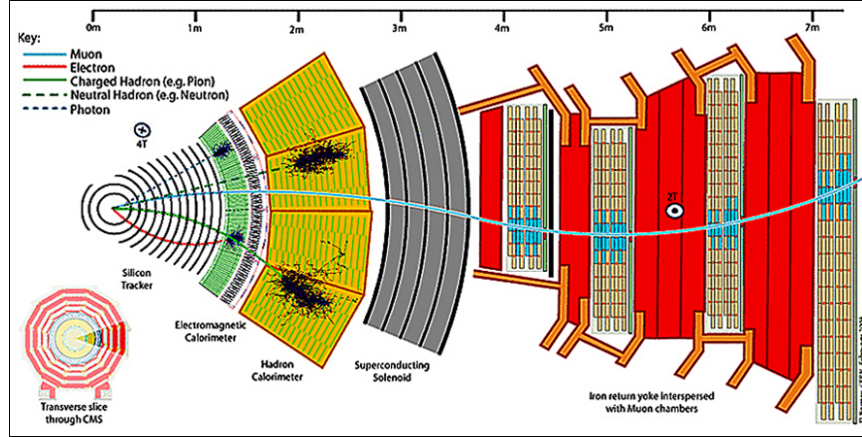


Figure 4.1 : A cross section of the CMS detector, oriented by looking down the direction of the beam pipe.

100 kHz. Then a high-level trigger processor farm which reduces the event rate to about 1 kHz for storage and analysis.

The coordinate system of CMS has the origin at the nominal collision point in the center of the detector. The y -axis points vertically upward, x -axis points radially inward toward the center of the LHC, and z -axis points along the beam directions toward the Jura mountains from LHC Point 5. The polar angle θ is measured from the z -axis and the azimuthal angle ϕ is measured in the $x - y$ plane from the x -axis. The pseudorapidity of a particle is defined as $\eta = -\ln \tan(\theta/2)$, where θ is the angle between the particle momentum and the positive direction of the beam axis, two notable values are $\eta = 0$ at $\theta = \pi/2$ and $\eta = \infty$ at $\theta = 0$. Rapidity, $y = \frac{1}{2} \ln \frac{E+p_z c}{E-p_z c}$, is quite useful since the difference of rapidities is Lorentz invariant. For particles with large momentum, $pc \gg mc^2$, the pseudorapidity, η , can be defined as $\eta = \frac{1}{2} \ln \frac{|\vec{p}| + p_L}{|\vec{p}| - p_L}$. The transverse components of momentum, p_T , and energy, E_T , are computed using the x and y components of the particles. The LHC is a parton-

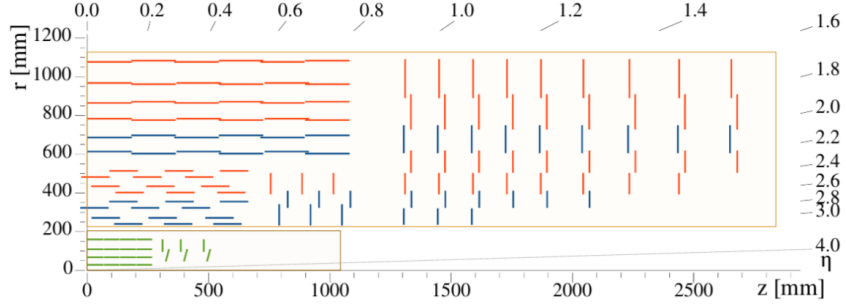


Figure 4.2 : Geometry of the CMS Tracker, the inner most region in green is the pixel detector while the outer region in blue and red are the silicon strips.

parton collider with collisions at 13 TeV, and at these energy scales the particles are boosted in the beamline direction which is denoted as the z -axis. All quantities that are transverse to the beam axis are the same in all reference frames, such that these are the quantities we use for analyses.

4.1.1 Tracker

The silicon tracker is made up of two different detectors, the silicon pixels and the silicon strip tracker. This is the inner most detector for CMS and receives the largest flux of particles during operation. This requires it to be radiation hard and operate with a fine granularity.

4.1.1.1 Pixel Detector

The pixel detector was recently upgraded during the winter of 2016/2017. It is approximately 1 m long with four barrel layers ranging from 3.0, 6.8, 10.2, and 16.0 cm from the beam axis and three endcap disks, see Fig. 4.2. Since it is the closest detector to the interaction vertex, it therefore has the highest particle flux at

$10^7/\text{cm}^2/\text{s}$ at $r = 10 \text{ cm}$. The resolution is $9.4 \mu\text{m}$ in $r - \phi$ and $20 - 45 \mu\text{m}$ in z [50].

The pixel detector contains 1,184 modules in the barrel pixels (BPIX) and 672 modules in the forward pixels (FPIX). The number of individual pixels is 79 (45) million in the BPIX (FPIX) regions, respectively, with a pixel size of $100 \times 150 \mu\text{m}^2$. A pixel module contains two layers, a silicon layer that is bump bonded to 16 Readout Chips (ROCs) which form a module of 66560 pixels, see Fig. 4.3. Each unit is controlled with one or more Token Bit Managers (TBMs) which control the readout of the digital signal from the pixels to the Front-end Driver (FED). For BPIX Layers 3, 4, and all of FPIX there is 1 TBM per module. BPIX layer 2 has 2 TBMs with each one controlling 8 ROCs, while BPIX layer 1 has 4 TBMs with each one controlling 4 ROCs. The information from each module is split into two channels with each containing 8, 4, or 2 ROCs. These are encoded together by the TBM before being sent to the FED [50].

The silicon pixel system is set up as a reverse p-n junction, where the pixels are in the n-type region. As a charged particle travels through the silicon it creates electron-hole pairs. A voltage difference is applied to the silicon such that the electrons will deposit onto the pixels. Since the detector is inside of the magnetic field, a Lorentz drift will cause the electrons to reach more than one pixel and increase the resolution. As the pixel system continues to be irradiated with large quantities of particles the voltage in the silicon increases to provide a consistent current for charged particle interactions. This will lead to less charge sharing between the pixels and a decrease in resolution of particle locations [50].

The data from the pixels, is sent via optical fiber to the FED where it is decodes and processes the information. The FED is responsible for identifying the relevant data, determining possible error states, and packaging the information to be sent to the central Data Acquisition (cDAQ) of CMS. Each of the 108 FEDs for the pixels

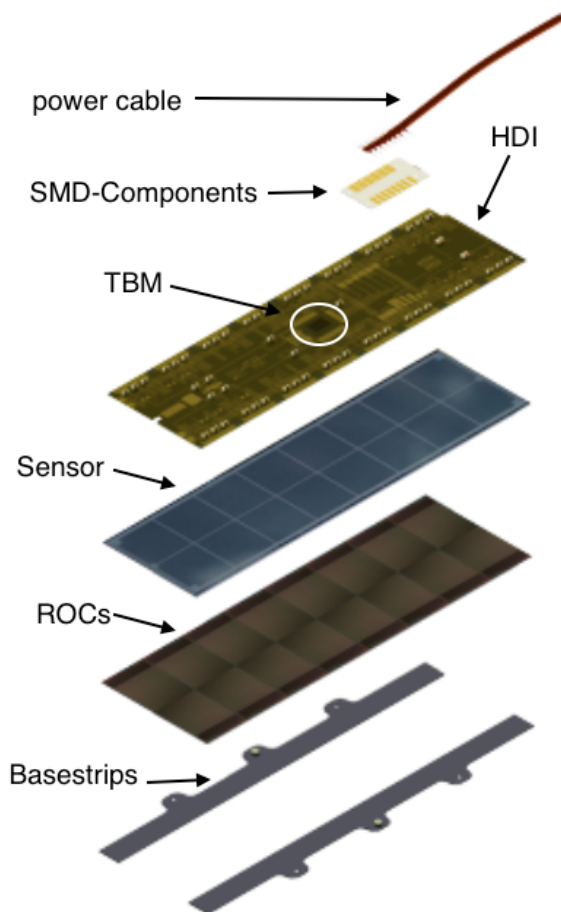


Figure 4.3 : Components of the pixel modules. Made up of a silicon layer, a grid of 8 ROCs, which are attached via bump bonds. This is all controlled with a TBM connection to read out data.

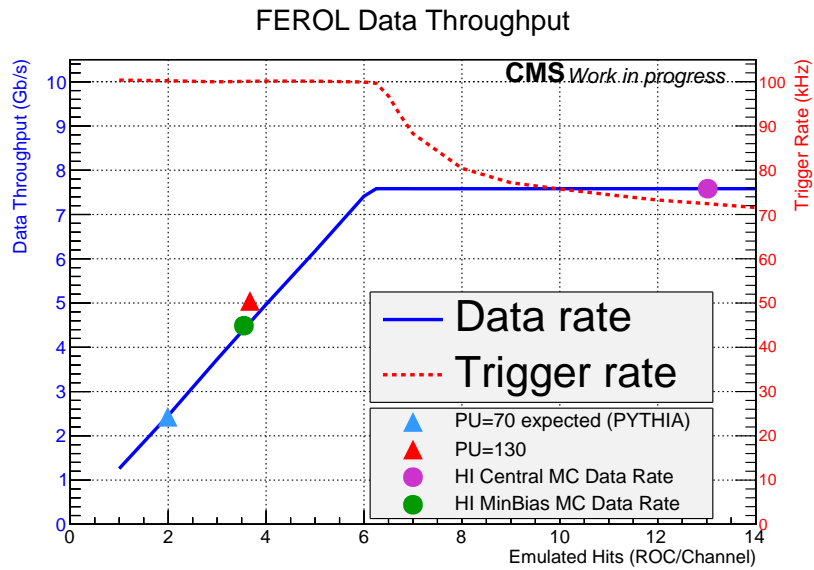


Figure 4.4 : Measuring the throughput of the FED with the emulated and simulated events provided by the FED Tester. The Data rate is shown as the solid blue line with the corresponding trigger rate as the dotted red line. The simulated event sizes are shown as their equivalent emulated hits/ROC/channel on the data line [51].

receives 24 independent fibers from the detector. Each of these fibers contains 2 channels from the pixel module. Through robust testing with the FED Tester [51], we have confirmed that the FED is able to attain a maximum data throughput of approximately 7.5 Gbps, see Fig. 4.4.

4.1.1.2 Silicon Strips

The silicon strips have a 200 m^2 active region with 15,148 modules that are distributed in 10 barrel layers and 9 + 3 endcap disks. This has a cell size ranging from $10 \text{ cm} \times 80 \mu\text{m}$ to $25 \text{ cm} \times 180 \mu\text{m}$ [52] since the particle flux decreases further away from the vertex, Fig. 4.5. It has a resolution of $23 - 24 \mu\text{m}$ in $r - \phi$ and $23 \mu\text{m}$ in z for the microstrip tracker.

There are two types of silicon strip modules, see Fig. 4.5, which are in the layers shown in Fig. 4.2. The orange modules are single sided reverse p-n silicon sensors, while the blue modules are double sided by having two single modules mounted back-to-back at a 100 mrad angle. This improves the 3D tracking, but unlike the pixel detector this is an analog readout system.

4.1.2 Electromagnetic Calorimeter

The ECAL is a homogeneous calorimeter made out of 61,200 lead tungstate (PbWO_4) crystals in the barrel and 7,324 crystals in each endcap. The barrel region has an inner radius of 129 cm and covers a pseudorapidity range of $0 < |\eta| < 1.479$. The encaps are 314 cm from the interaction point and cover a range $1.479 < |\eta| < 3.0$ in pseudorapidity. Lead tungstate was chosen for the crystals since it has a short radiation length, $X_0 = 0.89 \text{ cm}$, fast with 80% of the light being emitted within 25 ns, and it's radiation hard. Each crystal in the barrel has a cross section of \approx

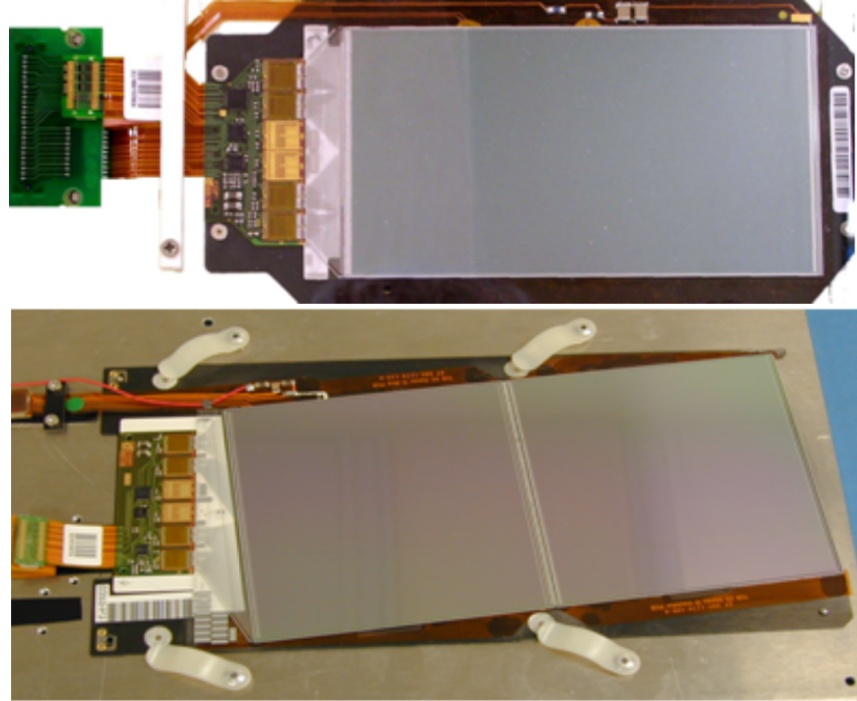


Figure 4.5 : The top module is a single sided reverse p-n silicon sensor. The bottom module is two silicon sensors mounted back-to-back at a 100 mrad angle.

$22 \times 22 \text{ mm}^2$ and length of 230 mm, while the endcap crystals are $28.6 \times 28.6 \text{ mm}^2$ and length of 220 mm corresponding to $25.8X_0$ and $24.7X_0$, respectively [53]. An ECAL uses electromagnetic showers to detect particles that interact electromagnetically. Electrons travelling through the material will radiate a photon via bremsstrahlung, then the photon will pair produce two electrons. Combining these two processes leads to electromagnetic showers as the particles travel through the detector. The process will continue until a critical energy is reached such that an electron cannot radiate any further and will then lose energy via collisions. The hadrons that are created in the collisions will also interact in this way, but because of their large mass they penetrate through the entire ECAL. The resulting light is recorded by silicon

avalanche photodiode (vacuum phototriodes) in the barrel (endcap) [53], [54].

4.1.3 Hadronic Calorimeter

The HCAL is a hermetic calorimeter consisting of alternating layers of brass as the absorber material and a scintillator. Brass is chosen since it is non-magnetic and has a relatively short interaction length. In the scintillator, a portion of the energy from the hadron is converted into visible light, which is then measured by hybrid photodiode tubes to measure the energy. The barrel part of the HCAL consists of 2304 towers that are segmented into $\Delta\eta \times \Delta\phi = 0.087 \times 0.087$ pieces that cover a region $0 < |\eta| < 1.4$ in pseudorapidity. The endcap region consists of 2304 towers with varying segmentation sizes and a coverage of $1.3 < |\eta| < 3.0$ [55], [54].

There are two additional parts of the HCAL to allow for maximum coverage of the detector volume. There is an outer hadron detector that is located outside the superconducting solenoid, which covers a slightly smaller pseudorapidity range compared to the barrel region. They serve as a tail catcher for hadron showers that penetrate all the way through the inner HCAL and solenoid. A forward hadron calorimeter, located 11.2 m from the interaction point covering a pseudorapidity $3.0 < \eta < 5.0$, made out of steel/quartz fiber is specifically designed for the columnated Cerenkov light in this region [55], [54].

4.1.4 Superconducting solenoid

Surrounding most of this is the superconducting solenoid which is 12.6 m long with a 5.9 m radius. The field strength is 3.8 T which has a stored energy of approximately 2.7 GJ. The magnet is designed such that a muon with momentum, $p = 1$ TeV, will have a momentum resolution of $\Delta p/p \approx 10\%$. The solenoid is a high-

purity aluminium-stabilized conductor, which is a similar material used in other large solenoids [54].

4.1.5 Muon Chambers

The muon system has three main detection systems that are used to identify a muon candidate. In the barrel region, drift tube (DT) chambers are used since the neutron background, muon rate, and magnetic field are all small. In the endcaps, cathode strip chambers (CSCs) are used since the relative values stated before are much larger. The neutron background is largely radially dependent so the CSCs will receive a larger flux, while the muon rate is dominated by low p_T muons which will interact in the endcap regions. Included throughout the whole system are resistive plate chambers (RPC) [54].

The DT consists on 250 chambers in 4 barrel layers at a radii of 4.0, 4.9, 5.9, and 7.0 m from the beam axis. A DT chamber is an array of anode wires in a gaseous medium where the walls are cathodes. A muon passing through the gas will ionize some atoms which are then forced towards the anode wires by the electric field. The drift time of the electrons can then be measured to within a couple of ns such that a good spatial resolution is achieved. The maximum designed drift length is 2.0 cm. Each station of the DT will give muon vector for each candidate with a ϕ precision of 100 μm in position and 1 mrad in direction [54].

The CSC system uses the same concept as the DT system, but also includes a measurement of the ions that follow the electric field to the cathode strips. In this system the anode wires and the cathode strips are perpendicular so the collected charge on both provide an accurate position measurement. The RPC system contains two parallel plates, anode and cathode, and the charge is measured by external

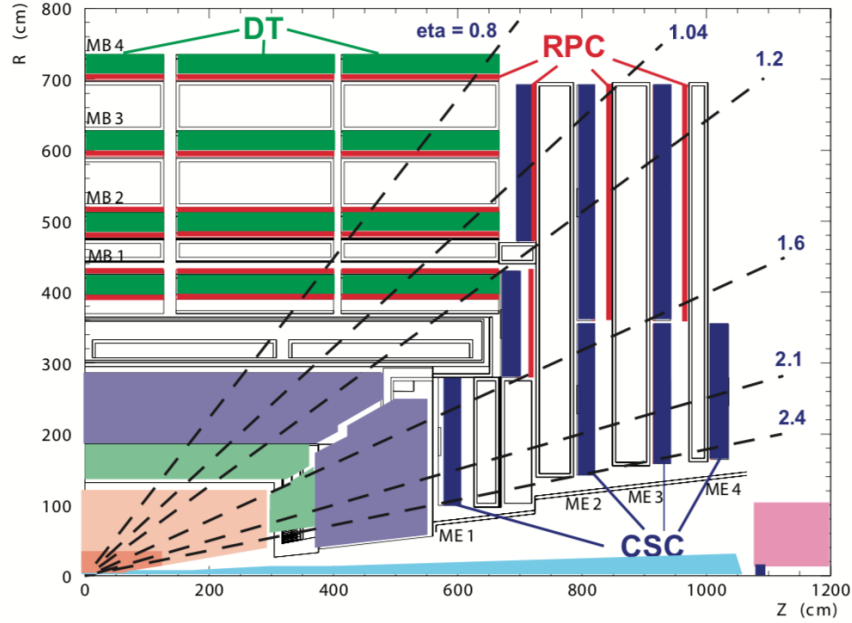


Figure 4.6 : A quarter cross section of the three muon detection systems for CMS [54].

metallic strips that can quickly measure the momentum of a muon and decide if the event should be triggered [54].

4.2 Detector Methods

Using the objects and information from each of the subdetectors we can measure the important information required for doing innovative physics analysis, such as, the \tilde{t}_1 search. Since the search is dependent on large missing energies, it is dependent on measuring all forms of energy in the standard model and checking for any inefficiencies. The CMS detector is designed to be a general purpose detector to measure multiple processes in the SM and beyond.

Chapter 5

Search Strategy

5.1 Physics Objects

We will reconstruct many different physics objects, interesting particle tagging methods or kinematic variables unique to the collisions. There are many different types of particles that we are interested in when working with particle physics measurements. These particles have very short lifetimes $\tau_t \approx 10^{-25}$ s for the t quark [56] and $\tau_b \approx 10^{-12}$ s for the b quark [57]. We are interested in certain physics objects such as jets (N_j), Heavy object tagging (N_b , N_t , N_{res} , N_W), missing transverse momentum (p_T^{miss}), soft-b tagging (N_{SV}), Initial State Radiation, and lepton identification. We will look into each of these objects further in this chapter.

5.1.1 Jets

In an interaction, whenever a quark is produced, it comes in pairs ($q\bar{q}$). When a quark pair is produced they form a color flux tube. As they quickly start to move away from each other, in the center-of-momentum frame, the energy density of the color flux tube will increase to the point that another $q\bar{q}$ pair can be produced. This will continue to occur in a sequence of radiating gluons or photons and the production of pairs of particles, see Fig. 5.1. In the detector, the energy deposited in the HCAL is a cluster of charged or neutral particles of a radius, $\Delta R = \sqrt{\Delta\eta^2 + \Delta\phi^2}$. There are many algorithms to reconstruct the jets which must satisfy the requirements in

Ref. [58]. We are mainly interested in the anti- k_T Jet algorithm [59] method which uses the transverse momentum of the particles within a certain radius $\Delta R = 0.4(0.8)$ for AK4(AK8) jets [60,61].

The measurement of interest is the distance d_{ij} between the particles (i) and pseudojets (j) and d_{iB} as the distance between the particle and the beam (B). The clustering identifies the smallest distance and if it is d_{ij} the particle is added to the pseudojet, while if it is the distance d_{iB} it is classified as a jet and removed from consideration. The distances are recalculated and repeated for all particles, see Fig. 5.2. The generalized algorithm is defined by the following distance measurement,

$$\begin{aligned} d_{ij} &= \min(k_{ti}^{2p}, k_{tj}^{2p}) \frac{\Delta_{ij}^2}{R^2}, \\ d_{iB} &= k_{ti}^{2p} \end{aligned} \quad (5.1)$$

where $\Delta_{ij}^2 = (y_i - y_j)^2 + (\phi_i - \phi_j)^2$, k_{ti} is the transverse momentum, y_i is the rapidity, ϕ_i is the azimuthal angle, and R is the radius parameter of the pseudojet. The above becomes the anti- k_T algorithm when $p = -1$. The jet area of the reconstructed jets are circular since the anti- k_T jets are unaffected by soft radiation. It is also insensitive to pileup which is of particular importance in CMS. An additional feature is that it is infrared safe, such that soft emissions of particles will not effect the reconstructed jets.

A charged hadron subtraction is also used to correct for the pileup, the number of collisions seen during a single proton beam crossing [62,63]. For AK8 jets the pileup contribution is accounted for using the "pileup per particle identification" method [63,64], where each particle is weighted by its probability of originating from the primary vertex. Once the jets have been identified, we can analyze their respective properties to determine the likelihood of the particle it originated from,

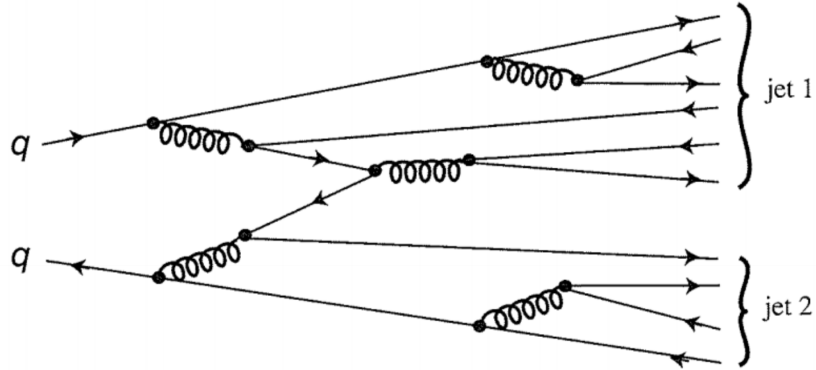


Figure 5.1 : A diagram of a quark pair radiating gluons that decay into more quark pairs in a process called hadronization [23].

such as a b , t , or W .

5.1.2 Heavy Object Tagging

Since this search is looking for a massive particle which then decays to slightly less massive particles we need to be able to identify and distinguish between them. We use various algorithms and neural networks to identify jets from b quarks, t quarks, or from W bosons.

5.1.2.1 B-Tagging

The ability to identify secondary vertices is essential in searches for the top squark, see Sec. 6.1. Since the b quark is a long lived particle, about 10^{-12} seconds, it will travel many millimeters before decaying into other particles. A b quark is identified during reconstruction, where the jet originating from a point separated from the primary vertex (PV), known as the secondary vertex (SV). The displaced vertex of the long lived b quark with low p_T has many interesting kinematic properties that

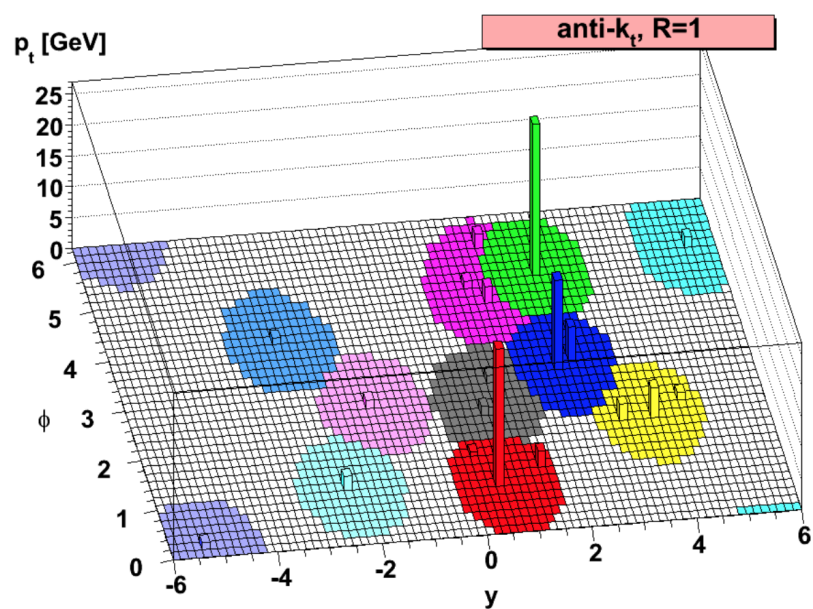


Figure 5.2 : A sample parton level event with random soft particles that is clustered with the anti- k_T algorithm [59].

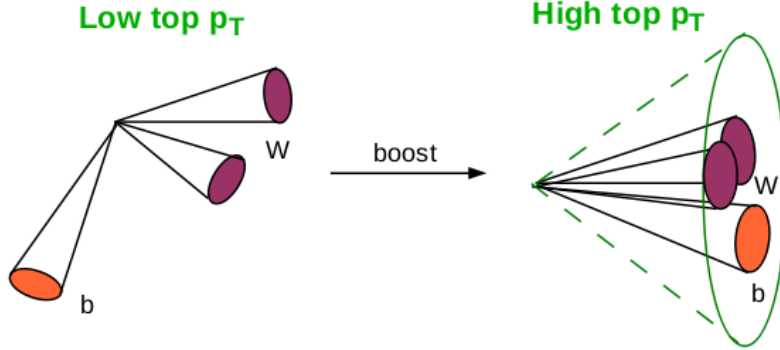


Figure 5.3 : The two types of top quark reconstructions, when each decay product is easily identifiable (resolved) or when the particles are close together (boosted).

we can use to identify them, *b*-tagging.

Now *b*-tagged jets are jets that are likely to have originated from a *b* quark. For *b* quarks with large transverse momentum, we use a Deep Combined Secondary Vertex (DeepCSV) algorithm that involves neural networks [65]. The medium working point recommended by the B-tag Physics Object Group (POG), corresponding to a threshold of 0.6324 0.4941, and 0.4184 for the 2016, 2017, and 2018 eras, respectively [66–69]. The medium working point is defined such that the percentage of a light jet being misidentified as a *b* jet is 1%.

5.1.2.2 Top/W Tagging

Top quark tagging is an essential part of our analysis. The top quark tagging algorithm is designed to have a high reconstruction efficiency for entire p_T spectrum of the top quark in our signal models. The anti- k_T algorithm using a distance parameter, $\Delta R = 0.8$, is expected to contain the energy clusters of all of the decay products of boosted *t* quarks [70, 71], see Fig. 5.3, with $p_T > 300$ GeV or *W* bosons

with $p_T > 200$ GeV. These decays are reminiscent of the expected decay, $t \rightarrow b\bar{q}\bar{q}'$, when it is a highly Lorentz boosted t quark decay. The requirements are:

- Medium working point $> 0.937, 0.895, 0.895(0.973, 0.991, 0.991)$ for boosted t (W) for the separate 2016, 2017, and 2018 eras, respectively [72].
- Reconstructed soft drop [73, 74] mass: $105 < m_t < 210$ GeV and $65 < m_W < 105$ GeV.
- Boosted tops: $p_T = 300$ GeV, $|\eta| < 2.0$ and W : $p_T = 200$ GeV, $|\eta| < 2.0$.

There is another type of top that can be reconstructed, which is when each subjet of the top decay can be resolved into each individual jet, denoted as a resolved top [72], see Fig. 5.3. The requirements are:

- Medium working point: 0.92 for all eras.
- $|\eta(j_{1,2,3})| < 2.4$ and b -tag discriminator: $> 0.6324, 0.4941, 0.4184$ for the separate 2016, 2017, and 2018 eras, respectively. The number of jets in the event that pass these cuts should be ≥ 2 .

These object definitions, N_t , N_W , N_{res} , are chosen such that there is no overlap in their definitions and are used to bin our search and control regions.

5.1.3 Missing Transverse Momentum

The missing transverse momentum [75, 76] is the negative vector sum of the total transverse momentum measured in the detector,

$$p_T^{\text{miss}} = - \sum_{i \in \text{vis}} \vec{p}_{i,T}, \quad (5.2)$$

where the sum of the momentum runs over every visible (vis) particle in the event [77,78]. We use the transverse component of the momentum because the z component of the particle momentum is not exactly known. We know the center-of-momentum for the system but cannot know how each proton is boosted. Since the x and y components are orthogonal to the direction of the boost they are unaffected by the boost of each individual interaction. Ideally, if the detector was 100% efficient this quantity would always be zero due to conservation of momentum, but many things, such as detector efficiency, particle misidentification, or particles that are weakly interacting such as neutrinos or $\tilde{\chi}_1^0$. Because of these, p_T^{miss} is a good discriminator for searching for physics beyond the SM [79].

5.1.4 H_T

Another interesting quantity is H_T , which is the scalar sum of the p_T of all of the jets in an event [80],

$$H_T = \sum_{i \in \text{jets}} p_{i,T}. \quad (5.3)$$

This quantity is quite useful when trying to identify massive particles and is quite good at suppressing QCD multijet background. Since H_T is a sum of all jets, it is specifically good at identifying particles that are massive and produce jets that can be measured in the CMS calorimeters. For QCD events that mainly contain quark(gluon) jets that are not t tend to not have as much energy as such that the H_T is small.

5.1.5 Soft b -Tagging

Soft b -tagging is used for b quarks that have low p_T . This search also targets models that produce very soft (low p_T) bottom or charm quarks. A large fraction of

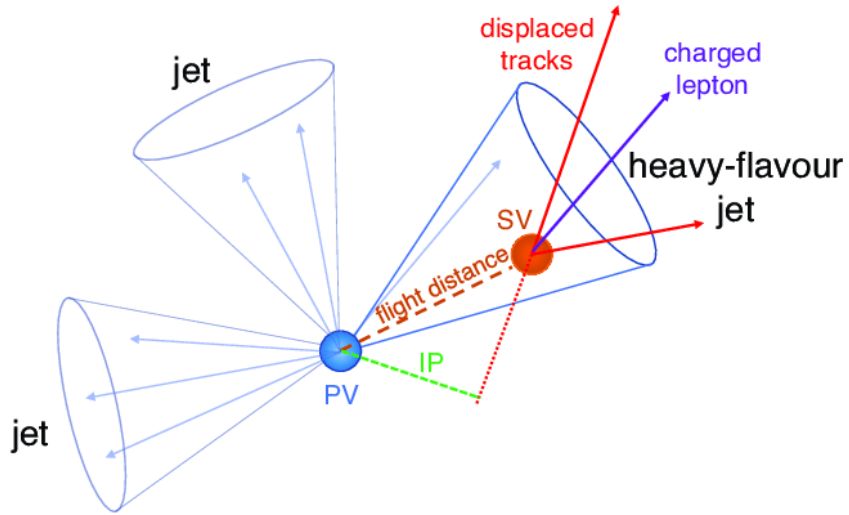


Figure 5.4 : An interaction that produces a long lived particle that has a reconstructed SV.

events contain b quarks with p_T below the 20 GeV jet threshold which may fail to be reconstructed as jets or become b-tagged due to either the SUSY mass spectrum or kinematics causing a large boost along the beam line. Identification of these soft quarks improves our ability to separate potential signal events from the SM background. We therefore aim to identify b or c quarks based on the presence of a SV reconstructed using the Inclusive Vertex Finder (IVF) [81, 82]. Additional requirements on the SV observable are applied to suppress the background originating from light quarks. These selected SV may be referred to as soft b -tags and are constructed to be an addition to the jets and b-tagged jets used in this analysis to improve efficiency.

The requirements on each SV to pass the soft b-tagging definition are:

- The distance in the transverse plane between the SV and the PV ≤ 3 cm.

- The significance of the distance between the SV and the PV in 3D, $\sigma_{IP}^{3D} \geq 4$.
- The pointing angle, defined as $\cos(\overrightarrow{PV}, \overrightarrow{SV}, \overrightarrow{p_{SV}}) \geq 0.98$, where $\overrightarrow{PV}, \overrightarrow{SV}$ is the vector pointing from PV to SV and $\overrightarrow{p_{SV}}$ is the total four-momentum of the tracks associated with the SV.
- The number of tracks associated with the SV is greater or equal to 3.
- The p_T of the particles associated SV is less than 20 GeV.

Identification of soft b-quarks is necessary for a potential signal region where the stop does not directly decay into a top quark and is essential for some of our search region bins.

5.1.6 Initial-state Radiation

Initial-state radiation (ISR) may be clustered into one of the large- R jets clustered with a distance parameter, $\Delta R = 0.8$. We use the larger radius jets to be sensitive to ISR with gluon splitting, when a jet radiates a gluon that pair produces two quarks. The ISR jet is identified as being the hardest of the large- R jets with $p_T > 200$ GeV which fails the loose b-tagging working point and is not identified as a top or W. This is a good parameter for jets that are neither tagged as t or W in the low Δm region of our search.

5.1.7 Electron and Muon Identification

This is a search for all-hadronic decays so no leptons are expected in the search region, however, for some control regions we require exactly one lepton so an efficient tagging method is necessary. There are two sets of selection criteria used in the analysis for electrons [83] and muons [84, 85]. The set of criteria used to efficiently

reject events with an isolated electron is done with a "Veto" ID. An electron with a Veto ID must pass the following cuts for the barrel (endcap) regions of the detector:

- $|\Delta\eta| < 0.007(0.01)$, $|\Delta\phi| < 0.8(0.7)$ for the EM showers in the ECAL,
- $\sigma_{i\eta i\eta} = \frac{\sum(\eta_i - \bar{\eta})^2 w_i}{\sum w_i} < 0.01(0.03)$ where $\bar{\eta} = \frac{\sum \eta_i w_i}{\sum w_i}$ and $w_i = \max(0, 4.7 + \log(E_i/E_{5\times 5}))$ where the sum is over a 5×5 crystal matrix centered around the most energetic crystal in the ECAL [77],
- $H/E < 0.15$ (not applicable) the ratio of hadronic energy over electromagnetic energy,
- PF isolation/ $p_T(\Delta R = 0.3) < 0.15(0.15)$ where we are calculating the p_T of the various energy deposits (charged hadrons, photons, and neutral hadrons) as the p_T for the PF Isolation and dividing it by the sum of the p_T of the listed candidates in a cone with a size of $\Delta R = 0.3$,
- $|d_0| < 0.04(0.04)$, $|d_z| < 0.2(0.2)$ where d_0 is the distance in the xy plane and d_z is the distance along the z -axis for the reconstructed candidate.

This veto ID is chosen such that the search region is most likely to be devoid of electrons, since it has a 95% efficiency [86].

We use the Loose muon definition recommended by the Muon POG for the purposes of the muon veto [87]. A Loose muon is identified as a Particle Flow (PF) [88] muon and can be either a global muon or an arbitrated tracker muon. Only candidates with transverse (longitudinal) impact parameter $|d_0| < 0.2$ cm ($|d_z| < 0.5$ cm,) with respect to the primary vertex, are considered. The electron and muon IDs are used in the definition of the Lost Lepton background which will be expanded upon further in Section 6.3.

5.1.8 Tau Identification

Identification of taus, which is a long lived particle $\tau_\tau = 2.9 \times 10^{-13}$ s, is necessary in an all-hadronic analysis, but a tau has the possibility of decaying hadronically, $\tau^+ \rightarrow \pi^+ \pi^0 \bar{\nu}_\tau$. The tau can decay both leptonically and hadronically with $\approx 17\%$ of decays to electrons or muons each, $\approx 51\%$ of decays to 1 hadron with ≥ 1 neutral hadrons, and $\approx 15\%$ for 3 hadrons with ≥ 1 neutral hadrons. The tau decays that are leptonic should be identified by the muon or electron IDs, but the hadronic decays are a bit more difficult. We are using a combined isolated track (IsoTrack) and MVA method for identifying a hadronically decaying tau.

The IsoTrack requirements are:

- $\text{pdgId} = 11$ or 13 (211) where pdgId is the particle data group Id from the reconstructed particle and $11 =$ electron, $13 =$ muon, and $211 =$ pion,
- $p_T \geq 5(10)$ GeV and $\text{iso} > 0.2(0.1)$ for electrons and muons (pions) where the isolation is the separation from other particle for a cone of $\Delta R = 0.2$,
- $m_T(l, p_T^{miss}) \leq 100$ GeV is the transverse mass between the candidate lepton and p_T^{miss} , see Sec. 5.1.9

The Tau ID has been studied extensively in tests which looked into the custom multivariate analysis (MVA) [89–91] similar to the one used in Ref. [39], a cut-based IsoTrack method, and Tau POG MVA method of identifying hadronically decaying taus. The methods which provide the best improvement to the efficiency of identifying taus with a small fake rate is the combination of IsoTrack and Tau POG MVA. With the inclusion of the combined method for identifying hadronically decaying taus, the veto percentage is $\frac{N_\tau > 0}{N_{gen} > 0} \approx 29.0\%(7.2\%)$ with an efficiency of the veto of $\frac{N_\tau > 0 \& N_\tau^{gen} > 0}{N_\tau^{gen} = 0} \approx 49.1\%(22.6\%)$ for $t\bar{t}$ background (signal), see Appendix. A.

For the IsoTrack method we require the following:

- $p_T \geq 5(10)\text{GeV}$, $\text{iso} \leq 0.2(0.1)$ for electrons and muons(pions);
- $m_T(\text{IsoTrack}, p_T^{miss}) < 100 \text{ GeV}$;

where $m_T(\text{IsoTrack}, p_T^{miss})$ is the transverse mass between the IsoTrack and p_T^{miss} .

For the Tau POG method we require:

- $p_T \geq 20\text{GeV}$, $|\eta| < 2.4$;
- Decay mode = $5(N_c - 1) + N_p \geq 0$ where N_c is the number of charged hadrons and N_p is the number of pions in the decay it is a descriminator developed to identify taus decaying to multiple prong events; and
- Medium working point.

With the inclusion of the separate electron/muon IDs and the combined IsoTrack + TauPOG IDs we have a method to efficiently veto leptons from our search region.

5.1.9 Transverse Energy between b quarks and p_T^{miss}

We will end up dividing the search regions we are interested in into two different groups. They will be distinguished by a parameter known as the transverse mass between the leading b jet and p_T^{miss} defined as:

$$M_T(b, p_T^{miss}) = \sqrt{2 \cdot p_T^{miss} \cdot p_T(b)(1 - \cos(\Delta\phi_{E,p_b}))}, \quad (5.4)$$

where $\Delta\phi_{E,p_b}$ is the angle, ϕ , between p_T^{miss} and the leading b jet, $(p(b))$. A feature of $M_T(b, p_T^{miss})$ when used for a parent particle that decays to a visible and invisible particles, such as $W^+ \rightarrow l^+\nu_l$ will have a peak at the W mass in the rest frame

[92]. This will be used to distinguish between our low and high mass search regions, see Section 5.3.1.

5.2 Samples and Filters

A detailed list of the samples and filters used in this analysis are described in Appendix B.

5.3 Baseline Selection

Following the same methods as above, we have a loose pre-selection which is referred to as the baseline selection. This will place a selection on jets and p_T^{miss} , which is used to eliminate a large fraction of background events. We define the baseline selection as:

- $N_{e,\mu} = 0, (p_T \geq 5 \text{ GeV}, |\eta| < 2.5(2.4), \text{miniISO} < 0.1(0.2))$ where the ISO is the sum of the p_T for the isolated tracks and calorimeter measurements divided by the lepton p_T ;
- $N_{e/\mu/\pi}^{\text{trk}} = 0, (p_T \geq 5(10) \text{ GeV}, \text{ISO} < 0.2(0.1)$ for electron/muons(pions));
- $N_\tau = 0, (p_T \geq 20 \text{ GeV}, |\eta| < 2.4)$, medium working point;
- $N_j \geq 2, (p_T \geq 30 \text{ GeV}, |\eta| < 2.4)$;
- $p_T^{miss} \geq 250 \text{ GeV}$, to reach the plateau of the trigger efficiency;
- $H_T \geq 300 \text{ GeV}$; and
- HEM Veto for part of 2018 data: $-3 \leq \eta \leq -1.4, -1.57 \leq \phi \leq -0.87$.

The HEM Veto is required due to a failure of two sectors of the HCAL endcaps on June 30th, 2018 which ended with the modules becoming unresponsive. These modules correspond to a region of $-3 \leq \eta \leq -1.4, -1.57 \leq \phi \leq -0.87$ which effect the lepton, jet, and p_T^{miss} reconstructions. This is applied to data from 2018 after Run 319077 and to the corresponding simulated events. In addition to this, we allow for two separate sets of additional selections to apply to the low and high Δm search regions to further reduce background where the $\Delta m = m_{\tilde{t}_1} - m_{\tilde{\chi}_1^0}$, see Fig. 5.5. The high Δm baseline selection includes the baseline selection and additionally:

- $N_j \geq 5, (p_T \geq 30 \text{ GeV}, |\eta| < 2.4);$
- $N_b \geq 1, (p_T \geq 20 \text{ GeV}, |\eta| < 2.4)$, medium DeepCSV working point;
- $\text{Min}[|\Delta\phi(p_T^{miss}, j_1)|, |\Delta\phi(p_T^{miss}, j_2)|, |\Delta\phi(p_T^{miss}, j_3)|, |\Delta\phi(p_T^{miss}, j_4)|] \equiv \Delta\phi_{1234} \geq 0.5$, where j_1, j_2, j_3, j_4 are the four leading jets in p_T . This requirement is to reduce the QCD multijet background since QCD events with p_T^{miss} are typically due to mis-measurement of the quark-gluon jets.

Next, the low Δm baseline selection has the following addition selections:

- $N_t = 0, N_W = 0, N_{res} = 0$, where N_t and N_W are the number of merged tops and W 's, respectively, and N_{res} is the number of resolved tops;
- An ISR jet as defined in Sec. 5.1.6 with $p_T(\text{ISR}) \geq 200 \text{ GeV}, |\eta| < 2.4, |\Delta\phi(j_{\text{ISR}}, p_T^{miss})| \geq 2.;$
- $p_T^{miss}/\sqrt{H_T} \equiv S_{p_T^{miss}} \geq 10$, where H_T is calculated as the scalar sum of the p_T of jets with $p_T \geq 30 \text{ GeV}$ and $|\eta| < 2.4$; and
- $|\Delta\phi(j_1, p_T^{miss})| \geq 0.5, |\Delta\phi(j_{2,3}, p_T^{miss})| \geq 0.15$, where j_1, j_2, j_3 are the three leading jets in p_T .

5.3.1 Search Regions

After applying the baseline selection criteria, we categorize events in the search sample into exclusive search regions that exploit the kinematic properties of different signal topologies, see [33, 34, 39]. The search regions will be binned using the physics objects and kinematics variables explained above, such as, N_j , N_b , N_t , N_{res} , N_W , p_T^{miss} , H_T , N_{SV} , $M_T(b_{1,2}, p_T^{\text{miss}})$, and $N_{\text{lep}} = 0$

For the search regions that mainly target high Δm signal models, we define two event categories in $M_T(b_{1,2}, p_T^{\text{miss}})$, see Section 5.4, and a variable defined as:

$$M_T(b_{1,2}, p_T^{\text{miss}}) \equiv \begin{cases} m_T(b, p_T^{\text{miss}}), & N_b = 1 \\ \text{Min}[m_T(b_1, p_T^{\text{miss}}), m_T(b_2, p_T^{\text{miss}})], & N_b \geq 2 \end{cases}, \quad (5.5)$$

where b_1, b_2 are the two selected b-tagged jets with the highest values of the DeepCSV discriminator. In $t\bar{t}$ events where the W bosons decays leptonically and is missed by the lepton tagging, which is known as Lost Lepton background, the $M_T(b_{1,2}, p_T^{\text{miss}})$ of such an event has a kinematic endpoint at the mass of the top quark, m_t .

We therefore define two event categories: $M_T(b_{1,2}, p_T^{\text{miss}}) > 175$ GeV and < 175 GeV, see Fig. 5.5. In the low- $M_T(b_{1,2}, p_T^{\text{miss}})$ category, to target signal models with moderate values of Δm , we define search regions by requiring $N_j \geq 7$ and $N_{\text{res}} \geq 1$ to benefit from potential ISR in signal events while suppressing the SM background. Events are then subdivided according to the number of b-tagged jets ($N_b = 1, = 2, \geq 3$) and different p_T^{miss} thresholds. The same subdivision is performed for events in the high- $M_T(b_{1,2}, p_T^{\text{miss}})$ category with $N_j \geq 7$, but containing no top- or W-tagged candidates. We then target signal models with sufficiently boosted top quarks or W bosons by defining categories in the high- $M_T(b_{1,2}, p_T^{\text{miss}})$ region that require the presence of at least one top- or W-tagged candidate. These categories do not have

any further N_j requirement beyond that of the high Δm baseline selection, and are further subdivided according to N_b, p_T^{miss}, H_T and the number of each kind of top- and W-tagged candidate. Table 5.1 summarizes the definitions of all 130 disjoint search regions targeting high Δm signal models.

Events originating from low Δm signal models are likely to have lower values of $M_T(b_{1,2}, p_T^{miss})$. We therefore only use the low- $M_T(b_{1,2}, p_T^{miss})$ category to define search regions targeting these signal models. These search regions are further defined by the number of b-tagged jets, the number of identified secondary vertices (N_{SV}), the ISR jet p_T ($p_T(b)$), and p_T^{miss} . Events in the $N_b = 0$ category, which targets very compressed signal models, are further subdivided according to N_j . Only events with very high ISR $p_T (> 500 \text{ GeV})$ are selected in this category, which is also categorized by the presence or absence of soft b-tagged secondary vertices. Events in the $N_b = 1$ category are further characterized according to the p_T of the b-tagged jet into two sub-categories, while those in the $N_b \geq 2$ are subdivided based on $p_T(b_{12})$ into three sub-categories, in order to take advantage of the softer b jet p_T spectrum expected in signal events compared to the SM background. Orthogonality to the high Δm event categories is achieved mostly by the $M_T(b_{1,2}, p_T^{miss})$ categorization. Table 5.2 summarizes the definitions of the 53 disjoint search regions targeting low Δm signal models.

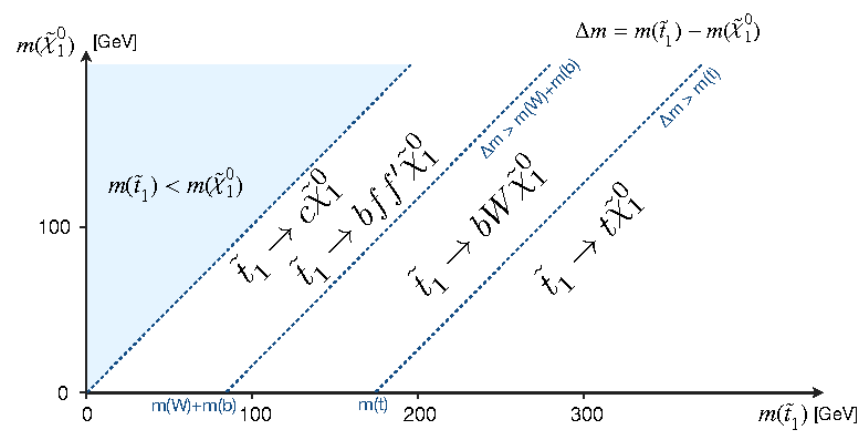


Figure 5.5 : Mass parameter space for different decay modes of the top squark.

Table 5.1 : Summary of the 130 disjoint search regions that mainly target high Δm signal models. The high Δm baseline selection is again $N_j \geq 5$, $p_T^{miss} > 250$ GeV, $N_b \geq 1$, and $\Delta\phi_{1234} > 0.5$.

$M_T(b_{1,2}, p_T^{miss}) < 175$ GeV						
N_j	N_b	N_t	N_W	N_{res}	H_T [GeV]	p_T^{miss} [GeV]
≥ 7	$1, \geq 2$	≥ 0	≥ 0	≥ 1	≥ 300	$250 - 300, 300 - 400, 400 - 500, \geq 500$
$M_T(b_{1,2}, p_T^{miss}) \geq 175$ GeV						
N_j	N_b	N_t	N_W	N_{res}	H_T [GeV]	p_T^{miss} [GeV]
≥ 5	$1, \geq 2$	0	0	0	≥ 1000	$250 - 350, 350 - 450, 450 - 550, \geq 550$
≥ 5	1	≥ 1	0	0	$300 - 1000, 1000 - 1500, \geq 1500$	$250 - 550, 550 - 650, \geq 650$
		0	≥ 1	0	$300 - 1300, \geq 1300$	$250 - 350, 350 - 450, \geq 450$
		0	0	≥ 1	$300 - 1000, 1000 - 1500, \geq 1500$	$250 - 350, 350 - 450, 450 - 550, 550 - 650, \geq 650$
		≥ 1	≥ 1	0	≥ 300	$250 - 550, \geq 550$
		≥ 1	0	≥ 1	≥ 300	$250 - 550, \geq 550$
		0	≥ 1	≥ 1	≥ 300	$250 - 550, \geq 550$
≥ 5	2	1	0	0	$300 - 1000, 1000 - 1500, \geq 1500$	$250 - 550, 550 - 650, \geq 650$
		0	1	0	$300 - 1300, \geq 1300$	$250 - 350, 350 - 450, \geq 450$
		0	0	1	$300 - 1000, 1000 - 1500, \geq 1500$	$250 - 350, 350 - 450, 450 - 550, 550 - 650, \geq 650$
		1	1	0	≥ 300	$250 - 550, \geq 550$
		1	0	1	$300 - 1300, \geq 1300$	$250 - 350, 350 - 450, \geq 450$
		0	1	1	≥ 300	$250 - 550, \geq 550$
		2	0	0	≥ 300	$250 - 450, \geq 450$
		0	2	0	≥ 300	≥ 250
		0	0	2	$300 - 1300, \geq 1300$	$250 - 450, \geq 450$
		$N_t + N_W + N_{res} \geq 3$			≥ 300	≥ 250
≥ 5	≥ 3	1	0	0	$300 - 1000, 1000 - 1500, \geq 1500$	$250 - 350, 350 - 550, \geq 550$
		0	1	0	≥ 300	$250 - 350, 350 - 550, \geq 550$
		0	0	1	$300 - 1000, 1000 - 1500, \geq 1500$	$250 - 350, 350 - 550, \geq 550$
		1	1	0	≥ 300	≥ 250
		1	0	1	≥ 300	$250 - 350, \geq 350$
		0	1	1	≥ 300	≥ 250
		2	0	0	≥ 300	≥ 250
		0	2	0	≥ 300	≥ 250
		0	0	2	≥ 300	$250 - 350, \geq 350$
		$N_t + N_W + N_{res} \geq 3$			≥ 300	≥ 250

Table 5.2 : Summary of the 53 disjoint search regions that mainly target low Δm signal models. The low Δm baseline selection is again $N_j \geq 2$, $p_T^{miss} > 250$ GeV, $N_t = N_W = N_{res} = 0$, $N_b \geq 0$, $M_T(b_{1,2}, p_T^{miss}) < 175$ GeV (when applicable), $|\Delta\phi(j_1, p_T^{miss})| > 0.5$, $|\Delta\phi(j_{2,3}, p_T^{miss})| > 0.15$, $p_T(\text{ISR}) > 200$ GeV, $|\eta(\text{ISR})| < 2.4$, $|\Delta\phi(j_{\text{ISR}}, p_T^{miss})| > 2$, and $S_{p_T^{miss}} > 10$.

N_j	N_b	N_{SV}	$p_T(\text{ISR})$ [GeV]	$p_T(b)$ [GeV]	p_T^{miss} [GeV]	
2 – 5 ≥ 6	0	0	> 500	-	450 – 550, 550 – 650, 650 – 750, > 750	
		0			450 – 550, 550 – 650, 650 – 750, > 750	
		≥ 1			450 – 550, 550 – 650, 650 – 750, > 750	
		≥ 1			450 – 550, 550 – 650, 650 – 750, > 750	
≥ 2	1	0	300 – 500	20 – 40	300 – 400, 400 – 500, 500 – 600, > 600	
		0	300 – 500	40 – 70	300 – 400, 400 – 500, 500 – 600, > 600	
		0	> 500	20 – 40	450 – 550, 550 – 650, 650 – 750, > 750	
		0	> 500	40 – 70	450 – 550, 550 – 650, 650 – 750, > 750	
		≥ 1	> 300	20 – 40	300 – 400, 400 – 500, > 500	
		≥ 0	300 – 500	40 – 80	300 – 400, 400 – 500, > 500	
≥ 2 ≥ 2 ≥ 7 ≥ 2 ≥ 2 ≥ 7	≥ 2		300 – 500	80 – 140	300 – 400, 400 – 500, > 500	
			300 – 500	> 140	300 – 400, 400 – 500, > 500	
			> 500	40 – 80	450 – 550, 550 – 650, > 650	
			> 500	80 – 140	450 – 550, 550 – 650, > 650	
			> 300	> 140	450 – 550, 550 – 650, > 650	

Chapter 6

Top Squark Production and Backgrounds

We have now motivated that the top squark, \tilde{t}_1 , could be the lightest squark, see Sec. 3.3.4. This allows us to possibly produce them at CMS. In Sec. 5.3, we have designed a search that will look for events with large amounts of p_T^{miss} and N_j . These events are being targeted in separate low Δm and high Δm search regions. For all of these we are interested in comparing the data and background in each search or control region. We will look at the production and decay modes of various \tilde{t}_1 interactions and the estimation of the SM background of each region.

6.1 Production and Decay Modes

To produce the top squark all we need is the collision of two proton-proton beams. It is shown as a black circle in Fig. 6.2 and 6.1. This is meant to represent many processes that can make a top squark. The main processes are gluon fusion, when two gluons fuse into a single gluon which then decays into a top and anti-top squark pair, or annihilation, where two quarks annihilate to a gluon propagator which thus decays into two top squarks.

The main decay mode of the top squark is $\tilde{t}_1 \rightarrow t + \tilde{\chi}_1^0$ and $\tilde{t}_1 \rightarrow b + \tilde{\chi}^\pm$, Fig. 6.1. The top quark most likely decays as, $t \rightarrow bW^+$, while the b quark will decay to either a c or an u quark in its decay chain with an additional W boson. The $\tilde{\chi}_1^0$ is proposed to be a stable dark matter candidate while the $\tilde{\chi}^\pm$ could decay as, $\tilde{\chi}^\pm \rightarrow \tilde{\chi}_1^0 W$. Next,

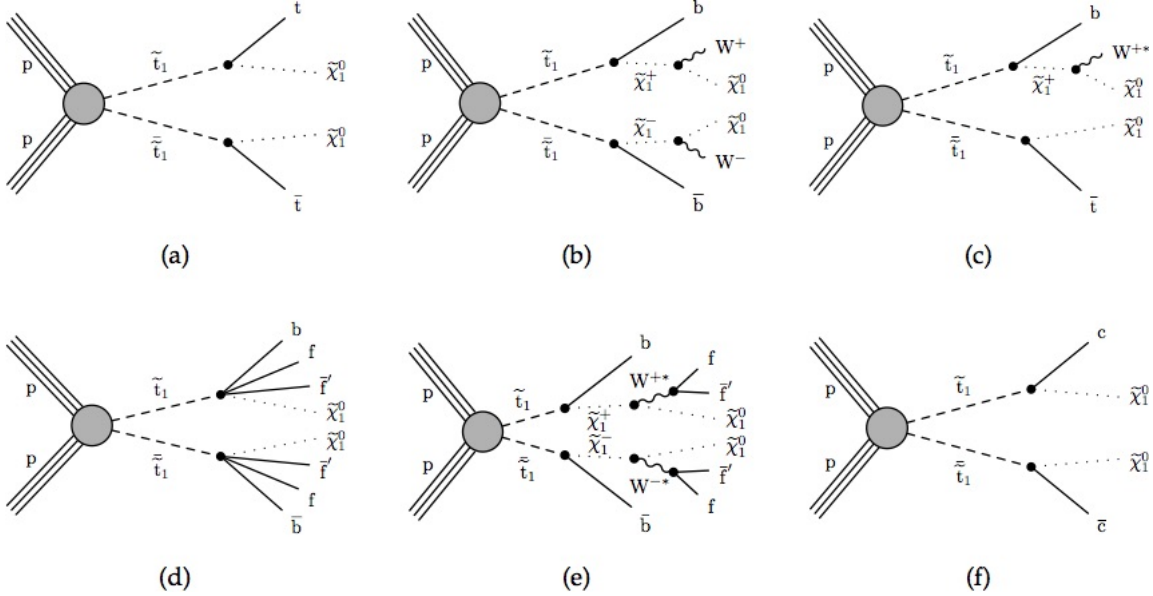


Figure 6.1 : Feynman diagrams for the direct \tilde{t}_1 production in SUSY. The allowed decay modes are (a) T2tt, (b) T2bW, (c) T2tb, (d, e) T2fbd, and (f) T2cc.

a four body decay is allowed for, $\tilde{t}_1 \rightarrow bff'\tilde{\chi}_1^0$, see Fig. 6.1(d, e). The final direct \tilde{t}_1 production we are interested in is the $\tilde{t}_1 \rightarrow c\tilde{\chi}_1^0$, see Fig. 6.1(f). To be as inclusive as possible, we are also including indirect top squark production [93] as seen in Fig. 6.2. We see that the \tilde{t}_1 will decay to multiple jets, N_j , and missing transverse energy, p_T^{miss} . Now we are going to try to estimate the SM background that could be in each of our search region bins.

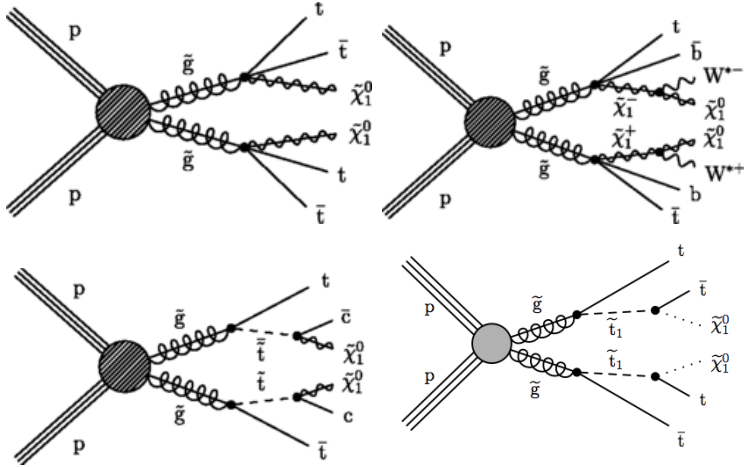


Figure 6.2 : Feynman diagrams for the indirect \tilde{t}_1 production in SUSY. The allowed decay modes are T1tttt (top left), T1ttbb (top right), T5ttcc (bottom left), and T5tttt (bottom right).

6.2 Standard Model Background

The standard model background for the top squark search is defined by a large p_T^{miss} and multiple jets. There are a couple types of SM background that can be misinterpreted as our signal. The most likely background is that which causes many tops (or heavy particles) and missing energy. Events in the SM like $t\bar{t}$ and $W+jets$ will have many jets produced and p_T^{miss} due to a missed lepton and neutrino. The production of heavy particles like $Z \rightarrow \nu\nu$ will give multiple jets and p_T^{miss} from the neutrinos being missed by the detector. QCD events often produce events with multiple jets, due to acceptances in the detector jets can sometimes be mis-measured which can cause large p_T^{miss} . There are also various processes that are quite rare but still need to be included. We will take an in-depth look into each of these backgrounds.

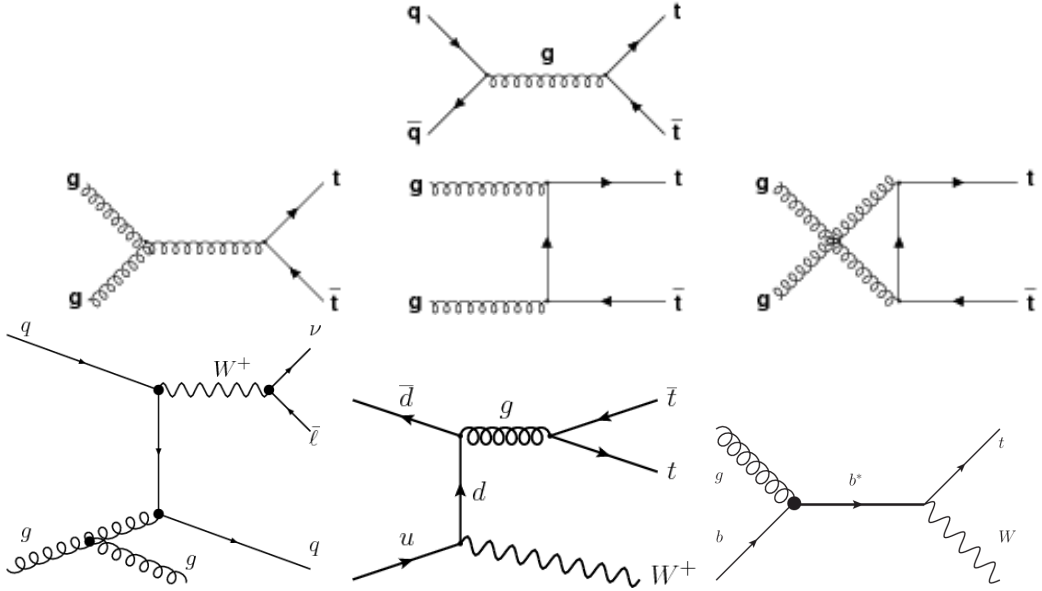


Figure 6.3 : Production Feynman diagrams for the LL backgrounds [94–96].

6.3 Lost Lepton

The contribution from the $t\bar{t}$ and $W + \text{jets}$ processes arise from leptonic decays of the W boson, where the charged lepton is outside the kinematic acceptance of CMS or evades identification by the dedicated lepton vetoes. Large p_T^{miss} can be generated by the associated neutrino and the lepton that is not reconstructed, allowing such events to enter the search regions. This background is collectively referred to as the "Lost Lepton" (LL) background. Contributions arising from tW , ttW and single-top processes also enter into this category, but with much smaller importance.

Studies in simulation indicate that the event kinematics for different lepton flavors are similar enough to allow us to estimate them collectively from a single control sample in data that has event characteristics similar to those of the search sample.

Because of this, we use the single-lepton control sample to estimate the LL background, using the method described in detail in Ref. [91]. The single-lepton sample consists of events that have one lepton satisfying the lepton-veto criteria. In order to suppress potential signal contamination, we require $M_T(l, p_T^{miss}) < 100 \text{ GeV}$. The requirement of low $M_T(l, p_T^{miss})$ also ensures orthogonality to the search regions used in direct top squark production in the single-lepton or double-lepton final state, making it possible to statistically combine the results of the two searches. The selection applied to the single-lepton control sample follows the same selection on the search variables as in the zero-lepton selection with the exception of classification according to the number of top and W -tagged candidates.

6.3.1 Combining All Run 2 Eras

Firstly, for this analysis we are interested in the possibility of combining the yields of each era into one estimation. This is initially done by looking at the p_T^{miss} distributions in each era. Since the LL estimation is done with the transfer factor method, a good confirmation would be the comparison of the transfer factor in each SR for each era.

6.3.2 Transfer Factors

The LL estimation in each search region is based upon the event count in data in the corresponding control region in the single-lepton sample. The count is extrapolated to the search region to obtain a prediction by means of a transfer factor obtained from simulation as follows:

$$N_{pred}^{LL} = TF_{LL} \cdot N_{data}(1l). \quad (6.1)$$

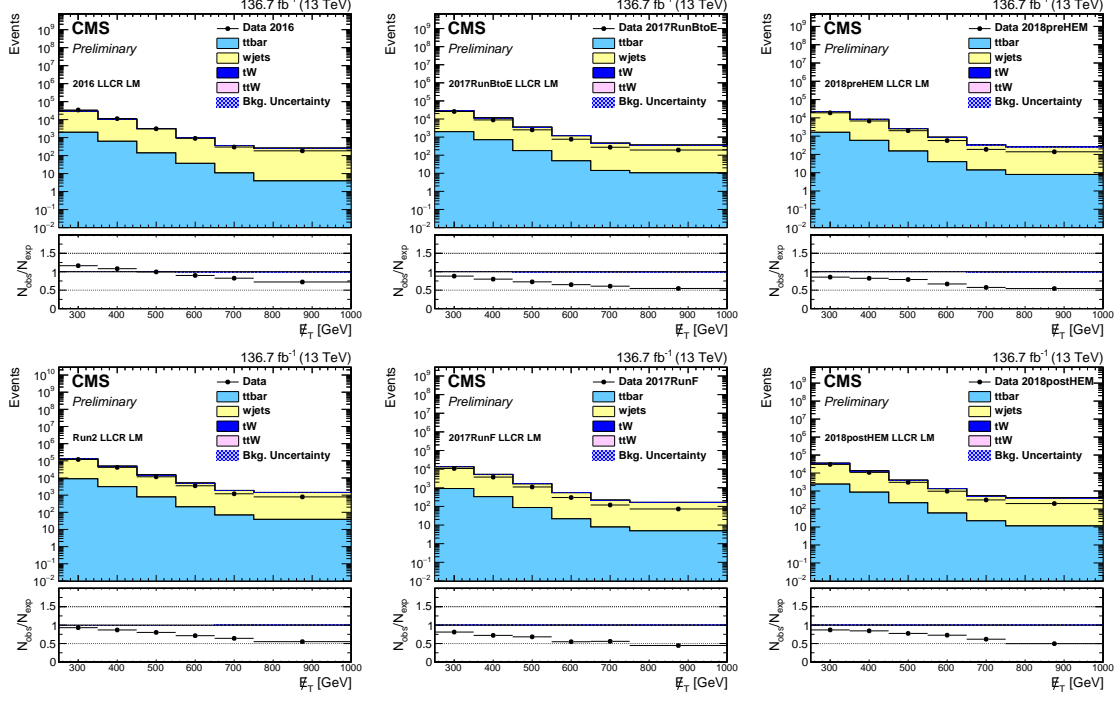


Figure 6.4 : Comparison of the Data and MC in the 1Lep CR for each era: Run2016, Run2017BtoE, Run2017F, Run2018preHEM, Run2018PostHEM, and the combination of all eras in the Low Δm region. Each era has a good agreement between Data and MC.

This allows us to have the same selection for the single-lepton control sample and the zero-lepton sample. The only exception is the number of top and W-tagged candidates. The LL estimation is dependent on the yield of data in the corresponding CR and the TF calculated by the single-lepton sample. The transfer factor is defined as,

$$TF_{LL} = \frac{N_{MC}(0l)}{N_{MC}(1l)}, \quad (6.2)$$

where $N_{MC}(1l)$ is the event count observed in the corresponding CR and $N_{MC}(0l)$ uses the event count in the corresponding SR.

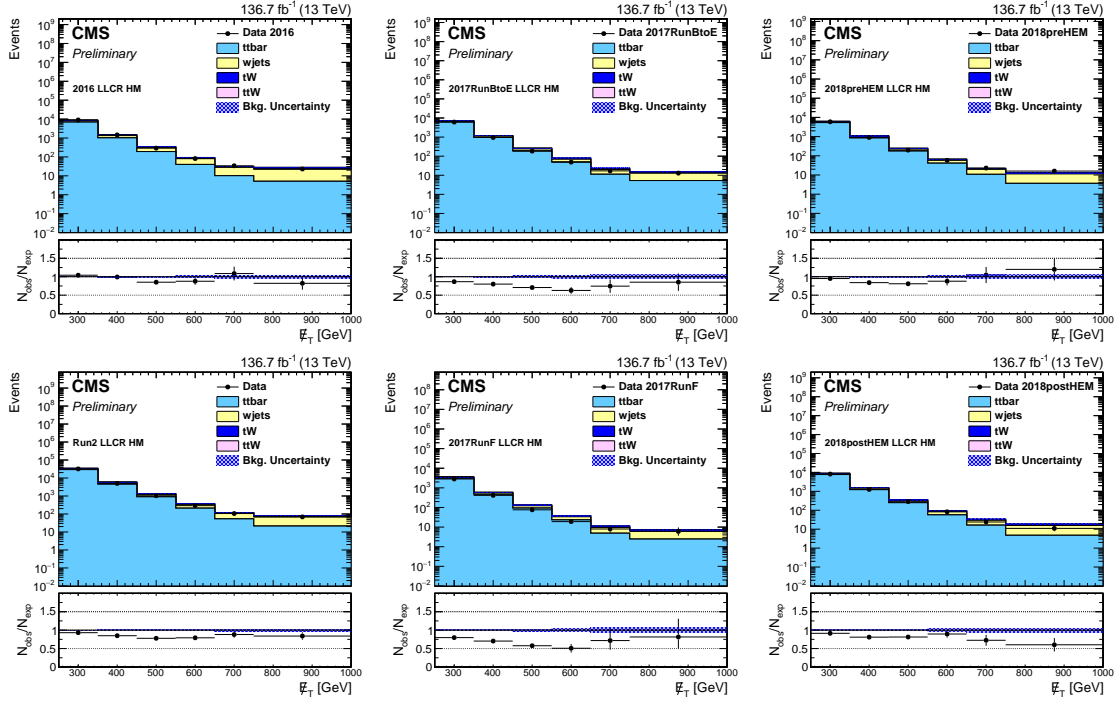


Figure 6.5 : Comparison of the Data and MC in the 1Lep CR for each era: Run2016, Run2017BtoE, Run2017F, Run2018preHEM, Run2018PostHEM, and the combination of all eras in the High Δm region. Each era has a good agreement between Data and MC.

The main motivation behind this approach is to increase the statistical precision of the background estimation. The performance of the t and W taggers has been studied in data and MC samples and a reasonably good agreement is observed allowing us to proceed with this approach. Data-to-MC scale factors are extracted and applied to MC to account for residual differences of the tagging performance in data. Detailed studies comparing the performance of the t and W taggers in data and MC are found at Ref. [39].

The control regions utilized to predict the LL background are displayed in Figs.

6.8 to 6.14. Figures 6.8 and 6.9 display the control regions specific to the low Δm selection, where the regions are binned following the search region definition. Figures 6.10 to 6.14 display the control regions dedicated for the high Δm selection. Due to the nature of the background estimation method applied in the high Δm search, control regions are utilized for the prediction of multiple search regions.

Tables 6.1 to 6.4 summarize the yields in data observed in the single-lepton sample, the derived transfer factor, and the resulting LL predictions for the low Δm and high Δm search regions, respectively. The transfer factors in the high Δm region actually account for two levels of extrapolation. The CR for the high Δm is loose, such that, there is no binning in tops or W tagging. We then extrapolate to the SR with the inclusion of the top and W tags, along with scale factors, to estimate the LL background in the region with:

$$\begin{aligned} TF_{LL} &= TF_{LL}^{CR-SR} \times TF_{LL}^{SR-extrap} \\ &= \frac{N_{MC}(0l)(N_j, N_b, p_T^{miss})}{N_{MC}(1l)(N_j, N_b, p_T^{miss})} \times \frac{N_{MC}(0l)(N_j, N_b, p_T^{miss}, N_t, N_{\text{res}}, N_W)}{N_{MC}(0l)(N_j, N_b, p_T^{miss})}. \end{aligned} \quad (6.3)$$

We now want to consider how the transfer factor for each era relates to the total transfer factor. In Figs. 6.6 and 6.7, we see the comparison for the total TF_{LL} for each era of the data and simulation. These are all in quite good agreement, but we see an extended tail due to the low statistics of the extrapolation in t and W . Once we alter the comparison for the TF_{LL} to separate the CR-to-SR and the SR-to-Extrapolation, we see a much better agreement when for the CR-to-SR comparison. These are improved because of the better statistics in the region.

Now that we have confirmed that the LL background is valid to be combined for all the eras we can combine the transfer factors and control region comparisons of each era in the final estimation. Now, we can consider the combination of the other

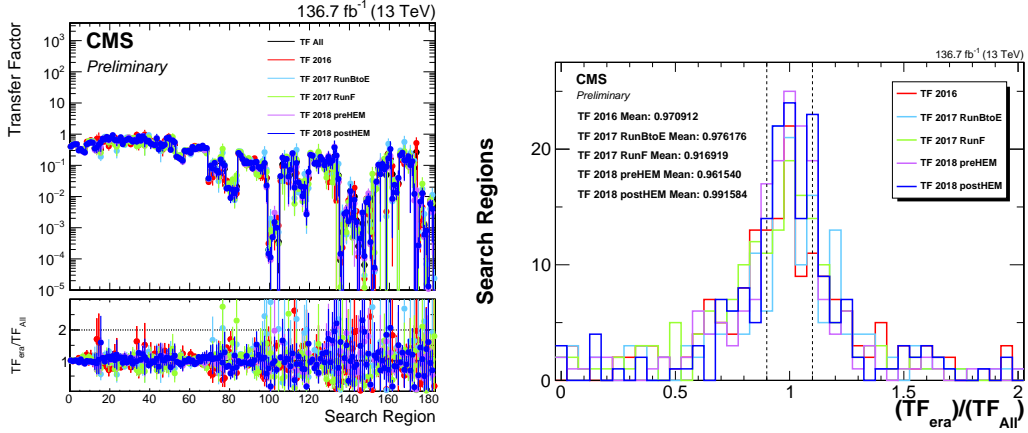


Figure 6.6 : Comparisons of the transfer factors for each era of MC in the low and high Δm regions. The values are shown in their separate bins on the left plot and in a combined form on the right. The mean for each is also shown.

background estimations.

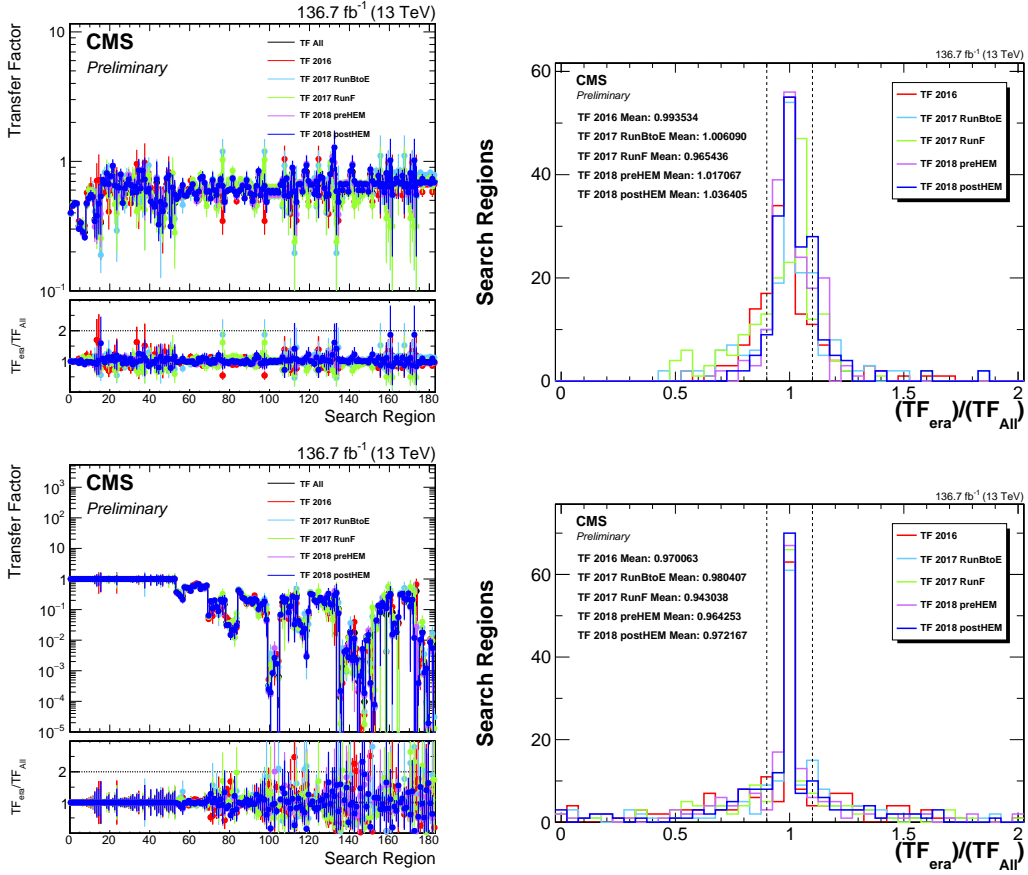


Figure 6.7 : Comparisons of the transfer factors, separated into the CR-to-SR (top) and SR-to-extrapolation (bottom), for each era of MC in the low and high Δm regions. The values are shown in their separate bins on the left plot and in a combined form on the right. The mean for each is also shown.

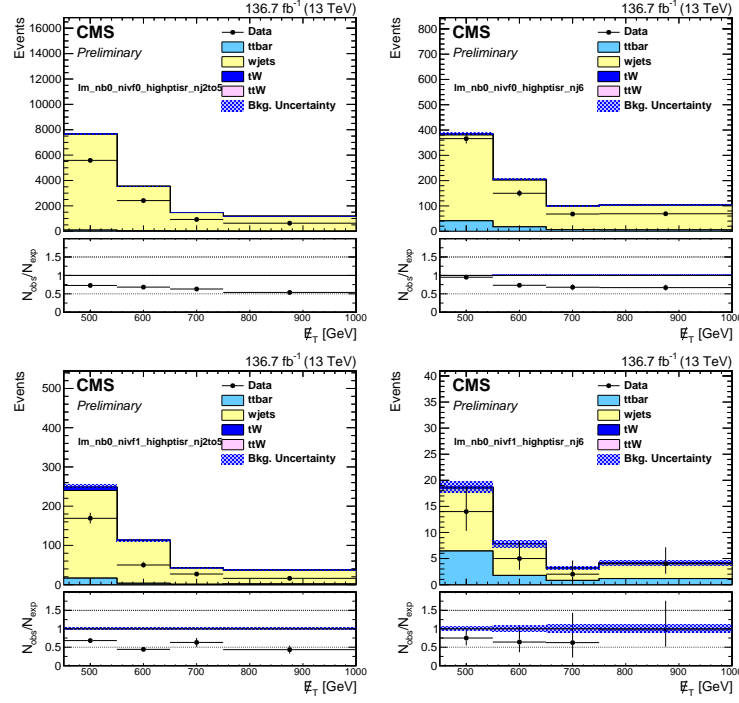


Figure 6.8 : Comparison of the p_T^{miss} distribution in the single-lepton sample after applying the low Δm baseline selection in the $N_b = 0$ region. Data and simulation are represented by the black points and stacked histograms, respectively. The error bars on the ratio of observed data to simulation correspond to the data statistical uncertainty and the shaded blue band represents the statistical uncertainty on the simulation. These regions are included with the search regions in the simultaneous fit for the signal extraction in order to estimate the LL contribution.

Search Region	$p_T^{\text{miss}}[\text{GeV}]$	$N_{\text{data}}(II)$	TF_{LL}	$N_{\text{pred}}^{\text{LL}}$
low Δm , $N_b = 0$, $N_{SV} = 0$, $p_T(\text{ISR}) \geq 500 \text{ GeV}$, $2 \leq N_j \leq 5$				
0	450–550	5585	0.396±0.003	2212.80±34.21
1	550–650	2415	0.459±0.004	1108.97±24.16
2	650–750	927	0.474±0.004	439.19±14.87
3	≥ 750	632	0.470±0.004	296.80±12.13
low Δm , $N_b = 0$, $N_{SV} = 0$, $p_T(\text{ISR}) \geq 500 \text{ GeV}$, $N_j \geq 6$				
4	450–550	366	0.317±0.006	115.86±6.49
5	550–650	150	0.319±0.009	47.78±4.14
6	650–750	68	0.294±0.011	20.00±2.53
7	≥ 750	69	0.285±0.008	19.69±2.44
low Δm , $N_b = 0$, $N_{SV} \geq 1$, $p_T(\text{ISR}) \geq 500 \text{ GeV}$, $2 \leq N_j \leq 5$				
8	450–550	169	0.473±0.019	79.87±6.94
9	550–650	50	0.533±0.022	26.63±3.92
10	650–750	27	0.562±0.028	15.18±3.02
11	≥ 750	16	0.558±0.035	8.93±2.30
low Δm , $N_b = 0$, $N_{SV} \geq 1$, $p_T(\text{ISR}) \geq 500 \text{ GeV}$, $N_j \geq 6$				
12	450–550	14	0.357±0.042	4.99±1.46
13	550–650	5	0.418±0.069	2.09±1.00
14	650–750	2	0.486±0.085	0.97±0.71
15	≥ 750	4	0.332±0.076	1.33±0.73
low Δm , $N_b = 1$, $N_{SV} = 0$, $M_T(b_{1,2}, p_T^{\text{miss}}) < 175 \text{ GeV}$, $300 \leq p_T(\text{ISR}) < 500 \text{ GeV}$, $p_T(b) < 40 \text{ GeV}$				
16	300–400	1923	0.654±0.014	1258.07±38.72
17	400–500	317	0.685±0.030	217.02±15.45
18	500–600	32	0.738±0.062	23.60±4.62
19	≥ 600	6	0.568±0.066	3.41±1.45
low Δm , $N_b = 1$, $N_{SV} = 0$, $M_T(b_{1,2}, p_T^{\text{miss}}) < 175 \text{ GeV}$, $300 \leq p_T(\text{ISR}) < 500 \text{ GeV}$, $40 < p_T(b) < 70 \text{ GeV}$				
20	300–400	1062	0.727±0.018	771.93±30.49
21	400–500	133	0.801±0.047	106.55±11.12
22	500–600	12	0.642±0.077	7.70±2.41
23	≥ 600	6	0.533±0.115	3.20±1.48
low Δm , $N_b = 1$, $N_{SV} = 0$, $M_T(b_{1,2}, p_T^{\text{miss}}) < 175 \text{ GeV}$, $p_T(\text{ISR}) \geq 500 \text{ GeV}$, $p_T(b) < 40 \text{ GeV}$				
24	450–550	140	0.571±0.026	79.90±7.69
25	550–650	43	0.721±0.038	31.00±5.00
26	650–750	13	0.508±0.031	6.61±1.88
27	≥ 750	15	0.560±0.034	8.40±2.23
low Δm , $N_b = 1$, $N_{SV} = 0$, $M_T(b_{1,2}, p_T^{\text{miss}}) < 175 \text{ GeV}$, $p_T(\text{ISR}) \geq 500 \text{ GeV}$, $40 < p_T(b) < 70 \text{ GeV}$				
28	450–550	100	0.702±0.040	70.23±8.09
29	550–650	22	0.727±0.045	15.99±3.55
30	650–750	11	0.596±0.053	6.56±2.06
31	≥ 750	5	0.645±0.065	3.23±1.48
low Δm , $N_b = 1$, $N_{SV} \geq 1$, $M_T(b_{1,2}, p_T^{\text{miss}}) < 175 \text{ GeV}$, $p_T(b) < 40 \text{ GeV}$				
32	300–400	111	0.645±0.046	71.55±8.47
33	400–500	24	0.577±0.067	13.85±3.25
34	≥ 500	14	0.624±0.071	8.74±2.54
low Δm , $N_b \geq 2$, $M_T(b_{1,2}, p_T^{\text{miss}}) < 175 \text{ GeV}$, $300 \leq p_T(\text{ISR}) < 500 \text{ GeV}$, $p_T(b_{12}) < 80 \text{ GeV}$				
35	300–400	247	0.590±0.026	145.70±11.29
36	400–500	36	0.695±0.068	25.02±4.83
37	≥ 500	8	0.641±0.154	5.13±2.19
low Δm , $N_b \geq 2$, $M_T(b_{1,2}, p_T^{\text{miss}}) < 175 \text{ GeV}$, $300 \leq p_T(\text{ISR}) < 500 \text{ GeV}$, $80 < p_T(b_{12}) < 140 \text{ GeV}$				
38	300–400	607	0.572±0.015	347.33±16.63
39	400–500	105	0.722±0.045	75.78±8.80
40	≥ 500	17	0.540±0.081	9.19±2.62
low Δm , $N_b \geq 2$, $M_T(b_{1,2}, p_T^{\text{miss}}) < 175 \text{ GeV}$, $300 \leq p_T(\text{ISR}) < 500 \text{ GeV}$, $p_T(b_{12}) \geq 140 \text{ GeV}$, $N_j \geq 7$				
41	300–400	124	0.483±0.023	59.88±6.06
42	400–500	26	0.465±0.041	12.09±2.60
43	≥ 500	7	0.669±0.116	4.68±1.95
low Δm , $N_b \geq 2$, $M_T(b_{1,2}, p_T^{\text{miss}}) < 175 \text{ GeV}$, $p_T(\text{ISR}) \geq 500 \text{ GeV}$, $p_T(b_{12}) < 80 \text{ GeV}$				
44	450–550	19	0.404±0.050	7.67±2.00
45	550–650	7	0.407±0.078	2.85±1.21
46	≥ 650	2	0.400±0.066	0.80±0.58
low Δm , $N_b \geq 2$, $M_T(b_{1,2}, p_T^{\text{miss}}) < 175 \text{ GeV}$, $p_T(\text{ISR}) \geq 500 \text{ GeV}$, $80 < p_T(b_{12}) < 140 \text{ GeV}$				
47	450–550	58	0.455±0.034	26.41±3.99
48	550–650	16	0.657±0.073	10.51±2.88
49	≥ 650	6	0.732±0.105	4.39±1.90
low Δm , $N_b \geq 2$, $M_T(b_{1,2}, p_T^{\text{miss}}) < 175 \text{ GeV}$, $p_T(\text{ISR}) \geq 500 \text{ GeV}$, $p_T(b_{12}) \geq 140 \text{ GeV}$, $N_j \geq 7$				
50	450–550	37	0.398±0.038	14.74±2.79
51	550–650	12	0.572±0.072	6.87±2.16
52	≥ 650	3	0.457±0.076	1.37±0.82

Table 6.1 : The LL estimate in the various low Δm search regions, bins 0 to 52, using the 136.7 fb^{-1} dataset.

Search Region	$p_T^{\text{miss}}[\text{GeV}]$	$N_{\text{data}}(1l)$	TF_{LL}	$TF_{LL}^{\text{CR-SR}}$	$TF_{LL}^{\text{SR-extrap}}$	$N_{\text{pred}}^{\text{LL}}$
high Δm , $N_b = 1$, $M_T(b_{1,2}, p_T^{\text{miss}}) < 175 \text{ GeV}$, $N_j \geq 7$, $N_{\text{res}} \geq 1$						
53	250–300	1151	0.196±0.004	0.519	0.378	225.43±8.24
54	300–400	697	0.187±0.005	0.550	0.340	130.35±6.21
55	400–500	129	0.180±0.011	0.577	0.313	23.26±2.53
56	≥ 500	43	0.157±0.016	0.598	0.263	6.77±1.25
high Δm , $N_b \geq 2$, $M_T(b_{1,2}, p_T^{\text{miss}}) < 175 \text{ GeV}$, $N_j \geq 7$, $N_{\text{res}} \geq 1$						
57	250–300	2250	0.292±0.004	0.539	0.542	657.73±16.12
58	300–400	1256	0.286±0.005	0.548	0.522	359.11±11.69
59	400–500	236	0.278±0.010	0.582	0.478	65.56±4.92
60	≥ 500	99	0.259±0.017	0.625	0.415	25.67±3.06
high Δm , $N_b = 1$, $M_T(b_{1,2}, p_T^{\text{miss}}) \geq 175 \text{ GeV}$, $N_t = 0$, $N_{\text{res}} = 0$, $N_W = 0$, $H_T \geq 1000$						
61	250–350	570	0.383±0.007	0.657	0.583	218.28±10.01
62	350–450	233	0.369±0.011	0.614	0.602	86.03±6.16
63	450–550	102	0.362±0.015	0.544	0.666	36.97±3.96
64	≥ 550	109	0.352±0.013	0.531	0.663	38.39±3.93
high Δm , $N_b \geq 2$, $M_T(b_{1,2}, p_T^{\text{miss}}) \geq 175 \text{ GeV}$, $N_t = 0$, $N_{\text{res}} = 0$, $N_W = 0$, $H_T \geq 1000$						
65	250–350	186	0.359±0.013	0.738	0.486	66.78±5.49
66	350–450	57	0.379±0.021	0.675	0.561	21.58±3.11
67	450–550	23	0.334±0.027	0.616	0.542	7.69±1.72
68	≥ 550	32	0.317±0.025	0.537	0.590	10.14±1.97
high Δm , $N_b = 1$, $M_T(b_{1,2}, p_T^{\text{miss}}) \geq 175 \text{ GeV}$, $N_t \geq 1$, $N_{\text{res}} = 0$, $N_W = 0$, $H_T < 1000$						
69	250–550	11329	0.035±0.001	0.601	0.058	397.77±7.71
70	550–650	87	0.081±0.010	0.553	0.147	7.07±1.14
71	≥ 650	29	0.075±0.015	0.684	0.110	2.18±0.59
high Δm , $N_b = 1$, $M_T(b_{1,2}, p_T^{\text{miss}}) \geq 175 \text{ GeV}$, $N_t \geq 1$, $N_{\text{res}} = 0$, $N_W = 0$, $1000 \leq H_T < 1500$						
72	250–550	739	0.111±0.004	0.621	0.179	81.90±4.07
73	550–650	36	0.063±0.011	0.507	0.125	2.27±0.55
74	≥ 650	42	0.053±0.011	0.539	0.098	2.23±0.56
high Δm , $N_b = 1$, $M_T(b_{1,2}, p_T^{\text{miss}}) \geq 175 \text{ GeV}$, $N_t \geq 1$, $N_{\text{res}} = 0$, $N_W \geq 1$, $H_T < 1300$						
75	250–550	166	0.131±0.008	0.690	0.190	21.70±2.19
76	550–650	8	0.124±0.030	0.637	0.195	0.99±0.43
77	≥ 650	23	0.079±0.019	0.506	0.156	1.81±0.57
high Δm , $N_b = 1$, $M_T(b_{1,2}, p_T^{\text{miss}}) \geq 175 \text{ GeV}$, $N_t = 0$, $N_{\text{res}} = 0$, $N_W \geq 1$, $H_T \geq 1300$						
81	250–350	206	0.023±0.003	0.718	0.032	4.67±0.68
82	350–450	87	0.011±0.002	0.607	0.018	0.94±0.22
83	≥ 450	87	0.021±0.004	0.545	0.038	1.82±0.37
high Δm , $N_b = 1$, $M_T(b_{1,2}, p_T^{\text{miss}}) \geq 175 \text{ GeV}$, $N_t = 0$, $N_{\text{res}} \geq 1$, $N_W = 0$, $H_T < 1000$						
84	250–350	9356	0.253±0.002	0.592	0.427	2362.92±30.67
85	350–450	1627	0.227±0.004	0.640	0.355	369.27±11.50
86	450–550	346	0.169±0.007	0.652	0.259	58.49±4.01
87	550–650	87	0.123±0.011	0.553	0.223	10.73±1.49
88	≥ 650	29	0.118±0.017	0.684	0.173	3.44±0.80
high Δm , $N_b = 1$, $M_T(b_{1,2}, p_T^{\text{miss}}) \geq 175 \text{ GeV}$, $N_t = 0$, $N_{\text{res}} \geq 1$, $N_W = 0$, $1000 \leq H_T < 1500$						
89	250–350	470	0.126±0.005	0.639	0.198	59.43±3.64
90	350–450	187	0.128±0.008	0.619	0.207	23.93±2.35
91	450–550	82	0.089±0.009	0.520	0.171	7.28±1.11
92	550–650	36	0.121±0.016	0.507	0.239	4.36±0.93
93	≥ 650	42	0.086±0.011	0.539	0.160	3.61±0.73

Table 6.2 : The LL estimate in the various high Δm search regions, bins 53 to 93, using the 136.7 fb^{-1} dataset.

Search Region	p_T^{miss} [GeV]	$N_{\text{data}}(1l)$	TF_{LL}	$TF_{LL}^{\text{CR-SR}}$	$TF_{LL}^{\text{SR-extrap}}$	$N_{\text{pred}}^{\text{LL}}$
high Δm , $N_b = 1$, $M_T(b_{1,2}, p_T^{\text{miss}}) \geq 175$ GeV, $N_t = 0$, $N_{\text{res}} \geq 1$, $N_W = 0$, $H_T \geq 1500$						
94	250–350	100	0.075±0.008	0.744	0.100	7.46±1.06
95	350–450	46	0.069±0.011	0.589	0.118	3.19±0.68
96	450–550	20	0.087±0.017	0.649	0.135	1.75±0.52
97	550–650	8	0.101±0.029	0.637	0.158	0.80±0.37
98	≥ 650	23	0.040±0.011	0.506	0.079	0.92±0.31
high Δm , $N_b = 1$, $M_T(b_{1,2}, p_T^{\text{miss}}) \geq 175$ GeV, $N_t \geq 1$, $N_{\text{res}} = 0$, $N_W \geq 1$						
99	250–550	12234	0.000±0.000	0.604	0.000	2.42±0.44
100	≥ 550	225	0.001±0.000	0.557	0.001	0.16±0.10
high Δm , $N_b = 1$, $M_T(b_{1,2}, p_T^{\text{miss}}) \geq 175$ GeV, $N_t \geq 1$, $N_{\text{res}} \geq 1$, $N_W = 0$						
101	250–550	12234	0.001±0.000	0.604	0.001	6.76±0.80
102	≥ 550	225	0.002±0.001	0.557	0.003	0.35±0.13
high Δm , $N_b = 1$, $M_T(b_{1,2}, p_T^{\text{miss}}) \geq 175$ GeV, $N_t = 0$, $N_{\text{res}} \geq 1$, $N_W \geq 1$						
103	250–550	12234	0.001±0.000	0.604	0.002	17.29±1.17
104	≥ 550	225	0.000±0.000	0.557	0.001	0.08±0.07
high Δm , $N_b = 2$, $M_T(b_{1,2}, p_T^{\text{miss}}) \geq 175$ GeV, $N_t = 1$, $N_{\text{res}} = 0$, $N_W = 0$, $H_T < 1000$						
105	250–550	2055	0.040±0.001	0.650	0.062	82.37±3.55
106	550–650	15	0.108±0.022	0.614	0.176	1.62±0.53
107	≥ 650	7	0.084±0.030	0.737	0.115	0.59±0.31
high Δm , $N_b = 2$, $M_T(b_{1,2}, p_T^{\text{miss}}) \geq 175$ GeV, $N_t = 1$, $N_{\text{res}} = 0$, $N_W = 0$, $1000 \leq H_T < 1500$						
108	250–550	151	0.149±0.009	0.710	0.210	22.56±2.25
109	550–650	7	0.042±0.016	0.521	0.080	0.29±0.15
110	≥ 650	13	0.089±0.028	0.539	0.165	1.16±0.48
high Δm , $N_b = 2$, $M_T(b_{1,2}, p_T^{\text{miss}}) \geq 175$ GeV, $N_t = 1$, $N_{\text{res}} = 0$, $N_W = 0$, $H_T \geq 1500$						
111	250–550	45	0.202±0.022	0.819	0.246	9.07±1.67
112	550–650	3	0.052±0.035	0.418	0.126	0.16±0.14
113	≥ 650	5	0.134±0.044	0.446	0.301	0.67±0.37
high Δm , $N_b = 2$, $M_T(b_{1,2}, p_T^{\text{miss}}) \geq 175$ GeV, $N_t = 0$, $N_{\text{res}} = 0$, $N_W = 1$, $H_T < 1300$						
114	250–350	1742	0.025±0.001	0.657	0.038	43.11±2.60
115	350–450	340	0.023±0.002	0.656	0.036	7.96±0.92
116	≥ 450	121	0.014±0.003	0.601	0.023	1.71±0.40
high Δm , $N_b = 2$, $M_T(b_{1,2}, p_T^{\text{miss}}) \geq 175$ GeV, $N_t = 0$, $N_{\text{res}} = 0$, $N_W = 1$, $H_T \geq 1300$						
117	250–350	52	0.028±0.006	0.793	0.036	1.47±0.38
118	350–450	21	0.017±0.008	0.828	0.021	0.36±0.19
119	≥ 450	25	0.035±0.011	0.566	0.062	0.87±0.33
high Δm , $N_b = 2$, $M_T(b_{1,2}, p_T^{\text{miss}}) \geq 175$ GeV, $N_t = 0$, $N_{\text{res}} = 1$, $N_W = 0$, $H_T < 1000$						
120	250–350	1661	0.225±0.004	0.651	0.346	373.86±11.68
121	350–450	317	0.196±0.009	0.659	0.297	62.06±4.44
122	450–550	77	0.147±0.014	0.605	0.243	11.32±1.69
123	550–650	15	0.143±0.026	0.614	0.234	2.15±0.68
124	≥ 650	7	0.173±0.048	0.737	0.235	1.21±0.57
high Δm , $N_b = 2$, $M_T(b_{1,2}, p_T^{\text{miss}}) \geq 175$ GeV, $N_t = 0$, $N_{\text{res}} = 1$, $N_W = 0$, $1000 \leq H_T < 1500$						
125	250–350	105	0.171±0.011	0.752	0.227	17.91±2.12
126	350–450	30	0.119±0.014	0.663	0.180	3.57±0.78
127	450–550	16	0.102±0.018	0.590	0.172	1.63±0.49
128	550–650	7	0.104±0.026	0.521	0.199	0.73±0.33
129	≥ 650	13	0.110±0.028	0.539	0.204	1.43±0.54
high Δm , $N_b = 2$, $M_T(b_{1,2}, p_T^{\text{miss}}) \geq 175$ GeV, $N_t = 0$, $N_{\text{res}} = 1$, $N_W = 0$, $H_T \geq 1500$						
130	250–350	28	0.125±0.020	0.812	0.154	3.49±0.87
131	350–450	14	0.090±0.024	0.844	0.106	1.26±0.48
132	450–550	3	0.194±0.064	0.800	0.243	0.58±0.39
133	550–650	3	0.094±0.052	0.418	0.225	0.28±0.23
134	≥ 650	5	0.044±0.020	0.446	0.099	0.22±0.14

Table 6.3 : The LL estimate in the various high Δm search regions, bins 94 to 134, using the 136.7 fb^{-1} dataset.

Search Region	p_T^{miss} [GeV]	$N_{\text{data}}(1)$	TF_{LL}	$TF_{LL}^{\text{CR-SR}}$	$TF_{LL}^{\text{SR-extrap}}$	$N_{\text{pred}}^{\text{LL}}$
high Δm , $N_b = 2$, $M_T(b_{1,2}, p_T^{\text{miss}}) \geq 175$ GeV, $N_t = 1$, $N_{\text{res}} = 0$, $N_W = 1$						
135	250–550	2251	0.000±0.000	0.659	0.000	0.21±0.09
136	≥ 550	50	0.001±0.001	0.566	0.001	0.04±0.03
high Δm , $N_b = 2$, $M_T(b_{1,2}, p_T^{\text{miss}}) \geq 175$ GeV, $N_t = 1$, $N_{\text{res}} = 1$, $N_W = 0$, $H_T < 1300$						
137	250–350	1742	0.003±0.000	0.657	0.004	4.39±0.66
138	350–450	340	0.002±0.001	0.656	0.003	0.72±0.22
139	≥ 450	121	0.005±0.001	0.601	0.008	0.57±0.19
high Δm , $N_b = 2$, $M_T(b_{1,2}, p_T^{\text{miss}}) \geq 175$ GeV, $N_t = 1$, $N_{\text{res}} = 1$, $N_W = 0$, $H_T \geq 1300$						
140	250–350	52	0.015±0.005	0.793	0.019	0.79±0.29
141	350–450	21	0.002±0.001	0.828	0.002	0.04±0.02
142	≥ 450	25	0.010±0.005	0.566	0.018	0.25±0.13
high Δm , $N_b = 2$, $M_T(b_{1,2}, p_T^{\text{miss}}) \geq 175$ GeV, $N_t = 0$, $N_{\text{res}} = 1$, $N_W = 1$						
143	250–550	2251	0.002±0.000	0.659	0.003	3.93±0.59
144	≥ 550	50	0.000±0.000	0.566	0.000	0.01±0.01
high Δm , $N_b = 2$, $M_T(b_{1,2}, p_T^{\text{miss}}) \geq 175$ GeV, $N_t = 2$, $N_{\text{res}} = 0$, $N_W = 0$						
145	250–450	2155	0.000±0.000	0.662	0.000	0.66±0.23
146	≥ 450	146	0.001±0.001	0.596	0.002	0.20±0.13
high Δm , $N_b = 2$, $M_T(b_{1,2}, p_T^{\text{miss}}) \geq 175$ GeV, $N_t = 0$, $N_{\text{res}} = 0$, $N_W = 2$						
147	≥ 250	2301	0.000±0.000	0.657	0.000	0.15±0.06
high Δm , $N_b = 2$, $M_T(b_{1,2}, p_T^{\text{miss}}) \geq 175$ GeV, $N_t = 0$, $N_{\text{res}} = 2$, $N_W = 0$, $H_T < 1300$						
148	250–450	2082	0.008±0.001	0.656	0.012	15.82±1.28
149	≥ 450	121	0.007±0.002	0.601	0.012	0.86±0.26
high Δm , $N_b = 2$, $M_T(b_{1,2}, p_T^{\text{miss}}) \geq 175$ GeV, $N_t = 0$, $N_{\text{res}} = 2$, $N_W = 0$, $H_T \geq 1300$						
150	250–450	73	0.002±0.001	0.803	0.002	0.11±0.08
151	≥ 450	25	0.012±0.006	0.566	0.022	0.31±0.16
high Δm , $N_b = 2$, $M_T(b_{1,2}, p_T^{\text{miss}}) \geq 175$ GeV, $(N_t + N_{\text{res}} + N_W) \geq 3$						
152	≥ 250	2301	0.000±0.000	0.657	0.000	0.10±0.05
high Δm , $N_b \geq 3$, $M_T(b_{1,2}, p_T^{\text{miss}}) \geq 175$ GeV, $N_t = 1$, $N_{\text{res}} = 0$, $N_W = 0$, $H_T < 1000$						
153	250–350	373	0.027±0.003	0.715	0.037	9.94±1.15
154	350–550	93	0.080±0.010	0.682	0.117	7.43±1.19
155	≥ 550	8	0.077±0.033	0.737	0.104	0.62±0.34
high Δm , $N_b \geq 3$, $M_T(b_{1,2}, p_T^{\text{miss}}) \geq 175$ GeV, $N_t = 1$, $N_{\text{res}} = 0$, $N_W = 0$, $1000 \leq H_T < 1500$						
156	250–350	41	0.112±0.017	0.645	0.174	4.60±1.01
157	350–550	13	0.099±0.020	0.603	0.165	1.29±0.44
158	≥ 550	1	0.050±0.037	0.735	0.068	0.05±0.06
high Δm , $N_b \geq 3$, $M_T(b_{1,2}, p_T^{\text{miss}}) \geq 175$ GeV, $N_t = 1$, $N_{\text{res}} = 0$, $N_W = 0$, $H_T \geq 1500$						
159	250–350	12	0.227±0.052	0.722	0.314	2.72±1.01
160	350–550	4	0.156±0.060	0.532	0.294	0.63±0.39
161	≥ 550	3	0.055±0.049	0.697	0.079	0.17±0.18
high Δm , $N_b \geq 3$, $M_T(b_{1,2}, p_T^{\text{miss}}) \geq 175$ GeV, $N_t = 0$, $N_{\text{res}} = 0$, $N_W = 1$						
162	250–350	426	0.029±0.003	0.708	0.041	12.41±1.31
163	350–550	110	0.017±0.003	0.659	0.026	1.85±0.41
164	≥ 550	12	0.027±0.013	0.730	0.037	0.32±0.18
high Δm , $N_b \geq 3$, $M_T(b_{1,2}, p_T^{\text{miss}}) \geq 175$ GeV, $N_t = 0$, $N_{\text{res}} = 1$, $N_W = 0$, $H_T < 1000$						
165	250–350	373	0.222±0.009	0.715	0.310	82.74±5.40
166	350–550	93	0.201±0.017	0.682	0.295	18.73±2.52
167	≥ 550	8	0.213±0.067	0.737	0.289	1.70±0.81
high Δm , $N_b \geq 3$, $M_T(b_{1,2}, p_T^{\text{miss}}) \geq 175$ GeV, $N_t = 0$, $N_{\text{res}} = 1$, $N_W = 0$, $1000 \leq H_T < 1500$						
168	250–350	41	0.162±0.020	0.645	0.251	6.65±1.33
169	350–550	13	0.152±0.025	0.603	0.252	1.98±0.63
170	≥ 550	1	0.152±0.057	0.735	0.207	0.15±0.16
high Δm , $N_b \geq 3$, $M_T(b_{1,2}, p_T^{\text{miss}}) \geq 175$ GeV, $N_t = 0$, $N_{\text{res}} = 1$, $N_W = 0$, $H_T \geq 1500$						
171	250–350	12	0.114±0.035	0.722	0.158	1.37±0.57
172	350–550	4	0.084±0.032	0.532	0.157	0.33±0.21
173	≥ 550	3	0.281±0.132	0.697	0.402	0.84±0.63
high Δm , $N_b \geq 3$, $M_T(b_{1,2}, p_T^{\text{miss}}) \geq 175$ GeV, $N_t = 1$, $N_{\text{res}} = 0$, $N_W = 1$						
174	≥ 250	548	0.001±0.000	0.697	0.001	0.29±0.13
high Δm , $N_b \geq 3$, $M_T(b_{1,2}, p_T^{\text{miss}}) \geq 175$ GeV, $N_t = 1$, $N_{\text{res}} = 1$, $N_W = 0$						
175	250–350	426	0.005±0.001	0.708	0.007	2.09±0.47
176	≥ 350	122	0.012±0.003	0.666	0.017	1.41±0.37
high Δm , $N_b \geq 3$, $M_T(b_{1,2}, p_T^{\text{miss}}) \geq 175$ GeV, $N_t = 0$, $N_{\text{res}} = 1$, $N_W = 1$						
177	≥ 250	548	0.001±0.000	0.697	0.002	0.67±0.25
high Δm , $N_b \geq 3$, $M_T(b_{1,2}, p_T^{\text{miss}}) \geq 175$ GeV, $N_t = 2$, $N_{\text{res}} = 0$, $N_W = 0$						
178	≥ 250	548	0.001±0.000	0.697	0.001	0.32±0.16
high Δm , $N_b \geq 3$, $M_T(b_{1,2}, p_T^{\text{miss}}) \geq 175$ GeV, $N_t = 0$, $N_{\text{res}} = 0$, $N_W = 2$						
179	≥ 250	548	0.000±0.000	0.697	0.000	0.00±0.00
high Δm , $N_b \geq 3$, $M_T(b_{1,2}, p_T^{\text{miss}}) \geq 175$ GeV, $N_t = 0$, $N_{\text{res}} = 2$, $N_W = 0$						
180	250–350	426	0.006±0.001	0.708	0.008	2.55±0.48
181	≥ 350	122	0.006±0.002	0.666	0.009	0.72±0.25
high Δm , $N_b \geq 3$, $M_T(b_{1,2}, p_T^{\text{miss}}) \geq 175$ GeV, $(N_t + N_{\text{res}} + N_W) \geq 3$						
182	≥ 250	548	0.000±0.000	0.697	0.000	0.00±0.00

Table 6.4 : The LL estimate in the various high Δm search regions, bins 135 to 182, using the 136.7 fb^{-1} dataset.

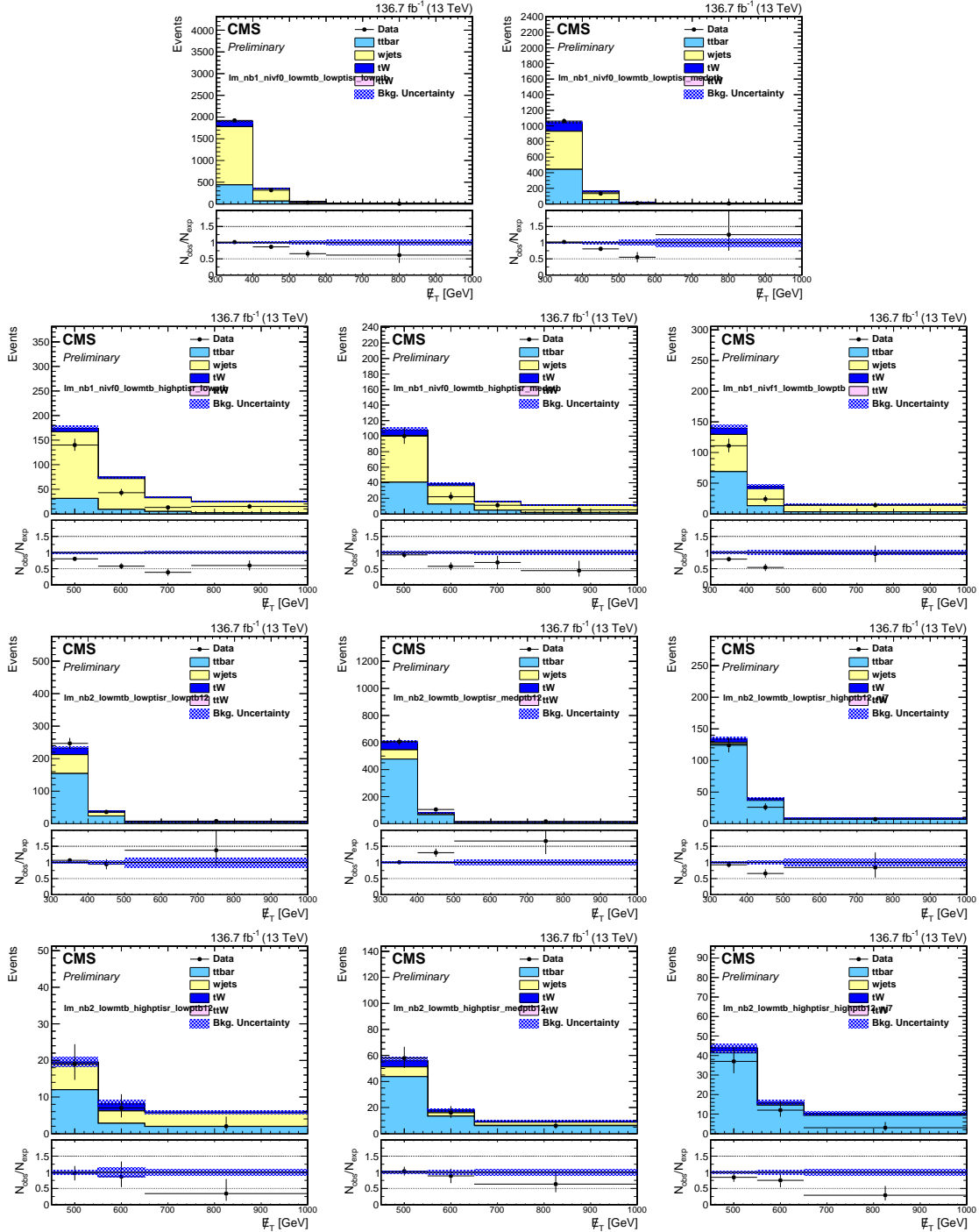


Figure 6.9 : Comparison of the p_T^{miss} distribution in the single-lepton sample after applying the low Δm baseline selection. Two top rows: Events with $N_b = 1$; Two bottom rows: Events with $N_b \geq 2$; Data and simulation are represented by the black points and stacked histograms, respectively. The error bars on the ratio of observed data to simulation correspond to the data statistical uncertainty and the shaded blue band represents the statistical uncertainty on the simulation. These regions are included with the search regions in the simultaneous fit for the signal extraction in order to estimate the LL contribution.

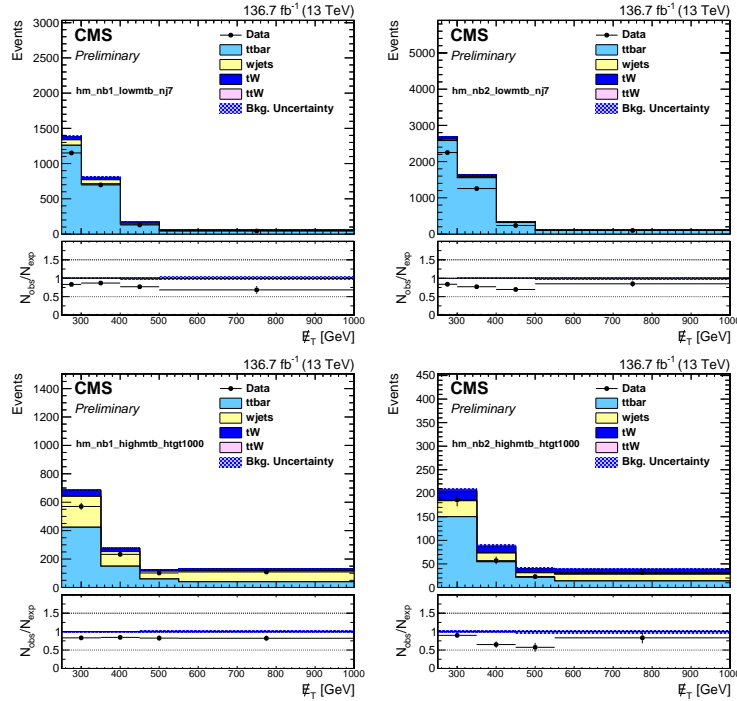


Figure 6.10 : Comparison of the p_T^{miss} distribution in the single-lepton sample after applying the high Δm baseline selection in the $M_T(b_{1,2}, p_T^{miss}) < 175$ GeV and $N_t = 0$, $N_{res} = 0$, and $N_W = 0$ region. Data and simulation are represented by the black points and stacked histograms, respectively. The error bars on the ratio of observed data to simulation correspond to the data statistical uncertainty and the shaded blue band represents the statistical uncertainty on the simulation. These regions are included with the search regions in the simultaneous fit for the signal extraction in order to estimate the LL contribution.

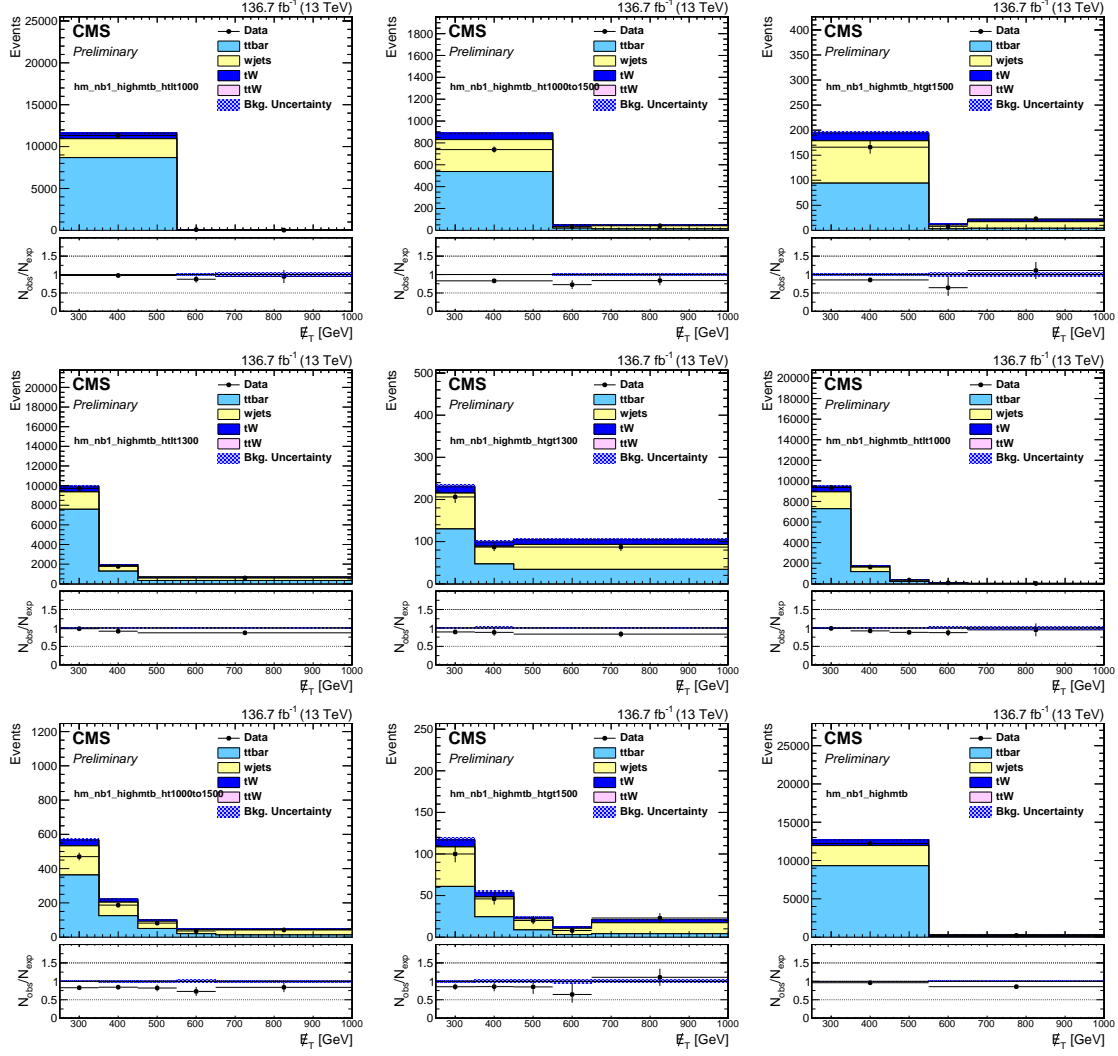


Figure 6.11 : Comparison of the p_T^{miss} distribution in the single-lepton sample after applying the high Δm baseline selection in the $N_b = 1$ region where there are ≥ 1 heavy object tags. Data and simulation are represented by the black points and stacked histograms, respectively. The error bars on the ratio of observed data to simulation correspond to the data statistical uncertainty and the shaded blue band represents the statistical uncertainty on the simulation. These regions are included with the search regions in the simultaneous fit for the signal extraction in order to estimate the LL contribution.

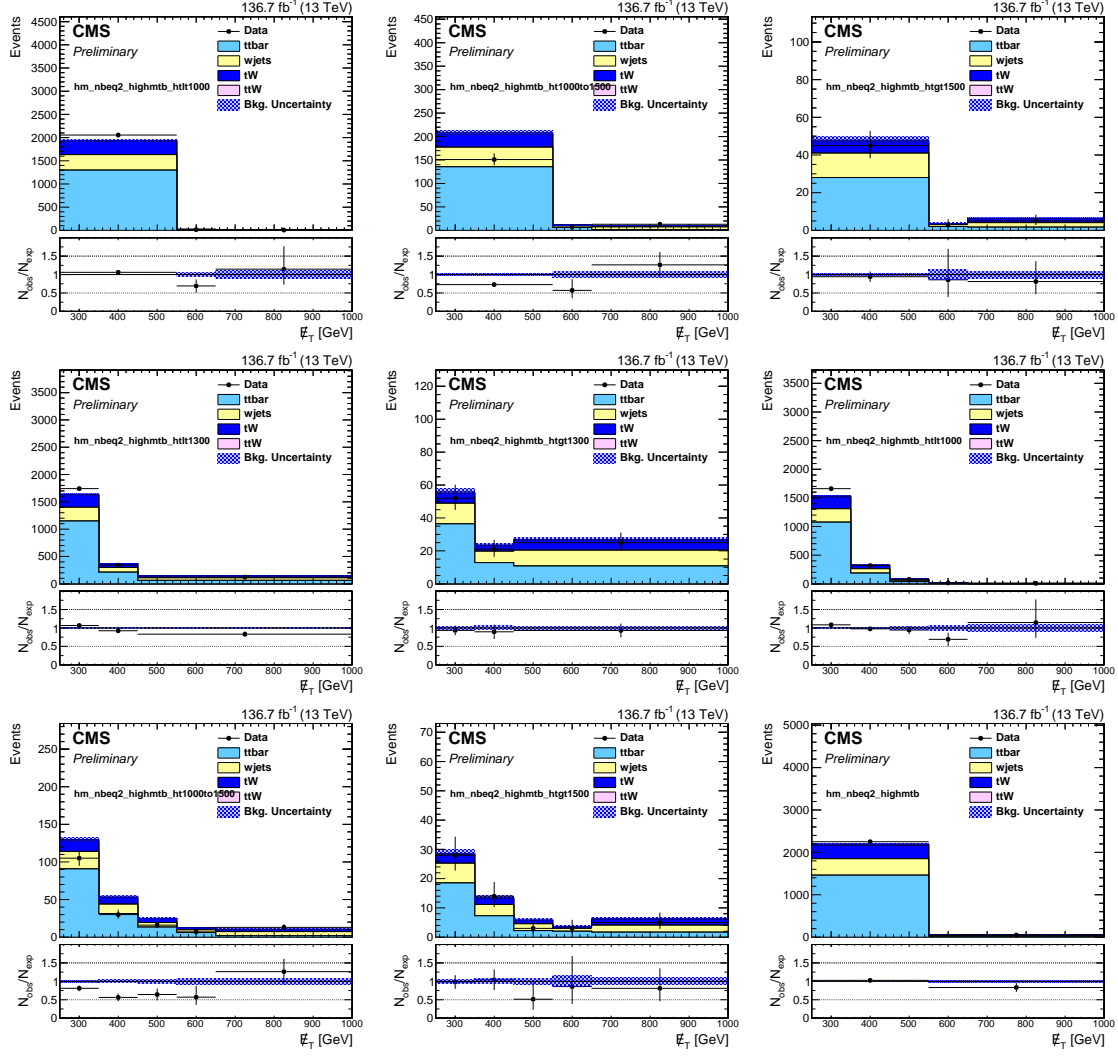


Figure 6.12 : Comparison of the p_T^{miss} distribution in the single-lepton sample after applying the high Δm baseline selection in the $N_b = 2$ and $N_t = 1, N_{res} = 1$, or $N_W = 1$ regions. Data and simulation are represented by the black points and stacked histograms, respectively. The error bars on the ratio of observed data to simulation correspond to the data statistical uncertainty and the shaded blue band represents the statistical uncertainty on the simulation. These regions are included with the search regions in the simultaneous fit for the signal extraction in order to estimate the LL contribution.

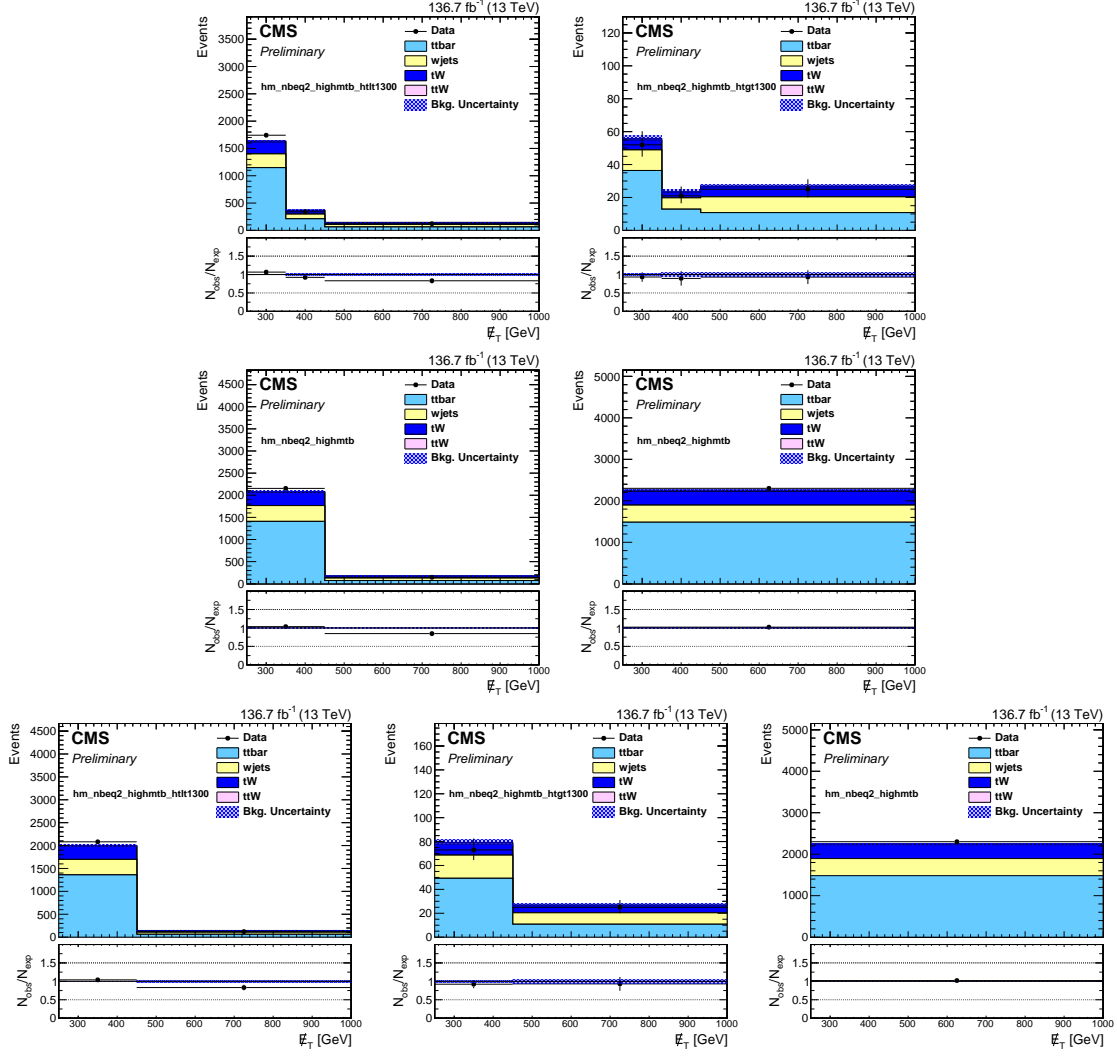


Figure 6.13 : Comparison of the p_T^{miss} distribution in the single-lepton sample after applying the high Δm baseline selection in the $N_b = 2$ and $N_t = 2, N_{res} = 2$, or $N_W = 2$ region. Data and simulation are represented by the black points and stacked histograms, respectively. The error bars on the ratio of observed data to simulation correspond to the data statistical uncertainty and the shaded blue band represents the statistical uncertainty on the simulation. These regions are included with the search regions in the simultaneous fit for the signal extraction in order to estimate the LL contribution.

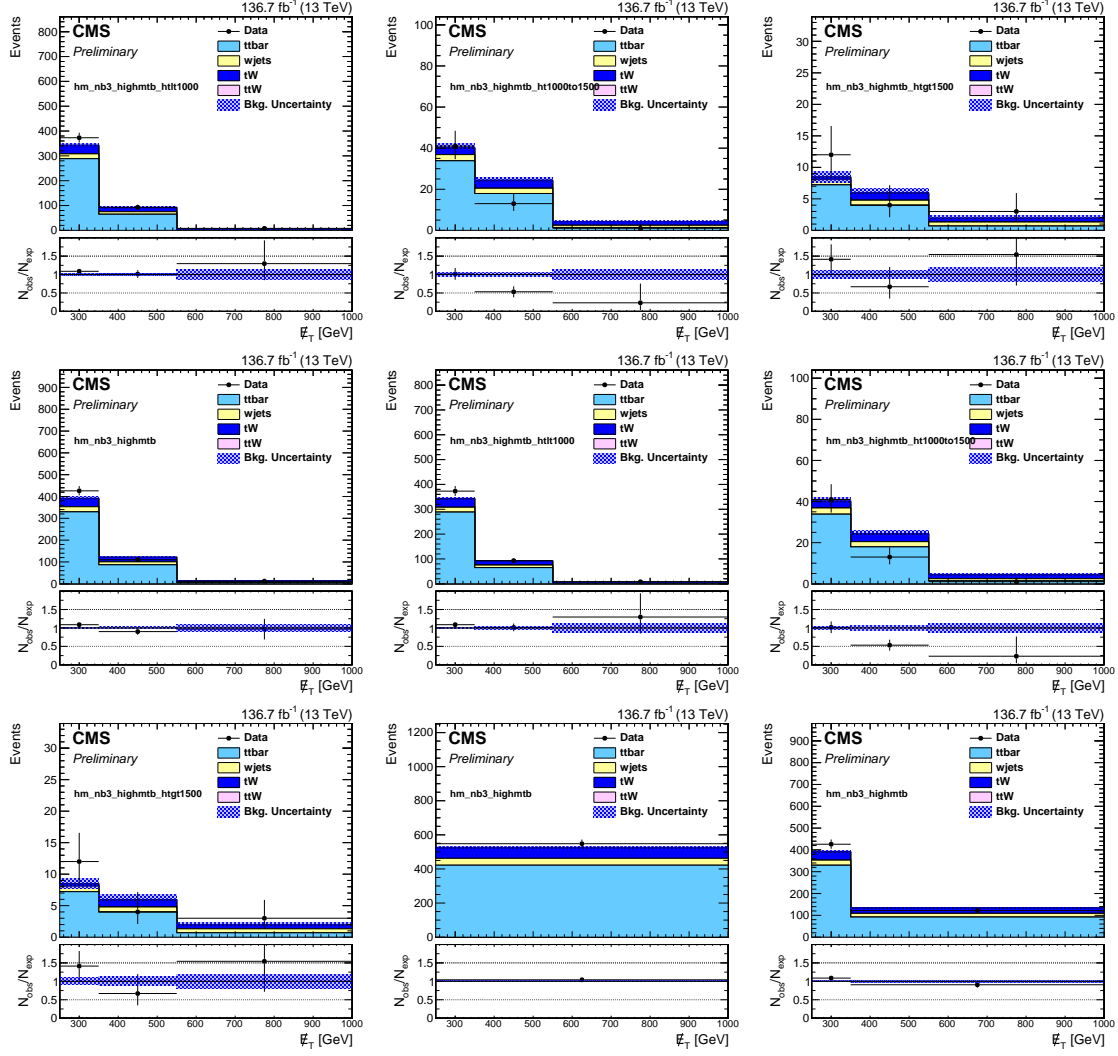


Figure 6.14 : Comparison of the p_T^{miss} distribution in the single-lepton sample after applying the high Δm baseline selection in the $N_b \geq 3$ and $N_t = 1, N_{res} = 1$, or $N_W = 1$ region. Data and simulation are represented by the black points and stacked histograms, respectively. The error bars on the ratio of observed data to simulation correspond to the data statistical uncertainty and the shaded blue band represents the statistical uncertainty on the simulation. These regions are included with the search regions in the simultaneous fit for the signal extraction in order to estimate the LL contribution.

6.4 Z Boson Decay to Neutrinos

An important source of background for the zero-lepton search is from events in which a Z boson decays to neutrinos. Since neutrinos are weakly interacting they are missed by the CMS detector which results in p_T^{miss} . Two methods are traditionally used to estimate the $Z \rightarrow \nu\nu$ background. The first method makes use of a sample dominated by $Z \rightarrow ll + \text{jets}$ events which has similar kinematics, but has much lower statistics in the tight search regions. The second method utilizes a $\gamma + \text{jets}$ sample which has a factor of 5 or more large cross section and similar leading Feynman diagrams. The main differences are quark-boson couplings and the fact that the Z boson is very massive. In the realm of the analysis, where events have large boson p_T these effects become less important. The p_T^{miss} of the $\gamma + \text{jets}$ process is calculated after removing the photon from the event to mimic the $Z \rightarrow \nu\nu$ process.

We use a hybrid method to estimate the $Z \rightarrow \nu\nu$ background that makes use of both the $\gamma + \text{jets}$ and the $Z \rightarrow ll + \text{jets}$ processes. The photon and the dilepton system are removed from the events before calculating p_T^{miss} and other kinematic variables related to p_T^{miss} , and the modified p_T^{miss} is denoted by $p_T^{miss\gamma}$ and p_T^{missll} for $\gamma + \text{jets}$ and the $Z \rightarrow ll + \text{jets}$ processes, respectively. The $Z \rightarrow ll + \text{jets}$ sample is used to measure the normalization of the $Z \rightarrow \nu\nu$ process in different ranges of N_b and N_{SV} , and we take advantage of the much higher statistics of the $\gamma + \text{jets}$ sample to extract shape corrections.

6.4.1 Prediction Method

The prediction of the $Z \rightarrow \nu\nu$ background is given by:

$$N_{pred}^{Z \rightarrow \nu\nu} = N_{MC}^{Z \rightarrow \nu\nu} \cdot R_Z \cdot S_\gamma \quad (6.4)$$

where $N_{MC}^{Z \rightarrow \nu\nu}$ is the expected number of $Z \rightarrow \nu\nu$ events obtained from simulation in a given search region, R_Z is a factor used to account for any difference between data and simulation in the cross section of the $Z \rightarrow \nu\nu$ process, and S_γ accounts for any shape difference in the $Z \rightarrow \nu\nu$ process between data and simulation and is integrated in top and W tags. We use the same extrapolation method, see sec. 6.3, for the CR-to-SR transfer factor. The merged bins in t and W tags increases the limited statistics in these regions.

The factor R_Z is calculated by comparing the observed and expected $Z \rightarrow ll$ yields after applying a relaxed definition of the baseline selection, with the $\Delta\phi(j, p_T^{missll})$ cut removed. The purity of the sample is improved by requiring the dilepton invariant mass to be near the Z -mass window ($80 < M_{ll} < 100$ GeV) with a $p_T > 200$ GeV cut for the entire system. Unfortunately the $t\bar{t}$ contamination is not negligible in the $N_b \geq 1$ region. To account for this we define a factor R_T for $t\bar{t}$ events which is calculated by using events outside the Z -mass window ($50 < M_{ll} < 80$ or $M_{ll} > 100$ GeV). The relation between the factors, R_Z and R_T , and the observed and expected yields inside and outside the Z -mass window, is expressed as:

$$\begin{bmatrix} \text{Data}_{\text{on}-Z} \\ \text{Data}_{\text{off}-Z} \end{bmatrix} = \begin{bmatrix} \text{MC}_{\text{on}-Z}(Z \rightarrow ll) & \text{MC}_{\text{on}-Z}(t\bar{t}) \\ \text{MC}_{\text{off}-Z}(Z \rightarrow ll) & \text{MC}_{\text{off}-Z}(t\bar{t}) \end{bmatrix} \cdot \begin{bmatrix} R_Z \\ R_T \end{bmatrix}. \quad (6.5)$$

The small contributions from tZ, ttZ, WZ , and ZZ are included in R_Z , while the processes tW, ttW , and WW are included in R_T .

6.4.2 Combination of Eras and Prediction

We want to make sure that the normalization and shape corrections in the electron and muon control regions are in relative agreement to be able to combine them into

a single normalization and shape correction. Figures 6.17 and 6.15 compare the normalized $p_T^{miss\gamma}$ distributions for $\gamma+\text{jets}$ in data and simulation in each separate low Δm control region and era of the analysis. In Figures 6.18 and 6.16, we have a comparison of the normalization of $p_T^{miss\gamma}$ distributions for $\gamma+\text{jets}$ in data and simulation in each separate high Δm control region and era of the analysis. The agreement between each era and in each region is good which indicates that we can combine them before doing the normalization. The photon shape comparison are shown in Figs. 6.19 and 6.20 for the low and high Δm , respectively. The shape factors also show good agreement between each era to allow us to combine the era and provide a single shape factor.

A comparison between the electron and muon control regions and the combinations is shown in Fig. 6.21 and 6.22. The shape correction is in good agreement between each era so we are able to combine them all together. In Fig. 6.19, we have the shape correction in the low Δm photon control region separated into each era. Each of the eras are in good agreement so we should be able to combine all of the eras for each part of the analysis together. Tables 6.5, 6.6, 6.7, and 6.8 summarizes the yields of the $Z \rightarrow \nu\nu$ background and the prediction in each search region after applying the appropriate normalization and shape factors.

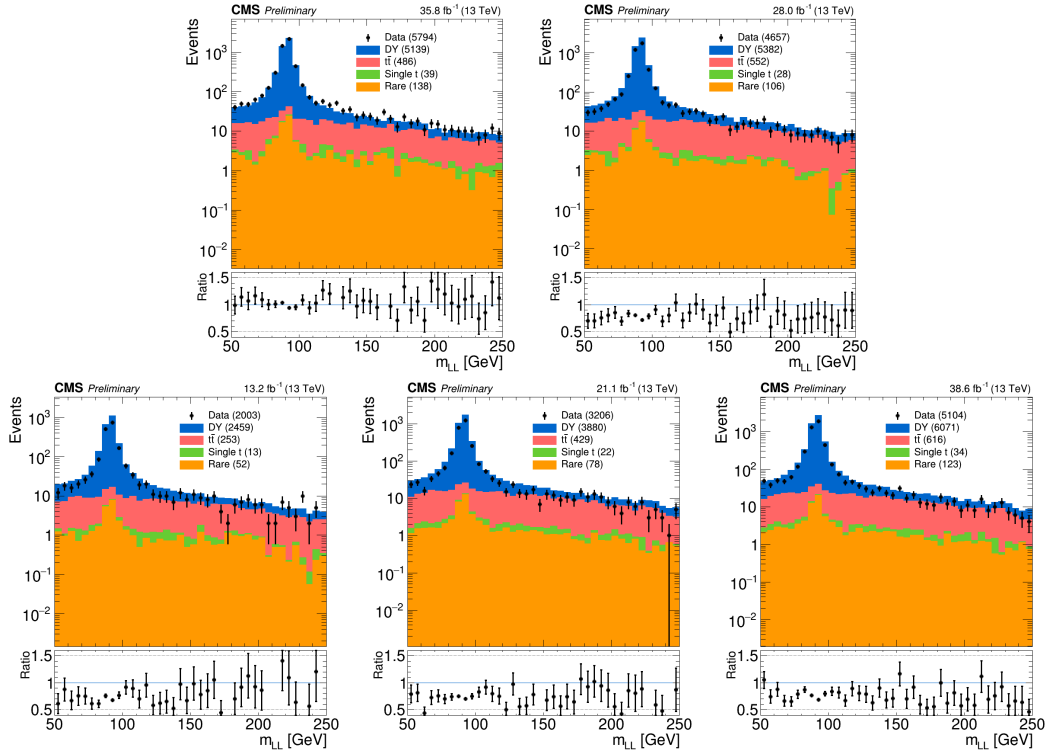


Figure 6.15 : The $Z \rightarrow \nu\nu$ normalization separated by era for the muon control region. The selection is the low Δm , $N_b = 0$, $N_{SV} = 0$ in the muon control region.

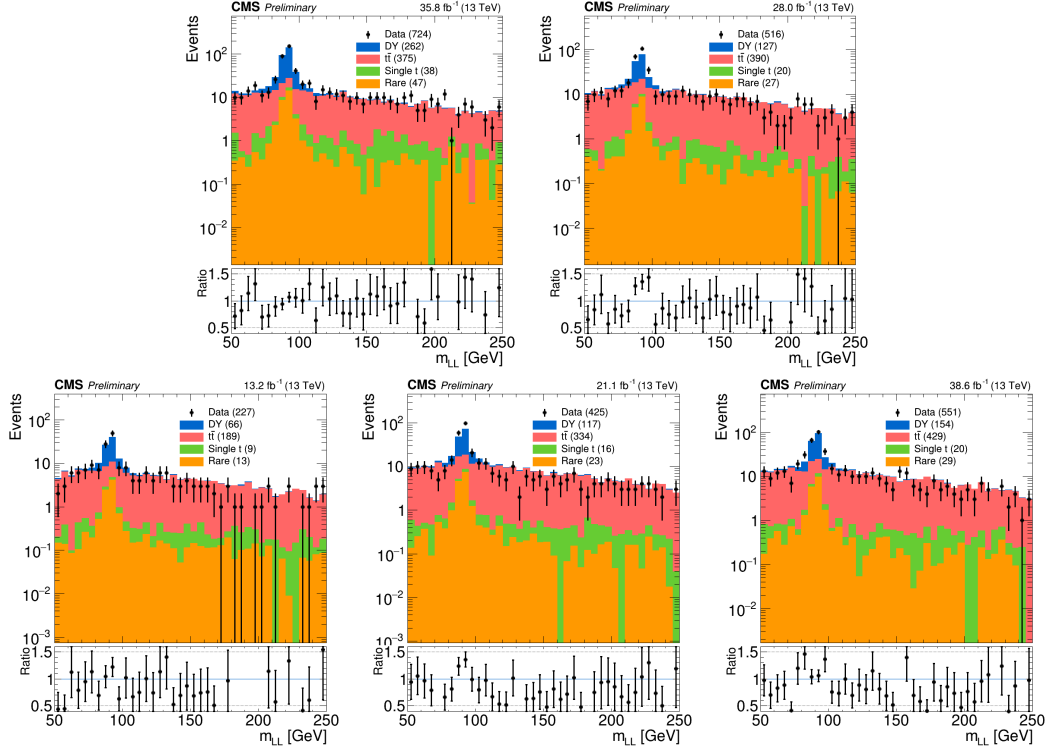


Figure 6.16 : The $Z \rightarrow \nu\nu$ normalization separated by era for the muon control region. The selection is the high Δm , $N_b = 1, = 2, \geq 2, \geq 3$ in the muon control region.

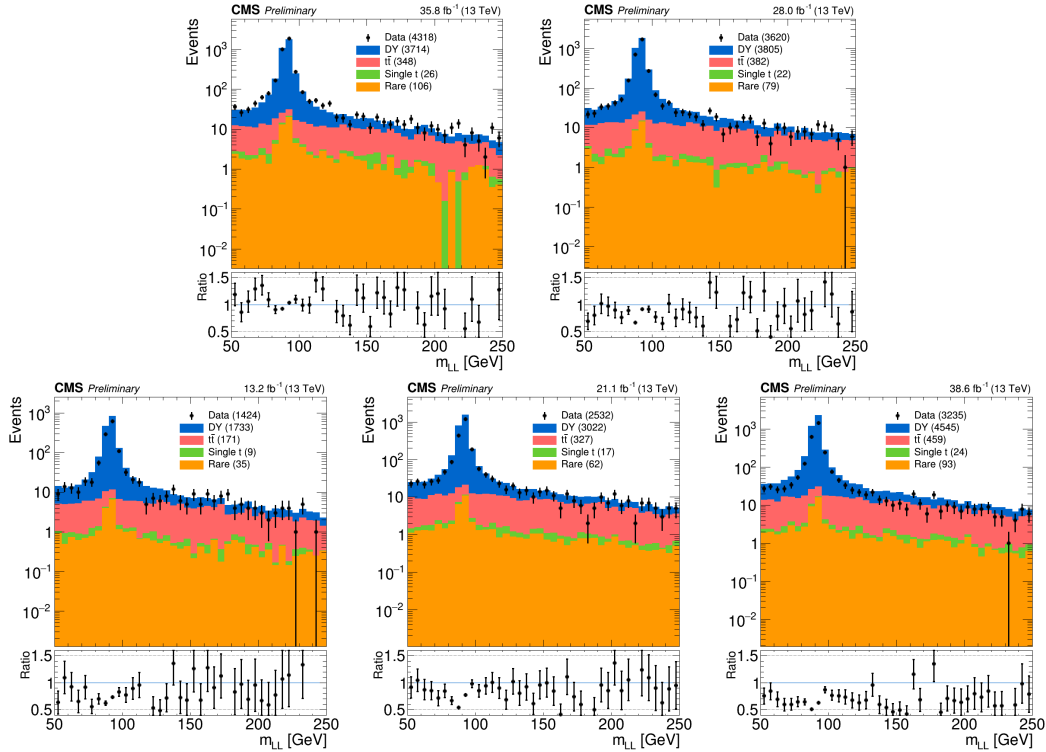


Figure 6.17 : The $Z \rightarrow \nu\nu$ normalization separated by era for the electron control region. The selection is the low Δm , $N_b = 0$, $N_{SV} = 0$ in the electron control region.

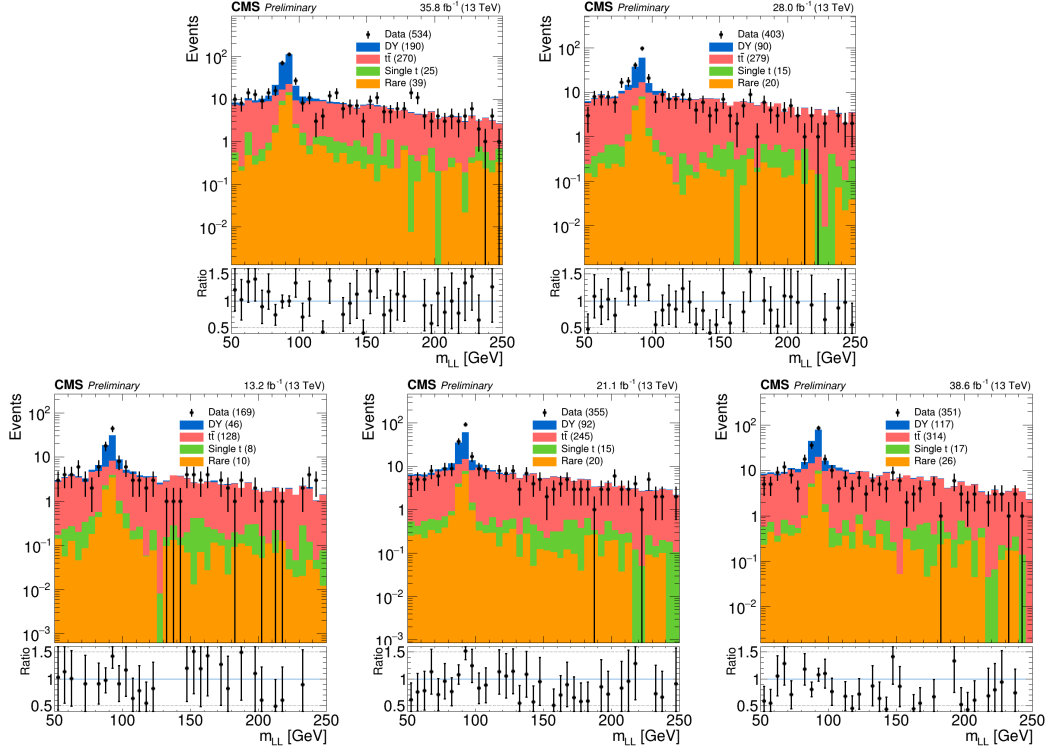


Figure 6.18 : The $Z \rightarrow \nu\nu$ normalization separated by era for the electron control region. The selection is the high Δm , $N_b = 1, = 2, \geq 2, \geq 3$ in the electron control region.

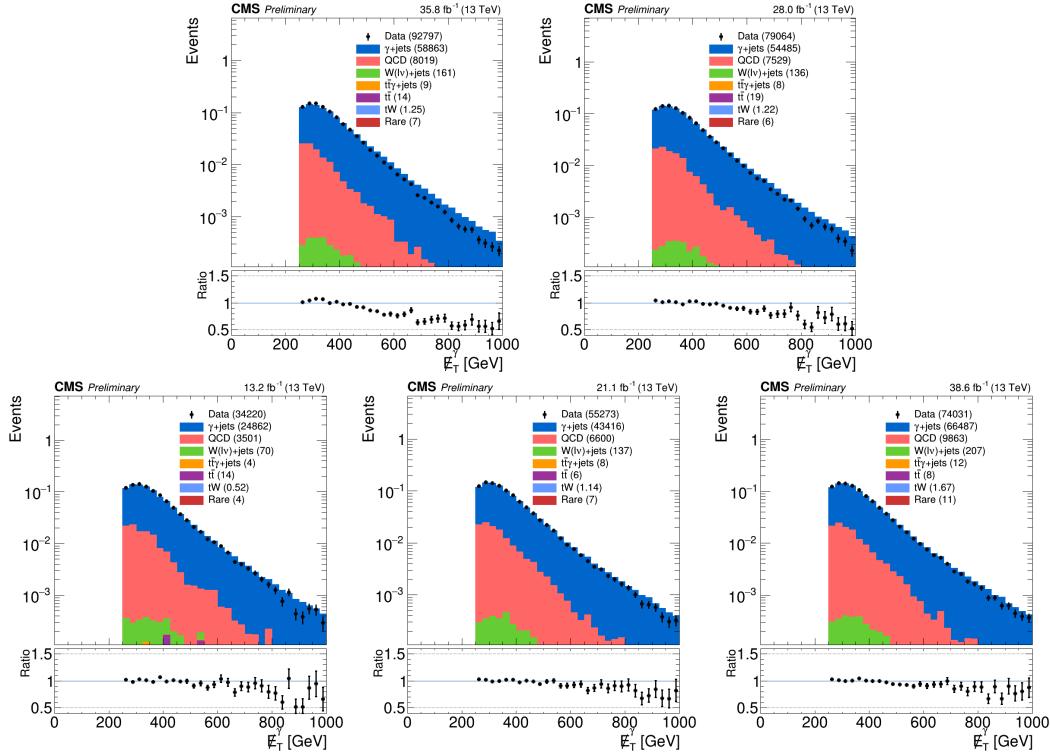


Figure 6.19 : The $Z \rightarrow \nu\nu$ shape corrections separated by era for the low Δm control region. The selection is the low Δm , $N_b = 0, 2 \leq N_j \leq 5$ in the photon control region.

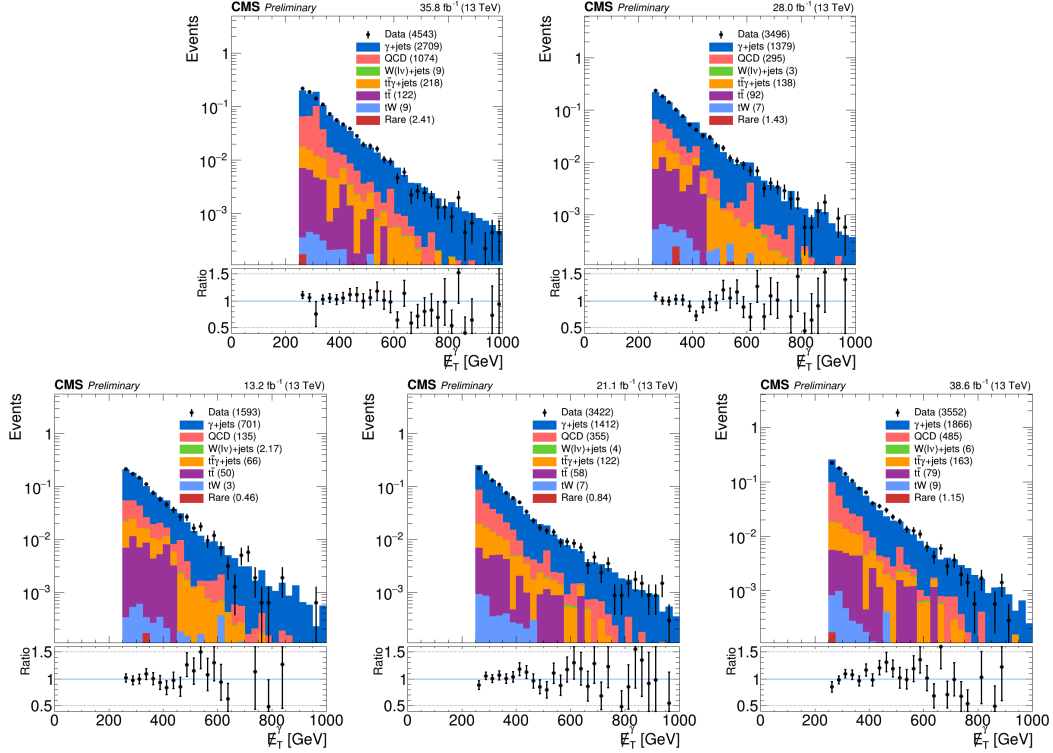


Figure 6.20 : The $Z \rightarrow \nu\nu$ shape corrections separated by era for the high Δm control region. The selection is the low Δm , $N_b = 0, 2 \leq N_j \leq 5$ in the photon control region.

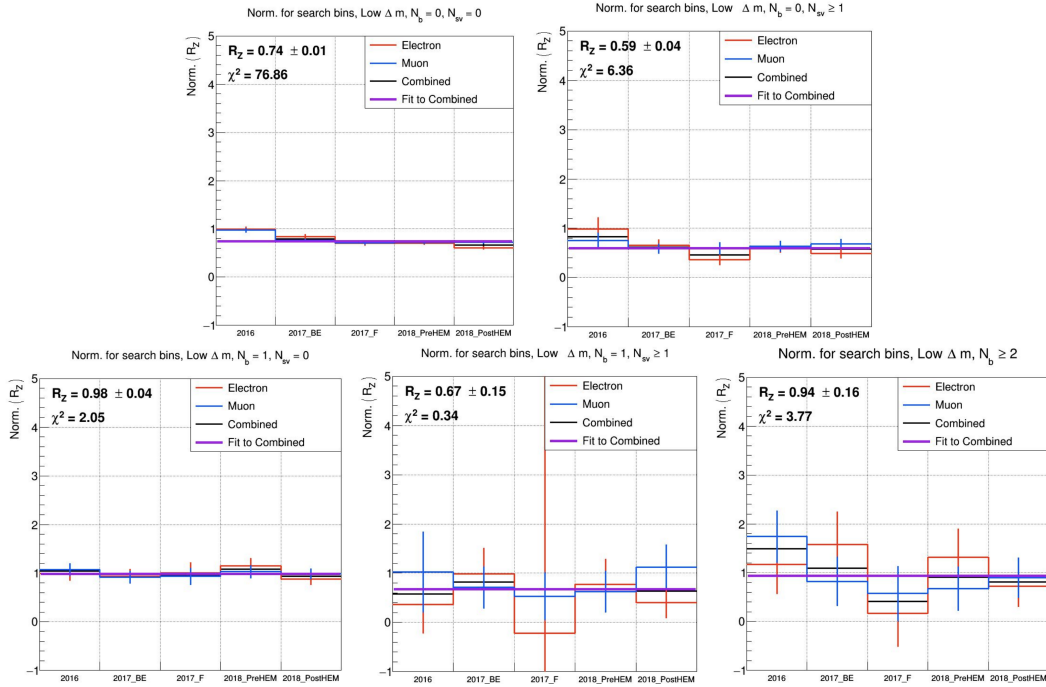


Figure 6.21 : The $Z \rightarrow \nu\nu$ normalization comparisons for each era in the electron and muon control region for different regions in the low Δm , $N_b = 0, = 1, \geq 2$, $N_{SV} = 0, \geq 1$.

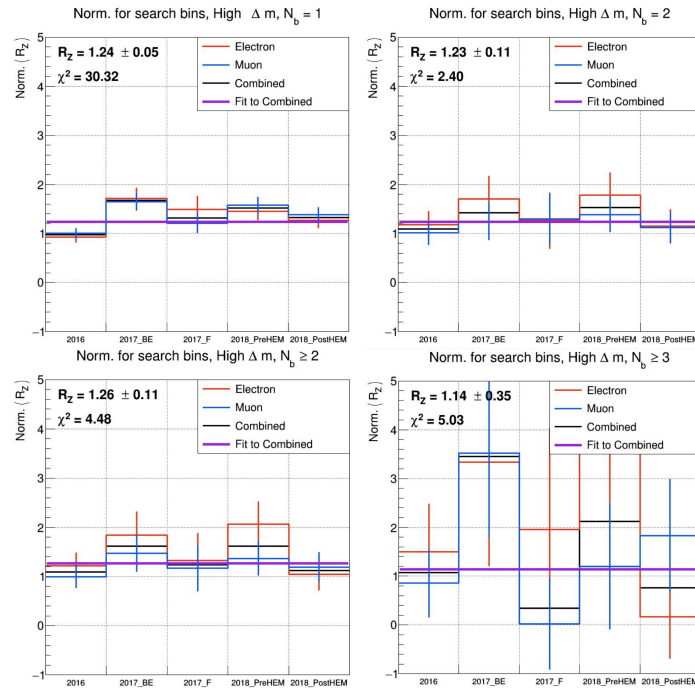


Figure 6.22 : The $Z \rightarrow \nu\nu$ normalization comparisons for each era in the electron and muon control region for different regions in the high $\Delta m, N_b = 1, = 2, \geq 2$, and ≥ 3 .

Search Region	$p_T^{miss}[\text{GeV}]$	$N_{MC}^{Z \rightarrow \nu\nu}$	$N_{\text{pred}}^{Z \rightarrow \nu\nu}$
low Δm , $N_b = 0$, $N_{SV} = 0$, $p_T(\text{ISR}) \geq 500 \text{ GeV}$, $2 \leq N_j \leq 5$			
0	450 – 550	7256.263 ± 19.884	5208.311 ± 76.401
1	550 – 650	5411.438 ± 14.579	3526.854 ± 60.845
2	650 – 750	2671.714 ± 8.082	1640.922 ± 36.527
3	≥ 750	2628.838 ± 8.373	1435.498 ± 37.419
low Δm , $N_b = 0$, $N_{SV} = 0$, $p_T(\text{ISR}) \geq 500 \text{ GeV}$, $N_j \geq 6$			
4	450 – 550	142.274 ± 1.975	109.280 ± 6.374
5	550 – 650	92.175 ± 1.561	67.417 ± 5.987
6	650 – 750	53.798 ± 1.197	49.864 ± 5.190
7	≥ 750	70.683 ± 1.421	45.003 ± 5.664
low Δm , $N_b = 0$, $N_{SV} \geq 1$, $p_T(\text{ISR}) \geq 500 \text{ GeV}$, $2 \leq N_j \leq 5$			
8	450 – 550	212.081 ± 3.384	122.858 ± 6.501
9	550 – 650	160.857 ± 2.554	84.854 ± 4.589
10	650 – 750	83.583 ± 1.497	41.669 ± 2.377
11	≥ 750	78.561 ± 1.513	34.971 ± 2.074
low Δm , $N_b = 0$, $N_{SV} \geq 1$, $p_T(\text{ISR}) \geq 500 \text{ GeV}$, $N_j \geq 6$			
12	450 – 550	4.999 ± 0.381	3.141 ± 0.339
13	550 – 650	2.894 ± 0.291	1.788 ± 0.256
14	650 – 750	1.642 ± 0.242	1.293 ± 0.247
15	≥ 750	2.840 ± 0.294	1.510 ± 0.259
low Δm , $N_b = 1$, $N_{SV} = 0$, $M_T(b_{1,2}, p_T^{miss}) < 175 \text{ GeV}$, $300 \leq p_T(\text{ISR}) < 500 \text{ GeV}$, $p_T(b) < 40 \text{ GeV}$			
16	300 – 400	985.010 ± 11.471	994.981 ± 44.192
17	400 – 500	234.210 ± 4.993	212.599 ± 12.399
18	500 – 600	27.269 ± 1.151	23.612 ± 2.169
19	≥ 600	5.843 ± 0.392	5.567 ± 0.666
low Δm , $N_b = 1$, $N_{SV} = 0$, $M_T(b_{1,2}, p_T^{miss}) < 175 \text{ GeV}$, $300 \leq p_T(\text{ISR}) < 500 \text{ GeV}$, $40 < p_T(b) < 70 \text{ GeV}$			
20	300 – 400	416.933 ± 7.066	420.647 ± 19.396
21	400 – 500	77.689 ± 2.660	71.123 ± 4.579
22	500 – 600	7.063 ± 0.444	6.177 ± 0.632
23	≥ 600	1.448 ± 0.181	1.371 ± 0.220
low Δm , $N_b = 1$, $N_{SV} = 0$, $M_T(b_{1,2}, p_T^{miss}) < 175 \text{ GeV}$, $p_T(\text{ISR}) \geq 500 \text{ GeV}$, $p_T(b) < 40 \text{ GeV}$			
24	450 – 550	89.469 ± 2.246	83.374 ± 5.664
25	550 – 650	43.078 ± 1.145	34.743 ± 3.843
26	650 – 750	22.023 ± 0.772	23.572 ± 3.910
27	≥ 750	16.925 ± 0.685	19.063 ± 3.716
low Δm , $N_b = 1$, $N_{SV} = 0$, $M_T(b_{1,2}, p_T^{miss}) < 175 \text{ GeV}$, $p_T(\text{ISR}) \geq 500 \text{ GeV}$, $40 < p_T(b) < 70 \text{ GeV}$			
28	450 – 550	43.452 ± 1.485	40.451 ± 2.916
29	550 – 650	17.811 ± 0.669	14.281 ± 1.632
30	650 – 750	7.014 ± 0.425	7.328 ± 1.250
31	≥ 750	6.412 ± 0.425	7.164 ± 1.469
low Δm , $N_b = 1$, $N_{SV} \geq 1$, $M_T(b_{1,2}, p_T^{miss}) < 175 \text{ GeV}$, $p_T(b) < 40 \text{ GeV}$			
32	300 – 400	71.110 ± 3.266	47.063 ± 9.630
33	400 – 500	19.866 ± 1.270	11.198 ± 2.441
34	≥ 500	12.494 ± 0.755	7.547 ± 1.621
low Δm , $N_b \geq 2$, $M_T(b_{1,2}, p_T^{miss}) < 175 \text{ GeV}$, $300 \leq p_T(\text{ISR}) < 500 \text{ GeV}$, $p_T(b_{12}) < 80 \text{ GeV}$			
35	300 – 400	65.112 ± 2.838	62.074 ± 9.733
36	400 – 500	17.910 ± 1.404	13.174 ± 2.841
37	≥ 500	4.292 ± 0.849	3.364 ± 0.935
low Δm , $N_b \geq 2$, $M_T(b_{1,2}, p_T^{miss}) < 175 \text{ GeV}$, $300 \leq p_T(\text{ISR}) < 500 \text{ GeV}$, $80 < p_T(b_{12}) < 140 \text{ GeV}$, $N_j \geq 7$			
38	300 – 400	78.522 ± 2.758	76.869 ± 11.902
39	400 – 500	19.902 ± 1.252	14.495 ± 3.120
40	≥ 500	2.641 ± 0.266	2.409 ± 0.544
low Δm , $N_b \geq 2$, $M_T(b_{1,2}, p_T^{miss}) < 175 \text{ GeV}$, $p_T(\text{ISR}) \geq 500 \text{ GeV}$, $p_T(b_{12}) \geq 140 \text{ GeV}$, $N_j \geq 7$			
41	300 – 400	1.938 ± 0.256	7.399 ± 14.091
42	400 – 500	0.576 ± 0.111	-1.796 ± 3.170
43	≥ 500	0.220 ± 0.070	-1.288 ± 2.305
low Δm , $N_b \geq 2$, $M_T(b_{1,2}, p_T^{miss}) < 175 \text{ GeV}$, $p_T(\text{ISR}) \geq 500 \text{ GeV}$, $p_T(b_{12}) \geq 140 \text{ GeV}$, $N_j \geq 7$			
44	450 – 550	5.117 ± 0.354	3.551 ± 0.824
45	550 – 650	4.043 ± 0.307	3.292 ± 0.950
46	≥ 650	2.714 ± 0.251	4.148 ± 1.290
low Δm , $N_b \geq 2$, $M_T(b_{1,2}, p_T^{miss}) < 175 \text{ GeV}$, $p_T(\text{ISR}) \geq 500 \text{ GeV}$, $80 < p_T(b_{12}) < 140 \text{ GeV}$			
47	450 – 550	8.715 ± 0.498	6.463 ± 1.423
48	550 – 650	4.707 ± 0.409	3.786 ± 1.087
49	≥ 650	3.214 ± 0.277	5.198 ± 1.662
low Δm , $N_b \geq 2$, $M_T(b_{1,2}, p_T^{miss}) < 175 \text{ GeV}$, $p_T(\text{ISR}) \geq 500 \text{ GeV}$, $p_T(b_{12}) \geq 140 \text{ GeV}$, $N_j \geq 7$			
50	450 – 550	0.557 ± 0.130	1.364 ± 1.139
51	550 – 650	0.267 ± 0.083	0.437 ± 0.471
52	≥ 650	0.354 ± 0.109	-5.232 ± 8.317

Table 6.5 : The $Z \rightarrow \nu\nu$ estimate in the various low Δm search regions, bins 0 to 52, using the 136.7 fb^{-1} dataset.

Search Region	$p_T^{\text{miss}} [\text{GeV}]$	$N_{MC}^{Z \rightarrow \nu\nu}$	$N_{\text{pred}}^{Z \rightarrow \nu\nu}$
high Δm , $N_b = 1$, $M_T(b_{1,2}, p_T^{\text{miss}}) < 175 \text{ GeV}$, $N_j \geq 7$, $N_{\text{res}} \geq 1$			
53	250 – 300	7.227 ± 0.671	8.161 ± 1.731
54	300 – 400	4.664 ± 0.414	5.827 ± 0.930
55	400 – 500	1.115 ± 0.157	1.762 ± 0.340
56	≥ 500	1.175 ± 0.212	1.397 ± 0.355
high Δm , $N_b \geq 2$, $M_T(b_{1,2}, p_T^{\text{miss}}) < 175 \text{ GeV}$, $N_j \geq 7$, $N_{\text{res}} \geq 1$			
57	250 – 300	7.040 ± 0.666	9.220 ± 2.070
58	300 – 400	5.418 ± 0.606	7.500 ± 1.538
59	400 – 500	1.436 ± 0.175	2.244 ± 0.536
60	≥ 500	0.907 ± 0.140	0.799 ± 0.279
high Δm , $N_b = 1$, $M_T(b_{1,2}, p_T^{\text{miss}}) \geq 175 \text{ GeV}$, $N_t = 0$, $N_{\text{res}} = 0$, $N_W = 0$, $H_T \geq 1000$			
61	250 – 350	174.544 ± 2.195	219.327 ± 15.411
62	350 – 450	101.459 ± 1.665	130.446 ± 6.753
63	450 – 550	62.139 ± 1.323	83.367 ± 5.201
64	≥ 550	120.674 ± 1.875	140.392 ± 8.978
high Δm , $N_b \geq 2$, $M_T(b_{1,2}, p_T^{\text{miss}}) \geq 175 \text{ GeV}$, $N_t = 0$, $N_{\text{res}} = 0$, $N_W = 0$, $H_T \geq 1000$			
65	250 – 350	26.815 ± 0.850	35.406 ± 3.703
66	350 – 450	18.766 ± 0.698	23.182 ± 2.581
67	450 – 550	12.745 ± 0.588	15.712 ± 2.105
68	≥ 550	23.555 ± 0.795	22.626 ± 3.261
high Δm , $N_b = 1$, $M_T(b_{1,2}, p_T^{\text{miss}}) \geq 175 \text{ GeV}$, $N_t \geq 1$, $N_{\text{res}} = 0$, $N_W = 0$, $H_T < 1000$			
69	250 – 550	22.898 ± 1.171	29.511 ± 2.094
70	550 – 650	3.399 ± 0.336	4.569 ± 0.595
71	≥ 650	2.112 ± 0.233	2.178 ± 0.306
high Δm , $N_b = 1$, $M_T(b_{1,2}, p_T^{\text{miss}}) \geq 175 \text{ GeV}$, $N_t \geq 1$, $N_{\text{res}} = 0$, $N_W = 0$, $1000 \leq H_T < 1500$			
72	250 – 550	8.321 ± 0.471	10.788 ± 0.835
73	550 – 650	0.917 ± 0.156	1.137 ± 0.227
74	≥ 650	1.693 ± 0.223	1.715 ± 0.276
high Δm , $N_b = 1$, $M_T(b_{1,2}, p_T^{\text{miss}}) \geq 175 \text{ GeV}$, $N_t \geq 1$, $N_{\text{res}} = 0$, $N_W = 0$, $H_T \geq 1500$			
75	250 – 550	2.397 ± 0.263	3.017 ± 0.388
76	550 – 650	0.237 ± 0.080	0.267 ± 0.095
77	≥ 650	0.382 ± 0.121	0.375 ± 0.130
high Δm , $N_b = 1$, $M_T(b_{1,2}, p_T^{\text{miss}}) \geq 175 \text{ GeV}$, $N_t = 0$, $N_{\text{res}} = 0$, $N_W \geq 1$, $H_T < 1300$			
78	250 – 350	17.309 ± 0.921	19.688 ± 2.408
79	350 – 450	9.976 ± 0.860	11.894 ± 1.263
80	≥ 450	5.631 ± 0.383	6.236 ± 0.607
high Δm , $N_b = 1$, $M_T(b_{1,2}, p_T^{\text{miss}}) \geq 175 \text{ GeV}$, $N_t = 0$, $N_{\text{res}} = 0$, $N_W \geq 1$, $H_T \geq 1300$			
81	250 – 350	1.235 ± 0.179	1.401 ± 0.260
82	350 – 450	0.563 ± 0.115	0.641 ± 0.141
83	≥ 450	0.746 ± 0.135	0.807 ± 0.164
high Δm , $N_b = 1$, $M_T(b_{1,2}, p_T^{\text{miss}}) \geq 175 \text{ GeV}$, $N_t = 0$, $N_{\text{res}} \geq 1$, $N_W = 0$, $H_T < 1000$			
84	250 – 350	195.175 ± 4.837	251.383 ± 16.983
85	350 – 450	74.884 ± 2.420	97.067 ± 5.751
86	450 – 550	26.313 ± 1.155	34.960 ± 2.636
87	550 – 650	10.278 ± 0.501	13.003 ± 1.193
88	≥ 650	5.139 ± 0.356	4.945 ± 0.565
high Δm , $N_b = 1$, $M_T(b_{1,2}, p_T^{\text{miss}}) \geq 175 \text{ GeV}$, $N_t = 0$, $N_{\text{res}} \geq 1$, $N_W = 0$, $1000 \leq H_T < 1500$			
89	250 – 350	8.008 ± 0.446	10.110 ± 0.929
90	350 – 450	5.178 ± 0.363	6.583 ± 0.575
91	450 – 550	3.186 ± 0.286	4.299 ± 0.478
92	550 – 650	2.187 ± 0.237	2.741 ± 0.381
93	≥ 650	3.978 ± 0.324	4.073 ± 0.485

Table 6.6 : The $Z \rightarrow \nu\nu$ estimate in the various high Δm search regions, bins 53 to 93, using the 136.7 fb^{-1} dataset.

Search Region	$p_T^{\text{miss}}[\text{GeV}]$	$N_{MC}^{Z \rightarrow \nu\nu}$	$N_{\text{pred}}^{Z \rightarrow \nu\nu}$
high Δm , $N_b = 1$, $M_T(b_{1,2}, p_T^{\text{miss}}) \geq 175 \text{ GeV}$, $N_t = 0$, $N_{\text{res}} \geq 1$, $N_W = 0$, $H_T \geq 1500$			
94	250 – 350	1.434 ± 0.206	1.735 ± 0.295
95	350 – 450	0.902 ± 0.163	1.163 ± 0.226
96	450 – 550	0.615 ± 0.131	0.822 ± 0.189
97	550 – 650	0.288 ± 0.083	0.298 ± 0.091
98	≥ 650	1.129 ± 0.173	1.008 ± 0.193
high Δm , $N_b = 1$, $M_T(b_{1,2}, p_T^{\text{miss}}) \geq 175 \text{ GeV}$, $N_t \geq 1$, $N_{\text{res}} = 0$, $N_W \geq 1$			
99	250 – 550	0.110 ± 0.048	0.112 ± 0.051
100	≥ 550	0.001 ± 0.002	0.001 ± 0.002
high Δm , $N_b = 1$, $M_T(b_{1,2}, p_T^{\text{miss}}) \geq 175 \text{ GeV}$, $N_t \geq 1$, $N_{\text{res}} \geq 1$, $N_W = 0$			
101	250 – 550	0.398 ± 0.102	0.479 ± 0.129
102	≥ 550	0.260 ± 0.081	0.307 ± 0.106
high Δm , $N_b = 1$, $M_T(b_{1,2}, p_T^{\text{miss}}) \geq 175 \text{ GeV}$, $N_t = 0$, $N_{\text{res}} \geq 1$, $N_W \geq 1$			
103	250 – 550	1.145 ± 0.290	1.374 ± 0.400
104	≥ 550	0.118 ± 0.046	0.114 ± 0.047
high Δm , $N_b = 2$, $M_T(b_{1,2}, p_T^{\text{miss}}) \geq 175 \text{ GeV}$, $N_t = 1$, $N_{\text{res}} = 0$, $N_W = 0$, $H_T < 1000$			
105	250 – 550	6.792 ± 0.557	8.638 ± 1.096
106	550 – 650	1.649 ± 0.580	1.514 ± 0.611
107	≥ 650	0.786 ± 0.140	0.855 ± 0.230
high Δm , $N_b = 2$, $M_T(b_{1,2}, p_T^{\text{miss}}) \geq 175 \text{ GeV}$, $N_t = 1$, $N_{\text{res}} = 0$, $N_W = 0$, $1000 \leq H_T < 1500$			
108	250 – 550	2.581 ± 0.256	3.281 ± 0.454
109	550 – 650	0.201 ± 0.066	0.186 ± 0.069
110	≥ 650	0.608 ± 0.117	0.587 ± 0.161
high Δm , $N_b = 2$, $M_T(b_{1,2}, p_T^{\text{miss}}) \geq 175 \text{ GeV}$, $N_t = 1$, $N_{\text{res}} = 0$, $N_W = 0$, $H_T \geq 1500$			
111	250 – 550	0.289 ± 0.083	0.359 ± 0.109
112	550 – 650	0.102 ± 0.058	0.092 ± 0.055
113	≥ 650	0.253 ± 0.084	0.282 ± 0.117
high Δm , $N_b = 2$, $M_T(b_{1,2}, p_T^{\text{miss}}) \geq 175 \text{ GeV}$, $N_t = 0$, $N_{\text{res}} = 0$, $N_W = 1$, $H_T < 1300$			
114	250 – 350	2.668 ± 0.351	3.328 ± 0.584
115	350 – 450	1.094 ± 0.175	1.241 ± 0.274
116	≥ 450	1.024 ± 0.150	1.073 ± 0.217
high Δm , $N_b = 2$, $M_T(b_{1,2}, p_T^{\text{miss}}) \geq 175 \text{ GeV}$, $N_t = 0$, $N_{\text{res}} = 0$, $N_W = 1$, $H_T \geq 1300$			
117	250 – 350	0.060 ± 0.036	0.070 ± 0.044
118	350 – 450	0.138 ± 0.053	0.153 ± 0.066
119	≥ 450	0.069 ± 0.036	0.069 ± 0.038
high Δm , $N_b = 2$, $M_T(b_{1,2}, p_T^{\text{miss}}) \geq 175 \text{ GeV}$, $N_t = 0$, $N_{\text{res}} = 1$, $N_W = 0$, $H_T < 1000$			
120	250 – 350	50.003 ± 2.431	65.511 ± 7.190
121	350 – 450	21.195 ± 1.350	24.494 ± 3.139
122	450 – 550	6.467 ± 0.494	7.814 ± 1.257
123	550 – 650	3.162 ± 0.285	2.865 ± 0.614
124	≥ 650	1.199 ± 0.159	1.325 ± 0.322
high Δm , $N_b = 2$, $M_T(b_{1,2}, p_T^{\text{miss}}) \geq 175 \text{ GeV}$, $N_t = 0$, $N_{\text{res}} = 1$, $N_W = 0$, $1000 \leq H_T < 1500$			
125	250 – 350	1.885 ± 0.205	2.449 ± 0.367
126	350 – 450	1.374 ± 0.182	1.625 ± 0.286
127	450 – 550	0.996 ± 0.153	1.166 ± 0.239
128	550 – 650	0.776 ± 0.141	0.700 ± 0.184
129	≥ 650	0.906 ± 0.140	0.901 ± 0.233
high Δm , $N_b = 2$, $M_T(b_{1,2}, p_T^{\text{miss}}) \geq 175 \text{ GeV}$, $N_t = 0$, $N_{\text{res}} = 1$, $N_W = 0$, $H_T \geq 1500$			
130	250 – 350	0.398 ± 0.103	0.535 ± 0.155
131	350 – 450	0.247 ± 0.081	0.275 ± 0.098
132	450 – 550	0.395 ± 0.110	0.461 ± 0.143
133	550 – 650	0.098 ± 0.046	0.092 ± 0.051
134	≥ 650	0.275 ± 0.086	0.299 ± 0.131

Table 6.7 : The $Z \rightarrow \nu\nu$ estimate in the various high Δm search regions, bins 94 to 134, using the 136.7 fb^{-1} dataset.

Search Region	p_T^{miss} [GeV]	$N_{MC}^{Z \rightarrow \nu\nu}$	$N_{\text{pred}}^{Z \rightarrow \nu\nu}$
high Δm , $N_b = 2$, $M_T(b_{1,2}, p_T^{\text{miss}}) \geq 175$ GeV, $N_t = 1$, $N_{\text{res}} = 0$, $N_W = 1$			
135	250 – 550	0.026 ± 0.026	0.030 ± 0.030
136	≥ 550	0.026 ± 0.025	0.022 ± 0.022
high Δm , $N_b = 2$, $M_T(b_{1,2}, p_T^{\text{miss}}) \geq 175$ GeV, $N_t = 1$, $N_{\text{res}} = 1$, $N_W = 0$, $H_T < 1300$			
137	250 – 350	0.051 ± 0.030	0.064 ± 0.038
138	350 – 450	0.111 ± 0.050	0.138 ± 0.064
139	≥ 450	0.177 ± 0.077	0.206 ± 0.096
high Δm , $N_b = 2$, $M_T(b_{1,2}, p_T^{\text{miss}}) \geq 175$ GeV, $N_t = 1$, $N_{\text{res}} = 1$, $N_W = 0$, $H_T \geq 1300$			
140	250 – 350	0.008 ± 0.009	0.010 ± 0.010
141	350 – 450	0.027 ± 0.027	0.031 ± 0.032
142	≥ 450	0.090 ± 0.049	0.095 ± 0.053
high Δm , $N_b = 2$, $M_T(b_{1,2}, p_T^{\text{miss}}) \geq 175$ GeV, $N_t = 0$, $N_{\text{res}} = 1$, $N_W = 1$			
143	250 – 550	0.212 ± 0.066	0.252 ± 0.086
144	≥ 550	0.035 ± 0.027	0.027 ± 0.021
high Δm , $N_b = 2$, $M_T(b_{1,2}, p_T^{\text{miss}}) \geq 175$ GeV, $N_t = 2$, $N_{\text{res}} = 0$, $N_W = 0$			
145	250 – 450	0.000 ± 0.002	0.000 ± 0.002
146	≥ 450	0.000 ± 0.002	0.000 ± 0.002
high Δm , $N_b = 2$, $M_T(b_{1,2}, p_T^{\text{miss}}) \geq 175$ GeV, $N_t = 0$, $N_{\text{res}} = 0$, $N_W = 2$			
147	≥ 250	0.019 ± 0.020	0.022 ± 0.023
high Δm , $N_b = 2$, $M_T(b_{1,2}, p_T^{\text{miss}}) \geq 175$ GeV, $N_t = 0$, $N_{\text{res}} = 2$, $N_W = 0$, $H_T < 1300$			
148	250 – 450	0.657 ± 0.203	0.831 ± 0.293
149	≥ 450	0.190 ± 0.068	0.198 ± 0.076
high Δm , $N_b = 2$, $M_T(b_{1,2}, p_T^{\text{miss}}) \geq 175$ GeV, $N_t = 0$, $N_{\text{res}} = 2$, $N_W = 0$, $H_T \geq 1300$			
150	250 – 450	0.000 ± 0.002	0.000 ± 0.002
151	≥ 450	0.019 ± 0.019	0.019 ± 0.019
high Δm , $N_b = 2$, $M_T(b_{1,2}, p_T^{\text{miss}}) \geq 175$ GeV, $(N_t + N_{\text{res}} + N_W) \geq 3$			
152	≥ 250	0.000 ± 0.002	0.000 ± 0.002
high Δm , $N_b \geq 3$, $M_T(b_{1,2}, p_T^{\text{miss}}) \geq 175$ GeV, $N_t = 1$, $N_{\text{res}} = 0$, $N_W = 0$, $H_T < 1000$			
153	250 – 350	0.175 ± 0.054	0.308 ± 0.211
154	350 – 550	0.276 ± 0.080	0.566 ± 0.301
155	≥ 550	0.340 ± 0.096	0.235 ± 0.167
high Δm , $N_b \geq 3$, $M_T(b_{1,2}, p_T^{\text{miss}}) \geq 175$ GeV, $N_t = 1$, $N_{\text{res}} = 0$, $N_W = 0$, $1000 \leq H_T < 1500$			
156	250 – 350	0.152 ± 0.063	0.212 ± 0.170
157	350 – 550	0.221 ± 0.071	0.397 ± 0.206
158	≥ 550	0.238 ± 0.088	0.213 ± 0.152
high Δm , $N_b \geq 3$, $M_T(b_{1,2}, p_T^{\text{miss}}) \geq 175$ GeV, $N_t = 1$, $N_{\text{res}} = 0$, $N_W = 0$, $H_T \geq 1500$			
159	250 – 350	0.057 ± 0.039	0.034 ± 0.092
160	350 – 550	0.000 ± 0.002	0.000 ± 0.002
161	≥ 550	0.063 ± 0.046	0.038 ± 0.047
high Δm , $N_b \geq 3$, $M_T(b_{1,2}, p_T^{\text{miss}}) \geq 175$ GeV, $N_t = 0$, $N_{\text{res}} = 0$, $N_W = 1$			
162	250 – 350	0.232 ± 0.074	0.355 ± 0.228
163	350 – 550	0.234 ± 0.083	0.079 ± 0.125
164	≥ 550	0.027 ± 0.018	0.020 ± 0.021
high Δm , $N_b \geq 3$, $M_T(b_{1,2}, p_T^{\text{miss}}) \geq 175$ GeV, $N_t = 0$, $N_{\text{res}} = 1$, $N_W = 0$, $H_T < 1000$			
165	250 – 350	3.020 ± 0.452	4.522 ± 2.638
166	350 – 550	2.826 ± 0.428	6.297 ± 2.829
167	≥ 550	0.195 ± 0.065	0.353 ± 0.257
high Δm , $N_b \geq 3$, $M_T(b_{1,2}, p_T^{\text{miss}}) \geq 175$ GeV, $N_t = 0$, $N_{\text{res}} = 1$, $N_W = 0$, $1000 \leq H_T < 1500$			
168	250 – 350	0.399 ± 0.096	0.717 ± 0.365
169	350 – 550	0.217 ± 0.066	0.415 ± 0.218
170	≥ 550	0.348 ± 0.093	0.482 ± 0.311
high Δm , $N_b \geq 3$, $M_T(b_{1,2}, p_T^{\text{miss}}) \geq 175$ GeV, $N_t = 0$, $N_{\text{res}} = 1$, $N_W = 0$, $H_T \geq 1500$			
171	250 – 350	0.054 ± 0.035	0.079 ± 0.069
172	350 – 550	0.035 ± 0.024	0.056 ± 0.057
173	≥ 550	0.032 ± 0.028	0.016 ± 0.022
high Δm , $N_b \geq 3$, $M_T(b_{1,2}, p_T^{\text{miss}}) \geq 175$ GeV, $N_t = 1$, $N_{\text{res}} = 0$, $N_W = 1$			
174	≥ 250	0.022 ± 0.022	0.023 ± 0.027
high Δm , $N_b \geq 3$, $M_T(b_{1,2}, p_T^{\text{miss}}) \geq 175$ GeV, $N_t = 1$, $N_{\text{res}} = 1$, $N_W = 0$			
175	250 – 350	0.001 ± 0.002	0.000 ± 0.002
176	≥ 350	0.142 ± 0.051	0.390 ± 0.197
high Δm , $N_b \geq 3$, $M_T(b_{1,2}, p_T^{\text{miss}}) \geq 175$ GeV, $N_t = 0$, $N_{\text{res}} = 1$, $N_W = 1$			
177	≥ 250	0.000 ± 0.002	0.000 ± 0.002
high Δm , $N_b \geq 3$, $M_T(b_{1,2}, p_T^{\text{miss}}) \geq 175$ GeV, $N_t = 2$, $N_{\text{res}} = 0$, $N_W = 0$			
178	≥ 250	0.038 ± 0.028	0.050 ± 0.057
high Δm , $N_b \geq 3$, $M_T(b_{1,2}, p_T^{\text{miss}}) \geq 175$ GeV, $N_t = 0$, $N_{\text{res}} = 0$, $N_W = 2$			
179	≥ 250	0.000 ± 0.002	0.000 ± 0.002
high Δm , $N_b \geq 3$, $M_T(b_{1,2}, p_T^{\text{miss}}) \geq 175$ GeV, $N_t = 0$, $N_{\text{res}} = 2$, $N_W = 0$			
180	250 – 350	0.018 ± 0.018	0.027 ± 0.031
181	≥ 350	0.023 ± 0.014	0.049 ± 0.043
high Δm , $N_b \geq 3$, $M_T(b_{1,2}, p_T^{\text{miss}}) \geq 175$ GeV, $(N_t + N_{\text{res}} + N_W) \geq 3$			
182	≥ 250	0.000 ± 0.002	0.000 ± 0.002

Table 6.8 : The $Z \rightarrow \nu\nu$ estimate in the various high Δm search regions, 135 to 182, using the 136.7 fb^{-1} dataset.

6.5 Quantum Chromodynamic Events

Simulation predicts negligible levels of QCD contamination in the various search regions. However, the QCD multijet simulation has limited statistics and there are uncertainties related to the description of physics in the simulation, particularly for the rare scenarios that would lead to a multijet event passing all of the final search region selection criteria. For these reasons, it is necessary to perform a data-driven QCD background estimation. We follow an approach similar to those described for other SM backgrounds, first using a QCD-enhanced control region and use it to validate the simulation, then extrapolate the event count in the control region to a prediction in the search region.

p_T^{miss} is generated in QCD events through either jet p_T mis-measurement or semileptonic heavy flavor decay and for the purposes of this section both sources of p_T^{miss} will be generally referred to as "mis-measurement". This leads to the characteristic of p_T^{miss} being aligned to one of the leading jets, which motivates including a veto on such events in the baseline selection. On the other hand, inverting and tightening the $\Delta\phi_{1234} \geq 0.5$ selection from the high Δm region, or the $|\Delta\phi(j_1, p_T^{miss})| \geq 0.5$, $|\Delta\phi(j_{2,3}, p_T^{miss})| \geq 0.15$ selection from the low Δm region, to $\Delta\phi_{123} < 0.1$ for both the high and low Δm regions result in regions with fairly pure samples of QCD events. The QCD search region yields are estimated with data yields in a series of control regions with this modified baseline selection after subtracting the contamination of non-QCD processes. The control region yields are related to search region yields with the following simulation transfer factors:

$$TF_{QCD} = \frac{N_{MC}^{QCD}(SR)}{N_{MC}^{QCD}(\Delta\phi_{123} < 0.1)}, \quad (6.6)$$

where $N_{MC}^{QCD}(SR)$ are the expected QCD yields from simulation for the signal regions, ($\Delta\phi_{1234} \geq 0.5$ for high Δm and $|\Delta\phi(j_1, p_T^{miss})| \geq 0.5$, $|\Delta\phi(j_{2,3}, p_T^{miss})| \geq 0.15$ for low Δm) and $N_{MC}^{QCD}(\Delta\phi_{123} < 0.1)$ is the expected QCD yield from simulation for the control region. The QCD estimate, N_{pred}^{QCD} , is defined as:

$$N_{pred}^{QCD} = TF_{QCD} \cdot (N_{data} - N_{MC}^{non-QCD}), \quad (6.7)$$

where N_{data} is the number of events in the $\Delta\phi_{123} < 0.1$ control sample described above, and $N_{MC}^{non-QCD}$ is the number of non-QCD events in this sample as estimated by the background predictions. This method is used to make the comparison with only the QCD events from data. The transfer factors in the high Δm region actually account for two levels of extrapolation, i.e., the extrapolation from the control regions to the search regions without the requirement of top and W tags, and the extrapolation in top and W tags in the search regions after correcting the top- and W-tagging efficiencies:

$$\begin{aligned} TF_{QCD} &= TF_{QCD}^{CR-SR} \times TF_{QCD}^{SR-extrap} \\ &= \frac{N_{MC}(SR)(N_j, N_b, p_T^{miss})}{N_{MC}(\Delta\phi_{123} < 0.1)(N_j, N_b, p_T^{miss})} \times \frac{N_{MC}(SR)(N_j, N_b, p_T^{miss}, N_t, N_{res}, N_W)}{N_{MC}(SR)(N_j, N_b, p_T^{miss})}, \end{aligned} \quad (6.8)$$

where we have split the transfer function into two different parts, a control region to search region comparison and a search region to search region extrapolation.

The QCD control region estimation uses an extrapolation method for the high Δm region, similar to Sec. 6.3. The selection for these regions are the same except for the N_t , N_{res} , and N_W tags, see Eqn. 6.8. This method allows for the measurement of the efficiency directly in data. This also allows for the statistical error on the estimation

to be greatly improved. The lepton vetoes are still applied to the $N_{MC}^{non-QCD}$ and N_{data} , but not the TF_{QCD} estimation. For the low Δm control region, it is binned in the same manner as the search region with the same cuts applied. Unfortunately, the QCD purity is low for the regions with one or more b-tags. To improve the statistics in these regions we merge the p_T^{miss} bins to improve the precision of the prediction in these regions.

6.5.1 QCD Local Smearing

The local smearing methods for QCD use a parameterization of the reconstructed (reco) jet. The reco jet is used when defining the jet response, see Eqn. 6.9. The analysis of the jet response spans many orders of magnitude and is binned in p_T and jet flavor, see Figs. 6.23 and 6.24.

The QCD events that fail the $\Delta\phi_{1234} \geq 0.5$ or $|\Delta\phi(j_1, p_T^{miss})| \geq 0.5$, $|\Delta\phi(j_{2,3}, p_T^{miss})| \geq 0.15$ selection cuts, for the high and low Δm regions respectively, enter the search region due to a leading jet undergoing such severe mis-measurement that it is reco as one of the sub-leading jets. Mis-measurement is parameterized by the jet response, defined as:

$$r_{jet} = \frac{(p_T)_{reco}}{(p_T)_{gen}}, \quad (6.9)$$

where $(p_T)_{reco}$ is the p_T of the reco jet and $(p_T)_{gen}$ is the p_T of the gen-level jet that is matched to the reco jet.

Smearing is done by taking the response, Eqn. 6.9, and adjusting it using a small probability window. With the new response, we calculate what the new jet p_T for the new event using the gen-level jet p_T of the original event. This is done on the two reco jets that are matched to the leading and sub-leading gen-level jets. We then recalculate the missing energy parameters, but all other properties of the

event are unaltered. We then store all event that pass, $p_T^{miss} > 200$ GeV to reduce storage space. This allows for the improvement of the limited statistics of the original simulation.

6.5.2 QCD Corrections

The QCD jet response, r_{jet} , is known to have a mismatch between data and simulation. To account for this, we devide the r_{jet} distribution into five bins which are then normalized to the data, see Fig. 6.25. The scale factor for 2018 post-HEM is large but the r_{jet} is in good agreement after the correction. The r_{jet} distribution after corrections is show in Fig. 6.26. We can see each era has a good agreement between data and simulation.

6.5.3 QCD Prediction

The statistical uncertainty on TF_{QCD} is reduced by increasing the effective luminosity of the QCD multijet sample with a method referred to as "local smearing." The method relies on the parameterization of r_{jet} , which is only dependent on jet properties. Tables 6.9, 6.10, 6.11, and 6.12 summarize the yields in data, the derived transfer factors, and the resulting QCD predictions in all 136.7 fb^{-1} of Run 2 data for the high Δm and low Δm search regions, respectively.

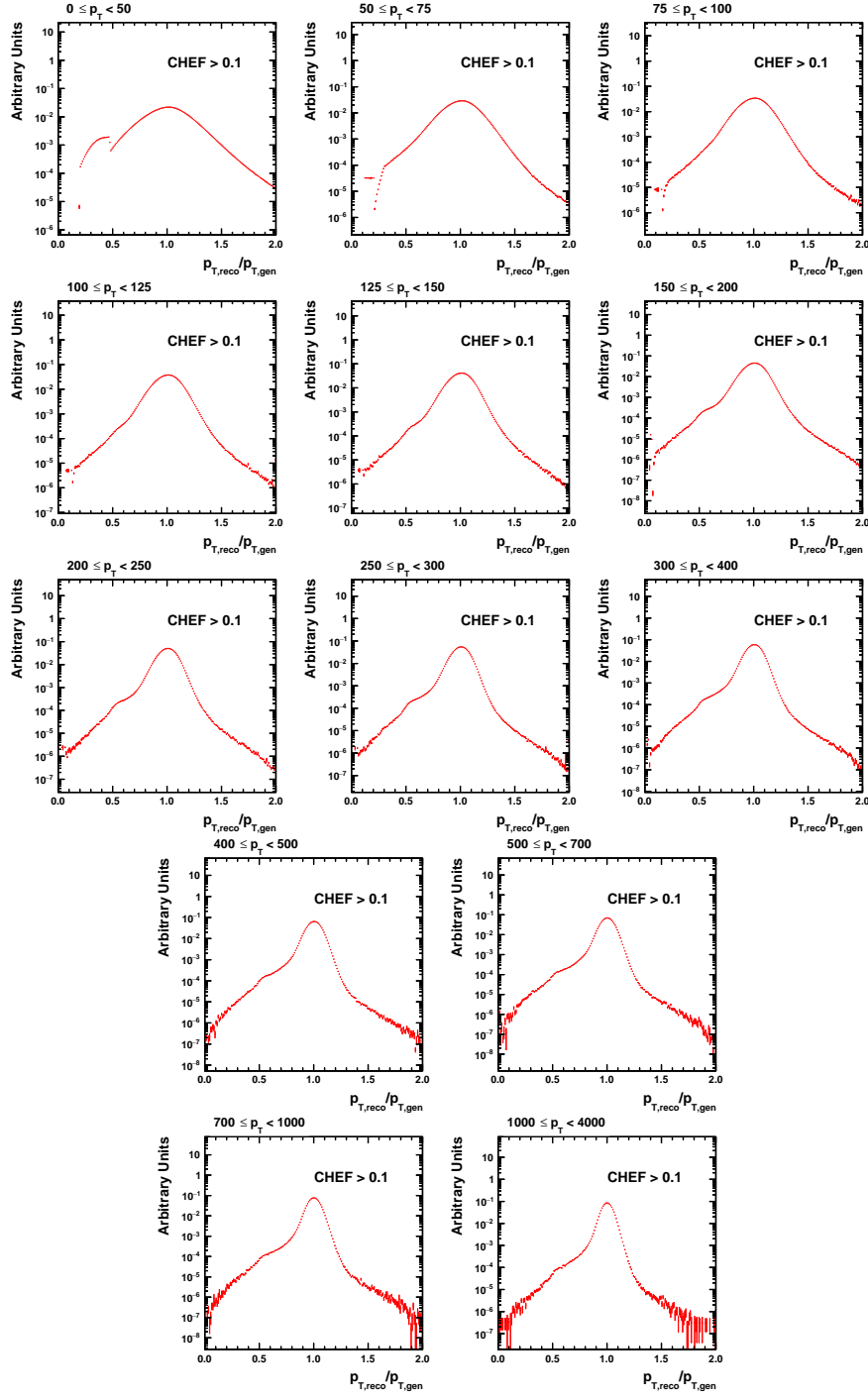


Figure 6.23 : Jet response for light tagged jets in the 2016 QCD simulation. Separated into multiple p_T bins.

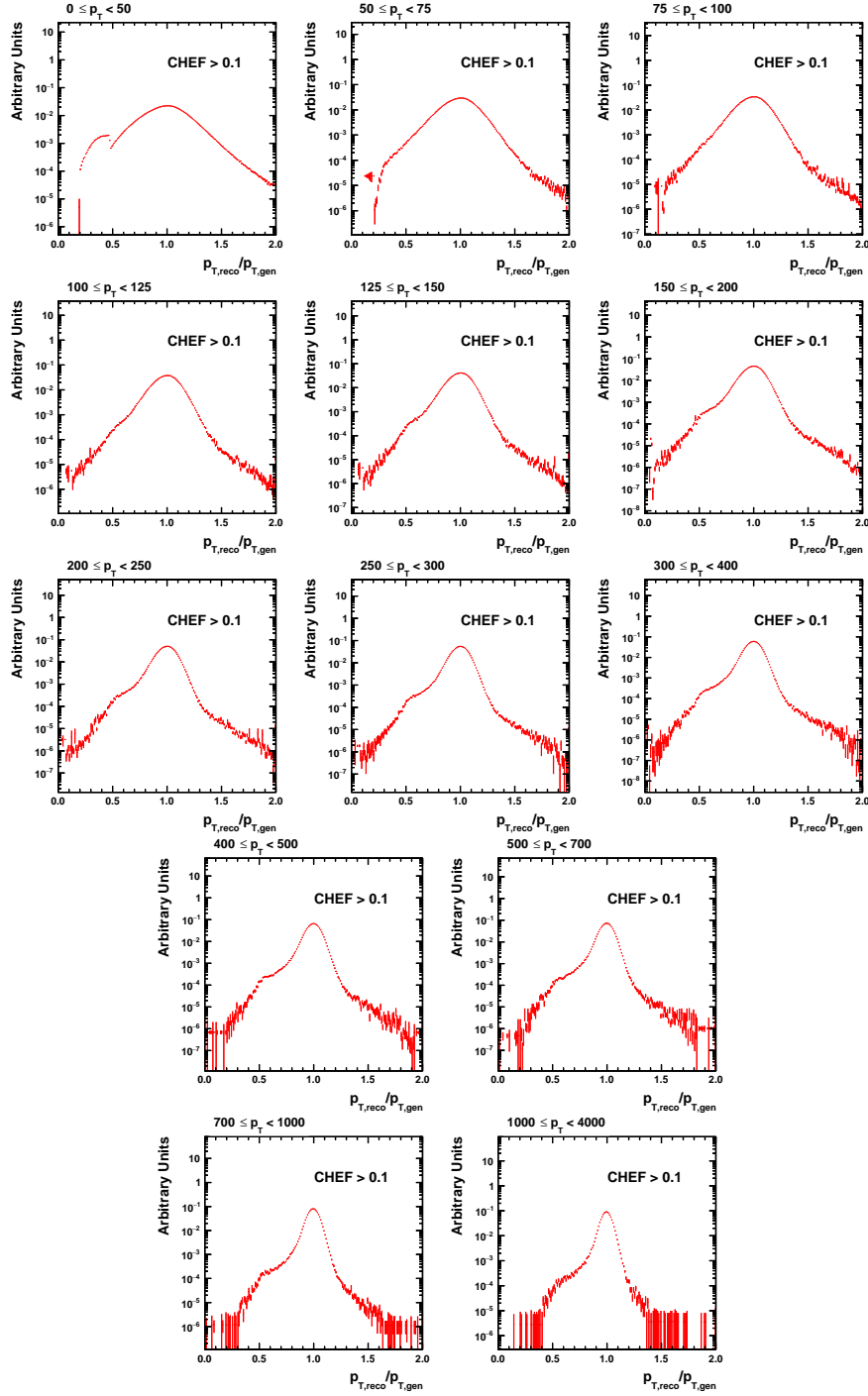


Figure 6.24 : Jet response for b tagged jets in the 2016 QCD simulation. Separated into multiple p_T bins.

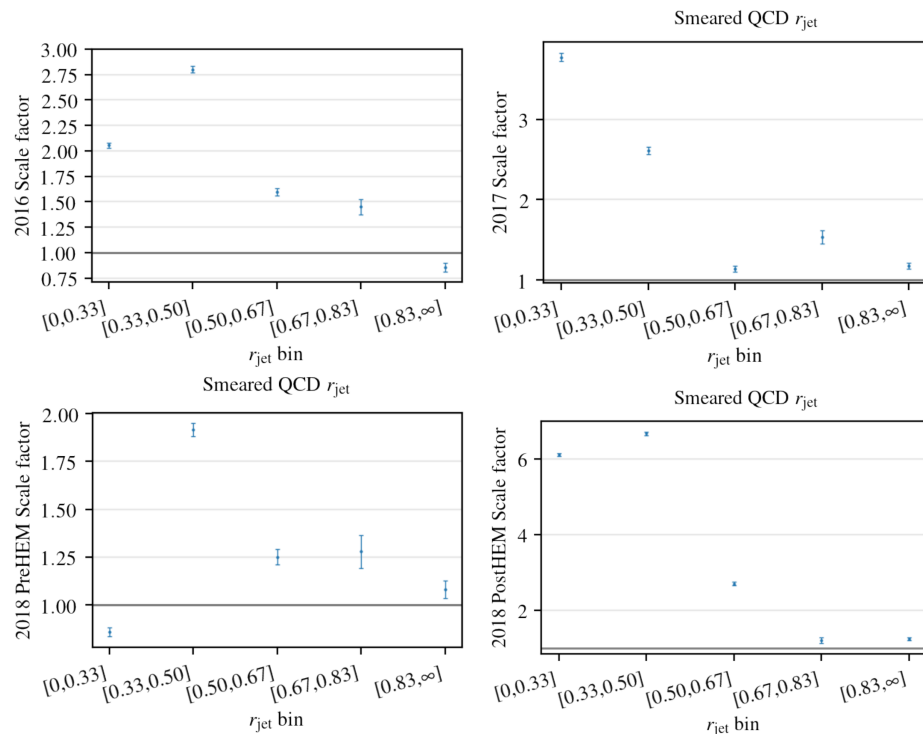


Figure 6.25 : The scale factor for the smeared QCD when comparing the data to simulation for 2016, 2017, 2018 pre-HEM, and 2018 post-HEM.

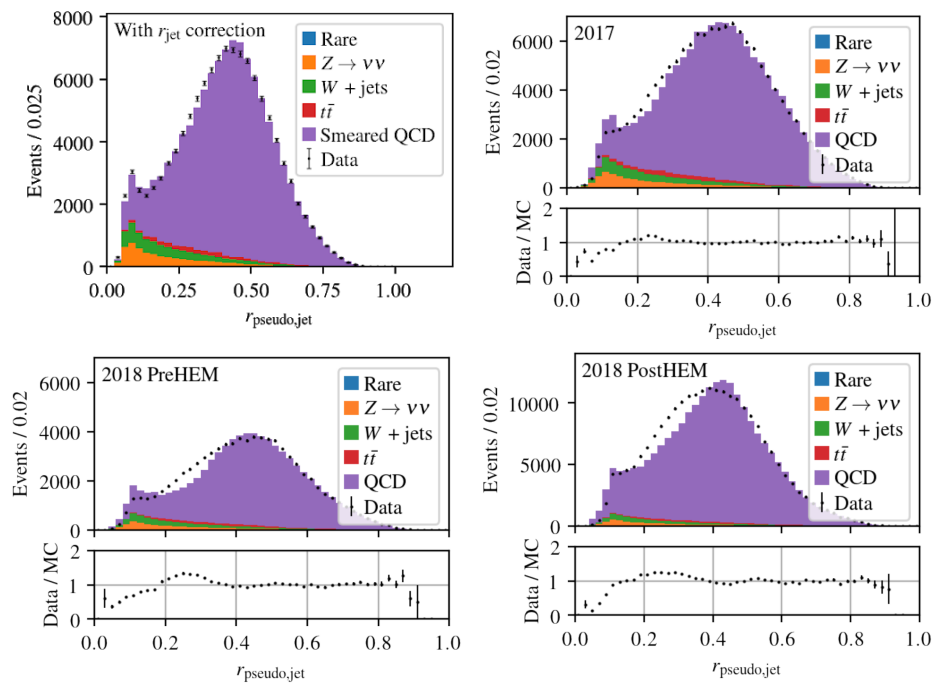


Figure 6.26 : The correction for each event that has the corresponding b-jet or light jet that is then associated with the response of the jet.

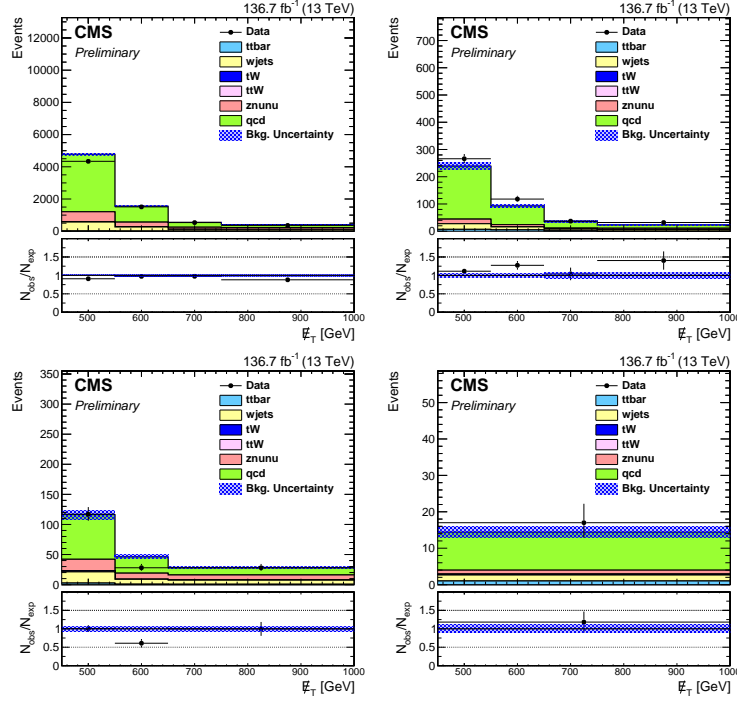


Figure 6.27 : Comparison of the p_T^{miss} distribution in the QCD multijet sample after applying the low Δm baseline selection in the $N_b = 0$ region. Data and simulation are represented by the black points and stacked histograms, respectively. The error bars on the ratio of observed data to simulation correspond to the data statistical uncertainty and the shaded blue band represents the statistical uncertainty on the simulation. These regions are included with the search regions in the simultaneous fit for the signal extraction in order to estimate the QCD contribution.

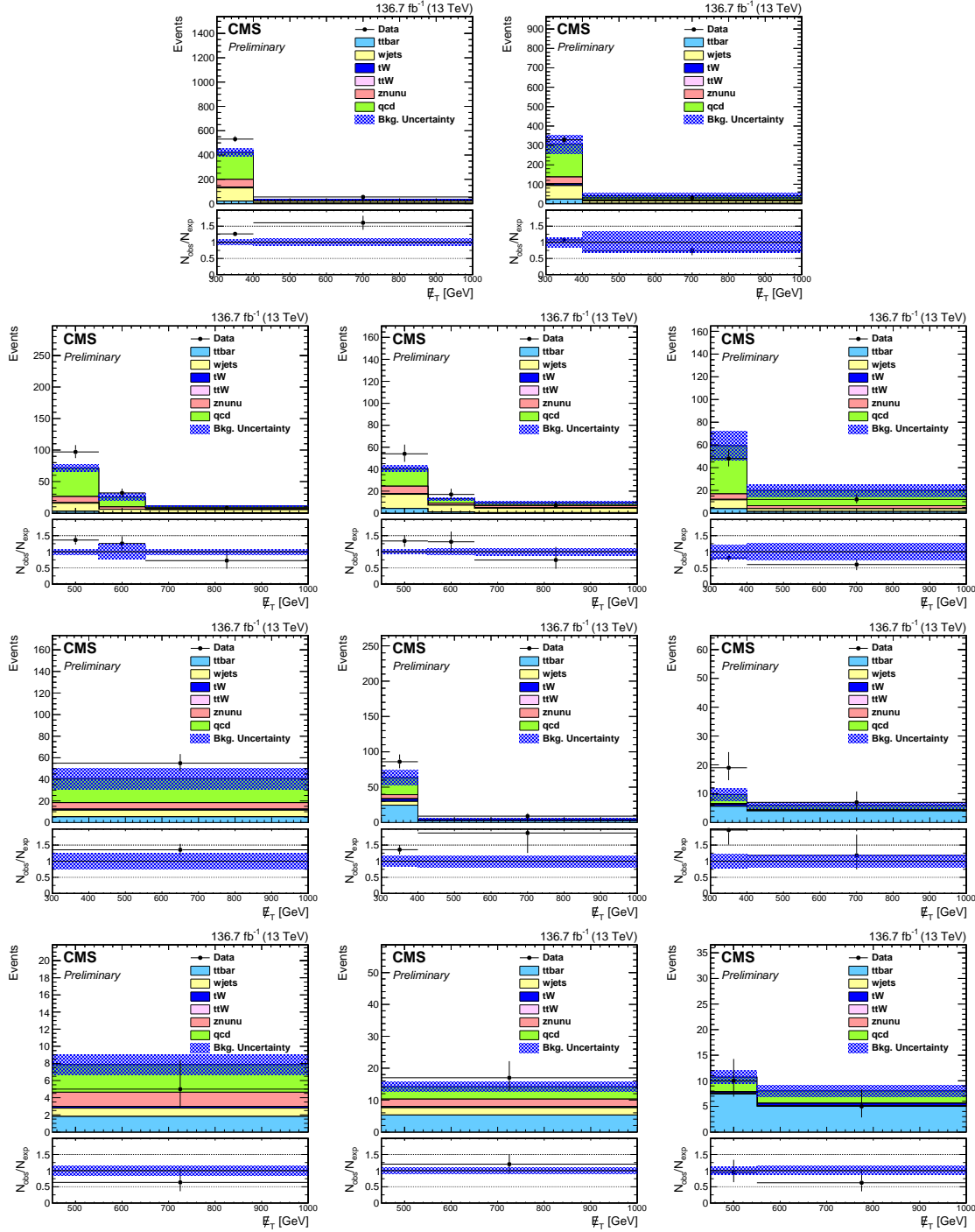


Figure 6.28 : Comparison of the p_T^{miss} distribution in the QCD multijet sample after applying the low Δm baseline selection. Two top rows: Events with $N_b = 1$; Two bottom rows: Events with $N_b \geq 2$; Data and simulation are represented by the black points and stacked histograms, respectively. The error bars on the ratio of observed data to simulation correspond to the data statistical uncertainty and the shaded blue band represents the statistical uncertainty on the simulation. These regions are included with the search regions in the simultaneous fit for the signal extraction in order to estimate the QCD contribution.

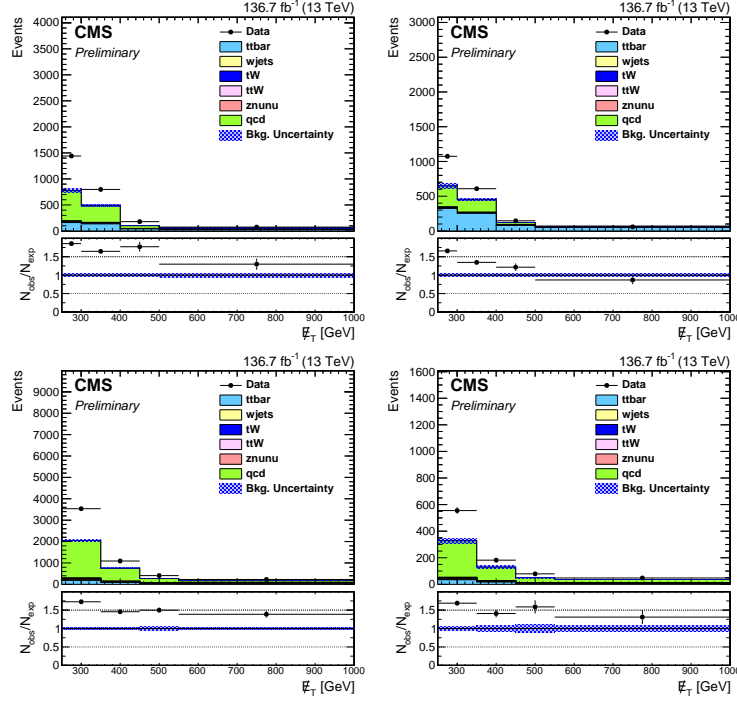


Figure 6.29 : Comparison of the p_T^{miss} distribution in the QCD multijet sample after applying the high Δm baseline selection in the $M_T(b_{1,2}, p_T^{miss}) < 175 \text{ GeV}$ and $N_t = 0, N_{\text{res}} = 0$, and $N_W = 0$ region. Data and simulation are represented by the black points and stacked histograms, respectively. The error bars on the ratio of observed data to simulation correspond to the data statistical uncertainty and the shaded blue band represents the statistical uncertainty on the simulation. These regions are included with the search regions in the simultaneous fit for the signal extraction in order to estimate the QCD contribution.

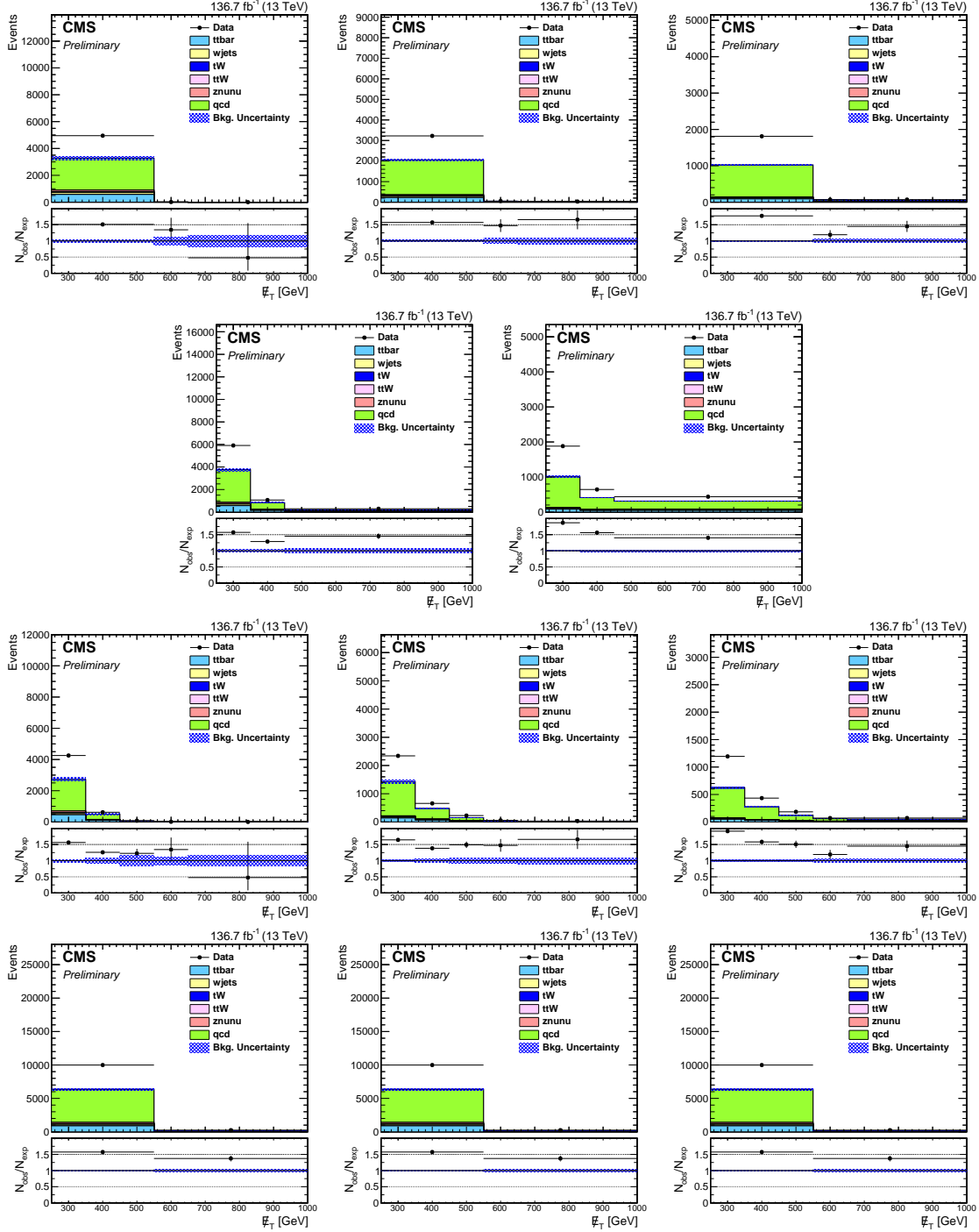


Figure 6.30 : Comparison of the p_T^{miss} distribution in the QCD multijet sample after applying the high Δm baseline selection in the $N_b = 1$ region where there are ≥ 1 heavy object tags. Data and simulation are represented by the black points and stacked histograms, respectively. The error bars on the ratio of observed data to simulation correspond to the data statistical uncertainty and the shaded blue band represents the statistical uncertainty on the simulation. These regions are included with the search regions in the simultaneous fit for the signal extraction in order to estimate the QCD contribution.

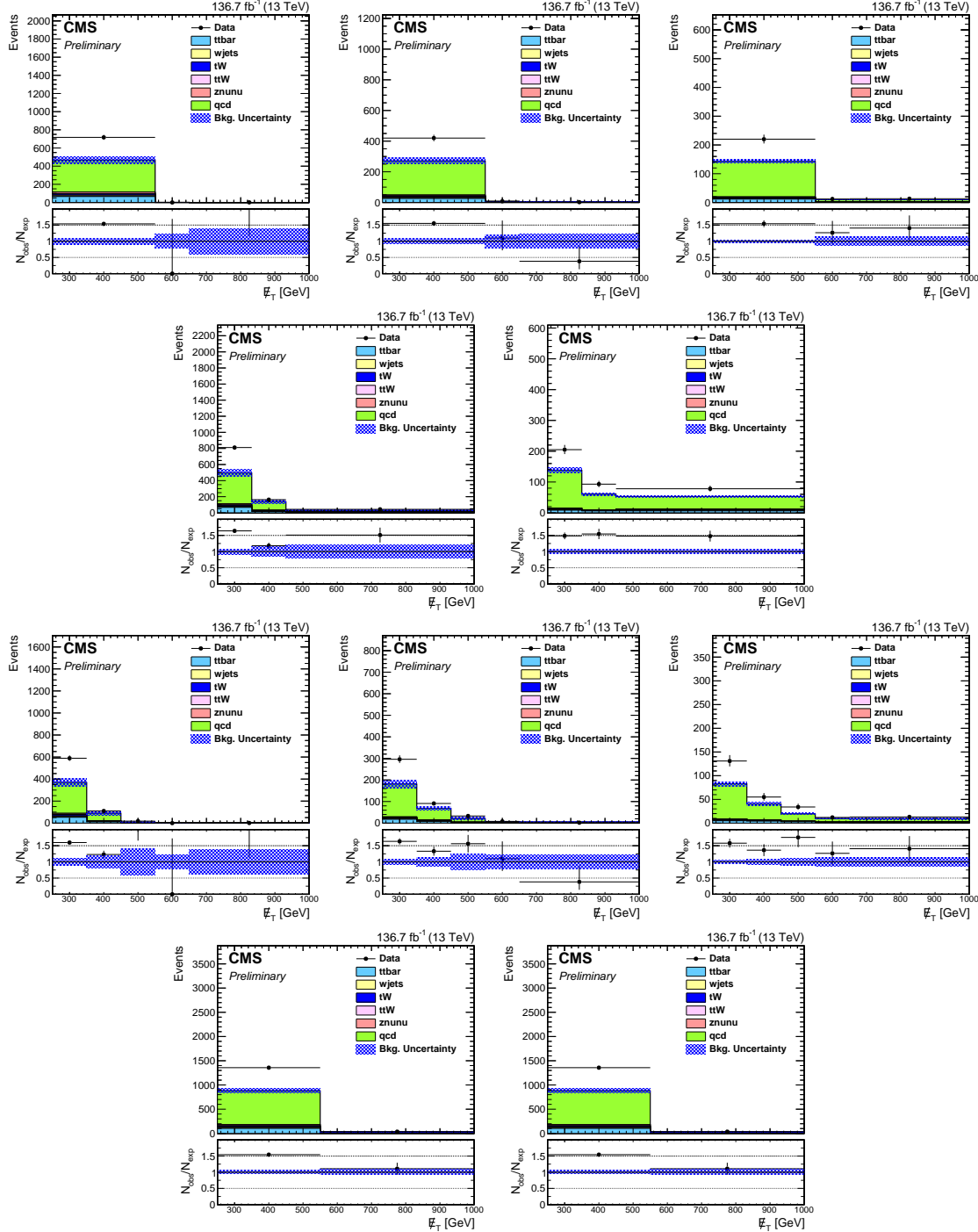


Figure 6.31 : Comparison of the p_T^{miss} distribution in the QCD multijet sample after applying the high Δm baseline selection in the $N_b = 2$ and $N_t = 1$, $N_{\text{res}} = 1$, or $N_W = 1$ regions. Data and simulation are represented by the black points and stacked histograms, respectively. The error bars on the ratio of observed data to simulation correspond to the data statistical uncertainty and the shaded blue band represents the statistical uncertainty on the simulation. These regions are included with the search regions in the simultaneous fit for the signal extraction in order to estimate the QCD contribution.

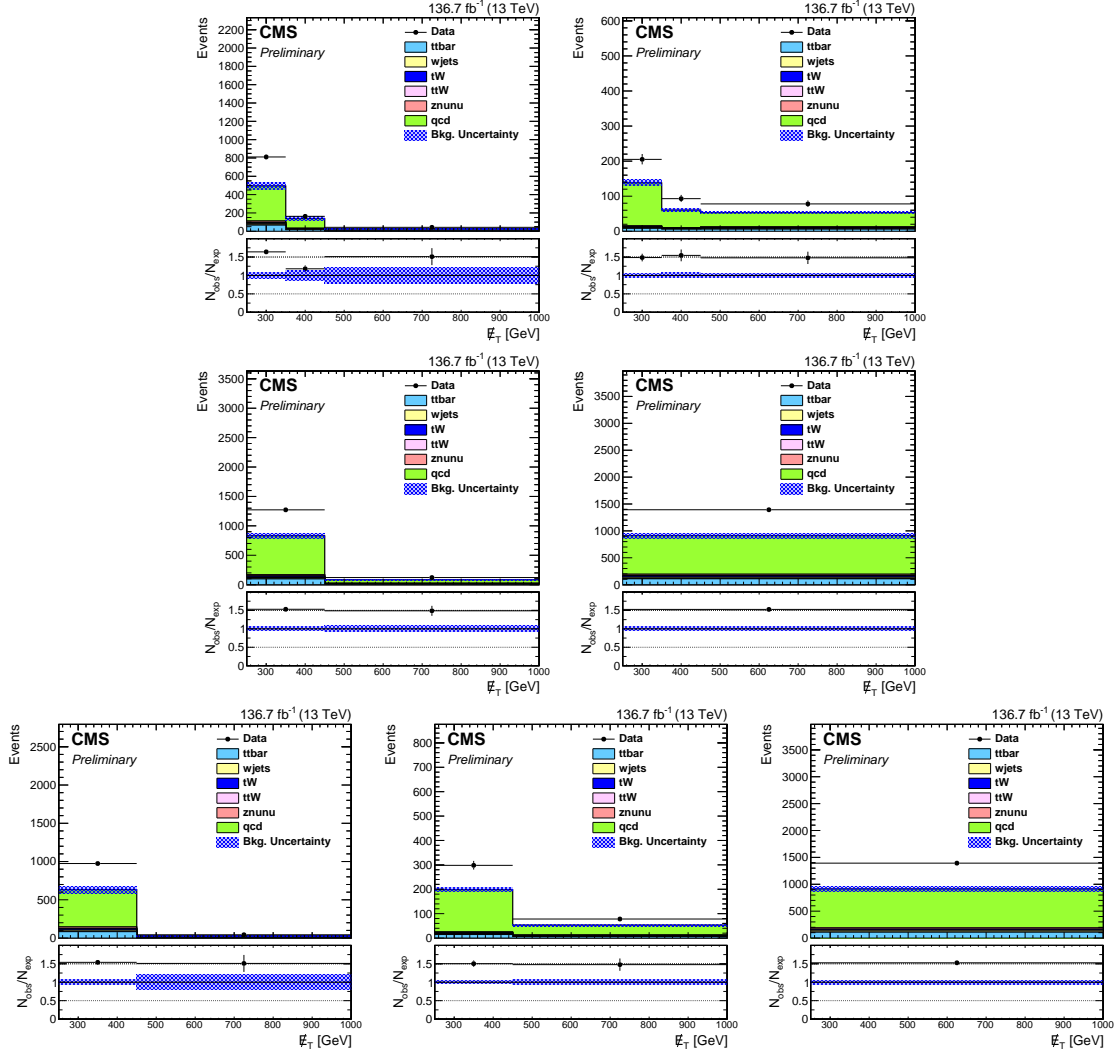


Figure 6.32 : Comparison of the p_T^{miss} distribution in the QCD multijet sample after applying the high Δm baseline selection in the $N_b = 2$ and $N_t = 2$, $N_{res} = 2$, or $N_W = 2$ region. Data and simulation are represented by the black points and stacked histograms, respectively. The error bars on the ratio of observed data to simulation correspond to the data statistical uncertainty and the shaded blue band represents the statistical uncertainty on the simulation. These regions are included with the search regions in the simultaneous fit for the signal extraction in order to estimate the QCD contribution.

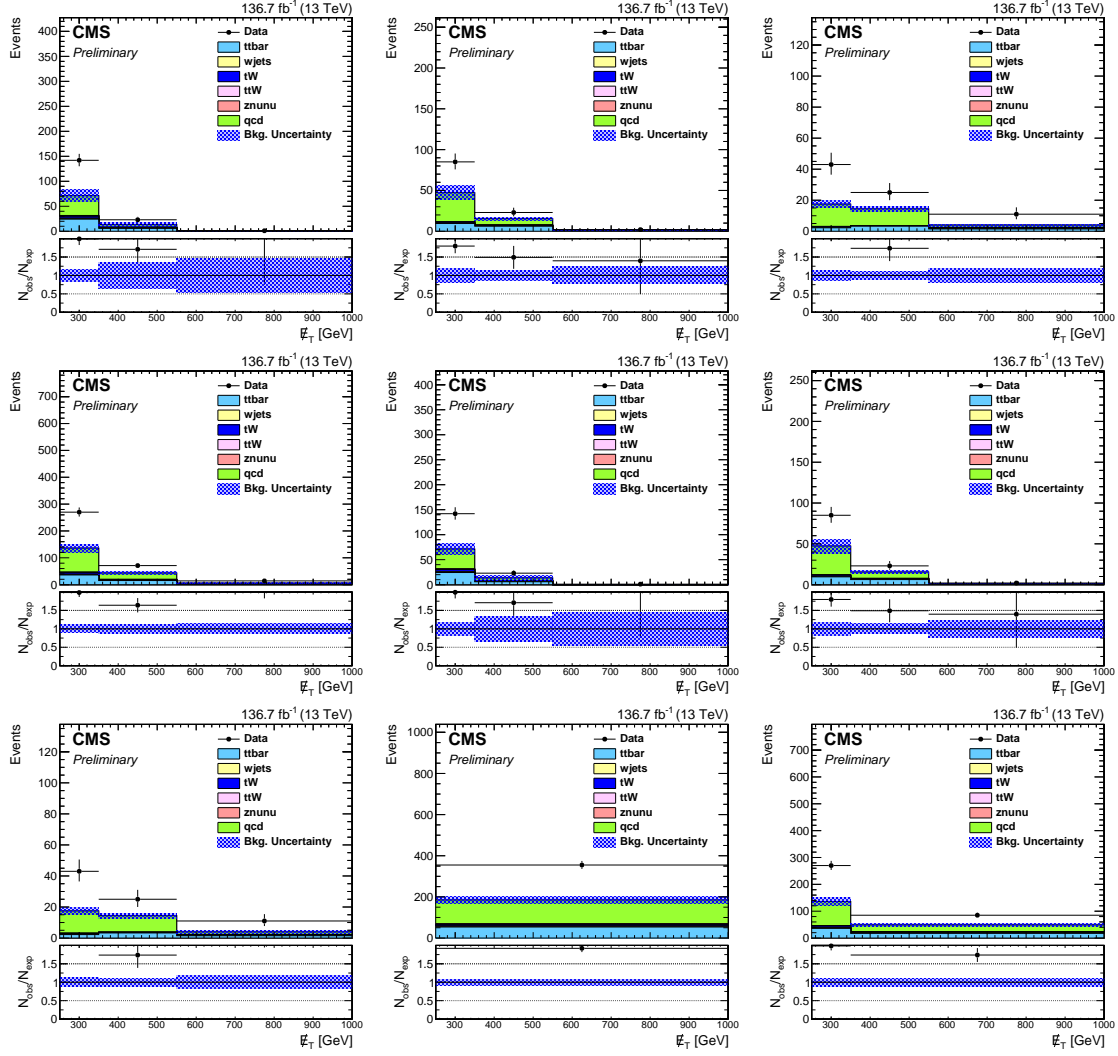


Figure 6.33 : Comparison of the p_T^{miss} distribution in the QCD multijet sample after applying the high Δm baseline selection in the $N_b \geq 3$ and $N_t = 1$, $N_{res} = 1$, or $N_W = 1$ region. Data and simulation are represented by the black points and stacked histograms, respectively. The error bars on the ratio of observed data to simulation correspond to the data statistical uncertainty and the shaded blue band represents the statistical uncertainty on the simulation. These regions are included with the search regions in the simultaneous fit for the signal extraction in order to estimate the QCD contribution.

Search Region	$p_T^{\text{miss}}[\text{GeV}]$	$N_{\text{data}}(II)$	TF_{QCD}	$N_{\text{pred}}^{\text{LL}}$
low Δm , $N_b = 0$, $N_{SV} = 0$, $p_T(\text{ISR}) \geq 500 \text{ GeV}$, $2 \leq N_j \leq 5$				
0	450–550	4340	0.029±0.003	123.96±12.42
1	550–650	1511	0.010±0.001	14.69±2.10
2	650–750	537	0.006±0.002	3.23±1.02
3	≥ 750	360	0.006±0.002	2.16±0.59
low Δm , $N_b = 0$, $N_{SV} = 0$, $p_T(\text{ISR}) \geq 500 \text{ GeV}$, $N_j \geq 6$				
4	450–550	266	0.075±0.010	20.02±3.05
5	550–650	118	0.063±0.017	7.43±2.10
6	650–750	37	0.032±0.022	1.20±0.82
7	≥ 750	32	0.027±0.026	0.86±0.83
low Δm , $N_b = 0$, $N_{SV} \geq 1$, $p_T(\text{ISR}) \geq 500 \text{ GeV}$, $2 \leq N_j \leq 5$				
8	450–550	117	0.041±0.016	4.77±1.92
9	550–650	28	0.003±0.002	0.08±0.06
10	650–750	28	0.309±0.220	8.66±6.38
11	≥ 750	28	0.000±0.000	0.00±0.00
low Δm , $N_b = 0$, $N_{SV} \geq 1$, $p_T(\text{ISR}) \geq 500 \text{ GeV}$, $N_j \geq 6$				
12	450–550	17	0.019±0.020	0.33±0.34
13	550–650	17	0.000±0.000	0.00±0.00
14	650–750	17	0.003±0.002	0.05±0.04
15	≥ 750	17	0.000±0.000	0.00±0.00
low Δm , $N_b = 1$, $N_{SV} = 0$, $M_T(b_{1,2}, p_T^{\text{miss}}) < 175 \text{ GeV}$, $300 \leq p_T(\text{ISR}) < 500 \text{ GeV}$, $p_T(b) < 40 \text{ GeV}$				
16	300–400	531	0.140±0.052	74.23±27.74
17	400–500	55	0.007±0.006	0.37±0.35
18	500–600	55	0.000±0.000	0.00±0.00
19	≥ 600	55	0.000±0.000	0.00±0.00
low Δm , $N_b = 1$, $N_{SV} = 0$, $M_T(b_{1,2}, p_T^{\text{miss}}) < 175 \text{ GeV}$, $300 \leq p_T(\text{ISR}) < 500 \text{ GeV}$, $40 < p_T(b) < 70 \text{ GeV}$				
20	300–400	329	0.044±0.027	14.40±8.77
21	400–500	30	0.000±0.000	0.00±0.00
22	500–600	30	0.000±0.000	0.00±0.00
23	≥ 600	30	0.000±0.000	0.00±0.00
low Δm , $N_b = 1$, $N_{SV} = 0$, $M_T(b_{1,2}, p_T^{\text{miss}}) < 175 \text{ GeV}$, $p_T(\text{ISR}) \geq 500 \text{ GeV}$, $p_T(b) < 40 \text{ GeV}$				
24	450–550	97	0.104±0.089	10.11±8.74
25	550–650	32	0.034±0.027	1.08±0.90
26	650–750	8	0.000±0.000	0.00±0.00
27	≥ 750	8	0.000±0.000	0.00±0.00
low Δm , $N_b = 1$, $N_{SV} = 0$, $M_T(b_{1,2}, p_T^{\text{miss}}) < 175 \text{ GeV}$, $p_T(\text{ISR}) \geq 500 \text{ GeV}$, $40 < p_T(b) < 70 \text{ GeV}$				
28	450–550	54	0.033±0.018	1.80±1.01
29	550–650	17	0.044±0.038	0.74±0.67
30	650–750	7	0.000±0.000	0.00±0.00
31	≥ 750	7	0.068±0.054	0.47±0.42
low Δm , $N_b = 1$, $N_{SV} \geq 1$, $M_T(b_{1,2}, p_T^{\text{miss}}) < 175 \text{ GeV}$, $p_T(b) < 40 \text{ GeV}$				
32	300–400	48	0.201±0.120	9.67±5.95
33	400–500	12	0.337±0.276	4.04±3.51
34	≥ 500	12	0.000±0.000	0.00±0.00
low Δm , $N_b \geq 2$, $M_T(b_{1,2}, p_T^{\text{miss}}) < 175 \text{ GeV}$, $300 \leq p_T(\text{ISR}) < 500 \text{ GeV}$, $p_T(b_{12}) < 80 \text{ GeV}$				
35	300–400	55	0.000±0.000	0.00±0.00
36	400–500	55	0.000±0.000	0.00±0.00
37	≥ 500	55	0.000±0.000	0.00±0.00
low Δm , $N_b \geq 2$, $M_T(b_{1,2}, p_T^{\text{miss}}) < 175 \text{ GeV}$, $300 \leq p_T(\text{ISR}) < 500 \text{ GeV}$, $80 < p_T(b_{12}) < 140 \text{ GeV}$, $N_j \geq 7$				
38	300–400	86	0.539±0.434	46.39±37.63
39	400–500	9	0.000±0.000	0.00±0.00
40	≥ 500	9	0.000±0.000	0.00±0.00
low Δm , $N_b \geq 2$, $M_T(b_{1,2}, p_T^{\text{miss}}) < 175 \text{ GeV}$, $p_T(\text{ISR}) \geq 500 \text{ GeV}$, $p_T(b_{12}) < 80 \text{ GeV}$				
44	450–550	5	0.000±0.000	0.00±0.00
45	550–650	5	0.000±0.000	0.00±0.00
46	≥ 650	5	0.000±0.000	0.00±0.00
low Δm , $N_b \geq 2$, $M_T(b_{1,2}, p_T^{\text{miss}}) < 175 \text{ GeV}$, $p_T(\text{ISR}) \geq 500 \text{ GeV}$, $80 < p_T(b_{12}) < 140 \text{ GeV}$				
47	450–550	17	0.000±0.000	0.00±0.00
48	550–650	17	0.000±0.000	0.00±0.00
49	≥ 650	17	0.000±0.000	0.00±0.00
low Δm , $N_b \geq 2$, $M_T(b_{1,2}, p_T^{\text{miss}}) < 175 \text{ GeV}$, $p_T(\text{ISR}) \geq 500 \text{ GeV}$, $p_T(b_{12}) \geq 140 \text{ GeV}$, $N_j \geq 7$				
50	450–550	10	0.162±0.088	1.62±1.01
51	550–650	5	0.037±0.039	0.18±0.21
52	≥ 650	5	0.000±0.000	0.00±0.00

Table 6.9 : The QCD estimate in the various low Δm search regions, bins 0 to 52, using the 136.7 fb^{-1} dataset.

Search Region	$p_T^{\text{miss}}[\text{GeV}]$	$N_{\text{data}}(1I)$	TF_{QCD}	$TF_{QCD}^{\text{GR-SR}}$	$TF_{QCD}^{\text{SR-extrap}}$	$N_{\text{pred}}^{\text{LL}}$
high Δm , $N_b = 1$, $M_T(b_{1,2}, p_T^{\text{miss}}) < 175 \text{ GeV}$, $N_j \geq 7$, $N_{\text{res}} \geq 1$						
53	250–300	1440	0.006±0.006	0.263	0.024	9.18±8.23
54	300–400	798	0.014±0.010	0.270	0.052	11.28±8.05
55	400–500	179	0.009±0.006	0.174	0.049	1.53±1.14
56	≥ 500	74	0.000±0.000	0.053	0.000	0.00±0.00
high Δm , $N_b \geq 2$, $M_T(b_{1,2}, p_T^{\text{miss}}) < 175 \text{ GeV}$, $N_j \geq 7$, $N_{\text{res}} \geq 1$						
57	250–300	1074	0.035±0.022	0.412	0.085	37.66±23.14
58	300–400	608	0.001±0.001	0.178	0.006	0.70±0.52
59	400–500	146	0.076±0.070	0.240	0.317	11.14±10.20
60	≥ 500	59	0.000±0.000	0.028	0.000	0.00±0.00
high Δm , $N_b = 1$, $M_T(b_{1,2}, p_T^{\text{miss}}) \geq 175 \text{ GeV}$, $N_t = 0$, $N_{\text{res}} = 0$, $N_W = 0$, $H_T \geq 1000$						
61	250–350	3536	0.027±0.005	0.028	0.948	95.17±16.59
62	350–450	1091	0.009±0.002	0.011	0.805	9.73±2.25
63	450–550	409	0.012±0.005	0.012	1.000	5.03±1.86
64	≥ 550	228	0.001±0.001	0.001	1.000	0.29±0.20
high Δm , $N_b \geq 2$, $M_T(b_{1,2}, p_T^{\text{miss}}) \geq 175 \text{ GeV}$, $N_t = 0$, $N_{\text{res}} = 0$, $N_W = 0$, $H_T \geq 1000$						
65	250–350	555	0.024±0.005	0.029	0.807	13.04±2.79
66	350–450	182	0.017±0.006	0.021	0.817	3.18±1.14
67	450–550	79	0.002±0.002	0.002	1.000	0.17±0.18
68	≥ 550	48	0.001±0.001	0.001	1.000	0.06±0.06
high Δm , $N_b = 1$, $M_T(b_{1,2}, p_T^{\text{miss}}) \geq 175 \text{ GeV}$, $N_t \geq 1$, $N_{\text{res}} = 0$, $N_W = 0$, $H_T < 1000$						
69	250–550	4952	0.000±0.000	0.038	0.000	0.00±0.00
70	550–650	13	0.000±0.000	0.001	0.000	0.00±0.00
71	≥ 650	1	0.000±0.000	0.000	-nan	0.00±0.00
high Δm , $N_b = 1$, $M_T(b_{1,2}, p_T^{\text{miss}}) \geq 175 \text{ GeV}$, $N_t \geq 1$, $N_{\text{res}} = 0$, $N_W = 0$, $1000 \leq H_T < 1500$						
72	250–550	3224	-0.000±0.000	0.020	-0.005	-0.29±0.22
73	550–650	56	0.000±0.000	0.000	-nan	0.00±0.00
74	≥ 650	31	0.000±0.000	0.006	0.000	0.00±0.00
high Δm , $N_b = 1$, $M_T(b_{1,2}, p_T^{\text{miss}}) \geq 175 \text{ GeV}$, $N_t \geq 1$, $N_{\text{res}} = 0$, $N_W = 0$, $H_T \geq 1500$						
75	250–550	1812	0.001±0.000	0.028	0.025	1.29±0.52
76	550–650	70	0.000±0.000	0.002	0.000	0.00±0.00
77	≥ 650	71	0.000±0.000	0.000	-nan	0.00±0.00
high Δm , $N_b = 1$, $M_T(b_{1,2}, p_T^{\text{miss}}) \geq 175 \text{ GeV}$, $N_t = 0$, $N_{\text{res}} = 0$, $N_W \geq 1$, $H_T \geq 1300$						
78	250–350	5910	0.000±0.000	0.038	0.000	0.00±0.00
79	350–450	1066	0.000±0.000	0.011	0.000	0.00±0.00
80	≥ 450	291	0.000±0.000	0.008	0.000	0.00±0.00
high Δm , $N_b = 1$, $M_T(b_{1,2}, p_T^{\text{miss}}) \geq 175 \text{ GeV}$, $N_t = 0$, $N_{\text{res}} = 0$, $N_W \geq 1$, $H_T \geq 1300$						
81	250–350	1881	0.000±0.000	0.030	0.002	0.09±0.09
82	350–450	644	0.000±0.000	0.017	0.026	0.28±0.23
83	≥ 450	438	0.000±0.000	0.007	0.000	0.00±0.00
high Δm , $N_b = 1$, $M_T(b_{1,2}, p_T^{\text{miss}}) \geq 175 \text{ GeV}$, $N_t = 0$, $N_{\text{res}} \geq 1$, $N_W = 0$, $H_T < 1000$						
84	250–350	4255	0.002±0.001	0.042	0.044	7.99±5.91
85	350–450	619	0.000±0.000	0.016	0.000	0.00±0.00
86	450–550	78	0.000±0.000	0.000	-nan	0.00±0.00
87	550–650	13	0.000±0.000	0.001	0.000	0.00±0.00
88	≥ 650	1	0.000±0.000	0.000	-nan	0.00±0.00
high Δm , $N_b = 1$, $M_T(b_{1,2}, p_T^{\text{miss}}) \geq 175 \text{ GeV}$, $N_t = 0$, $N_{\text{res}} \geq 1$, $N_W = 0$, $1000 \leq H_T < 1500$						
89	250–350	2342	0.001±0.000	0.025	0.022	1.25±0.69
90	350–450	657	0.003±0.002	0.008	0.411	2.04±1.23
91	450–550	225	0.000±0.000	0.013	0.000	0.00±0.00
92	550–650	56	0.000±0.000	0.000	-nan	0.00±0.00
93	≥ 650	31	0.000±0.000	0.006	0.000	0.00±0.00

Table 6.10 : The LL estimate in the various high Δm search regions, bins 53 to 93, using the 136.7 fb^{-1} dataset.

Search Region	$p_T^{\text{miss}}[\text{GeV}]$	$N_{\text{data}}(1l)$	TF_{QCD}	$TF_{QCD}^{\text{CR-SR}}$	$TF_{QCD}^{\text{SR-extrap}}$	$N_{\text{pred}}^{\text{LL}}$
high Δm , $N_b = 1$, $M_T(b_{1,2}, p_T^{\text{miss}}) \geq 175 \text{ GeV}$, $N_t = 0$, $N_{\text{res}} \geq 1$, $N_W = 0$, $H_T \geq 1500$						
94	250–350	1194	0.002±0.001	0.037	0.043	1.89±1.38
95	350–450	434	0.000±0.000	0.017	0.000	0.00±0.00
96	450–550	184	0.000±0.000	0.012	0.000	0.00±0.00
97	550–650	70	0.000±0.000	0.002	0.000	0.00±0.00
98	≥ 650	71	0.000±0.000	0.000	-nan	0.00±0.00
high Δm , $N_b = 1$, $M_T(b_{1,2}, p_T^{\text{miss}}) \geq 175 \text{ GeV}$, $N_t \geq 1$, $N_{\text{res}} = 0$, $N_W \geq 1$						
99	250–550	9988	0.000±0.000	0.030	0.000	0.00±0.00
100	≥ 550	242	0.000±0.000	0.001	0.000	0.00±0.00
high Δm , $N_b = 1$, $M_T(b_{1,2}, p_T^{\text{miss}}) \geq 175 \text{ GeV}$, $N_t \geq 1$, $N_{\text{res}} \geq 1$, $N_W = 0$						
101	250–550	9988	0.000±0.000	0.030	0.003	1.05±0.78
102	≥ 550	242	0.000±0.000	0.001	0.000	0.00±0.00
high Δm , $N_b = 1$, $M_T(b_{1,2}, p_T^{\text{miss}}) \geq 175 \text{ GeV}$, $N_t = 0$, $N_{\text{res}} \geq 1$, $N_W \geq 1$						
103	250–550	9988	0.000±0.000	0.030	0.000	0.00±0.00
104	≥ 550	242	0.000±0.000	0.001	0.000	0.00±0.00
high Δm , $N_b = 2$, $M_T(b_{1,2}, p_T^{\text{miss}}) \geq 175 \text{ GeV}$, $N_t = 1$, $N_{\text{res}} = 0$, $N_W = 0$, $H_T < 1000$						
105	250–550	717	0.000±0.000	0.018	0.000	0.00±0.00
106	550–650	1	0.000±0.000	0.000	-nan	0.00±0.00
107	≥ 650	1	0.000±0.000	0.000	-nan	0.00±0.00
high Δm , $N_b = 2$, $M_T(b_{1,2}, p_T^{\text{miss}}) \geq 175 \text{ GeV}$, $N_t = 1$, $N_{\text{res}} = 0$, $N_W = 0$, $1000 \leq H_T < 1500$						
108	250–550	420	0.000±0.000	0.018	0.000	0.00±0.00
109	550–650	8	0.000±0.000	0.000	-nan	0.00±0.00
110	≥ 650	2	0.000±0.000	0.000	-nan	0.00±0.00
high Δm , $N_b = 2$, $M_T(b_{1,2}, p_T^{\text{miss}}) \geq 175 \text{ GeV}$, $N_t = 1$, $N_{\text{res}} = 0$, $N_W = 0$, $H_T \geq 1500$						
111	250–550	220	0.005±0.004	0.044	0.118	1.13±0.91
112	550–650	12	0.000±0.000	0.000	-nan	0.00±0.00
113	≥ 650	13	0.000±0.000	0.004	0.000	0.00±0.00
high Δm , $N_b = 2$, $M_T(b_{1,2}, p_T^{\text{miss}}) \geq 175 \text{ GeV}$, $N_t = 0$, $N_{\text{res}} = 0$, $N_W = 1$, $H_T < 1300$						
114	250–350	811	0.000±0.000	0.021	0.000	0.00±0.00
115	350–450	163	0.000±0.000	0.001	0.000	0.00±0.00
116	≥ 450	43	0.000±0.000	0.000	-nan	0.00±0.00
high Δm , $N_b = 2$, $M_T(b_{1,2}, p_T^{\text{miss}}) \geq 175 \text{ GeV}$, $N_t = 0$, $N_{\text{res}} = 0$, $N_W = 1$, $H_T \geq 1300$						
117	250–350	205	0.002±0.002	0.046	0.048	0.46±0.46
118	350–450	93	0.000±0.000	0.043	0.000	0.00±0.00
119	≥ 450	78	0.000±0.000	0.003	0.000	0.00±0.00
high Δm , $N_b = 2$, $M_T(b_{1,2}, p_T^{\text{miss}}) \geq 175 \text{ GeV}$, $N_t = 0$, $N_{\text{res}} = 1$, $N_W = 0$, $H_T < 1000$						
120	250–350	589	0.002±0.001	0.023	0.065	0.90±0.66
121	350–450	110	0.000±0.000	0.000	-nan	0.00±0.00
122	450–550	18	0.000±0.000	0.000	-nan	0.00±0.00
123	550–650	1	0.000±0.000	0.000	-nan	0.00±0.00
124	≥ 650	1	0.000±0.000	0.000	-nan	0.00±0.00
high Δm , $N_b = 2$, $M_T(b_{1,2}, p_T^{\text{miss}}) \geq 175 \text{ GeV}$, $N_t = 0$, $N_{\text{res}} = 1$, $N_W = 0$, $H_T \geq 1500$						
125	250–350	296	0.004±0.003	0.023	0.155	1.05±0.79
126	350–450	91	0.005±0.005	0.013	0.386	0.45±0.46
127	450–550	33	0.000±0.000	0.000	-nan	0.00±0.00
128	550–650	8	0.000±0.000	0.000	-nan	0.00±0.00
129	≥ 650	2	0.000±0.000	0.000	-nan	0.00±0.00
high Δm , $N_b = 2$, $M_T(b_{1,2}, p_T^{\text{miss}}) \geq 175 \text{ GeV}$, $N_t = 0$, $N_{\text{res}} = 1$, $N_W = 0$, $H_T \geq 1500$						
130	250–350	131	0.003±0.002	0.052	0.061	0.42±0.31
131	350–450	55	0.000±0.000	0.045	0.000	0.00±0.00
132	450–550	34	0.000±0.000	0.005	0.000	0.00±0.00
133	550–650	12	0.000±0.000	0.000	-nan	0.00±0.00
134	≥ 650	13	0.000±0.000	0.004	0.000	0.00±0.00

Table 6.11 : The LL estimate in the various high Δm search regions, bins 94 to 134, using the 136.7 fb^{-1} dataset.

Search Region	p_T^{miss} [GeV]	$N_{\text{data}}(1)$	TF_{QCD}	$TF_{QCD}^{\text{CR-SR}}$	$TF_{QCD}^{\text{SR-extrap}}$	$N_{\text{pred}}^{\text{LL}}$
high Δm , $N_b = 2$, $M_T(b_{1,2}, p_T^{\text{miss}}) \geq 175$ GeV, $N_t = 1$, $N_{\text{res}} = 0$, $N_W = 1$						
135	250–550	1357	0.000±0.000	0.022	0.000	0.00±0.00
136	≥ 550	36	0.000±0.000	0.001	0.000	0.00±0.00
high Δm , $N_b = 2$, $M_T(b_{1,2}, p_T^{\text{miss}}) \geq 175$ GeV, $N_t = 1$, $N_{\text{res}} = 1$, $N_W = 0$, $H_T < 1300$						
137	250–350	811	0.000±0.000	0.021	0.000	0.00±0.00
138	350–450	163	0.000±0.000	0.001	0.000	0.00±0.00
139	≥ 450	43	0.000±0.000	0.000	-nan	0.00±0.00
high Δm , $N_b = 2$, $M_T(b_{1,2}, p_T^{\text{miss}}) \geq 175$ GeV, $N_t = 1$, $N_{\text{res}} = 1$, $N_W = 0$, $H_T \geq 1300$						
140	250–350	205	0.000±0.000	0.046	0.000	0.00±0.00
141	350–450	93	0.000±0.000	0.043	0.000	0.00±0.00
142	≥ 450	78	0.000±0.000	0.003	0.000	0.00±0.00
high Δm , $N_b = 2$, $M_T(b_{1,2}, p_T^{\text{miss}}) \geq 175$ GeV, $N_t = 0$, $N_{\text{res}} = 1$, $N_W = 1$						
143	250–550	1357	0.000±0.000	0.022	0.000	0.00±0.00
144	≥ 550	36	0.000±0.000	0.001	0.000	0.00±0.00
high Δm , $N_b = 2$, $M_T(b_{1,2}, p_T^{\text{miss}}) \geq 175$ GeV, $N_t = 2$, $N_{\text{res}} = 0$, $N_W = 0$						
145	250–450	1272	0.000±0.000	0.024	0.000	0.00±0.00
146	≥ 450	121	0.000±0.000	0.002	0.000	0.00±0.00
high Δm , $N_b = 2$, $M_T(b_{1,2}, p_T^{\text{miss}}) \geq 175$ GeV, $N_t = 0$, $N_{\text{res}} = 0$, $N_W = 2$						
147	≥ 250	1393	0.000±0.000	0.021	0.000	0.00±0.00
high Δm , $N_b = 2$, $M_T(b_{1,2}, p_T^{\text{miss}}) \geq 175$ GeV, $N_t = 0$, $N_{\text{res}} = 2$, $N_W = 0$, $H_T < 1300$						
148	250–450	974	0.000±0.000	0.017	0.000	0.00±0.00
149	≥ 450	43	0.000±0.000	0.000	-nan	0.00±0.00
high Δm , $N_b = 2$, $M_T(b_{1,2}, p_T^{\text{miss}}) \geq 175$ GeV, $N_t = 0$, $N_{\text{res}} = 2$, $N_W = 0$, $H_T \geq 1300$						
150	250–450	298	0.000±0.000	0.045	0.000	0.00±0.00
151	≥ 450	78	0.000±0.000	0.003	0.000	0.00±0.00
high Δm , $N_b = 2$, $M_T(b_{1,2}, p_T^{\text{miss}}) \geq 175$ GeV, $(N_t + N_{\text{res}} + N_W) \geq 3$						
152	≥ 250	1393	0.000±0.000	0.021	0.000	0.00±0.00
high Δm , $N_b \geq 3$, $M_T(b_{1,2}, p_T^{\text{miss}}) \geq 175$ GeV, $N_t = 1$, $N_{\text{res}} = 0$, $N_W = 0$, $H_T < 1000$						
153	250–350	142	0.000±0.000	0.035	0.000	0.00±0.00
154	350–550	23	0.000±0.000	0.000	-nan	0.00±0.00
155	≥ 550	1	0.000±0.000	0.000	-nan	0.00±0.00
high Δm , $N_b \geq 3$, $M_T(b_{1,2}, p_T^{\text{miss}}) \geq 175$ GeV, $N_t = 1$, $N_{\text{res}} = 0$, $N_W = 0$, $1000 \leq H_T < 1500$						
156	250–350	85	0.000±0.000	0.000	-nan	0.00±0.00
157	350–550	23	0.000±0.000	0.000	-nan	0.00±0.00
158	≥ 550	2	0.000±0.000	0.000	-nan	0.00±0.00
high Δm , $N_b \geq 3$, $M_T(b_{1,2}, p_T^{\text{miss}}) \geq 175$ GeV, $N_t = 0$, $N_{\text{res}} = 0$, $N_W = 1$						
159	250–350	43	0.000±0.000	0.049	0.000	0.00±0.00
160	350–550	25	0.000±0.000	0.000	-nan	0.00±0.00
161	≥ 550	11	0.000±0.000	0.000	-nan	0.00±0.00
high Δm , $N_b \geq 3$, $M_T(b_{1,2}, p_T^{\text{miss}}) \geq 175$ GeV, $N_t = 0$, $N_{\text{res}} = 0$, $N_W = 1$						
162	250–350	270	0.000±0.000	0.024	0.000	0.00±0.00
163	350–550	71	0.000±0.000	0.000	-nan	0.00±0.00
164	≥ 550	14	0.000±0.000	0.000	-nan	0.00±0.00
high Δm , $N_b \geq 3$, $M_T(b_{1,2}, p_T^{\text{miss}}) \geq 175$ GeV, $N_t = 0$, $N_{\text{res}} = 1$, $N_W = 0$, $H_T < 1000$						
165	250–350	142	0.000±0.000	0.035	0.000	0.00±0.00
166	350–550	23	0.000±0.000	0.000	-nan	0.00±0.00
167	≥ 550	1	0.000±0.000	0.000	-nan	0.00±0.00
high Δm , $N_b \geq 3$, $M_T(b_{1,2}, p_T^{\text{miss}}) \geq 175$ GeV, $N_t = 0$, $N_{\text{res}} = 1$, $N_W = 0$, $1000 \leq H_T < 1500$						
168	250–350	85	0.000±0.000	0.000	-nan	0.00±0.00
169	350–550	23	0.000±0.000	0.000	-nan	0.00±0.00
170	≥ 550	2	0.000±0.000	0.000	-nan	0.00±0.00
high Δm , $N_b \geq 3$, $M_T(b_{1,2}, p_T^{\text{miss}}) \geq 175$ GeV, $N_t = 0$, $N_{\text{res}} = 1$, $N_W = 0$, $H_T \geq 1500$						
171	250–350	43	0.000±0.000	0.049	0.000	0.00±0.00
172	350–550	25	0.000±0.000	0.000	-nan	0.00±0.00
173	≥ 550	11	0.000±0.000	0.000	-nan	0.00±0.00
high Δm , $N_b \geq 3$, $M_T(b_{1,2}, p_T^{\text{miss}}) \geq 175$ GeV, $N_t = 1$, $N_{\text{res}} = 0$, $N_W = 1$						
174	≥ 250	355	0.000±0.000	0.018	0.000	0.00±0.00
high Δm , $N_b \geq 3$, $M_T(b_{1,2}, p_T^{\text{miss}}) \geq 175$ GeV, $N_t = 1$, $N_{\text{res}} = 1$, $N_W = 0$						
175	250–350	270	0.000±0.000	0.024	0.000	0.00±0.00
176	≥ 350	85	0.000±0.000	0.000	-nan	0.00±0.00
high Δm , $N_b \geq 3$, $M_T(b_{1,2}, p_T^{\text{miss}}) \geq 175$ GeV, $N_t = 0$, $N_{\text{res}} = 1$, $N_W = 1$						
177	≥ 250	355	0.000±0.000	0.018	0.000	0.00±0.00
high Δm , $N_b \geq 3$, $M_T(b_{1,2}, p_T^{\text{miss}}) \geq 175$ GeV, $N_t = 2$, $N_{\text{res}} = 0$, $N_W = 0$						
178	≥ 250	355	0.000±0.000	0.018	0.000	0.00±0.00
high Δm , $N_b \geq 3$, $M_T(b_{1,2}, p_T^{\text{miss}}) \geq 175$ GeV, $N_t = 0$, $N_{\text{res}} = 0$, $N_W = 2$						
179	≥ 250	355	0.000±0.000	0.018	0.000	0.00±0.00
high Δm , $N_b \geq 3$, $M_T(b_{1,2}, p_T^{\text{miss}}) \geq 175$ GeV, $N_t = 0$, $N_{\text{res}} = 2$, $N_W = 0$						
180	250–350	270	0.000±0.000	0.024	0.000	0.00±0.00
181	≥ 350	85	0.000±0.000	0.000	-nan	0.00±0.00
high Δm , $N_b \geq 3$, $M_T(b_{1,2}, p_T^{\text{miss}}) \geq 175$ GeV, $(N_t + N_{\text{res}} + N_W) \geq 3$						
182	≥ 250	355	0.000±0.000	0.018	0.000	0.00±0.00

Table 6.12 : The LL estimate in the various high Δm search regions, bins 135 to 182, using the 136.7 fb^{-1} dataset.

6.6 Rare Interactions

The contributions of diboson, WW, WZ, and ZZ, processes are relatively small compared to the other backgrounds, but they mainly affect the search regions targeting low Δm signal models. The contribution of the $t\bar{t}Z$ background is also generally very small due to the two vertex factor suppression of the leading-order process, see Fig. 6.34. Although, in search regions that require the presence of more than one top- or W-tagged candidate, this process can be a significant fraction of the total SM background due to the suppression of the other SM processes. We define a three-lepton control sample which requires the presence of exactly three electrons or muons satisfying $p_T > 40$ GeV for the leading lepton, $p_T > 20$ GeV for the second and third leptons, and no additional lepton with $p_T > 10$ GeV with an additional requirement of at least five jets, at least two of which are b-tagged.

A Z boson mass window of 81 to 101 GeV is placed on the invariant mass of the same-flavor dilepton p_T of the lepton pair is further required to be at least 100 GeV, in order to probe a kinematic region close to the one relevant for the analysis. In order to check the extrapolation from the lower Z - p_T region of this control sample to the search sample, we evaluate the $t\bar{t}Z$ scale factor in bins of reconstructed Z boson

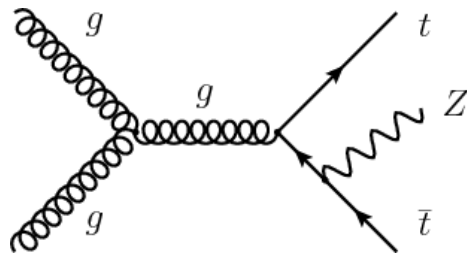


Figure 6.34 : The first order Feynman diagrams that are responsible for the main rare background.

p_T as far as statistics permit. The p_T -binned scale factors are found to be consistent with the inclusive scale factor evaluated for $p_T(Z) > 100$ GeV. Figure 6.35 shows the comparison between 2016, 2017, and 2018 in the muon control region. Since there is relatively good agreement between the eras we can indeed combine them into a single estimation. The final estimation is included in the datacards in Sec. 7.5

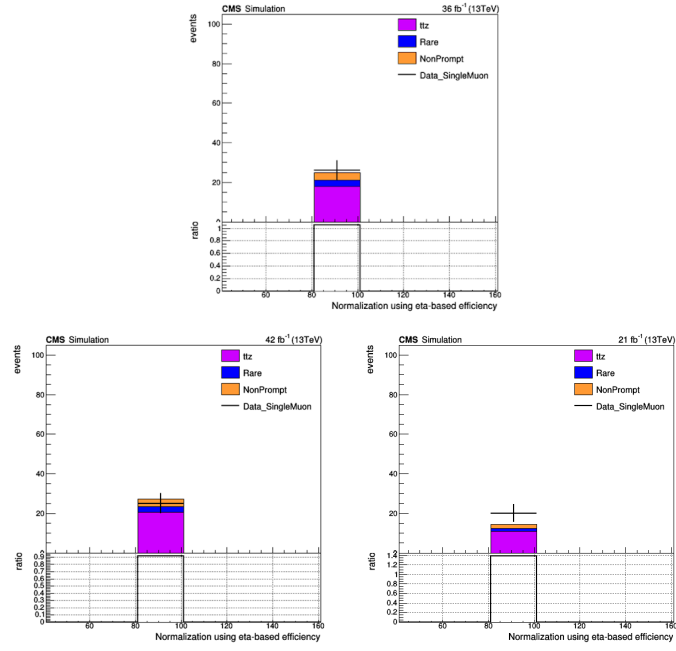


Figure 6.35 : The ttZ normalization comparisons for each era in the electron and muon control region for different regions in the low Δm , $N_b = 0, = 1, \geq 2$, $N_{SV} = 0, \geq 1$.

Chapter 7

Uncertainties and Estimation

We now have a robust method for the prediction of SM background for our search for the top squark. Along with a prediction for each of the backgrounds, we need to include the systematic uncertainties for our methods. Once we incorporate them we can confirm that our methods are correct by looking at the validation regions. Finally, we can then compare the final comparisons of data to simulation in our SR, which will allow us to set limits on the top squark mass.

7.1 Systematic Uncertainties

We will look at the various categories of systematic uncertainties that can affect the analysis.

- **Statistical uncertainty of control regions in data:** The dominant uncertainty in data-driven background prediction methods is generally the result of limited statistics of the control regions that are used to derive the background estimate for the signal regions.
- **Statistical uncertainty of simulated samples:** In some cases, the uncertainties on transfer factors derived from simulation also have a significant statistical component due to limited statistics in the simulated samples.
- **Uncertainties related to extrapolation from control to signal regions:**

Each data-driven background estimation method relies on an extrapolation from a control region to the signal region. This leads to uncertainties specific to each method, related to the nature of the extrapolation. For instance, the LL prediction strategy uses the region with a selected lepton to estimate the background yield in the vetoes region. Appropriate correction factors are applied to both selected and vetoes regions to account for differences in the lepton selection efficiency between data and simulation. The precision of these corrections affects the uncertainty in the background estimation. For the QCD prediction, we rely on an extrapolation from the low $\Delta\phi_{12}$ region, which is mostly in the core of the jet response distribution, to a region of high values of $\Delta\phi_{12}$, which is mostly in the tail of the distribution. We therefore assign an uncertainty in the QCD prediction for the potential effects of severe jet mis-measurements in the jet response tails.

- **Uncertainties related to b -tagging:** Effects related to the b -tagging are estimated to impact the scale factors up to 3% for top-jets and between 5 to 10% for $W+jets$. Uncertainties due to the top- p_T reweighting, pile-up, or matching criteria results effect smaller than 3% for both top and W tags.
- **Uncertainties related to soft b -tagging:** The soft b -tagging methods are dependent on low- p_T jets and track reconstruction. The impact of these uncertainties are negligible for $t\bar{t}$ and $W+jets$ and around 5% for QCD events.
- **Uncertainties related to the merged top and W -tagging:** The impact of different effects on the determination of the scale factors are studied. One of the dominant sources is related to the description of the parton showering which results in uncertainties of 5 to 25% and 8 to 15%, for top and W tagging,

respectively. Another source of systematics is due to the modeling of the $t\bar{t}$ topology. The evaluated uncertainties range between 1 to 3% (1 to 12%) in top (W) tagging.

- **Uncertainties related to the Resolved Top Tagging:** A similar list of the sources of systematic uncertainties is evaluated for the resolved tagger, as in the case of Merged tops. The most important sources stems from the description of the parton showering, which ranges between 8 to 31%. The modeling of the $t\bar{t}$ topology can be as high as 4%, whereas potential dependence on the b -tagging results to uncertainties from 1 to 6%. Uncertainties due to the top- p_T reweighting, pile-up, or matching criteria results to effect smaller than 3%.
- **Uncertainties related to lepton identification:** The control region of the LL is defined as having a single muon or electron. We must account for the acceptance and scale factor corrections for each particle. The impact is an approx. 1% and <1% uncertainty for electrons and muons, respectively. It is also necessary to account for the misidentification of leptons (electrons, muons, and taus) that can contaminate our search region.

$$SF_l = 1 + \frac{N_l^{yield} - N_l^{SF}}{N_{SR}} \quad (7.1)$$

This is shown in Eqn. 7.1 where N_l^{yield} and N_l^{SF} are the yield of simulation in the search region with a requirement of $N_l \geq 1$ with and without the lepton scale factor and N_{SR} is the yield in the search region with the lepton veto.

Table 7.1 : Summary of the 19 disjoint validation regions that mainly target low Δm signal models. The low Δm baseline selection is again $N_j \geq 2$, $p_T^{miss} > 250$ GeV, $N_t = N_W = N_{res} = 0$, $N_b \geq 0$, $M_T(b_{1,2}, p_T^{miss}) < 175$ GeV (when applicable), $p_T(ISR) > 200$ GeV, $|\eta(ISR)| < 2.4$, $|\Delta\phi(j_{ISR}, p_T^{miss})| > 2$, and $S_{p_T^{miss}} > 10$.

N_j	N_b	N_{SV}	$p_T(ISR)$ [GeV]	$p_T(b)$ [GeV]	p_T^{miss} [GeV]
$ \Delta\phi(j_1, p_T^{miss}) \geq 0.5, \Delta\phi(j_{2,3}, p_T^{miss}) \geq 0.15$					
2 – 5	0	0	≥ 500	-	250 – 400
≥ 6		0			250 – 400
2 – 5		≥ 1			250 – 400
≥ 6		≥ 1			250 – 400
≥ 2	1	0	300 – 500	20 – 40	250 – 300
		0	300 – 500	40 – 70	250 – 300
		0	≥ 500	20 – 40	250 – 400
		0	≥ 500	40 – 70	250 – 400
		≥ 1	≥ 300	20 – 40	250 – 300
≥ 2	≥ 2	≥ 0	300 – 500	40 – 80	250 – 300
			300 – 500	80 – 140	250 – 300
			300 – 500	≥ 140	250 – 300
			≥ 500	40 – 80	250 – 400
			≥ 500	80 – 140	250 – 400
			≥ 300	≥ 140	250 – 400
$0.15 \leq \Delta\phi(j_1, p_T^{miss}) \leq 0.5, \Delta\phi(j_{2,3}, p_T^{miss}) \geq 0.15$					
≥ 2	0	0	≥ 200	≥ 20	≥ 250
≥ 2	0	1	≥ 200	≥ 20	≥ 250
≥ 2	1	0	≥ 200	≥ 20	≥ 250
≥ 2	1	1	≥ 200	≥ 20	≥ 250

7.2 Validation

In order to test and validate the background estimation strategy in data, we carry out the background estimation method in a lower p_T^{miss} region of the zero-lepton sample that is adjacent to the search sample, "low p_T^{miss} validation sample", and check the agreement between data and background prediction. The validation sample has sig-

Table 7.2 : Summary of the 25 disjoint validation regions that mainly target high Δm signal models. The high Δm baseline selection is again $N_j \geq 5$, $p_T^{miss} > 250\text{ GeV}$, $N_b \geq 1$, and $|\Delta\phi(j_1, p_T^{miss})| \geq 0.5$, $|\Delta\phi(j_{2,3}, p_T^{miss})| \geq 0.15$ and $\neg\Delta\phi_{1234} < 0.5$.

$M_T(b_{1,2}, p_T^{miss}) < 175\text{ GeV}$					
N_j	N_b	N_t	N_W	N_{res}	$p_T^{miss} [\text{GeV}]$
≥ 7	$1, \geq 2$	≥ 0	≥ 0	≥ 1	$250 - 400, \geq 400$
$M_T(b_{1,2}, p_T^{miss}) \geq 175\text{ GeV}$					
N_j	N_b	N_t	N_W	N_{res}	$p_T^{miss} [\text{GeV}]$
≥ 5	$1, \geq 2$	0	0	0	$250 - 400, \geq 400$
≥ 5	1	1	0	0	$250 - 400, \geq 400$
		0	1	0	$250 - 400, \geq 400$
		0	0	1	$250 - 400, \geq 400$
		$N_t + N_W + N_{\text{res}} \geq 3$			≥ 400
≥ 5	2	1	0	0	$250 - 400, \geq 400$
		0	1	0	$250 - 400, \geq 400$
		0	0	1	$250 - 400, \geq 400$
		$N_t + N_W + N_{\text{res}} \geq 3$			≥ 400

nificantly larger statistics than the search sample and is signal-depleted. Apart from the difference in the p_T^{miss} selection, the search selection on the other search variables is applied to the validation sample, with an exception of the regions with more than one top- or W-tags, where relaxed selections (i.e. drop selection in $M_T(b_{1,2}, p_T^{miss})$) are applied to gain more statistics, see Tables 7.2 and 7.1. Figures 7.1 and 7.2 displays the SM estimate and the observed data in the different validation regions. Statistical uncertainties, as well as systematic uncertainties resulting from the top- and W-tagging correction in the background predictions are shown in this plot. The data agrees well with the estimated background yields within uncertainties. Now that we have shown that the bins for the low and high Δm match well with data we can move to a full comparison of the data and simulation in the SR. To do this we combine

the predictions from the LL, $Z \rightarrow \nu\nu$, QCD, and Rare backgrounds.

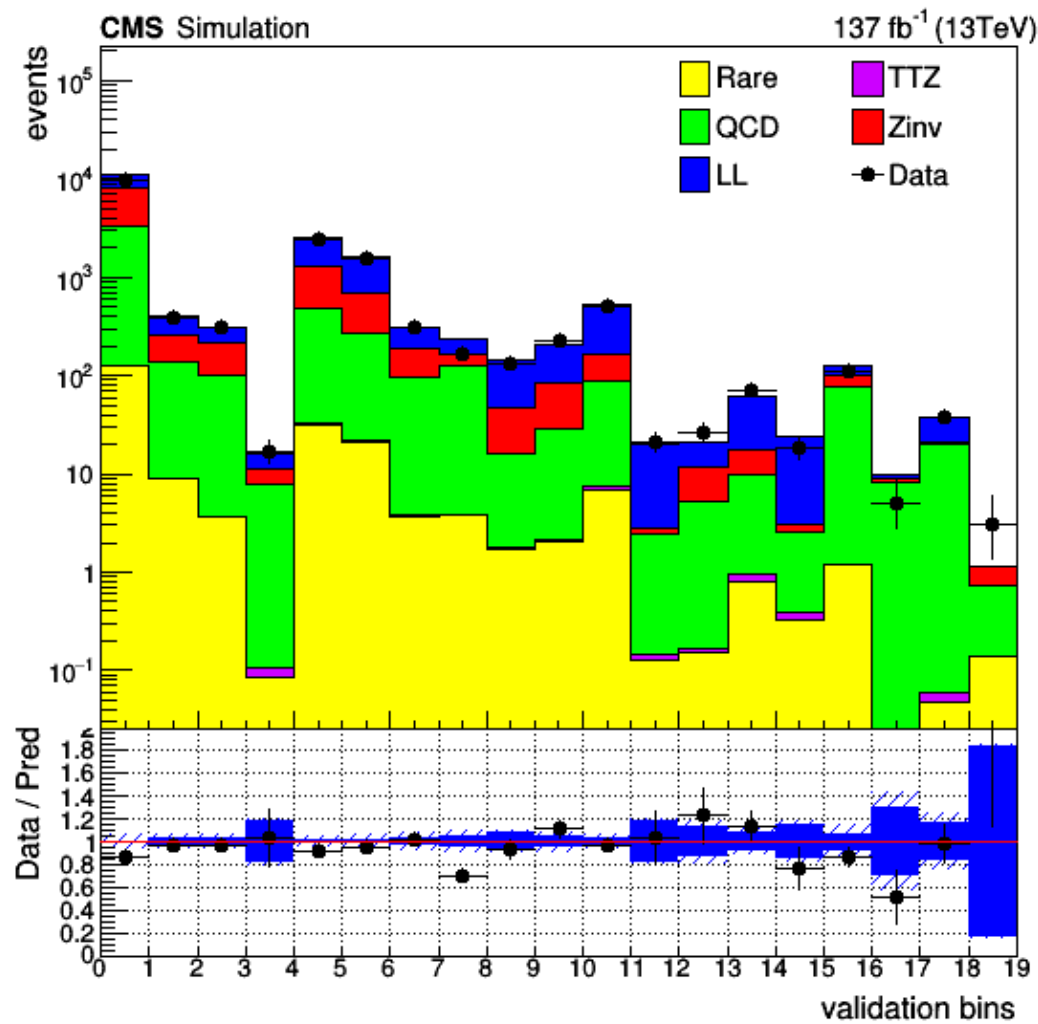


Figure 7.1 : Comparison of the data and SM backgrounds in the Low Δm validation regions. The uncertainty on the data is a Poisson statistical uncertainty, while simulation is split between a weighted statistical and a systematic uncertainty.

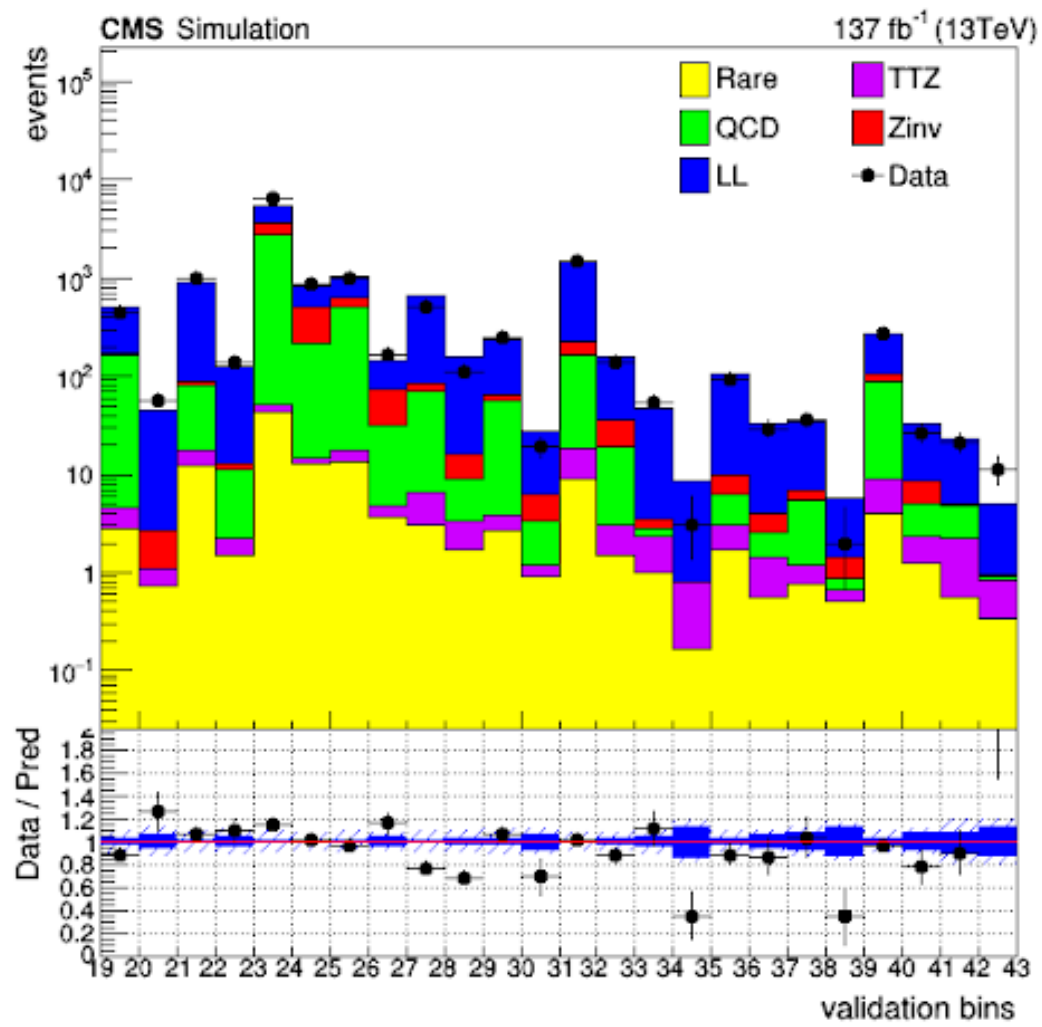


Figure 7.2 : Comparison of the data and SM backgrounds in the High Δm validation regions. The uncertainty on the data is a Poisson statistical uncertainty, while simulation is split between a weighted statistical and a systematic uncertainty.

7.3 Statistics

For the combination of multiple analyses that are sensitive to different signal production mechanisms and different decay modes, we are required to set limits on a common signal strength modifier μ that is used to alter the cross sections of all the production mechanisms. It is conventional to require a 95% confidence level (CL) to exclude a signal. The interpretation of the CL, however, is quite complicated. We use a modified classical frequentist method such that we can include systematic uncertainties in the results. The method for constructing a unified confidence interval is based on the likelihood-ratio test statistic [97],

$$q_\mu = -2\ln \frac{\mathcal{L}(\text{data}|\mu s + b)}{\mathcal{L}(\text{data}|\hat{\mu}s + b)}, \quad (7.2)$$

where $\hat{\mu}$ is used to maximize the likelihood $\mathcal{L}(\text{data}|\mu s + b)$, and s and b are the signal and background, respectively. In order to add systematics on the signal and background rates, $s(\theta)$ and $b(\theta)$, we include a prior pdf for the nuisance θ as $\rho(\theta|\tilde{\theta})$ where $\tilde{\theta}$ is the nominal value of the nuisance parameter. We interpret the systematic uncertainty as posteriors of the measurements.

7.3.1 Profile Likelihood Asymptotic Approximation

The profile likelihood ratio is shown in Eqn. 7.2 with the addition of the constraint $0 \leq \hat{\mu} \leq \mu$ which ensures that the obtained limits are one-sided. Additionally, this can be approximated by an asymptotic formula which is based on the Wilks and Wald theorems [98]. Since we include the physical constraint $\hat{\mu} > 0$, the asymptotic features of $f(\tilde{q}_\mu|\text{signal+background})$, where f is the probability density function

(*pdf*) of q_μ assuming the hypothesis μ , is provided by the well defined formula [98],

$$f(\tilde{q}_\mu|\mu) = \frac{1}{2}\delta(\tilde{q}_\mu) + \begin{cases} \frac{1}{2}\frac{1}{\sqrt{2\pi}}\frac{1}{\sqrt{\tilde{q}_\mu}}e^{-\tilde{q}_\mu/2} & 0 < \tilde{q}_\mu \leq \mu^2/\sigma^2 \\ \frac{1}{\sqrt{2\pi}(2\mu/\sigma)}\exp[-\frac{1}{2}\frac{(\tilde{q}_\mu + \mu^2/\sigma^2)^2}{(2\mu/\sigma)^2}] & \tilde{q}_\mu > \mu^2/\sigma^2 \end{cases}, \quad (7.3)$$

where $\sigma^2 = \frac{\mu^2}{q_{\mu,A}}$ with $q_{\mu,A}$ is evaluated with the expected background and nominal nuisance parameters.

7.4 Higgs Combined Tool

The Higgs Combined Tool [99] uses a modified frequentist method to compute the CL [100–102] for each of the cross section limits. The tool is able to convert the datacards into a Likelihood function to calculate the limits. The Likelihood function is [99]:

$$\mathcal{L}(\mu, \theta) = \prod_i \frac{[\mu \cdot s_i(\theta) + b_i(\theta)]^{n_i}}{n_i!} e^{-[\mu \cdot s_i(\theta) + b_i(\theta)]} \prod_\kappa e^{-\frac{1}{2}\theta_\kappa^2}, \quad (7.4)$$

where μ is the POI which is constrained only by the observed data; $s_i(\theta)$ and $b_i(\theta)$ are nuisance parameters for signal and background. Both the signal and background are subject to multiple uncertainties that are dealt with by using nuisance parameters, θ . Each of these three parameters are jointly fitted to get a value of μ . Systematic uncertainties are accounted for by using nuisance parameters θ that have a *pdf*, $\rho(\theta)$, with a $\tilde{\theta}$ that is associated with the nuisance parameter. We use a log-normal [99] *pdf*,

$$\rho(\theta) = \frac{1}{\sqrt{2\pi}\ln(\kappa)} \exp\left(-\frac{(\ln(\theta/\tilde{\theta}))^2}{2(\ln\kappa)^2}\right) \frac{1}{\tilde{\theta}}, \quad (7.5)$$

where the width is adjusted by the parameter κ . We will be using an asymptotic CL method to compute the limits for this analysis.

7.4.1 Observed Limits

To compute the observed limit the likelihood function, $\mathcal{L}(\mu, \theta)$ from Eqn. 7.4. Comparing the compatibility of the data with the background-only and signal+background hypotheses to get

$$\tilde{q}_\mu = -2\ln \frac{\mathcal{L}(\mu, \hat{\theta}_\mu)}{\mathcal{L}(\mu, \theta)}, \quad (7.6)$$

with a constraint $0 \leq \hat{\mu} \leq \mu$ where $\hat{\theta}_\mu$ is the conditional maximum likelihood estimators of θ given the signal strength μ and data, and the estimators $\hat{\mu}$ and $\hat{\theta}$ are the global maximum of the likelihood.

From this, we get the observed value of \tilde{q}_μ^{obs} for a given value of μ . A toy Monte Carlo pseudo-data is used to construct the PDFs $f(\tilde{q}_\mu | \mu, \hat{\theta}_\mu^{obs})$ and $f(\tilde{q}_\mu | 0, \hat{\theta}_0^{obs})$ where we have a signal with strength μ in the signal+background and a background-only hypothesis. Two p -values are defined and associated with the two hypotheses, p_μ and p_b ,

$$p_\mu = P(\tilde{q}_\mu \geq \tilde{q}_\mu^{obs} | \text{signal+background}) = \int_{\tilde{q}_\mu^{obs}}^{\infty} f(\tilde{q}_\mu | \mu, \hat{\theta}_\mu^{obs}) d\tilde{q}_\mu, \quad (7.7)$$

we then have

$$1 - p_b = P(\tilde{q}_\mu \geq \tilde{q}_\mu^{obs} | \text{background-only}) = \int_{\tilde{q}_\mu^{obs}}^{\infty} f(\tilde{q}_\mu | 0, \hat{\theta}_0^{obs}) d\tilde{q}_\mu, \quad (7.8)$$

using both of these we can calculate the $CL_s(\mu)$ as

$$CL_s(\mu) = \frac{p_\mu}{1 - p_b}. \quad (7.9)$$

Finally, to quote a 95% confidence level on the upper limit on μ , μ is adjusted until the $CL_s = 0.05$ such that the confidence level is $(1 - \alpha)$ where $CL_s \leq \alpha$.

7.4.2 Expected Limits

Along with the observed limits we are also interested in calculating the expected median upper-limit, $\pm 1\sigma$, and $\pm 2\sigma$ bands for the background-only hypothesis. To do this we generate a large set of background-only pseudo-data, using the toy Monte Carlo method, and calculate the CL_s as if it was real data. The calculation for the expected limit is done by finding the cumulative probability distribution function (CDF) of results and starting the integration. The point at which the CDF crosses the 50% band is the median expected value. Then the $\pm 1\sigma$ band is defined by the 16% and 84% band and the $\pm 2\sigma$ band is the 2.5% and 97.5% crossings.

7.5 Combination of Search region

As we have seen, this analysis has quite a large parameter space of interesting mass points. This combined with the number of SR bins and different backgrounds in each bin it is necessary to discuss how we plan on combining all of this to get a final estimation. To do this we use a datacard to input the combination and uncertainty calculation for our counting experiment. In Figure 7.3, we have an example of a single bin from our SR, specifically bin 61 (high Δm , $N_b = 1$, $M_T(b_{1,2}, p_T^{miss}) \geq 175$, $N_t = 0$, $N_{res} = 0$, $N_W = 0$, $H_T \geq 1000$, $250 \leq p_T^{miss} < 350$), for a single signal sample, T2tt(175, 1).

Lets go through Figure 7.3, so that we can understand what is going on. The parameter $imax$ is the number of final states analyzed in the datacard, $jmax$ is the number of independent physical processes whose yields are provided minus 1, and

```

# Datacard produced by CombineHarvester with git status: analysis-HIG-16-006-freeze-080416-794-g1f6819a-dirty

imax 1 number of bins
jmax 5 number of processes minus 1
kmax * number of nuisance parameters
----- shapes * bin_hm_nbl_highmbt_nt0_nrt0_nw0_htgt1000_MET_pt250to350 FAKE
bin bin_hm_nbl_highmbt_nt0_nrt0_nw0_htgt1000_MET_pt250to350
observation 1.0
----- bin_hm_nbl_highmbt_nt0_nrt0_nw0_htgt1000_MET_pt250to350 bin_hm_nbl_highmbt_nt0_nrt0_nw0_htgt1000_MET_pt250to350 bin_hm_nbl_highmbt_nt0_nrt0_nw0_htgt1000_MET_pt250to350 bin_hm_nbl_highmbt_nt0_nrt0_nw0_htgt1000_MET_pt250to350
process signal ttbarplusw znuunu qcd ttz diboson
process 0 1 3 4 5
rate 1.08043 1 1 1 1.83807 3.3886
----- ISR_Weight lnN 0.745155/1.14943 1.01244/0.992847 - 1/1 - - 1.07181 1.04201
JER_Unc lnN 0.873191/1.07101 1.00457/0.997025 - - - - -
PU_Weight lnN 0.984793/1.01681 0.999705/1.00029 - 0.950468/1.04971 1.0014 1.0119
PDF_Weight lnN 0.996635/1.00364 0.999747/1.00026 - 1.00009/0.999946 1.00499 1.00224
Prefire_Weight lnN 0.999904/1.0001 - - - - -
Scale_Unc lnN 0.9990074/1.00747 0.988665/1.01087 - 0.991942/1.00698 1.01376 1.04719
b lnN 0.970164/1.02984 1.05489/1.047292 - 0.999131/1.00085 - -
eff_e lnN 1/1 - - - - -
eff_stop lnN 0.995999/1.0034 1.03245/0.99696 - 1.00918/0.99999 - -
eff_lnu lnN 1/1 1.01367/0.98692 - 1.00253/0.997489 - -
eff_toptag lnN 1/1 1.00316/0.99662 - 1.00109/0.998917 - -
eff_wtag lnN 1/1 - - - - -
err_mu lnN 0.998482/1.00152 1.00319/0.99616 - 0.999946/1.00005 - -
ivfunc lnN 0.996378/1.00362 1.00022/0.99978 - - - -
ivfunc_err lnN - - - - 0.999446/1.00053 - -
metstats_diboson_bin_hm_nbl_highmbt_nt0_nrt0_nw0_htgt1000_MET_pt250to350 lnN - - - - - -
metstats_gglnu_bin_hm_nbl_highmbt_nt0_nrt0_nw0_htgt1000_MET_pt250to350 lnN - - - - - -
metstats_signal_bin_hm_nbl_highmbt_nt0_nrt0_nw0_htgt1000_MET_pt250to350 lnN 1.19358 - - - -
metstats_ttZ_bin_hm_nbl_highmbt_nt0_nrt0_nw0_htgt1000_MET_pt250to350 lnN - - - - 1.07155 -
metstats_ttbarplusw_bin_hm_nbl_highmbt_nt0_nrt0_nw0_htgt1000_MET_pt250to350 lnN - - - - - -
metstats_znuunu_bin_hm_nbl_highmbt_nt0_nrt0_nw0_htgt1000_MET_pt250to350 lnN - - - - - -
metres lnN 0.988686/1.04068 0.996265/1.00374 - - - -
trigger_eff lnN 0.998148/1.00117 1.00001/0.999935 - 0.999796/1.00019 1.00179 1.00092
----- R_qm_bin_hm_nbl_highmbt_nt0_nrt0_nw0_htgt1000_MET_pt250to350 rateParam qcd $(0+0.303522*#1*14.16884+62*56_*790391)
R_qm_blin_qcdcr_hm_nbl_highmbt_nt130to1500_MET_pt250to350,R_blin_qcdcr_hm_nbl_highmbt_htgt1500_MET_pt250to350
R_ttbarplusw_hm_nbl_highmbt_nt0_nrt0_nw0_htgt1000_MET_pt250to350 rateParam ttbarplusw $(0+19.445933*#1+45.881732*#2+57.290734)
R_lllepcr_hm_nbl_highmbt_nt130to1500_MET_pt250to350,R_lllepcr_hm_nbl_highmbt_htgt1500_MET_pt250to350
R_znuunu_blin_hm_nbl_highmbt_nt0_nrt0_nw0_htgt1000_MET_pt250to350 rateParam znuunu $(0+42.208518*#1+12.512125*#2+15.727317)
R_llphocr_hm_nbl_highmbt_nt130to1300_MET_pt250to350,R_llphocr_hm_nbl_highmbt_htgt1500_MET_pt250to350

```

Figure 7.3 : An example of the datacard for a single bin of $T2tt(175, 1)$ with background and uncertainties.

$kmax$ is the number of independent systematic uncertainties. Here we put "*" and allow the computation to figure that out. Next, we have the number of observed events from data in this particular bin, shown as *observation*, where the bin above it is a unique name. Then, in the five lines following, we have the yields for the different processes included in this bin. The first process denoted as *signal* is the yield from T2tt(175, 1), then the other four processes are the SM backgrounds in this bin.

The next major portion of the datacard is the various systematics of the signal and background processes. The most common type of uncertainty is the log-normal which is denoted by $\ln N$, see Eqn. 7.5. For these, the distribution is described by the parameter κ , which is a multiplicative error. A $+1\sigma$ deviation corresponds to a yield scaled by κ while a -1σ scales the yields by $\frac{1}{\kappa}$. If the uncertainties are small

```
# Datacard produced by CombineHarvester with git status: analysis-HIG-16-006-freeze-080416-794-g1f6819a-dirty
imax    1 number of bins
jmax    1 number of processes minus 1
kmax    * number of nuisance parameters
-----
shapes * bin_lepcr_hm_nbl_highmtb_ht1000to1300_MET_pt250to350 FAKE
-----
bin      bin_lepcr_hm_nbl_highmtb_ht1000to1300_MET_pt250to350
observation 457.0
-----
bin_lepcr_hm_nbl_highmtb_ht1000to1300_MET_pt250to350
process          signal           ttbarplusw
process          0                 1
rate             98.9035        563.306
-----
mcstats_signal_bin_lepcr_hm_nbl_highmtb_ht1000to1300_MET_pt250to350 lnN   1.41043   -
mcstats_ttbarplusw_bin_lepcr_hm_nbl_highmtb_ht1000to1300_MET_pt250to350 lnN   -         1.01187
R_bin_lepcr_hm_nbl_highmtb_ht1000to1300_MET_pt250to350      rateParam *       ttbarplusw 1 [0.01,5]
```

Figure 7.4 : An example of the datacard for the LL CR with signal contamination.

```
# Datacard produced by CombineHarvester with git status: analysis-HIG-16-006-freeze-080416-794-g1f6819a-dirty
imax    1 number of bins
jmax    1 number of processes minus 1
kmax    * number of nuisance parameters
-----
shapes * bin_phocr_hm_nbl_highmtb_ht1000to1300_MET_pt250to350 FAKE
-----
bin      bin_phocr_hm_nbl_highmtb_ht1000to1300_MET_pt250to350
observation 82.0
-----
bin_phocr_hm_nbl_highmtb_ht1000to1300_MET_pt250to350
process          gjets           otherbkgs
process          1                 2
rate             61.0854        17.9363
-----
mcstats_gjets_bin_phocr_hm_nbl_highmtb_ht1000to1300_MET_pt250to350 lnN   1.04569   -
mcstats_otherbkgs_bin_phocr_hm_nbl_highmtb_ht1000to1300_MET_pt250to350 lnN   -         2
R_bin_phocr_hm_nbl_highmtb_ht1000to1300_MET_pt250to350      rateParam *       gjets     1 [0.01,5]
```

Figure 7.5 : An example of the datacard for the $Z \rightarrow \nu\nu$ CR with signal contamination.

```
# Datacard produced by CombineHarvester with git status: analysis-HIG-16-006-freeze-080416-794-g1f6819a-dirty
imax    1 number of bins
jmax    1 number of processes minus 1
kmax    * number of nuisance parameters
-----
shapes * bin_qcdcr_hm_nbl_highmtb_ht1000to1300_MET_pt250to350 FAKE
-----
bin      bin_qcdcr_hm_nbl_highmtb_ht1000to1300_MET_pt250to350
observation 2498.0
-----
bin_qcdcr_hm_nbl_highmtb_ht1000to1300_MET_pt250to350
process          qcd            otherbkgs
process          1               2
rate             1902.07        167.667
-----
mcstats_otherbkgs_bin_qcdcr_hm_nbl_highmtb_ht1000to1300_MET_pt250to350 lnN   -         2
mcstats_qcd_bin_qcdcr_hm_nbl_highmtb_ht1000to1300_MET_pt250to350    lnN   1.03535   -
R_bin_qcdcr_hm_nbl_highmtb_ht1000to1300_MET_pt250to350      rateParam *       qcd     1 [0.01,5]
```

Figure 7.6 : An example of the datacard for the QCD CR.

the log-normal error can be approximated by a gaussian and we can approximate $\kappa = 1 + \frac{\delta x}{x}$, where $\frac{\delta x}{x}$ is the relative uncertainty of the event yield. Each process has a value for the statistical uncertainty which is a poisson error of \sqrt{N} . Then each process can have a systematic error that may be correlated to other backgrounds. In each process, we can have a value for the uncertainty or a dash which means that the uncertainty does not contribute to the process.

Finally, at the bottom of the datacard we have the rate parameters for the backgrounds that require the extrapolation from units to SR bins. The units are a more basic definition of the SR bins that can be combined with the prediction of each background to give the total background in each SR bin. Since the LL, QCD, and $Z \rightarrow \nu\nu$ backgrounds use an extrapolation method for the high Δm bins, we have defined 112 CR units and 529 SR units. In the bottom of Fig. 7.3, are the expected rates for the LL, QCD, and $Z \rightarrow \nu\nu$ that show the combination of three units to give the prediction of each background in the respective bins. The rates from the LL and QCD background can be seen in Fig. 7.4, 7.5, and 7.6. These are an example of a single unit datacard. The calculation for each background from the unit CR is the data observation divided by the SM background in each, $\frac{N_{data}^{CR}}{(N_{LL}^{CR} + N_{Sg}^{CR})}$, where the LL CR is used as an example. Now to be able to make the estimation of the limit for the various SUSY processes that we are looking at, we need to combine the datacards for each SR bin for all of the signals in the mass parameter space. This can be easily accomplished thanks to the unique bin and process names for each signal. We can then input each of these combined datacards into the Higgs Combined Tool.

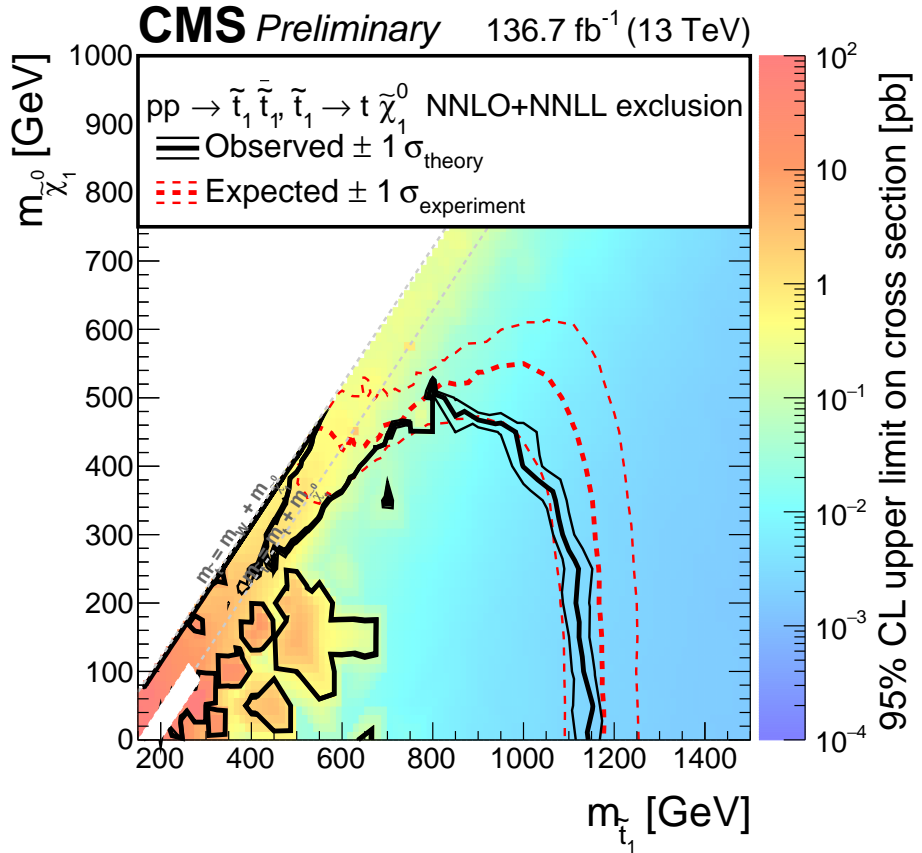


Figure 7.7 : Limits for the mass parameter space for $\tilde{t}_1 \rightarrow t \tilde{\chi}_1^0$ (T2tt) decays for Run 2 data. With a current limit approximately 1175 GeV for a minimal neutralino mass. The limit near the top mass corridor has been significantly improved.

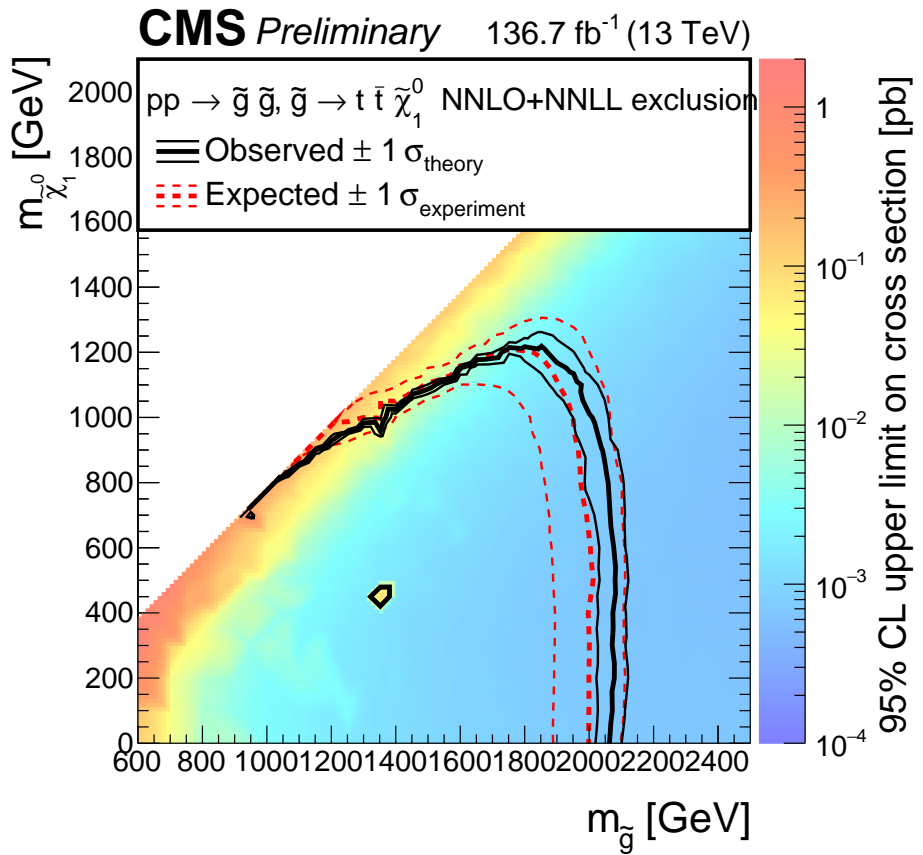


Figure 7.8 : Limits for the mass parameter space for $\tilde{g} \rightarrow t \bar{t} \tilde{\chi}_1^0$ (T2tt) decays for Run 2 data. With a current limit of 2.05 TeV for a minimal neutralino mass.

7.6 Results

After creating all of the datacards for each mass point we can calculate the expected and observed limits for the entire Run 2 analysis for each signal region, T2tt, T2bW, T2tb, T2fb, T2bWC, T1tttt, T1ttbb, T5ttcc, and T5tttt, see Sec. 6.1. In Figure 7.7 and 7.8, we have the expected limits for T2tt and T1tttt, respectively. The datacards are including the signal contamination in the lepton CR. The white covered area in the bottom left of Fig. 7.7, is an area defined in which the signal and background shapes are similar. Many parameters such as the Madgraph settings for extra partons are important for this region.

For the visible weakening of exclusion in the top corridor region when comparing Fig. 7.7 and 3.9. This could be due the limits were generally close to the theory cross section, σ_{theory} , in 2016 and the subtle cross section limit variation is more visible. Now the limits are improved in general and we may be insensitive to weakening of the limits for the exclusion contour. We can see that the expected limit has been improved to a $m_{\tilde{t}_1} = 1175$ GeV for a minimal neutralino mass. The peak expected and observed limit had also improved to approximately 550 GeV for the neutralino.

The the observed limit island in Fig. 7.8, at a mass point of $m_{\tilde{q}} = 1350$ GeV and $m_{\tilde{\chi}_1^0} = 430$ GeV, has a potential p_T^{miss} of 900 GeV. It is possible that the production of $t\bar{t}t\bar{t}$ has a statistical fluctuation in this region that is limiting the statistics. This island is not, however, seen in the previous analysis, see Fig. 3.14. The limits have improved for this model to include a limit on the mass up to 2.05 TeV for minimal neutralino mass.

Our analysis was designed to have a significant search parameter space that is inclusive as possible. We have analyzed two signals that show improvement compared to other methods.

Chapter 8

Conclusions

We have now combined all of the data, 136.7 fb^{-1} , and simulation from Run 2 of CMS and computed limits on the cross sections for the direct top squark production, $\tilde{t}_1 \rightarrow t\tilde{\chi}_1^0$, and an indirect top squark production mode, $\tilde{g} \rightarrow t\bar{t}\tilde{\chi}_1^0$.

8.1 Interpreting Results

The limits have been improved to a limit on the masses $m_{\tilde{t}_1} = 1175 \text{ GeV}$ and $m_{\tilde{g}} = 2.05 \text{ TeV}$, for the top squark and guino, respectively. Our analysis was however not able to exclude some low mass regions in the T2tt and a single island in the T1tttt mode. These regions are sensitive to SM fluctuations since they are of similar shape to the signals in this search.

It is possible that a SM processes such as $t\bar{t}t\bar{t}$ could have an over estimated cross section which potentially could cause the missing energy needed to for the island in T1tttt. The regions in T2tt that cannot be excluded are sensitive to $Z \rightarrow \nu\nu$ background. The $Z \rightarrow \nu\nu$ systematics on the normalization and shape could play a significant role in the limit on these cross sections.

8.2 Outlook

We have been able to exclude some potential masses at a 95% CL. This is by no means a statement that SUSY does not exist. As we have seen with the differences

in Fig. 7.7 and 3.9, taking more data and including improved estimations of backgrounds can still cause some of the previously excluded regions to not be excluded anymore. We still need to look at the CLs and limits for the other interesting signal in this search.

Appendix A

Tau Multivariate Analysis

The identification of taus that decay hadronically has been under extensive study to distinguish whether the custom tau multivariate analysis (tauMVA), the isolated track (isotrack) method, or the MVA from that is provided by the tau POG (tauPOG) has the highest efficiency to fake rate. The custom tauMVA was trained on PF charged hadron candidates with $p_T > 10 \text{ GeV}$ and $|\eta| < 2.4$ along with an additional PF photon candidate, if any, with $p_T > 5 \text{ GeV}$ and within a cone of $\Delta R \leq 0.2$ of the charged hadron candidate. The tau candidate is also required to have a transverse mass $m_T(\tau_h, p_T^{miss}) < 100 \text{ GeV}$, where $m_T(\tau_h, p_T^{miss})$ is defined as follows,

$$m_T(\tau_h, p_T^{miss}) = \sqrt{2 \cdot p_T(\tau_h + \text{nearest} \gamma) \cdot p_T^{miss} \cdot (1 - \cos \Delta\phi)}. \quad (\text{A.1})$$

The addition of photons in the final definition is due to the possibility of taus decaying to neutral pions. This improves the resolution for the hadronic tau candidate. The inputs for the MVA are as follows:

- The p_T and $|\eta|$ of the τ candidate.
- The sum p_T of charged particles associated to the primary vertex within ΔR cones of sizes 0.1, 0.2, 0.3, and 0.4 around the τ candidate.
- The summed p_T of all particles within ΔR cones of sizes 0.1, 0.2, 0.3, and 0.4 around the candidate, now including the neutral contribution from pileup parti-

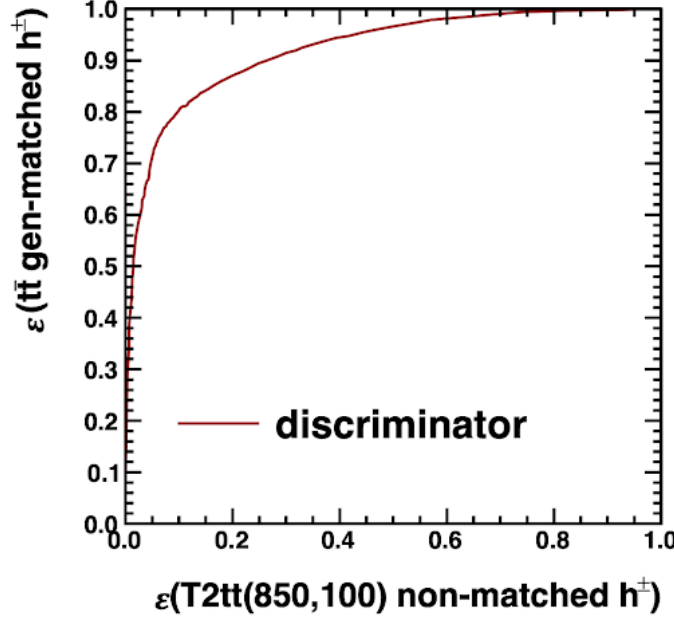


Figure A.1 : A Receiver Operator Characteristic curve for the tauMVA discriminator.

cles, which is reduced by applying the $\Delta\beta$ correction to the neutral component of the isolation quantity.

- The distance in ΔR to the nearest charged PF candidate with $p_T > 1 \text{ GeV}$.
- The distance in ΔR to the axis of the jet containing the τ candidate, and the b-tagging discriminant (DeepCSV) value for the jet, provided that the jet has $p_T > 30 \text{ GeV}$ and $|\eta| < 2.4$.

In Figure A.1, we have a Receiver Operator Characteristic curve to compare the efficiency of the TauMVA in identifying taus that have been gen-level matched and the fake rate of tagging a parton as a tau that has not been gen-level matched. This shows that the TauMVA can potentially be a good discriminator of vetoing taus in our SM background while also not vetoing potential signal events. Then in Fig. A.2,

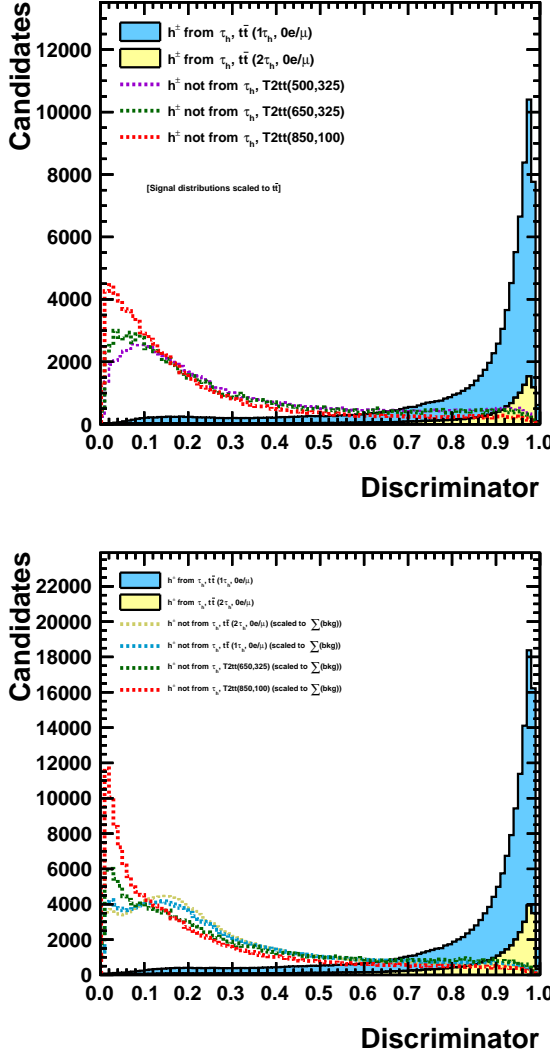


Figure A.2 : Tau MVA discriminator for different types of samples.

we compare the TauMVA discriminator for events that have been matched to a gen-level tau (solid) and those that are not matched (dotted). We see good separation in events that are indeed a tau having a discriminator of approx. 1 and events that

Type	Discriminator Cut	$t\bar{t}$ 1-lepton			$t\bar{t}$ Di-lepton		
		Efficiency	Fake Rate	Efficiency/Fake	Efficiency	Fake Rate	Efficiency/Fake
IsoTrack	-	27.9 %	6.1 %	4.541	24.8 %	6.1 %	4.084
TauMVA	0.68	34.9 %	6.9 %	5.046	24.7 %	5.3 %	4.689
TauMVA	0.70	34.6 %	6.5 %	5.355	24.4 %	4.9 %	4.997
TauMVA	0.71	34.4 %	6.2 %	5.525	24.2 %	4.7 %	5.170
TauMVA	0.73	33.9 %	5.7 %	5.914	23.8 %	4.3 %	5.540
TauMVA	0.74	33.6 %	5.5 %	6.119	23.6 %	4.1 %	5.712
TauMVA	0.75	33.4 %	5.2 %	6.356	23.4 %	3.9 %	5.961

Table A.1 : Comparing the efficiencies and Fake Rates of many difference discriminator cuts for the TauMVA and IsoTrack methods with SM simulation.

Type	Discriminator Cut	T1tttt(2000,100)			T2tt(850,100)		
		Efficiency	Fake Rate	Efficiency/Fake	Efficiency	Fake Rate	Efficiency/Fake
IsoTrack	-	7.4 %	2.9 %	2.503	5.5 %	2.0 %	2.704
TauMVA	0.68	5.7 %	8.1 %	0.696	4.8 %	4.7 %	1.017
TauMVA	0.70	5.5 %	7.5 %	0.735	4.7 %	4.4 %	1.075
TauMVA	0.71	5.5 %	7.2 %	0.760	4.7 %	4.2 %	1.102
TauMVA	0.73	5.4 %	6.6 %	0.806	4.6 %	3.9 %	1.175
TauMVA	0.74	5.3 %	6.3 %	0.832	4.5 %	3.7 %	1.214
TauMVA	0.75	5.2 %	6.0 %	0.869	4.5 %	3.5 %	1.262

Table A.2 : Comparing the efficiencies and Fake Rates of many difference discriminator cuts for the TauMVA and IsoTrack methods with two SUSY simulations.

Methods	$t\bar{t}$ 1-lepton		T1tttt(2000,100)		T2tt(850,100)	
	Veto Percentage	Veto Efficiency	Veto Percentage	Veto Efficiency	Veto Percentage	Veto Efficiency
TauMVA	32.2%	57.7%	12.9 %	10.7 %	6.5%	10.9 %
IsoTrack	21.3 %	37.9 %	4.4 %	2.5 %	2.6 %	6.6 %
TauPOG	171 %	29.7 %	7.0 %	3.2 %	5.2 %	2.5 %
IsoTrack + TauPOG	29.0 %	49.1 %	10.4 %	5.6 %	7.2 %	22.6 %

Table A.3 : Comparing the veto percentage and efficiency for the TauMVA, IsoTrack, TauPOG, and the IsoTrack + TauPOG methods with SM and SUSY simulations.

are not with a value of 0 to 0.2. This allows us to find a cut on the discriminator to maximize tagging real tau decays while also minimizing the fake taus.

Now that we have the definition for the TauMVA and have trained it on our samples to identify hadronically decaying taus. We want to compare the veto ef-

ficiencies and fake rates of the each method: TauMVA, IsoTrack, TauPOG, or a combination of IsoTrack and TauPOG. In Tables A.1 and A.2, we are comparing many different TauMVA cuts, ($> 0.68, > 0.70, > 0.71, > 0.73, > 0.74, > 0.75$), with the IsoTrack method for $t\bar{t}$ single lepton and dilepton SM samples, and T1tttt(2000, 100) and T2tt(850, 100) signal samples. The TauMVA cut of $MVA > 0.71$ gives us the largest efficiency identifying gen taus, while also not vetoing fake taus from the signal events we are interested in analyzing.

In Table A.3, we are now comparing the TauMVA, IsoTrack, TauPOG, and IsoTrack + TauPOG methods for identifying hadronically decaying taus. The TauMVA and IsoTrack + TauPOG methods have very similar veto percentages and efficiencies for SM events, but the IsoTrack + TauPOG method has a similar or better veto percentage and efficiency for signal samples. Thus, our analysis has decided to use that as our tau ID, see Sec. 5.1.8.

Appendix B

Samples

The primary dataset used for this analysis is the MET dataset, which is the data recorded after using the corresponding p_T^{miss} triggers. It contains events triggered by the High Level Trigger (HLT) paths HLT_PFMET x _PFMHT x _IDTight and HLT_PFMET

NoMu x _PFMHTNoMu x _IDTight where PFMET is the particle flow calculated p_T^{miss} , PFMHT is the particle flow calculated negative of H_T , NoMu are the triggers with no muon in the event, and $x = 100, 110, 120, 130$, and 140. The logical OR of these triggers is used to select the search sample.

Table B.1 lists all datasets together with the specific HLT paths of the triggers that were used for the selection of events. The datasets correspond to the full Run 2 dataset are: “Run2016B”, “Run2016C”, “Run2016D”, “Run2016E”, “Run2016F”, “Run2016G”, “Run2016H”, “Run2017B”, “Run2017C”, “Run2017D”, “Run2017E”, “Run2017F”, “Run2018A”, “Run2018B”, “Run2018C”, and “Run2018D” acquisition eras with a total luminosity of 136.7 fb^{-1} [103–105], Table B.1.

The simulated samples used in this analysis, all of which are listed in Table B.2 and B.3, were produced as part of the “Summer16”, “Fall17”, and “Autumn18” Monte Carlo production campaign for Run 2, using MadGraph [106, 107] and Pythia8 [108] in the “NanoAOD” data format. The SM simulated samples are produced at leading order (LO), an additional multiplicative k -factor is applied to the LO total cross section to account for the difference with the next-to-leading order (NLO) cross

Primary dataset	HLT path
	Search sample
MET	HLT_PFMET100_PFMHT100_IDTight OR HLT_PFMETNoMu100_PFMHTNoMu100_IDTight OR HLT_PFMET110_PFMHT110_IDTight OR HLT_PFMETNoMu110_PFMHTNoMu110_IDTight OR HLT_PFMET120_PFMHT120_IDTight OR HLT_PFMETNoMu120_PFMHTNoMu120_IDTight OR HLT_PFMET130_PFMHT130_IDTight OR HLT_PFMETNoMu130_PFMHTNoMu130_IDTight OR HLT_PFMET140_PFMHT140_IDTight OR HLT_PFMETNoMu140_PFMHTNoMu140_IDTight OR HLT_PFMET100_PFMHT100_IDTight_PFHT60 OR HLT_PFMETNoMu100_PFMHTNoMu100_IDTight_PFHT60 OR HLT_PFMET110_PFMHT110_IDTight_PFHT60 OR HLT_PFMETNoMu110_PFMHTNoMu110_IDTight_PFHT60 OR HLT_PFMET120_PFMHT120_IDTight_PFHT60 OR HLT_PFMETNoMu120_PFMHTNoMu120_IDTight_PFHT60 OR HLT_PFMET130_PFMHT130_IDTight_PFHT60 OR HLT_PFMETNoMu130_PFMHTNoMu130_IDTight_PFHT60 OR HLT_PFMET140_PFMHT140_IDTight_PFHT60 OR HLT_PFMETNoMu140_PFMHTNoMu140_IDTight_PFHT60

Table B.1 : Primary datasets used for the analysis and the HLT paths of the corresponding triggers. Datasets from Run2016 are “ReReco” legacy datasets from the 17Jul2018 re-reconstruction, Run2017 is from 31Mar2018 re-reconstruction, and Run2018 Run “A” to “C” are re-reconstruction while Run “D” is promptreco.

section [106, 109–115]. The simulated signal sample cross sections are calculated using LO, NLO, and next-to-leading logarithm (NLL) calculations [116].

B.0.1 Filters

The following filters, recommended by the JetMET POG, are applied to 2016, 2017, and 2018 eras:

- goodVertices where the event is required to have $|z| \leq 24$;
- HBHENoiseFilter, to reduce bad pulse-shape, timing, and hit multiplicity;
- HBHENoiseIsoFilter, to include a requirement on the number of isolated noise channels;
- EcalDeadCellTriggerPrimitiveFilter, to remove events where the energy measured in the ECAL is biased due to energy deposits in dead cell regions;
- BadPFPMuonFilter, to remove badly reconstructed muons from the PF algorithm;

Process	Generator	Dataset	Cross section [pb]
SM processes			
$t\bar{t}, 1\ell$	MADGRAPH	/TTJets_SingleLeptFromT_TuneCUETP8M1_13TeV-madgraphMLM-pythia8/<proc>	182.18
	MADGRAPH	/TTJets_SingleLeptFromTbar_TuneCUETP8M1_13TeV-madgraphMLM-pythia8/<proc>	182.18
	MADGRAPH	/TTJets_DiLept_TuneCUETP8M1_13TeV-madgraphMLM-pythia8/<proc>	87.31
$t\bar{t}, H_T$	MADGRAPH	/TTJets_HT-600to800_TuneCUETP8M1_13TeV-madgraphMLM-pythia8/<proc>	2.76
	MADGRAPH	/TTJets_HT-800to1200_TuneCUETP8M1_13TeV-madgraphMLM-pythia8/<proc>	1.1156
	MADGRAPH	/TTJets_HT-1200to2500_TuneCUETP8M1_13TeV-madgraphMLM-pythia8/<proc>	0.19775
	MADGRAPH	/TTJets_HT-2500toInf_TuneCUETP8M1_13TeV-madgraphMLM-pythia8/<proc>	0.00239
$t\bar{t}Z$	AMCATNLO	/TTZToLLNuNu_M-10_TuneCUETP8M1_13TeV-amcatnlo-pythia8/<proc>	0.2529
	AMCATNLO	/TTZToQQ_TuneCUETP8M1_13TeV-amcatnlo-pythia8/<proc>	0.5297
$t\bar{Z}q$	AMCATNLO	/tZq_ll_4f_13TeV-amcatnlo-pythia8_TuneCUETP8M1/<proc>	0.0758
$t\bar{W}$	MADGRAPH	/ST_tWl_5f_LO_13TeV-MadGraph-pythia8/<proc>	0.01104
	MADGRAPH	/ST_tWnumu_5f_LO_13TeV-MadGraph-pythia8/<proc>	0.02122
$t\bar{t}W$	AMCATNLO	/TTWJetsToLNu_TuneCUETP8M1_13TeV-amcatnloFXFX-madspin-pythia8/<proc>	0.2043
	AMCATNLO	/TTWJetsToQQ_TuneCUETP8M1_13TeV-amcatnloFXFX-madspin-pythia8/<proc>	0.4062
$t\bar{W}$	POWHEG	/ST_tW_top_5f_NoFullyHadronicDecays_13TeV-powheg_TuneCUETP8M1/<proc>	16.295
	POWHEG	/ST_tW_top_5f_inclusiveDecays_13TeV-powheg-pythia8_TuneCUETP8M1/<proc>	35.85
	POWHEG	/ST_tW_antitop_5f_NoFullyHadronicDecays_13TeV-powheg_TuneCUETP8M1/<proc>	16.295
	POWHEG	/ST_tW_antitop_5f_inclusiveDecays_13TeV-powheg-pythia8_TuneCUETP8M1/<proc>	35.85
$t\bar{W}$, t-channel	AMCATNLO	/ST_t-channel_top_4f_inclusiveDecays_13TeV-powhegV2-madspin-pythia8_TuneCUETP8M1/<proc>	136.065
	AMCATNLO	/ST_t-channel_antitop_4f_inclusiveDecays_13TeV-powhegV2-madspin-pythia8_TuneCUETP8M1/<proc>	80.97
$t\bar{W}$, s-channel	AMCATNLO	/ST_s-channel_4f_inclusiveDecays_13TeV-amcatnlo-pythia8_TuneCUETP8M1/<proc>	3.362
W+jets	MADGRAPH, HT bins	/WJetsToLNu_HT-70to100_TuneCUETP8M1_13TeV-madgraphMLM-pythia8/<proc>	1353
		/WJetsToLNu_HT-100to200_TuneCUETP8M1_13TeV-madgraphMLM-pythia8/<proc>	1345
		/WJetsToLNu_HT-200to400_TuneCUETP8M1_13TeV-madgraphMLM-pythia8/<proc>	359.7
		/WJetsToLNu_HT-400to600_TuneCUETP8M1_13TeV-madgraphMLM-pythia8/<proc>	48.91
		/WJetsToLNu_HT-600to800_TuneCUETP8M1_13TeV-madgraphMLM-pythia8/<proc>	12.05
		/WJetsToLNu_HT-800to1200_TuneCUETP8M1_13TeV-madgraphMLM-pythia8/<proc>	5.501
		/WJetsToLNu_HT-1200to2500_TuneCUETP8M1_13TeV-madgraphMLM-pythia8/<proc>	1.329
		/WJetsToLNu_HT-2500toInf_TuneCUETP8M1_13TeV-madgraphMLM-pythia8/<proc>	0.03216
$Z \rightarrow \nu\nu$	MADGRAPH, HT bins	/ZJetsToNuNu_HT-100To200_13TeV-madgraph/<proc>	280.35
		/ZJetsToNuNu_HT-200To400_13TeV-madgraph/<proc>	77.67
		/ZJetsToNuNu_HT-400To600_13TeV-madgraph/<proc>	10.73
		/ZJetsToNuNu_HT-600To800_13TeV-madgraph/<proc>	2.559
		/ZJetsToNuNu_HT-800To1200_13TeV-madgraph/<proc>	1.1796
		/ZJetsToNuNu_HT-1200To2500_13TeV-madgraph/<proc>	0.28833
		/ZJetsToNuNu_HT-2500ToInf_13TeV-madgraph/<proc>	0.006945
QCD	MADGRAPH, HT bins	/QCD_HT100to200_TuneCUETP8M1_13TeV-madgraphMLM-pythia8/<proc>	27990000
		/QCD_HT200to300_TuneCUETP8M1_13TeV-madgraphMLM-pythia8/<proc>	1712000
		/QCD_HT300to500_TuneCUETP8M1_13TeV-madgraphMLM-pythia8/<proc>	347700
		/QCD_HT500to700_TuneCUETP8M1_13TeV-madgraphMLM-pythia8/<proc>	32100
		/QCD_HT700to1000_TuneCUETP8M1_13TeV-madgraphMLM-pythia8/<proc>	6831
		/QCD_HT1000to1500_TuneCUETP8M1_13TeV-madgraphMLM-pythia8/<proc>	1207
		/QCD_HT1500to2000_TuneCUETP8M1_13TeV-madgraphMLM-pythia8/<proc>	119.9
		/QCD_HT2000toInf_TuneCUETP8M1_13TeV-madgraphMLM-pythia8/<proc>	25.24
gg+jets	MADGRAPH, HT bins	/GJets_HT-100To200_TuneCUETP8M1_13TeV-madgraphMLM-pythia8/<proc>	5391.0
		/GJets_HT-200To400_TuneCUETP8M1_13TeV-madgraphMLM-pythia8/<proc>	1168.0
		/GJets_HT-400To600_TuneCUETP8M1_13TeV-madgraphMLM-pythia8/<proc>	132.5
		/GJets_HT-600ToInf_TuneCUETP8M1_13TeV-madgraphMLM-pythia8/<proc>	44.05
$t\bar{t}gg+jets$	AMCATNLO	/TTGJets_TuneCUETP8M1_13TeV-amcatnloFXFX-madspin-pythia8/<proc>	3.697
DY+jets	MADGRAPH, HT bins	/DYJetsToLL_M-50_HT-70to100_TuneCUETP8M1_13TeV-madgraphMLM-pythia8/<proc>	169.9
		/DYJetsToLL_M-50_HT-100to200_TuneCUETP8M1_13TeV-madgraphMLM-pythia8/<proc>	147.4
		/DYJetsToLL_M-50_HT-200to400_TuneCUETP8M1_13TeV-madgraphMLM-pythia8/<proc>	40.99
		/DYJetsToLL_M-50_HT-400to600_TuneCUETP8M1_13TeV-madgraphMLM-pythia8/<proc>	5.678
		/DYJetsToLL_M-50_HT-600to800_TuneCUETP8M1_13TeV-madgraphMLM-pythia8/<proc>	1.367
		/DYJetsToLL_M-50_HT-800to1200_TuneCUETP8M1_13TeV-madgraphMLM-pythia8/<proc>	0.6304
		/DYJetsToLL_M-50_HT-1200to2500_TuneCUETP8M1_13TeV-madgraphMLM-pythia8/<proc>	0.1514
		/DYJetsToLL_M-50_HT-2500toInf_TuneCUETP8M1_13TeV-madgraphMLM-pythia8/<proc>	0.003565
WW	POWHEG	/WWTo2L2Nu_13TeV-powheg/<proc>	12.178
	POWHEG	/WWToLNuQQ_13TeV-powheg/<proc>	49.997
	POWHEG	/WWTo4Q_13TeV-powheg/<proc>	51.723
WZ	AMCATNLO	/WZTo1L1Nu2Q_13TeV_amcatnloFXFX_madspin_pythia8/<proc>	10.71
	POWHEG	/WZTo3LNu_13TeV_TuneCUETP8M1_13TeV-powheg-pythia8/<proc>	4.42965
	AMCATNLO	/WZTo2L2Q_13TeV_amcatnloFXFX_madspin_pythia8/<proc>	5.595
	AMCATNLO	/WZTo1L3Nu_13TeV_amcatnloFXFX_madspin_pythia8/<proc>	3.033
ZZ	AMCATNLO	/ZZTo2Q2Nu_13TeV_amcatnloFXFX_madspin_pythia8/<proc>	4.033
	AMCATNLO	/ZZTo2L2Q_13TeV_amcatnloFXFX_madspin_pythia8/<proc>	3.22
	POWHEG	/ZZTo2L2Nu_13TeV_powheg_pythia8/<proc>	0.564
	POWHEG	/ZZTo4L_13TeV_powheg_pythia8/<proc>	1.212
	AMCATNLO	/ZZTo4Q_13TeV_amcatnloFXFX_madspin_pythia8/<proc>	6.912

Table B.2 : Simulated event samples used for this analysis and the corresponding theoretical cross sections for the processes indicated. For some samples produced at leading order (LO), an additional multiplicative k -factor is applied to the LO total cross section to account for the difference with the next-to-leading order (NLO) cross section. Note that <proc> stands for the string “RunIISummer16MiniAODv3”, “RunIIFall17MiniAODv2”, and “RunIIAutumn18MiniAOD” for samples produced with the full detector simulation.

Process	Generator	Dataset		Cross section [pb]
Signal samples				
T1tttt, FullSim	MADGRAPH	/SMS-T1tttt_mGluino-2000_mLSP-100_TuneCUETP8M1_13TeV-madgraphMLM-pythia8/<proc>		0.000101
	MADGRAPH	/SMS-T1tttt_mGluino-1200_mLSP-800_TuneCUETP8M1_13TeV-madgraphMLM-pythia8/<proc>		0.0955
	MADGRAPH	/SMS-T1tttt_mGluino-1500_mLSP-100_TuneCUETP8M1_13TeV-madgraphMLM-pythia8/<proc>		0.0157
T2tt, FastSim	MADGRAPH	/SMS-T2tt_mStop-150to250_TuneCUETP8M1_13TeV-madgraphMLM-pythia8/<proc>		1.0
	MADGRAPH	/SMS-T2tt_mStop-250to350_TuneCUETP8M1_13TeV-madgraphMLM-pythia8/<fast_proc>		1.0
	MADGRAPH	/SMS-T2tt_mStop-350to400_TuneCUETP8M1_13TeV-madgraphMLM-pythia8/<fast_proc>		1.0
	MADGRAPH	/SMS-T2tt_mStop-400to1200_TuneCUETP8M1_13TeV-madgraphMLM-pythia8/<fast_proc>		1.0
	MADGRAPH	/SMS-T2tt_mStop-1200to2000_TuneCUETP8M1_13TeV-madgraphMLM-pythia8/<fast_proc>		1.0
T2tt, FullSim	MADGRAPH	/SMS-T2tt_mStop-225_mLSP-50_TuneCUETP8M1_13TeV-madgraphMLM-pythia8/<proc>		42.0
	MADGRAPH	/SMS-T2tt_mStop-250_mLSP-150_TuneCUETP8M1_13TeV-madgraphMLM-pythia8/<proc>		24.8
	MADGRAPH	/SMS-T2tt_mStop-250_mLSP-50_TuneCUETP8M1_13TeV-madgraphMLM-pythia8/<proc>		24.8
	MADGRAPH	/SMS-T2tt_mStop-300_mLSP-150_TuneCUETP8M1_13TeV-madgraphMLM-pythia8/<proc>		10.0
	MADGRAPH	/SMS-T2tt_mStop-325_mLSP-150_TuneCUETP8M1_13TeV-madgraphMLM-pythia8/<proc>		6.57
	MADGRAPH	/SMS-T2tt_mStop-425_mLSP-325_TuneCUETP8M1_13TeV-madgraphMLM-pythia8/<proc>		1.54
	MADGRAPH	/SMS-T2tt_mStop-500_mLSP-325_TuneCUETP8M1_13TeV-madgraphMLM-pythia8/<proc>		0.609
	MADGRAPH	/SMS-T2tt_mStop-650_mLSP-350_TuneCUETP8M1_13TeV-madgraphMLM-pythia8/<proc>		0.125
	MADGRAPH	/SMS-T2tt_mStop-850_mLSP-100_TuneCUETP8M1_13TeV-madgraphMLM-pythia8/<proc>		0.0216
T2fb, FastSim	MADGRAPH	/SMS-T2tb_dM-10to80_genHT-160_genMET-80_nWMin-0p1_TuneCUETP8M1_13TeV-madgraphMLM-pythia8/<fast_proc>		21.59-0.02833
T2cc, FastSim	MADGRAPH	/SMS-T2cc_genHT-160_genMET-80_TuneCUETP8M1_13TeV-madgraphMLM-pythia8/<fast_proc>		249.4-0.02833
T2bw, FastSim	MADGRAPH	/SMS-T2bw_TuneCUETP8M1_13TeV-madgraphMLM-pythia8/<fast_proc>		64.50-0.001598
T2tb, FastSim	MADGRAPH	/SMS-T2tb_TuneCUETP8M1_13TeV-madgraphMLM-pythia8/<fast_proc>		64.50-0.003074

Table B.3 : Simulated event samples used for this analysis and the corresponding theoretical cross sections for the processes indicated. The simulated signal sample cross sections are calculated using LO, NLO, and next-to-leading logarithm (NLL) calculations [116]. Note that <proc> stands for the string “RunIISummer16MiniAODv3”, “RunIIFall17MiniAODv2”, and “RunIAutumn18MiniAOD” for samples produced with the full detector simulation.

- GlobalSuperTightHalo2016Filter, to minimize effects of the beam halo which is a process when partons interact upstream of the detector; and
- eeBadScFilter, to remove crystals that are determined to be erroneous.

There is an addition ecalBadCalibFilter for 2017 and 2018 eras only for additional bad calorimeters for those years of data.

Appendix C

List of Acronyms and Initialisms

BPIX	Barrel Pixels
CL	Confidence Level
CMS	Compact Muon Solenoid
CR	Control Region
DeepCSV	Deep Combined Secondary Vertex
ECAL	Electromagnetic Calorimeter
EM	Electromagnetism
FED	Front-end Driver
FPIX	Forward Pixels
GUT	Grand Unified Theory
HCAL	Hadronic Calorimeter
ISR	Initial State Radiation
IVF	Inclusive Vertex Finder
LHC	Large Hadron Collider
LL	Lost Lepton

LSP	Lightest Supersymmetric Particle
MSSM	Minimal Supersymmetric Standard Model
NLL	Next-to-Leading Log
NLO	Next-to-Leading Order
POG	Physics Object Group
PV	Primary Vertex
QCD	Quantum Chromodynamics
QEC	Quantum Electrodynamics
SM	Standard Model
SUSY	Supersymmetry
SV	Secondary Vertex
SR	Search Region
TBM	Token Bit Manager
TF	Transfer Factor
ROC	Readout Chip

Bibliography

- [1] M. K. Gaillard, P. D. Grannis, and F. J. Sciulli, “The standard model of particle physics,” *Reviews of Modern Physics*, vol. 71, pp. S96–S111, Mar. 1999.
- [2] P. Ramond, “Dual Theory for Free Fermions,” *Physical Review D*, vol. 3, pp. 2415–2418, May 1971.
- [3] D. V. Volkov and V. P. Akulov, “Possible universal neutrino interaction,” *JETP Lett.*, vol. 16, pp. 438–440, 1972.
- [4] J. Wess and B. Zumino, “Supergauge transformations in four dimensions,” *Nuclear Physics B*, vol. 70, pp. 39–50, Feb. 1974.
- [5] P. Fayet, “Supergauge invariant extension of the Higgs mechanism and a model for the electron and its neutrino,” *Nuclear Physics B*, vol. 90, pp. 104–124, Jan. 1975.
- [6] R. Barbieri, S. Ferrara, and C. A. Savoy, “Gauge models with spontaneously broken local supersymmetry,” *Physics Letters B*, vol. 119, pp. 343–347, Dec. 1982.
- [7] A. H. Chamseddine, R. Arnowitt, and P. Nath, “Locally Supersymmetric Grand Unification,” *Physical Review Letters*, vol. 49, pp. 970–974, Oct. 1982.
- [8] L. Hall, J. Lykken, and S. Weinberg, “Supergravity as the messenger of supersymmetry breaking,” *Physical Review D*, vol. 27, pp. 2359–2378, May 1983.

- [9] G. L. Kane, C. Kolda, L. Roszkowski, and J. D. Wells, “Study of constrained minimal supersymmetry,” *Physical Review D*, vol. 49, pp. 6173–6210, June 1994.
- [10] M. Papucci, J. T. Ruderman, and A. Weiler, “Natural SUSY Endures,” *JHEP*, vol. 1209, p. 035, 2012.
- [11] J. L. Feng, “Dark Matter Candidates from Particle Physics and Methods of Detection,” *Annual Review of Astronomy and Astrophysics*, vol. 48, pp. 495–545, Aug. 2010. arXiv: 1003.0904.
- [12] G. Bertone and D. Merritt, “Dark Matter Dynamics and Indirect Detection,” *Modern Physics Letters A*, vol. 20, pp. 1021–1036, May 2005. arXiv: astro-ph/0504422.
- [13] H. Georgi and S. L. Glashow, “Unity of All Elementary-Particle Forces,” *Physical Review Letters*, vol. 32, pp. 438–441, Feb. 1974.
- [14] H. Georgi, H. R. Quinn, and S. Weinberg, “Hierarchy of Interactions in Unified Gauge Theories,” *Physical Review Letters*, vol. 33, pp. 451–454, Aug. 1974.
- [15] A. J. Buras, J. Ellis, M. K. Gaillard, and D. V. Nanopoulos, “Aspects of the grand unification of strong, weak and electromagnetic interactions,” *Nuclear Physics B*, vol. 135, pp. 66–92, Mar. 1978.
- [16] R. Barbier, C. BĀrat, M. BesanĀson, M. Chemtob, A. Deandrea, E. Dudas, P. Fayet, S. Lavignac, G. Moreau, E. Perez, and Y. Sirois, “R-Parity-violating supersymmetry,” *Physics Reports*, vol. 420, pp. 1–195, Nov. 2005.

- [17] Y. Grossman and H. E. Haber, “(S)neutrino properties in R-parity-violating supersymmetry: CP-conserving phenomena,” *Physical Review D*, vol. 59, p. 093008, Apr. 1999.
- [18] S. Chatrchyan and V. Khachatryan, “Observation of a new boson at a mass of 125 GeV with the CMS experiment at the LHC,” *Physics Letters B*, vol. 716, pp. 30–61, Sept. 2012.
- [19] G. Aad and T. Abajyan, “Observation of a new particle in the search for the Standard Model Higgs boson with the ATLAS detector at the LHC,” *Physics Letters B*, vol. 716, pp. 1–29, Sept. 2012.
- [20] S. Chatrchyan, V. Khachatryan, A. M. Sirunyan, and A. Tumasyan, “Observation of a new boson with mass near 125 GeV in pp collisions at $\sqrt{s}=7$ and 8 TeV,” *Journal of High Energy Physics*, vol. 2013, p. 81, June 2013.
- [21] A. Collaboration and C. Collaboration, “Combined Measurement of the Higgs Boson Mass in $\sqrt{s}=7$ and 8 TeV with the ATLAS and CMS Experiments,” *Physical Review Letters*, vol. 114, p. 191803, May 2015.
- [22] S. P. Martin, “A Supersymmetry Primer,” *arXiv:hep-ph/9709356*, Sept. 1997. arXiv: hep-ph/9709356.
- [23] D. Griffiths, *Introduction to elementary particles*. Weinheim, Germany: Wiley-VCH (2008) 454 p, 2008.
- [24] “<https://www.quantumdiaries.org/2014/03/14/the-standard-model-a-beautiful-but-flawed-theory/>.”
- [25] M. Peskin and D. Schroeder, *An Introduction to quantum field theory*. Addison-Wesley, 1995.

- [26] F. Halzen and A. D. Martin, *Quarks and Leptons: An Introductory Course in Modern Particle Physics*. New York, Usa: Wiley (1984) 396p, 1984.
- [27] “<https://www.quantumdiaries.org/2010/03/07/more-feynman-diagrams-momentum-conservation/>.”
- [28] Particle Data Group, M. Tanabashi, K. Hagiwara, and K. Hikasa, “Review of Particle Physics,” *Physical Review D*, vol. 98, p. 030001, Aug. 2018.
- [29] M. Kobayashi and T. Maskawa, “CP-Violation in the Renormalizable Theory of Weak Interaction,” *Progress of Theoretical Physics*, vol. 49, pp. 652–657, Feb. 1973.
- [30] A. H. Broeils, “The mass distribution of the dwarf spiral NGC 1560.,” *Astronomy and Astrophysics*, vol. 256, p. 19, Mar. 1992.
- [31] D. W. Saraniti, V. Petrosian, and R. Lynds, “Gravitational Lens Models of Arcs in Abell 2218,” *The Astrophysical Journal*, vol. 458, p. 57, Feb. 1996.
- [32] M. Francis, “A sort of particle-free supersymmetry found in exotic materials,” Apr. 2014.
- [33] J. Alwall, P. C. Schuster, and N. Toro, “Simplified models for a first characterization of new physics at the LHC,” *Physical Review D*, vol. 79, p. 075020, Apr. 2009.
- [34] J. Alwall, M.-P. Le, M. Lisanti, and J. G. Wacker, “Model-independent jets plus missing energy searches,” *Physical Review D*, vol. 79, p. 015005, Jan. 2009.
- [35] D. Alves, N. Arkani-Hamed, and S. Arora, “Simplified models for LHC new physics searches,” *Journal of Physics G: Nuclear and Particle Physics*, vol. 39,

- p. 105005, Sept. 2012.
- [36] D. S. M. Alves, E. Izaguirre, and J. G. Wacker, “Where the sidewalk ends: jets and missing energy search strategies for the 7 TeV LHC,” *Journal of High Energy Physics*, vol. 2011, p. 12, Oct. 2011.
- [37] “Phys. Rev. D 88, 052017 (2013) - Interpretation of searches for supersymmetry with simplified models.”
- [38] G. R. Farrar and P. Fayet, “Phenomenology of the production, decay, and detection of new hadronic states associated with supersymmetry,” *Physics Letters B*, vol. 76, pp. 575–579, July 1978.
- [39] C. Collaboration, “Search for direct production of top squark pairs decaying to all-hadronic final states in pp collisions at $\sqrt{s} = 13$ TeV,” 2016.
- [40] A. Collaboration, “Search for a scalar partner of the top quark in the jets plus missing transverse momentum final state at $\sqrt{s}=13$ TeV with the ATLAS detector,” *Journal of High Energy Physics*, vol. 2017, p. 85, Dec. 2017. arXiv: 1709.04183.
- [41] C. Collaboration, “Search for supersymmetry in multijet events with missing transverse momentum in proton-proton collisions at 13 TeV,” *Physical Review D*, vol. 96, p. 032003, Aug. 2017.
- [42] A. M. Sirunyan, A. Tumasyan, W. Adam, F. Ambrogi, F. Beaudette, A. Lobanov, P. Paganini, and R. Salerno, “Search for new phenomena with the M_{T2} variable in the all-hadronic final state produced in proton-proton collisions at $\sqrt{s} = 13$ TeV,” *The European Physical Journal C*, vol. 77, p. 710, Oct. 2017.

- [43] A. M. Sirunyan, A. Tumasyan, W. Adam, and F. Ambrogi, “Search for direct production of supersymmetric partners of the top quark in the all-jets final state in proton-proton collisions at $s=13\sqrt{s}=13 \text{ TeV}$,” *Journal of High Energy Physics*, vol. 2017, p. 5, Oct. 2017.
- [44] C. Collaboration, “Search for supersymmetry in the all-hadronic final state using top quark tagging in pp collisions at $\sqrt{s}=13\text{TeV}$,” *Physical Review D*, vol. 96, p. 012004, July 2017.
- [45] C. Collaboration, “Search for supersymmetry in proton-proton collisions at 13 {TeV} using identified top quarks,” vol. 97, p. 012007, 2018.
- [46] “<https://twiki.cern.ch/twiki/bin/view/CMSPublic/PhysicsResultsSUS>.”
- [47] T. C. Collaboration and S. Chatrchyan, “The CMS experiment at the CERN LHC,” *Journal of Instrumentation*, vol. 3, pp. S08004–S08004, Aug. 2008.
- [48] L. Evans and P. Bryant, “LHC Machine,” *Journal of Instrumentation*, vol. 3, pp. S08001–S08001, Aug. 2008.
- [49] C. Collaboration, “The CMS trigger system,” *Journal of Instrumentation*, vol. 12, pp. P01020–P01020, Jan. 2017.
- [50] “CMS Technical Design Report for the Pixel Detector Upgrade,” Sept. 2012.
- [51] M. Kilpatrick, “FED firmware interface testing with pixel phase 1 emulator,” *PoS*, vol. TWEPP-17, p. 074, Mar. 2018.
- [52] C. Collaboration, “Description and performance of track and primary-vertex reconstruction with the CMS tracker,” *Journal of Instrumentation*, vol. 9, pp. P10009–P10009, Oct. 2014. arXiv: 1405.6569.

- [53] “The CMS electromagnetic calorimeter project,” 1997.
- [54] T. C. Collaboration, “CMS Physics Technical Design Report, Volume II: Physics Performance,” *Journal of Physics G: Nuclear and Particle Physics*, vol. 34, pp. 995–1579, June 2007.
- [55] “The CMS hadron calorimeter project,” 1997.
- [56] A. Quadt, *Top Quark Physics at Hadron Colliders*. No. 28 in Advances in Physics of Particles and Nuclei, Berlin: Springer, 2007.
- [57] A. Lenz, “Lifetimes and HQE,” *arXiv:1405.3601 [hep-ex, physics:hep-ph]*, Sept. 2019. arXiv: 1405.3601.
- [58] “Jet Performance in pp Collisions at 7 TeV,” 2010.
- [59] M. Cacciari, G. P. Salam, and G. Soyez, “The anti-ktjet clustering algorithm,” *Journal of High Energy Physics*, vol. 2008, pp. 063–063, Apr. 2008.
- [60] “<https://twiki.cern.ch/twiki/bin/view/CMS/JetID>.”
- [61] “<https://twiki.cern.ch/twiki/bin/view/CMS/IntroToJEC>.”
- [62] M. Cacciari and G. P. Salam, “Pileup subtraction using jet areas,” *Physics Letters B*, vol. 659, pp. 119–126, Jan. 2008.
- [63] “Pileup Removal Algorithms,” 2014.
- [64] D. Bertolini, P. Harris, M. Low, and N. Tran, “Pileup per particle identification,” *Journal of High Energy Physics*, vol. 2014, p. 59, Oct. 2014.
- [65] “Performance of b tagging algorithms in proton-proton collisions at 13 TeV with Phase 1 CMS detector - CERN Document Server.”

- [66] “<https://twiki.cern.ch/twiki/bin/viewauth/CMS/BtagRecommendation2016legacy>.”
- [67] “<https://twiki.cern.ch/twiki/bin/viewauth/CMS/BtagRecommendation94x>.”
- [68] “<https://twiki.cern.ch/twiki/bin/viewauth/CMS/BtagRecommendation102x>.”
- [69] “<https://twiki.cern.ch/twiki/bin/viewauth/CMS/BTagSFMethods>.”
- [70] “Top Tagging with New Approaches - INSPIRE-HEP.”
- [71] “Identification of high transverse momentum top quarks in pp collisions at [equation] TeV with the ATLAS detector | SpringerLink.”
- [72] Y. Ganin and V. Lempitsky, “Unsupervised Domain Adaptation by Backpropagation,” *arXiv:1409.7495 [cs, stat]*, Feb. 2015. arXiv: 1409.7495.
- [73] A. J. Larkoski, S. Marzani, G. Soyez, and J. Thaler, “Soft drop,” *Journal of High Energy Physics*, vol. 2014, p. 146, May 2014.
- [74] M. Dasgupta, A. Fregoso, S. Marzani, and G. P. Salam, “Towards an understanding of jet substructure,” *Journal of High Energy Physics*, vol. 2013, p. 29, Sept. 2013.
- [75] C. G. Lester and D. J. Summers, “Measuring masses of semi-invisibly decaying particle pairs produced at hadron colliders,” *Physics Letters B*, vol. 463, pp. 99–103, Sept. 1999.
- [76] A. Barr, C. Lester, and P. Stephens, “A variable for measuring masses at hadron colliders when missing energy is expected\\$\\mathsemicolon\\$mT2: the truth behind the glamour,” *Journal of Physics G: Nuclear and Particle Physics*, vol. 29, pp. 2343–2363, Sept. 2003.

- [77] T. C. collaboration, “Missing transverse energy performance of the CMS detector,” *Journal of Instrumentation*, vol. 6, pp. P09001–P09001, Sept. 2011.
- [78] B. Penning, “The pursuit of dark matter at collidersâan overview,” *Journal of Physics G: Nuclear and Particle Physics*, vol. 45, p. 063001, May 2018.
- [79] “<https://twiki.cern.ch/twiki/bin/view/CMS/MissingETRun2corrections>.”
- [80] C. Collaboration, “Search for New Physics with Jets and Missing Transverse Momentum in pp collisions at $\sqrt{s} = 7$ TeV,” *Journal of High Energy Physics*, vol. 2011, p. 155, Aug. 2011. arXiv: 1106.4503.
- [81] “<https://twiki.cern.ch/twiki/bin/view/Main/InclusiveSecondaryVertexFinder>.”
- [82] R. Fruehwirth, W. Waltenberger, K. Prokofiev, T. Speer, P. Vanlaer, E. Chabanat, and N. Estre, “New vertex reconstruction algorithms for CMS,” *arXiv:physics/0306012*, June 2003. arXiv: physics/0306012.
- [83] “Performance of electron reconstruction and selection with the CMS detector in proton-proton collisions at $\sqrt{s}=8$ TeV,” *Journal of Instrumentation*, vol. 10, pp. P06005–P06005, June 2015.
- [84] T. C. collaboration, “The performance of the CMS muon detector in proton-proton collisions at $\sqrt{s}=7$ TeV at the LHC,” *Journal of Instrumentation*, vol. 8, pp. P11002–P11002, Nov. 2013.
- [85] C. Collaboration, “Performance of the CMS muon detector and muon reconstruction with proton-proton collisions at $\sqrt{s}=13$ TeV,” *Journal of Instrumentation*, vol. 13, pp. P06015–P06015, June 2018. arXiv: 1804.04528.
- [86] “<https://twiki.cern.ch/twiki/bin/view/CMS/CutBasedElectronIdentificationRun2>.”

- [87] “https://twiki.cern.ch/twiki/bin/view/CMSPublic/SWGuideMuonId#Loose_muon.”
- [88] “The CMS Particle Flow Algorithm - INSPIRE-HEP.”
- [89] B. P. Roe, H.-J. Yang, J. Zhu, Y. Liu, I. Stancu, and G. McGregor, “Boosted Decision Trees as an Alternative to Artificial Neural Networks for Particle Identification,” Aug. 2004.
- [90] A. Hoecker, P. Speckmayer, J. Stelzer, J. Therhaag, and A. Zemla, “TMVA - Toolkit for Multivariate Data Analysis,” *arXiv:physics/0703039*, Mar. 2007. arXiv: physics/0703039.
- [91] C. Bravo, “Search for Supersymmetric Top Quarks in pp Collisions at $\sqrt{s} = 13$ TeV,” vol. CMS-AN-15-027, 2015.
- [92] D. R. Tovey, “Transformation properties of the transverse mass under transverse Lorentz boosts at hadron colliders,” *The European Physical Journal C*, vol. 79, p. 294, Apr. 2019. arXiv: 1902.04476.
- [93] C. Collaboration, “Search for gluino mediated bottom- and top-squark production in multijet final states in pp collisions at 8 TeV,” *Physics Letters B*, vol. 725, pp. 243–270, Oct. 2013. arXiv: 1305.2390.
- [94] F. Fiedler, “Precision Measurements of the Top Quark Mass,”
- [95] V. Khachatryan, A. Sirunyan, A. Tumasyan, W. Adam, E. Asilar, T. Bergauer, J. Brandstetter, E. Brondolin, M. Dragicevic, J. Erö, M. Flechl, M. Friedl, R. Fröhlich, V. Ghete, C. Hartl, N. Härnemann, J. Hrubec, M. Jeitler, V. Knoblz, and N. Woods, “Search for the production of an excited bottom quark decaying to tW in proton-proton collisions at $s = 8 \text{ TeV}$,” *Journal of High Energy Physics*, vol. 2016, Jan. 2016.

- [96] G. Aad, “Measurement of hard double-parton interactions in $\infty(\rightarrow \ell\ell\nu) \mathcal{N}$ -jet events at $\sqrt{s} = 7$ TeV with the ATLAS detector,” *New Journal of Physics*, vol. 15, p. 033038, Mar. 2013.
- [97] G. J. Feldman and R. D. Cousins, “A Unified approach to the classical statistical analysis of small signals,” *Phys.Rev.*, vol. D57, pp. 3873–3889, 1998.
- [98] G. Cowan, K. Cranmer, E. Gross, and O. Vitells, “Asymptotic formulae for likelihood-based tests of new physics,” *The European Physical Journal C*, vol. 71, p. 1554, Feb. 2011. arXiv: 1007.1727.
- [99] “Procedure for the LHC Higgs boson search combination in Summer 2011,” Aug. 2011.
- [100] A. L. Read, “Presentation of search results: the CLs technique,” *Journal of Physics G: Nuclear and Particle Physics*, vol. 28, pp. 2693–2704, Sept. 2002.
- [101] T. Junk, “Confidence Level Computation for Combining Searches with Small Statistics,” *Nuclear Instruments and Methods in Physics Research Section A: Accelerators, Spectrometers, Detectors and Associated Equipment*, vol. 434, pp. 435–443, Sept. 1999. arXiv: hep-ex/9902006.
- [102] A. L. Read, “Modified frequentist analysis of search results (the CL_{s} method),” 2000.
- [103] “CMS Luminosity Measurements for the 2016 Data Taking Period,” 2017.
- [104] “CMS luminosity measurement for the 2017 data-taking period at $\sqrt{s} = 13\text{TeV}$,” 2018.

- [105] “CMS luminosity measurement for the 2018 data-taking period at $\sqrt{s} = 13\text{ TeV}$,” 2019.
- [106] “The automated computation of tree-level and next-to-leading order differential cross sections, and their matching to parton shower simulations | SpringerLink.”
- [107] J. Alwall, S. HÃ¶che, F. Krauss, N. Lavesson, L. LÃ¶nnblad, F. Maltoni, M. Mangano, M. Moretti, C. Papadopoulos, F. Piccinini, S. Schumann, M. Treccani, J. Winter, and M. Worek, “Comparative study of various algorithms for the merging of parton showers and matrix elements in hadronic collisions,” *The European Physical Journal C*, vol. 53, pp. 473–500, Feb. 2008.
- [108] T. SjÃ¶strand, S. Mrenna, and P. Skands, “A brief introduction to PYTHIA 8.1,” *Computer Physics Communications*, vol. 178, pp. 852–867, June 2008.
- [109] M. Czakon and A. Mitov, “Top++: A program for the calculation of the top-pair cross-section at hadron colliders,” *Computer Physics Communications*, vol. 185, pp. 2930–2938, Nov. 2014.
- [110] P. Kant, O. M. Kind, T. Kintscher, T. Lohse, T. Martini, S. MÃ¶lbitz, P. Rieck, and P. Uwer, “HatHor â for single top-quark production: Updated predictions and uncertainty estimates for single top-quark production in hadronic collisions,” *Computer Physics Communications*, vol. 191, pp. 74–89, June 2015.
- [111] M. Aliev, H. Lacker, U. Langenfeld, S. Moch, P. Uwer, and M. Wiedermann, “HATHOR â HAdronic Top and Heavy quarks crOss section calculatoR,” *Computer Physics Communications*, vol. 182, pp. 1034–1046, Apr. 2011.
- [112] T. Gehrmann, M. Grazzini, and S. Kallweit, “ $\mathcal{W}^+ \mathcal{W}^-$ Production at Hadron Colliders in Next to Next to Leading Order QCD,”

- Physical Review Letters*, vol. 113, p. 212001, Nov. 2014.
- [113] J. M. Campbell and R. K. Ellis, “Update on vector boson pair production at hadron colliders,” *Physical Review D*, vol. 60, p. 113006, Nov. 1999.
- [114] “Vector boson pair production at the LHC | SpringerLink.”
- [115] Y. Li and F. Petriello, “Combining QCD and electroweak corrections to dilepton production in the framework of the FEWZ simulation code,” *Physical Review D*, vol. 86, p. 094034, Nov. 2012.
- [116] C. Borschensky, M. KrÄmer, A. Kulesza, M. Mangano, S. Padhi, T. Plehn, and X. Portell, “Squark and gluino production cross sections in \$\$pp\$\$collisions at \$\$\sqrt{s} = 13, 14, 33\$\$and \$\$100\$\$tev,” *The European Physical Journal C*, vol. 74, p. 3174, Dec. 2014.